



HAL
open science

Ultrafast Nanoscale 3D Coherent X-ray Imaging

Joana Cristina Matos Raimundo Duarte De

► **To cite this version:**

Joana Cristina Matos Raimundo Duarte De. Ultrafast Nanoscale 3D Coherent X-ray Imaging. Optics / Photonic. Université Paris Saclay (COMUE), 2019. English. NNT : 2019SACLS372 . tel-03091993

HAL Id: tel-03091993

<https://theses.hal.science/tel-03091993>

Submitted on 1 Jan 2021

HAL is a multi-disciplinary open access archive for the deposit and dissemination of scientific research documents, whether they are published or not. The documents may come from teaching and research institutions in France or abroad, or from public or private research centers.

L'archive ouverte pluridisciplinaire **HAL**, est destinée au dépôt et à la diffusion de documents scientifiques de niveau recherche, publiés ou non, émanant des établissements d'enseignement et de recherche français ou étrangers, des laboratoires publics ou privés.

Ultrafast Nanoscale 3D Coherent X-ray Imaging

Thèse de doctorat de l'Université Paris-Saclay
préparée à l'Université Paris-Sud

École doctorale n°572 Ondes et matières (EDOM)
Spécialité de doctorat: Physique

Thèse présentée et soutenue à Gif-sur-Yvette, le 18 Octobre 2019, par

Joana Cristina de Matos Raimundo Duarte

Composition du Jury:

Dr. Philippe Zeitoun	Président
<i>Laboratoire d'Optique Appliquée, ENSTA ParisTech – France</i>	
Prof. Filipe Maia	Rapporteur
<i>Department of Physics and Astronomy, Molecular and Condensed Matter Physics, Uppsala University – Suède</i>	
Dr. Amelle Zaïr	Rapporteur
<i>Photonics & Nanotechnology Group, King's College London – Royaume-Uni</i>	
Dr. Kadda Medjoubi	Examineur
<i>Synchrotron Soleil - Division Expériences / Ligne Nanoscopium – France</i>	
Dr. Manuel Guizar-Sicairos	Examineur
<i>Paul Scherrer Institut – Suisse</i>	
Prof. Marta Fajardo	Co-Directrice de thèse
<i>Institute for Plasmas and Nuclear Fusion, Instituto Superior Técnico – Portugal</i>	
Dr. Hamed Merdji	Directeur de thèse
<i>Laboratoire LIDYL, CEA Saclay – France</i>	

Acknowledgments

I owe my gratitude to many incredible people for this achievement. From people that were directly involved in my academic research or collaborated in experiments; to those who provided advice, ideas and discussions; or gave me moral support and stood by my side during all the process, from celebration to frustration times.

Firstly, I would like to thank Hamed Merdji for his research guidance throughout these years. His participation in the success of this dissertation was constant, either through his availability to always discuss different approaches, either through the different opportunities that he has provided me. I can particularly thank him for the suggestion of interesting projects, partnerships or even the attendance to training schools and conferences, which made me grow in different directions parallel to my thesis.

I have to thank as well Marta Fajardo for all her fruitful contributions and her presence, particularly in the first moments of this thesis. She helped me substantially with her great intuition and inventiveness for approaching the problems, as well as her contagious enthusiasm for research. It was exactly this enthusiasm that made me sure of my decision when I enrolled in the challenge of this PhD.

As a third supervision element, I was lucky to have Willem Boutu, to whom I particularly acknowledge. I knew I could always count on Willem to solve all sorts of problems and to undertake all types of scientific discussions. His intelligence allied with his remarkable commitment and kindness made him an extraordinary person to work with and an absolute reference.

I also thank my dream team at CEA for being the best team ever to work with. Thank you Maria Kholodtsova, Shatha Kaassamani, David Gauthier, Dominik Franz, Rana Nicolas, Sven Fröhlich, Viktoria Nefedova, Ahmed Maghraoui, Julius Huijts, Julien Samaan, Rémy Cassin, Léa Krafft, Sara Fernandez, Robin Sureau, and Xu Liu. Thank you for bringing an absolutely great environment to the office and for making the experience of going to work every day so special. Thank you Maria, for always being there for coffee (and *bêtises*), for the great talks about the most random topics, the barbecues *chez toi*, and all the nice tips about for instance 'How to treat a sore throat', which I will definitely keep in my medical skillset forever ;). Thank you Shathita, my *voisine du cœur*, for being the absolute best office mate, for all your kindness, your amazing Lebanese aperitifs, and for your self-defence skillset and hints, which I will always save in my mind (as it might come in handy one day ;)...). Thank you David Gautchouer, my partner in crime, for the great partnerships in *bêtises*, the joggings every morning to catch the RER followed by your iconic 'Hodor' moments, the nice french lessons, and all the great work discussions

and lab moments, which were crucial for this thesis. Thank you Domichou, for your emblematic random whispers (of 'João', 'Ahmed', 'Kaassamani',...), for the french messages in Cyrillic, for all your availability to teach me something new in french, and for the amazing bouldering moments. Thank you Ranachou for being so kind, for your amazing yoga classes and for always having the right advice for every occasion: you are an absolute reference. Thank you Sven, the most Portuguese German I've ever known, for being such a great office mate, for always being present in the *soirées* of *Maison du Portugal* and for letting me play with your helicopter (I swear it was not me who broke it!). Thank you Vika for being such a great person, for our nice discussions, your wise advices, and your Robin Hood lessons which I hope someday can progress from an imaginary bow-and-arrow set to a real one. Thank you Ahmed for all the funny lab days and the whistling duets with the *Godfather* soundtrack. Thank you Julius for the valuable discussions, and for being such a nice colleague and office mate (sorry for stealing your desk when you left for Barcelona!). Thank you Julien for being there in the beginning and marking so positively my first moments in France. Thank you Rémy for your good office mood and your useful lab advices. Thank you Léa for all your kindness and cuteness. Thank you Sara for your great mood and your willingness to help everyone. Thank you Robin *des bois* for your great mood and for mentioning my watermelon in the acknowledgements of your internship report. Thank you Xu for being the real Xu (aka *chou*) of the group and for the nice hot pot.

I also thank my group in Portugal, which always allowed a good and friendly work environment and whose contribution was extremely important for me, particularly in the first moments of this thesis. Swen Künzel and Gareth Williams, for all their availability and help, as well as great and important discussions. Jayanath Koliyadu for his kindness and tireless collaboration in the lab. Thomas Wodzinski for being a great office mate and for his collaboration in the SLM experiment. Patrícia Estrela, for her kindness and availability during all our brief but interesting interactions.

I acknowledge CEA-Saclay, and especially the LIDYL group, for all the tools they provided me to develop this research work and thesis, from the space and equipment, to the amazing group of people, always available to help in the most diverse matters. I particularly acknowledge Dr. Philippe Martin, head of the lab, for his availability. Aura González for great discussions and fruitful collaboration on the topic of the spatial coherence. I acknowledge as well Caroline Lebe for all the help provided with bureaucratic issues and Ramona Corman for the Nanoxim data she provided.

I acknowledge all the IPFN, and especially the GoLP team, which welcomed me to the group and allowed great conviviality moments, as well as several interesting discussions on the most varied topics. A special thanks goes also to the people that shared the room with me at GoLP (before me and the team moved to the VOXEL room) which always allowed a good and friendly work environment. I also acknowledge Celso João and Hugo Pires for the availability in the lab, and João Rodrigues for great advice and discussions.

I am also very thankful to Dr. Philippe Zeitoun, from LOA, for my collaboration on the experiment of XUV in-line holography with correction of aberrations, for facilitating travel funds to perform this experiment, and for great discussions and support. From Dr. Zeitoun's group, I would like to thank Hugo

Dacasa for welcoming me to their lab and helping me in the setup of the experiment.

From INESC-MN, I acknowledge Dr. Susana Freitas for great support, and for giving me access to the lab and tools for the fabrication of the XUV test samples. I acknowledge as well Dr. Diana Leitão for all her availability, help and all the time she spent teaching me all the fabrication steps. I would like to particularly thank her for her kindness and the time she spent working on my samples without my presence there, in a period of tough deadlines for me.

I acknowledge as well Dr. Henry Chapman, Dr. Yoshinori Nishino and Dr. Ivan Vartaniants for interesting collaborations, discussions and for the data they provided for my tests. I thank Helena Contreiras for the help on transferring formulas to latex format, which made me reduce some working time on my thesis. I also thank my brother, Pedro Duarte, for reducing some hours of my work by helping me with some entries for my Glossary, Nomenclature and Bibliography sections.

To the members of my thesis committee, Dr. Philippe Zeitoun, Dr. Hamed Merdji, Prof. Marta Fajardo, Prof. Filipe Maia, Dr. Amelle Zaïr, Dr. Manuel Guizar-Sicairos, and Dr. Kadda Medjoubi. Thanks for taking the time to read this document, for the comments, discussions and all the valuable feedback. Thank you as well for all the support and friendly words on the day of my defence.

Also, many thanks to the FET Open H2020 VOXEL project (grant agreement no. 665207), which was the main source of funding and resources for my PhD, funding as well my participation in multiple conferences and meetings (Coherence 2018 in Port Jefferson, New York, USA; Face2Phase 2017 in Delft, Netherlands, etc.). Laserlab Europe (grant no. 654148), which funded my travelling and accommodation in the experiment of LOA. COST Action MP1203, which covered all my expenses from the meeting "X-ray optics metrology" in Athens, Greece. H2020 MEDEA Marie Skłodowska Curie Innovative Training Networks (grant no. 641789), which covered part of my expenses from the summer school "Ultrafast dynamics with intense radiation sources" in Crete, Greece. Without their funding, I could not have considered exploiting these opportunities.

A special thanks goes to all my friends, which provided me great moments of amusement and inspiration, being always there when I needed. I thank these important persons for all the love and support, which was crucial for my development and the success of this thesis. Moreover, I thank this thesis experience for introducing me to great people that I will keep calling friends for the rest of my life.

At last, I specially thank my dream family. Aos meus pais e ao meu irmão, pelo seu contínuo apoio e encorajamento durante todo o meu doutoramento. Agradeço-lhes por todas as oportunidades que me proporcionaram, não apenas neste período de tese, mas ao longo da minha vida, que me levaram a esta realização e a tantas outras. Eles são referências absolutas para mim de tantas maneiras que não consigo descrever. Agradeço-lhes o amor incondicional, as discussões e conselhos e todo o processo de separação para um país diferente pelo qual tiveram de passar para a realização desta tese. Agradeço-lhes a constante presença, mesmo com a separação imposta pela distância. Agradeço aos meus avós, padrinhos e primos por todo o amor e apoio incondicional ao longo de toda a minha vida, e em particular desta tese. Não tenho palavras para descrever toda a acumulação de gratidão que tenho por estas pessoas e toda a inspiração que elas me transmitem todos os dias da minha vida. Agradeço

aos restantes membros da minha família pelo seu apoio e por fazerem parte desta minha família de sonho.

Abstract

Ultrafast 3D structural imaging of single, non-periodic nanospecimens has become an increasingly important topic of research due to the capability of providing breakthrough discoveries on the study of macromolecular structure and dynamics, which can change our perception of biology and physics. This has motivated the development of X-ray sources and optics; and the improvement of coherent lensless imaging techniques. In coherent lensless imaging, one can reconstruct a complex-valued image of a sample, proportional to the object transmission function, from its diffraction pattern. This is accomplished using computational algorithms, which replace the conventional lens systems, overcoming the manufacturing difficulties of focusing elements for XUV and X-rays. Using these techniques with ultrafast and coherent light sources, such as free electron lasers (FELs) and high-order harmonics, one can investigate dynamic phenomena at femtosecond-time scales. In this thesis, we perform several studies employing different coherent lensless techniques, proposing and testing improvements for increasing performances in the quest for single-shot 3D imaging.

A first part of the work is dedicated to experimental studies at LUCA's high harmonics beamline of CEA Saclay, where computational corrections of spatial coherence in Fourier transform holography (FTH) are investigated. Here, we report the first experimental demonstration in single shot of a new technique for characterisation of the spatial coherence of a source, with application on Gaussian-Schell beams. It is based on the interferometry through a 2D non-redundant array (NRA) of apertures, designed in a strategic configuration to disentangle the degree of spatial coherence from the intensity distribution of a beam. This feature makes it compatible with single acquisition and robust against beam-pointing instabilities, two critical parameters for conventional coherence measurement techniques in the XUV/X-ray ranges.

In a second part, we propose and demonstrate a new approach, compatible with single-shot imaging, to correct in-line reconstructions from the aberrations of the illuminating beam. We propose an approach for simulation and reconstruction of holograms, generated from in-line holography with waves affected by aberrations, allowing for a compensation of the aberrations of the beam, while making use of magnification. We explore this first approach with simulations, using the experimental wavefront of an XUV beam focused by a KB optics system. We report a strong compromise of the quality of in-line reconstructions and demonstrate a correction of the effects of aberrations, when accounting with the beam wavefront. A new algorithm is also proposed for simultaneous correction of in-line holograms from optical aberrations

and twin image. The twin-image correction implementation is firstly tested with experimental data from a biological sample (phase and amplitude) illuminated by an aberration-free spherical-wave reference. Good compatibility of the routine with 3D imaging is reported. An experimental validation with an astigmatic wavefront is finally performed employing a HeNe laser. The setup is assembled with a wavefront sensor, which allows the measurement of the phase map and respective Zernike coefficients in the conditions whereby the hologram is recorded. We discuss briefly an implementation using XUV harmonics, which was not successfully accomplished due to a limited beamtime.

Finally, a third part of this manuscript is dedicated to the application of concepts from Computer Stereo vision to lensless X-ray imaging. In this context, a local algorithm for stereo matching is developed, with a 3D rendering applied to a lensless X-ray transmission scheme. We explore this scheme through simulations providing discussions on how to overcome the problems inherent to the transmission geometry in X-ray stereo imaging. We present an implementation of single-acquisition stereo lensless imaging in an XUV HHG-based setup, with a setup based on the separation of a high-order harmonics (HH) beam into two coherent sub-beams, which are later focused on the sample with a controllable angle. Under this scheme a stereo-pair of diffraction patterns can be captured in a single-femtosecond acquisition. Moreover, this system is perfectly suited to be implemented at XFELs and make use of the high brilliance of these sources. Implementing this setup in LUCA's harmonics beamline we report retrieving depth insights of a pure amplitude sample in a proof-of-principle of computed coherent-diffraction-stereo imaging. We apply as well computed X-ray stereo vision to biological samples with predominantly-curved topography, reporting that the stereo foundations often fail in these samples. With the aim of overcoming the stereo ambiguity in curved topographies and smooth composition gradients, we propose to use contrast surface labels. We exploit the idea using two views from a test sample composed by an arrangement of 50-nm-diameter gold spheres spread on a pyramid-shaped indentation. We are able to successfully reproduce the pyramidal distribution of nanoparticles and, as well, the object dimensions. Here, a 3D reconstruction is obtained without any *a priori* knowledge, proving that metallic nanoparticles (or clusters of them), offering high contrast to X-rays, can be used as surface labels to trace the 3D profile of objects. This is particularly impactful for curved surfaces or smooth composition gradients, allowing to overcome the limitations of the technique for these topographies.

French Summary

L'imagerie structurale ultrarapide en 3D de spécimens nanométriques isolés et non périodiques est devenue un sujet de recherche de plus en plus important. Cette technique ouvre la voie à l'étude de la structure et de la dynamique macromoléculaires avec des résolutions atto/femtoseconde, susceptible de modifier notre perception de la biologie et de la physique. Cela a motivé le développement des sources de rayons X, des optiques X et de nouvelles techniques d'imagerie ultra-résolvante. En imagerie cohérente sans lentille, il est possible de reconstruire une image complexe d'un échantillon, proportionnelle à la fonction de transmission de l'objet, à partir de sa figure de diffraction. Ceci est accompli en utilisant des algorithmes de calcul, qui remplacent les systèmes de lentilles conventionnels, surmontant les difficultés de fabrication des éléments de focalisation pour les rayons XUV et X. En utilisant ces techniques avec des sources de lumière ultra-rapides et cohérentes, telles que des lasers à électrons libres (en anglais *free electron lasers*) et des harmoniques d'ordre élevé, il est possible d'étudier des phénomènes dynamiques avec des résolutions femtoseconde et nanométrique. Dans cette thèse, nous réalisons plusieurs études utilisant différentes techniques cohérentes d'imagerie sans lentille, proposant et testant des améliorations pour augmenter les performances dans la quête de l'imagerie 3D en simple tir.

Une première partie du travail est consacrée aux études expérimentales réalisées sur la ligne de lumière à hautes harmoniques de LUCA du CEA Saclay, où l'on étudie les corrections informatiques de la cohérence spatiale en holographie par transformée de Fourier (en anglais *Fourier transform holography*). Nous rapportons ici la première démonstration expérimentale en simple tir d'une nouvelle technique de caractérisation de la cohérence spatiale d'une source, avec application sur des faisceaux de Gauss-Schell. La technique est basée sur l'interférométrie via un réseau d'ouvertures 2D non redondantes, conçues dans une configuration stratégique pour désintriquer le degré de cohérence spatiale de la distribution d'intensité d'un faisceau. Cette caractéristique la rend compatible avec les instabilités d'acquisition simple tir et de pointé de faisceau, deux paramètres critiques pour les techniques de mesure de cohérence conventionnelles dans les gammes XUV / rayons X. Nous montrons aussi que la cohérence partielle du faisceau a un effet limité sur les reconstructions holographique, en particulier lorsque comparée aux fortes variations d'intensité subies par le faisceau dans l'échantillon.

Dans une seconde partie, nous proposons de corriger les reconstructions en holographie en ligne à partir des aberrations du faisceau incident tout en conservant le grandissement. En effectuant des

simulations utilisant le front d'onde expérimental d'un faisceau XUV focalisé par un système optique KB, nous rapportons un fort compromis sur la qualité des reconstructions. Un nouvel algorithme est également proposé pour la correction de l'image jumelle. La mise en œuvre a été validée sur un échantillon biologique (phase et amplitude). Une validation expérimentale avec un front d'onde astigmatique est également réalisée sur un échantillon synthétique. La configuration est assemblée avec un capteur de front d'onde qui permet de capturer la carte de phase et les coefficients de Zernike respectifs dans les conditions dans lesquelles l'hologramme est enregistré. Nous discutons brièvement d'une implémentation utilisant des harmoniques XUV, qui n'a pas été finalisée avec succès en raison d'un temps de faisceau limité.

Finalement, une troisième partie de ce manuscrit est consacrée à l'application de concepts de machine vision à l'imagerie sans lentille. Dans ce contexte, un algorithme local d'appariement stéréo est développé et appliqué à différents cas: amplitude, phase et marqueurs nanométriques. La prise de donnée est effectuée en une acquisition unique, avec une configuration basée sur la séparation d'un faisceau d'harmoniques d'ordre élevé en deux sous-faisceaux cohérents, qui sont ensuite focalisés sur l'échantillon, avec un angle contrôlable. Selon ce schéma, une paire stéréo de figures de diffraction peut être capturée lors d'une acquisition d'un seul tir femtoseconde. De plus, ce système est parfaitement adapté aux laser à électrons libres permettant ainsi de tirer parti de la brillance élevée de ces sources. Une première démonstration de principe est faite sur la ligne de lumière harmonique de LUCA. Nous appliquons également la vision stéréoscopique aux rayons X à des échantillons biologiques ayant une topographie à prédominance incurvée, en indiquant que les contraintes stéréoscopiques échouent souvent sur ces échantillons. Dans le but de surmonter l'ambiguïté stéréo des topographies courbes et des dégradés de composition lisses, nous proposons d'utiliser des marqueurs de volume à fort contraste. Nous validons cette idée en utilisant deux vues d'un échantillon test composé d'un agencement de sphères d'or de 50 nm de diamètre, réparties sur une pyramide nanométrique en Si_3N_4 . Nous sommes capables de reproduire avec succès la distribution pyramidale des nanoparticules et également les dimensions de l'objet. Ici, une reconstruction 3D est obtenue sans aucune connaissance *a priori* de l'objet. Ceci est particulièrement intéressant pour les surfaces courbes ou les gradients de composition lisses, ce qui permet de surmonter les limites de la technique pour ces topographies.

Contents

Acknowledgments	iii
Abstract	vii
French Summary	ix
List of Figures	xv
List of Tables	xxi
1 Introduction	1
1.1 State of the Art	4
1.1.1 Coherent XUV and X-ray sources	4
1.1.2 Attosecond Pulses	7
1.1.3 XUV and X-ray Coherent Diffractive Imaging and Holography	8
1.2 Thesis Outline	10
2 Basics in Coherent Lensless Imaging	11
2.1 Fourier Relationships in Optics	11
2.2 Principle of Image Formation in Coherent Lensless Imaging	12
2.2.1 Diffraction	14
2.2.2 Transmittance of an Object in Projection Approximation	18
2.3 Detection and Reconstruction of Fraunhofer Diffraction Patterns	20
2.3.1 Coherent Diffraction Imaging	20
2.3.2 Fourier Transform Holography	25
2.3.3 Detection and Sampling of Fraunhofer Diffraction Patterns	29
2.4 Detection and Reconstruction of Fresnel Diffraction Patterns	32
2.4.1 In-Line Holography	32
2.4.2 Sampling Considerations in In-Line Holography	38
2.5 Image Quality in Coherent Lensless imaging	38
2.5.1 Resolution	38

2.5.2	Signal-to-noise Ratio (SNR)	40
2.6	Summary of Beam Requirements for Ultrafast Coherent Lensless Imaging	43
3	Experimental Studies of Spatial Coherence and Fourier Transform Holography in LUCA's	
	High Harmonic Generation Beamline	45
3.1	Introduction	45
3.2	High Order Harmonics Generation in Gases	46
3.2.1	Principle of HHG in Gases	47
3.2.2	Microscopic Effects: Three Step Model	48
3.2.3	Macroscopic Effects: Phase Matching	49
3.3	LUCA's Harmonic Beamline	50
3.3.1	Setup	50
3.3.2	Optimisation of the Harmonics Signal	52
3.4	Fabrication of the Test Samples	55
3.5	Single-Shot Characterisation of the Spatial Coherence of an XUV Source	55
3.5.1	Spatial Coherence	57
3.5.2	Description of the Method	58
3.5.3	Experimental Validation at LUCA's Harmonic Beamline	61
3.6	Case Study: Compensation of the Magnitude of Spatial Coherence in Fourier Transform Holography	64
3.6.1	Fourier Transform Holography with partially coherent sources	65
3.6.2	Experimental Studies at LUCA's Harmonic Beamline	68
3.7	Conclusion Notes	78
4	Digital In-line Holography corrected from Aberrations by Resorting to Wavefront Sensor	
	Measurements	81
4.1	Introduction	81
4.2	Aberrations and Generalised Pupil Function	83
4.2.1	Main types of Aberrations	84
4.2.2	Zernike Polynomials	84
4.2.3	Hartmann Wavefront Sensor	87
4.2.4	Quadriwave Lateral Shearing Interferometry Wavefront Sensor	87
4.3	In-line holography with waves with aberrations	88
4.4	Simulation	90
4.4.1	Transmittance of the Object-Plane	90
4.4.2	Phase-Map Definition	91
4.4.3	Hologram simulation	92
4.4.4	Object Reconstruction	93
4.4.5	Results and Discussion	94

4.5	In-line Holography with Correction of Aberrations and Twin Image	96
4.5.1	Experimental Test with a Phase Sample illuminated by an Aberration-free Spherical Wave Reference	99
4.6	Experimental Validation with a HeNe laser	101
4.6.1	Experimental Setup and Experimental Data	101
4.6.2	Data Analysis and Reconstruction Procedure	102
4.6.3	Results and Discussion	104
4.7	Conclusion Notes	106
5	Computed Stereo Lensless X-ray Imaging	111
5.1	Introduction	111
5.2	Computer Stereo Vision: Principle and Reconstruction Steps	112
5.2.1	Generation of the Stereo Image Pair	114
5.2.2	Stereo Correspondence and Image Rectification	115
5.2.3	Stereo Matching and Computation of the Disparity Maps	117
5.2.4	Retrieval of Depth Information and 3D Reconstruction	123
5.3	Simulations with a pure-amplitude <i>versus</i> phase sample	126
5.3.1	3D sample and Generation of the Stereo Views	126
5.3.2	Stereo Correspondence and Image Rectification	127
5.3.3	Stereo Matching and Computation of the Disparity Maps	128
5.3.4	Retrieval of Depth information and 3D Reconstruction	130
5.4	Computer Stereo XUV Imaging in Single Acquisition Using a Pure-amplitude Sample . . .	134
5.4.1	Experimental Setup	135
5.4.2	3D Sample and Generation of the Stereo Views	136
5.4.3	Pre-processing of the CDI Stereo Views	139
5.4.4	Stereo Matching and Computation of the Disparity Maps	141
5.4.5	Retrieval of Depth Information and 3D Reconstruction	142
5.5	Computer Stereo X-ray Imaging Applied to Curved Biological Samples	143
5.5.1	3D Sample and Generation of the Stereo Views	144
5.5.2	Pre-processing and Image Rectification	144
5.5.3	Stereo Matching and Computation of the Disparity Maps	146
5.5.4	Retrieval of Depth Information and 3D Reconstruction	147
5.6	Computer Stereo X-ray Imaging Using Nanoparticle Labels	150
5.6.1	3D Sample and Generation of the Stereo Views	150
5.6.2	Pre-processing of the CDI Stereo Views	150
5.6.3	Stereo Matching and Computation of the Disparity Maps	152
5.6.4	Retrieval of Depth Information and 3D Reconstruction	152
5.7	Conclusion Notes	154

6 Conclusions	159
6.1 Future Prospects: XUV SLM	163
6.1.1 Setup 1: Pump beam modulated with an SLM	163
6.1.2 Setup 2 : Interference of two pump beams	166
Bibliography	169
Nomenclature	195
Glossary	203
Author Contributions	207
A Coordinate Systems	A.1
B Convolution and Correlation Notation	B.3
C FT Theorems	C.5
D Batch file of the fabrication of in-line test samples	D.7
E Publications	E.13

List of Figures

1.1	XFELs peak brilliance and comparison with other X-ray sources [61].	5
2.1	Schematic comparison between conventional and lensless imaging systems.	13
2.2	Phenomenon of diffraction through a single slit (left) and double slit (right) [130].	14
2.3	Representation of the wave vector in Ewald's sphere [121].	16
2.4	Typical setup for coherent diffraction imaging.	21
2.5	Schematic drawing of the Gerchberg-Saxton phase determining algorithm [148].	23
2.6	Schematic drawing of a general algorithm for iterative phase retrieval [143].	24
2.7	Illustration of successive projections applied to x between two spaces of constraints [140].	25
2.8	Schematic of Fourier Transform Holography.	27
2.9	In-line holography schemes.	34
2.10	The limit of resolution, according to the Rayleigh criterion, shown by the overlapping diffraction patterns of two single Airy Disks. Image from [159].	39
3.1	Schematic of a setup for HHG.	47
3.2	Typical spectrum of high-order harmonics.	47
3.3	Schematic of the three-step model [20].	48
3.4	Macroscopic phase matching [20].	50
3.5	Photograph and scheme of LUCA's harmonic beamline.	51
3.6	LUCA's diffraction chamber and scheme of the setup employed for the measurements of spatial coherence and Fourier Transform holography.	52
3.7	Diagram of the etching of 2D samples with FIB.	55
3.8	SEM image of the membrane with the fabricated samples.	56
3.9	Example of a fabricated NRA and FTH test samples.	56
3.10	Spatial vs temporal coherence.	57
3.11	NRA's elementary block for achieving intensity-independent measurements and respective autocorrelation.	60
3.12	Example of a 7-aperture NRA for spatial coherence measurements and respective autocorrelation.	61

3.13 Simulations of NRA measurements of the degree of spatial coherence with variation of beam pointing.	62
3.14 SEM image of the NRA sample and respective simulated autocorrelation.	62
3.15 Measurement of the magnitude of spatial coherence of a single H25 pulse from LUCA's harmonic beamline.	65
3.16 Example of an FTH sample and respective reconstruction with corresponding separation vectors \vec{d}_r	67
3.17 Experimental diffraction patterns and respective reconstructions obtained for two different FTH objects.	69
3.18 Experimental diffraction pattern and respective NRA autocorrelation achieved with similar generation conditions to the FTH samples.	70
3.19 FTH reconstructions of before and after "correction" with the measured profile of $ \vec{\mu} $	71
3.20 FTH reconstructions of before and after "correction" with the measured profile of $ \vec{\mu} $	72
3.21 Experimental diffraction patterns and respective NRA autocorrelations achieved from H33 for a scan of values of gas pressure inside the generation cell.	73
3.22 Effect of the intensity profile of the illuminating beam in the NRA autocorrelation.	74
3.23 Calculation of the H33's degree of spatial coherence from the experimental data for different gas-pressure values, using the NRA of 5 apertures of Fig. 3.14.	75
3.24 FTH mask and holographic reconstructions with a clear effect of the partial spatial-coherence.	76
3.25 Fourier transform holography based on the use of extended references with a clear effect of the partial spatial-coherence [12].	79
4.1 Scheme of in-line holography with spherical waves <i>versus</i> waves with aberrations.	82
4.2 Schematic of the main aberrations.	85
4.3 Wavefront modes associated with each Zernike polynomial [214].	86
4.4 Principle of operation of the Hartmann wavefront sensor [220].	87
4.5 Transmission function $t(x, y)$ used in the simulation	90
4.6 Setup and phase map, with respective Zernike coefficients, obtained experimentally from the measurement of an XUV-HHG source with a Hartmann wavefront sensor.	92
4.7 Hologram simulation scheme for in-line holography with waves with aberrations.	93
4.8 Schematic of the reconstruction process.	94
4.9 Simulation results for in-line holography with waves with aberrations, using a phase map with Zernike coefficients measured experimentally from an XUV beam focused with KB optics.	95
4.10 Object with respective twin image [224]	96
4.11 Schematic of the reconstruction process of in-line holography with correction of aberrations and twin image.	98
4.12 In-line hologram of a zebrafish embryo and corresponding background image.	99

4.13 Amplitude and phase reconstructions for 1, 5 and 20 iterations of the reconstruction algorithm.	100
4.14 Amplitude reconstructions for different depth-planes of the sample, separated from 100 μm . 101	
4.15 Experimental setup used for testing the correction of aberrations by resorting to wavefront sensor measurements.	102
4.16 Different steps of the reconstruction procedure used in the experimental data.	103
4.17 Schematics of the process through which the experimental $R(X, Y)$ was obtained.	104
4.18 Experimental in-line reconstructions with and without correction of the beam aberrations and twin image.	105
4.19 HHG beamline and setup implemented at LOA to perform XUV in-line holography, corrected from the aberrations measured with a Hartmann wavefront sensor.	108
4.20 In-line XUV test samples fabricated at INESC-MN.	109
5.1 Steps followed in the reconstruction of the 3D structure of a sample from stereo data. . .	113
5.2 Example of a stereo image pair - "Man" - from Kim <i>et al.</i> [255].	114
5.3 Schematic representation of image rectification, by means of epipolar lines.	116
5.4 Example of a pair of disparity maps of the "Man" - images from Kim <i>et al.</i> [255].	118
5.5 Explanatory scheme of the disparity calculations.	118
5.6 Failure of the ordering constraint at the <i>Forbidden Zone</i> [278].	119
5.7 Schematic representation of the block-matching routine employed in the disparity estimations.	122
5.8 Example of a 3D reconstruction originating from a pair of stereo images. The sample is the "Man" - images from Kim <i>et al.</i> [255].	124
5.9 Stereo system geometry.	124
5.10 Simulated pure-amplitude sample and correspondent stereo views.	127
5.11 Pair of stereo images used in the simulation of a phase sample.	127
5.12 Stereo images of a pure-amplitude sample, with corresponding point matches, before and after rectification.	128
5.13 Stereo images of a phase sample, with corresponding point matches, before and after rectification.	128
5.14 Disparity maps obtained from the rectified stereo views of a pure-amplitude sample . . .	129
5.15 Disparity maps obtained from the rectified stereo views of a phase sample.	129
5.16 Stereo images of a phase sample submitted to a directional gradient along the x -axis - direction of the disparities.	130
5.17 Disparity maps obtained from the gradient-intensity stereo views of a phase sample. . . .	131
5.18 Different stages of the 3D reconstruction process of the simulated amplitude sample. . . .	133
5.19 Point cloud and final 3D reconstruction of the simulated phase sample.	134
5.20 Experimental setup for single acquisition 3D stereo imaging.	135

5.21 SEM (scanning electron microscopy) image of the experimental sample.	136
5.22 Typical dual diffraction pattern of the pure-amplitude cross sample.	137
5.23 Pair of diffraction patterns, from the pure-amplitude cross sample, after post-processing with HDR.	138
5.24 Pair of experimental stereo images from the pure-amplitude cross sample.	139
5.25 Stereo anaglyphs of the experimental pure-amplitude cross sample.	140
5.26 Experimental disparity maps computed from the stereo views of the pure-amplitude cross sample.	141
5.27 Point cloud and final 3D rendering of the experimental sample of a pure-amplitude cross.	143
5.28 Coherent hard X-ray diffraction microscopy of an unstained human chromosome and reconstructed 3D electron-density map [244].	144
5.29 Pair of CDI stereo images from an unstained human chromosome sample.	145
5.30 Stereo images of the human chromosome sample, with corresponding point matches, before and after rectification.	145
5.31 Masks employed for background removal in the human chromosome stereo views.	146
5.32 Final stereo views of the unstained human chromosome, after rectification and pre-processing.	146
5.33 Disparity maps obtained from the rectified stereo views of the human chromosome sample.	147
5.34 Point cloud and surface plot of the experimental sample of an unstained human chromosome.	148
5.35 Volume projections of the refractive index real and imaginary parts of a simulated cell, at 6 keV.	149
5.36 3D pyramid sample and diffraction pattern acquired from a central view.	151
5.37 Stereo image pair of the nanoparticles pyramid sample.	151
5.38 Masks employed for background removal in the pyramid stereo views.	151
5.39 Stereo anaglyph of the pyramidal structure of gold nanospheres.	152
5.40 Disparity maps obtained from the rectified stereo views of the nanoparticles pyramid sample.	153
5.41 Final depth reconstruction of the pyramidal arrangement of gold nanoparticles.	154
6.1 Setup for an XUV SLM, where the phase of a pump beam is modulated with a conventional SLM, generating a transient intensity map at the far field, which will imprint custom modulations on a grazing-incident XUV beam.	164
6.2 Schematic of the input and output images, used in the implementation of the Gerchberg-Saxton algorithm, to extract the phase map at the SLM.	165
6.3 Experimental measurement of a fork-grating intensity map at the far field of the SLM.	166
6.4 Example of a generated phase map introduced at the SLM and respective far-field measurements employing two different sources.	167
6.5 Setup for generation of a hologram at the VO ₂ film, which works as a transient diffraction optics to the harmonics beam, separating, focusing and imprinting OAM in each harmonic.	168

A.1	Coordinate system adopted for Fourier transform holography.	A.1
A.2	Coordinate system adopted for In-line holography.	A.1

List of Tables

3.1	Optimal experimental properties and respective parameters used for the generation of H25 from <i>Ar</i> at LUCA's harmonic beamline. Some values were obtained from previous theses at CEA [127, 162].	54
3.2	Optimal experimental properties used for the generation of H33 from <i>Ne</i> at LUCA's harmonic beamline. Some values were obtained from the thesis [162].	54
3.3	Optimal experimental parameters used for the generation of both H25 and H33 at LUCA's harmonic beamline.	54
4.1	Description of the main aberration with Zernike polynomials.	86
4.2	Zernike coefficients measured in the wavefront sensor. The measured RMS error was 4.873λ	102
4.3	Resolution values, \mathcal{R} , calculated from the experimental reconstructions and corresponding setup-achievable resolutions, δ_{lat}	105

Chapter 1

Introduction

Coherent short wavelength radiation in the extreme ultraviolet (XUV) and X-ray regions is opening new perspectives in lensless imaging, allowing nanometric resolutions at ultrafast time scales with a broad range of applications in spectroscopy, metrology, material science, physics, chemistry and biology.

Three-dimensional access to a protein's structure [1] and intact viruses [2, 3], as well as "movies" of molecular dynamics [4, 5] are recent pioneer works, which revolutionized the nanoscale-imaging concept, fueling the hope that dynamic real-space imaging of atomic structures may, ultimately, become possible. Imagine the impact of recording "movies" of molecules, viruses and live microbes in action, with atomic-spatial resolutions? What about the possibility of visualising femtosecond-to-attosecond ultrafast phenomena [4–8]? And how more profoundly advanced would be our understanding of nature if we could access to such information in three-dimensions?

High-resolution imaging of single, non-periodic nanospecimens remains a great challenge nowadays. Electron microscopy requires that the samples are frozen and deposited on a substrate, potentially modifying their structural content and operation mechanisms. Optical imaging techniques are limited in resolution. Moreover, these techniques have extremely low penetration depth in most materials and therefore are limited in their capability of imaging thick and buried structures. In contrast, intense femtosecond X-ray pulses from free-electron laser (FEL) sources allow "*diffraction-before-destruction*" *coherent lensless imaging* of individual nanospecimens within one single exposure [2, 3]. In this scheme, a single sample is injected from its native environment at room temperature into the FEL focus and, before the sample is vaporized by the X-ray pulse, a diffraction pattern is recorded [2, 9].

This large potential has triggered the development of large-scale facilities such as synchrotron light sources and X-ray free-electron lasers (XFELs), based on particle accelerator physics, as well as high-order harmonics generation (HHG) techniques, that employ tabletop femtosecond lasers. Thanks to a high spatial coherence, ultrashort pulse duration and high photon flux, XFELs carry a huge potential to resolve down to atomic scale processes, occurring on femtosecond ($1 \text{ fs} = 10^{-15} \text{ s}$) time scales [1, 2, 9–11]. On the other hand, laboratory-scale laser-driven coherent X-ray sources, such as HHG in gases, provide another alternative for ultrafast imaging at nanometer resolutions [12–15], moreover being the

only available source of attosecond pulses ($1 \text{ as} = 10^{-18} \text{ s}$) [16–19].

High-order harmonics generation in gases is a process in which noble gas atoms excited by an intense laser field at frequency ω_0 emit radiation of higher frequencies that are odd integer multiples of ω_0 . A typical spectrum of high-harmonic emission spans tens-to-hundreds of eVs in the extreme ultraviolet/soft X-ray regions [20]. Most applications that use HHG light have been limited to the extreme ultraviolet region of the spectrum ($<150 \text{ eV}$), where efficient frequency up-conversion is possible, with the use of the widely available Ti:sapphire lasers, operating at a wavelength of 800 nm [21–23]. High-harmonic sources reveal high brightness [24, 25], a high degree of spatial coherence [14, 26], ultrashort pulse duration [8, 13, 17], wide tunability, compactness and low equipment cost [14]. Among other possible applications, one can emphasize the possibility of probing the electron dynamics on its natural time scale, via attosecond pulses [16], and the high-resolution imaging with XUV lensless imaging techniques [14, 27]. Indeed, given recent advances in single-shot imaging with these sources [12, 13], "diffraction-before-destruction" coherent diffraction imaging (CDI) of individual nanospecimens may reach laboratory-scale experiments in a near future.

Coherent diffraction imaging (CDI) is a lensless imaging technique in which a coherent beam is incident on a reflective or transmissive object and the intensity pattern of the diffracted field is captured with a detector array, typically in the far field [2, 13]. This technique replaces conventional image-forming optics (such as mirrors, lenses, holographic optical elements...) by free-space propagation, a device for intensity detection and computational image reconstruction. For this reason, it bypasses the difficulties in fabricating X-ray focusing optics for high-resolutions, at which the manufacturing abilities are still beyond the state of the art [28]. For a highly-coherent beam and fulfilling sampling conditions, this technique allows diffraction-limited images of an object, with a resolution equivalent to what would be obtained by an optical system with an entrance pupil of the same size and shape of the detector array [29].

The central problem of indirect imaging methods, such as CDI, is the intrinsic loss of phase during the measurement process. Indeed, reconstructing CDI images requires solving the so-called "phase problem", usually accomplished with iterative algorithms. Throughout the years, several efforts have been invested into the development of phase retrieval algorithms [2, 30–36], allowing state-of-the-art resolutions amongst the X-ray lensless imaging techniques. Nevertheless, CDI reconstructions remain computationally demanding and often require guidance for selecting the object support. Particularly, noisy experimental data with missing data regions pose a real challenge [2] and sometimes lead to incompatible solutions [31]. Even though not achieving yet the state-of-the-art resolutions of CDI, lensless holographic approaches overcome the phase problem by encoding the relative phase between a reference wave and the wave diffracted by the object, reaching a deterministic solution [11, 12, 19, 37, 38].

When a coherent beam is incident on an isolated object, the interference of this reference beam with the diffraction of the object creates a hologram, which can be measured with a sensitive detector array. Fulfilling sampling conditions, this pattern can be used to reconstruct the original object, using a lensless imaging technique called *digital in-line holography* [38]. If, instead, the reference wave is generated by pinhole apertures drilled in the plane of the object, with this latest contained in a pupil/support area, the

interference pattern in the far field can also be used to retrieve the image of the object. This depicts a different technique called *Fourier transform holography* (FTH) [19, 37]. Even though both techniques can generate diffraction-limited reconstructions, experimental constraints often compromise the quality of reconstructions, particularly due to disagreements between reality and the reconstruction algorithms, which generally assume perfect wavefront and full coherence [19, 37–39].

The spatial *coherence* of the source is a critical factor for lensless imaging. Indeed, a premise of diffraction and, consequently, lensless imaging techniques is a fully-coherent illumination. However, XUV/X-ray radiation from FELs, synchrotrons or HHG sources exhibit only partial spatial coherence [26, 40, 41] and shot-to-shot variations of this parameter. Several authors have reported the effects of partial spatial coherence in lensless-imaging reconstructions [12, 15, 42–45]. Their works showed that in real-life experiments, an assumption of total coherence seems sometimes rather inaccurate. Even though some coherence compensations have been implemented in CDI reconstructions [42, 43, 46], this has not been yet reported for Fourier transform holographic reconstructions. Thus, new research on techniques for single-shot spatial coherence characterisation is an imperative step to improve X-ray sources and high-resolution imaging techniques. We will present our progress in this topic in Chapter 3.

The phenomenon of source *aberrations* is another particular issue of diffractive imaging. The wavefront of the beam, defined as a surface of constant phase of the propagating source, needs to be of high-optical quality in order to record a distortion-free image [47]. Equal objects in different positions, illuminated by the same non-optimised wavefront, were reported to exhibit different diffraction patterns [48]. Optimisations of the wavefront are already made [47], but they are not always accessible. There is, therefore, a need for a wavefront correction in the reconstructed image of an object in order to guarantee the image fidelity. This is particularly impactful for in-line holographic reconstructions, since this technique uses the incident beam as a reference wave for encoding the object's phase information [38]. We will present our progress in this topic in Chapter 4.

High-resolution lensless imaging techniques have also been playing an important role on the 3D knowledge of the nano-world. The single-shot technique of diffraction-before-destruction allows imaging radiation-sensitive nanospecimens in a close-to-natural state [2, 49, 50]. However, to retrieve a 3D reconstruction, it requires an enormous number of identical samples, not allowing imaging of unique objects or non-reproducible processes. Moreover, it generates an extremely large amount of data that needs to be sorted, classified and combined to provide a full set of consistent 3D data [1, 3]. Thus, there is an intensive research effort on decreasing the number of orientations in the direction of retrieving 3D information from a single acquisition. Techniques to retrieve the 3D structure from a single diffraction pattern have been proposed, but they work under limited circumstances and heavily rely on samples *a priori* knowledge [51–55]. We will present our progress in this topic in Chapter 5.

3D structural imaging with nanometric-spatial and atto/femtosecond-temporal resolutions promises novel ways in the quest to discover new physical and biological phenomena. This has motivated the development of X-ray sources and optics, and the improvement of lensless imaging techniques to make them more suited to the high demands of future breakthroughs [56]. In this manuscript, we will con-

tribute primarily to this later point. New advances in the XUV/X-ray imaging are emerging either through improvements on available techniques, or through novel approaches, some by adapting methods from cross-fields of study. Here we explore both. We propose and investigate improvements to available techniques, particularly by inputting computational corrections from source issues, such as coherence and wavefront aberrations. These corrections are respectively studied for Fourier transform holography and in-line holography. We also propose to adapt methods from vision science or machine learning, particularly *Computer Stereo Vision* [57], for increasing performances of lensless techniques in the quest for single-shot 3D imaging regardless of the nature of the sample. For these studies we use HHG as our main source of XUV radiation.

1.1 State of the Art

In 2011, the contribution of H. N. Chapman *et al.* changed the reality of structural imaging by reconstructing for the first time a 3-dimensional structure of a protein using nanocrystallography [1]. For that purpose, protein nanocrystals were streamed into the path of a hard X-ray free-electron laser (in Linac Coherent Light Source, LCLS) and illuminated with bursts of laser light so brief that the recorded diffraction patterns gathered all the information needed to make an image before they got destroyed. The 3D reconstruction was, then, obtained from millions of these diffraction images, after orientation recognition. Later in the same year, M. M. Seibert *et al.* recorded single "diffraction-before-destruction" images of sprayed uncrystallizable viruses [2], whose 3D reconstruction was achieved by similar means in 2015 [3], opening the way to single-particle 3D-imaging of non-reproducible samples.

In 2012, Vodungbo *et al.* took advantage of ultrafast XUV pulses from a high-harmonic generation (HHG) source, to follow the femtosecond laser-driven demagnetization process of a $[\text{Co/Pd}]_{30}$ multilayer film [8]. This combination of ultrashort-ultrabright pulses with ultrafast optical lasers - for "pumping" the target - has enabled the realisation of "molecular movies" where femtosecond changes in structures and electronic states are tracked in time [4, 5]. In 2019, Duarte *et al.* was able to extract 3D information in a single acquisition, employing an XUV femtosecond-pulsed laser [57]. This was accomplished by stereo-processing two images of a nanoscale object, taken simultaneously from two different angles.

With these signs of progress, the access to 3D structural information with nanometric-spatial resolutions at ultrafast-time scales foresees huge accomplishments, from the structure determination of single molecules and viruses, to the time-resolved study of structural changes of transient phenomena. Up to now, this quest has actively motivated the development of XUV/X-ray sources and the improvement of lensless imaging techniques, making them more suited to the high demands of future breakthroughs.

1.1.1 Coherent XUV and X-ray sources

Synchrotrons, free-electron lasers and the compact high-harmonic generation setups constitute the main sources of coherent XUV and X-ray radiation, with applications in lensless nanoscale imaging. The state-of-the-art features, regarding the motivation of this PhD work, will put the focus of this section on the two

latter cases.

An X-ray free-electron laser (XFEL) is a coherent source of X-rays in which the light amplification is achieved in an undulator, fed with accelerated relativistic electrons. This undulator is constituted by a periodic arrangement of magnets, which generate a periodically varying Lorentz force, forcing the electrons to radiate with a frequency that depends on their energy, the period of the magnets and, more weakly, on the magnetic field strength. Compared with other synchrotron radiation sources (pure undulators and wigglers), XFELs can generate an output beam with much higher spectral brightness and coherence. This 4th generation X-ray light source features a brilliance 1 billion higher than that of the most advanced synchrotrons (see Fig. 1.1), while producing ultrashort pulses of polarized and coherent light [58–60].

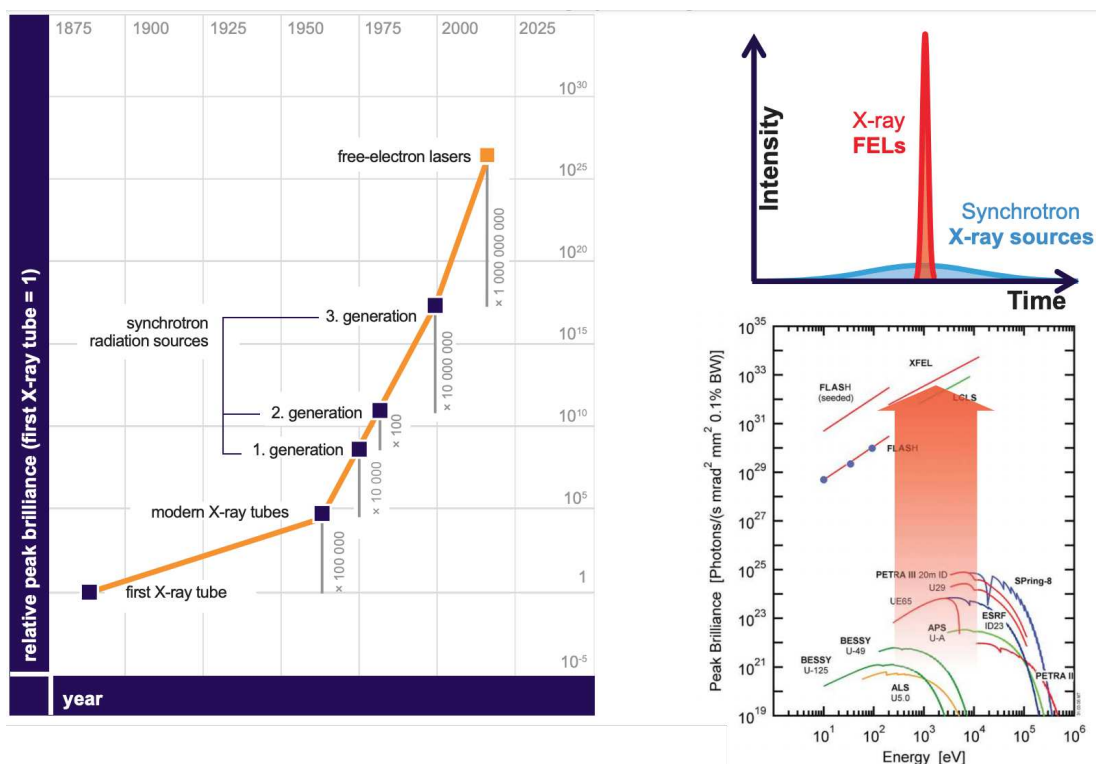


Figure 1.1: **XFELs peak brilliance and comparison with other X-ray sources [61].** Note that these data are prior to the hard X-ray FEL from Switzerland - the SwissFEL -, which was the last one to be built, inaugurated in December 2016 [60].

The Linac Coherent Light Source (LCLS) at the SLAC National Accelerator Laboratory, California, constitutes the first XFEL, online since 2009, running with wavelengths down to 0.1 nm and pulse durations below 50 fs [59, 62, 63]. Sub-ångström wavelengths were reached for the first time in 2011, at the SPring-8 Angstrom Compact Free Electron Laser (SACLA) of RIKEN in Harima, Japan [64]. Also in SACLA, intensities of 10^{20} Wcm^{-2} were obtained at 7.1 keV (1.75 nm wavelength) with pulses of 7 fs [65]. The most ambitious X-ray free-electron laser is probably the European XFEL in Hamburg, Germany, which produces hard X-ray light with unprecedented performance features (see Fig. 1.1). It is based on new superconducting accelerator technology, which enables it to generate 27,000 X-ray

flashes per second - more than 200 times the repetition rate of any other XFEL [58, 66]. It hosts wavelengths from 0.05 to 4.7 nm and pulse durations below 100 fs [58].

Indeed the key tendencies of the new XFELs are increased average brilliances, supported by high repetition rates, with a higher number of end stations accessible for users [56, 66]. This increased access has boosted as well the implementation of different setup configurations, pushing forward the diversity of experiments. For example, hard X-ray split-and-delay lines, compatible with the realisation of synchronised stereo experiments, are under design at SACLA XFEL [67] and at the European XFEL [68].

The unprecedented features of XFELs are crucial for breakthrough experiments in the most diverse scientific areas. The ultrashort duration of XFEL pulses allows data to be collected before radiation damage has time to set in, which is particularly important for resolving highly radiation-sensitive samples [1, 2, 49, 50]. Close-to-physiological states of single biological particles become as well accessible, as this "diffraction-before-destruction" allows to resolve structures at room temperature, without crystallization [11, 66, 69]. In addition, spatial and temporal resolutions, together, are crucial for capturing dynamics and fast processes, impossible to detect by other methods. This is the case, for example, of structural changes in enzymes [66, 70–72]. In addition, the polarized beams of FEL light allow the exploration of magnetic materials, key for new information technologies [73–75].

However, XFELs large and expensive setups restrict their use to only a few facilities in the world, limiting their access to the scientific community. Therefore, future advancements move also towards the development of "table-top" compact sources, capable of meeting the huge demand for coherent X-rays usage.

Contrarily to the limited XFEL facilities, high power ultrashort lasers are available worldwide in industrial and university-scale laboratories. Ultrafast pulse trains (pico-femtosecond duration) were possible with the emergence of mode-locked lasers and the ability to lock in phase, and amplify, equally spaced frequencies in a comb [76]. However, making even shorter pulses was difficult to handle in the 80s as the optical peak intensities became too high for the amplifying medium itself. This was overcome by the development of the chirped-pulse amplification (CPA) method, which was originally developed in the context of radar technology, but later applied to optical amplifiers [77].

Femtosecond lasers opened a new domain in light-matter interactions, with the new possibility of concentrating all laser's energy in a short period of time, thus, enabling the study of nonperturbative non-linear optics. When a very intense laser pulse (with optical intensities on the order of 10^{14} - 10^{15} Wcm⁻²) is focused into a noble gas, strong non-linear interactions can lead to the generation of several high-order odd harmonics of the pulse, in a phenomenon called *high-order harmonics generation* (HHG). HHG in gases was first reported in 1987, when McPherson *et al.* observed the harmonics of the fundamental driving laser up to the 17th order, in a neon medium [78]. Almost simultaneously, at CEA Saclay, harmonic light as high as the 33rd harmonic in the XUV range (32.2 nm wavelength) was generated in argon [79]. The first theoretical breakthrough of HHG came, in 1992, when Krause *et al.*, by solving the time-dependent Schrödinger equation numerically, showed the existence of a total maximum

photon energy - cutoff energy - in a high-order harmonics (HH) spectrum. Nowadays HHG is understood using the semi-classical three-step model, proposed by P. Corkum, in 1993 [80] and generalized by Lewenstein *et al.* in 1994 [81].

Compared to XFELs, the photon number of HHG is smaller (10^9 - 10^{11} photons/pulse), however it is still enough to carry out single-shot experiments [12, 13, 82]. Indeed, the low conversion efficiency is the largest limitation of HHG [83], affecting the harmonics peak flux, essential to collect diffraction data for imaging at the nanoscale. Recent phase-matched HHG conversion efficiencies reached 10^{-5} in the XUV region and 10^{-7} to 10^{-6} in the X-rays [23]. Besides these values, in 2002, at CEA Saclay, Hergott *et al.* reported a harmonic beam with microjoule energy, using an incident infrared (IR) laser of 27-mJ energy with loose focusing geometry in a xenon gas cell (5-m focal-length lens) [21]. Also, Hädrich *et al.* reached 100 mW of average power per harmonic in 2014 [84]. Strategies to improve this efficiency or peak flux can be employed as, for instance, using the HHG beam to seed a laser plasma amplifier [85] or a free-electron laser [86]. Below-threshold harmonics generated in a “seeding cell” can also boost the HHG process in a “generation cell” [87].

Besides the high availability, compactness and extremely low equipment cost, contrasting with the huge XFELs [14], high-harmonics sources reveal ultrashort pulse durations [8, 13, 17], high degree of spatial coherence [14, 26], high brightness [24, 25] and wide tunability. These features make HHG-based XUV sources of high interest to ultrafast high-resolution lensless imaging [14, 27]. Pulses from HHG in this wavelength range have already been used in applications such as single-shot coherent diffraction imaging (CDI) [13, 88], holography [12, 38], plasma diagnostics [89, 90] and pump-probe studies of ultrafast processes [8, 91]. Moreover, the wide spectral bandwidth of this source allows probing the electron dynamics on its natural time scale, using attosecond pulses [16].

1.1.2 Attosecond Pulses

The large spectral bandwidth associated with the HHG process holds an attosecond pulse-structure. During the HHG process, coherent attosecond bursts of light are emitted at each half-optical cycle. During propagation, these pulses interfere in the spectral domain to form a frequency comb with a period of twice the fundamental-laser frequency. This frequency comb forms the so-called “harmonic spectrum”, which corresponds in the time domain to a train of attosecond pulses. Allowing a single re-collision during the HHG process will generate a single attosecond pulse and no harmonics will be observed but a continuous spectrum.

The first attosecond pulses were observed in 1996, by Antoine *et al.* [92], when a Neon atom was exposed to an 825 nm wavelength radiation at an intensity of 4×10^{14} W cm⁻². The attosecond generation pushed the frontiers of temporal resolution to the timescale of the interactions of valence and inner-shell electrons, which hold characteristic times of 150 as and 2 as, respectively [93]. Different schemes have been realized to their production. Examples are phase-locking of many harmonics [92], compression of chirped harmonic pulses [94] and generation with a few-cycle driving laser [17, 95] and with CEP-stable pulses [17]. Attosecond-pulse generation has become a subject of intense effort in

the scientific community due to its potential of probing matter on an unprecedentedly short time scale. Theoretically, through HHG, pulses with durations as short as 2.5 as are, in principle, possible [23]. The current limit obtained experimentally for attosecond pulses is set at a duration of 43 as in a single isolated pulse [17].

Pioneer experiments already demonstrated electron-dynamics measurements with attosecond resolution through spectroscopic measurements. One can refer for instance to the measurements of the lifetime of M-shell vacancies of krypton in 2002 [96], of the intra-atomic transient electron dynamics in 2004 [97] and the observation of the motion of a $D2^+$ vibrational wave packet with a precision of about 200 attoseconds [98]. However, experimental implementations combining attosecond-time resolution with atomic-distance scales were not yet achieved. This remarkable challenge will require the development of new imaging techniques that deal with attosecond soft and hard-X-rays sources specific properties (bandwidth, coherence, wavefront, etc...). With such capacity, the 3D motion of electrons would finally be accessible, foreseeing a revolutionary new era for different research fields including physics, chemistry, biology and fostering the development of new technologies.

1.1.3 XUV and X-ray Coherent Diffractive Imaging and Holography

1.1.3.1 Coherent Diffraction Imaging

Coherent diffraction imaging (CDI) has its origins in crystallography, when in 1952 David Sayre proposed that the methods used in the technique could be adapted for imaging general non-periodic objects, suggesting a new form of lensless high-resolution imaging [99]. In 1978, J.R. Fienup proposed a phase-retrieval algorithm to solve the phase problem [35] and only in 1999 an image was recovered successfully from oversampled coherent X-ray diffraction data [30]. Nowadays several types of phase-retrieval algorithms are used to reconstruct CDI data [2, 30–33, 100].

In 2006, Chapman *et al.* reported the first experimental demonstration of diffraction-before-destruction using the FLASH soft-X-ray free-electron laser [50], opening new horizons [1–3]. Other ultrafast X-ray imaging of individual fragile specimens can also be mentioned such as aerosols [101] and live biospecimens [31]. These unique capabilities also enabled the investigation of metastable or transient states that exist only in the gas phase. Pioneering experiments have explored this frontier and demonstrated CDI of ultrafast nanoplasma formation [102] and explosion of laser-heated clusters [9].

Besides the XFEL accomplishments, CDI has also shown advances in single-shot imaging with tabletop lasers [15, 88], pioneered by our group [13], making the reality of diffraction-before-destruction of dose-sensitive samples accessible to laboratory-scale experiments. For instance, in 2017, single-shot gas-phase nanoscopy was first implemented with a HHG source, where isolated helium nanodroplets were imaged in single-shot. In 2019, Duarte *et al.* was able to extract 3D information from CDI reconstructions in a single acquisition, employing a XUV femtosecond-pulsed laser from HHG [57].

1.1.3.2 Digital In-Line Holography

Holography was discovered in 1948 by Dennis Gabor [103], but only in 1994, Schnars and Jueptner used for the first time a charge-coupled device (CCD) camera connected to a computer for digital recording and processing [104].

Since the beginning of X-ray holography, Gabor holography has been widely used, specially, in the hard X-rays regime. Even though a fine-focus X-ray tube was firstly used as a coherent source for X-ray Gabor holography [105], high-brilliance synchrotron radiation X-ray sources [106–109], free electron lasers [110] and high harmonic generation sources [38, 111] are now used for in-line holographic imaging in the XUV and X-ray spectral ranges.

In 2006, digital in-line holography was demonstrated using a fully coherent high-order harmonic source emitting at 32 nm [38]. The authors claimed that for increasing the spatial resolutions beyond 800 nm, the holograms were strongly distorted due to *beam aberrations*. Indeed, XUV holography with wavelength spatial resolution in a high-numerical-aperture Gabor configuration was reported using a compact, tabletop capillary-discharge XUV laser emitting at 46.9 nm. Even though these are, to our knowledge, the highest spatial resolution holograms obtained with a tabletop setup, the recording process was not digital. The highest resolution ever reported with digital in-line holography was 200 nm, generated by a spatial filter composed of a Fresnel zone plate (FZP) and a 200-nm-radius pinhole, employing 2.38-nm wavelength synchrotron radiation [112]. The authors claimed that the configuration still had room for further resolution enhancement, foreseeing sub-100 nm resolution in a near future [112].

1.1.3.3 Fourier Transform Holography

The unavailability of X-ray optics and limited coherence at X-ray wavelengths led to the proposal of lens-less Fourier transform holography (FTH), in 1965, by Stroke [113]. The first Fourier transform hologram to be recorded at X-ray wavelengths was only demonstrated in 1972 [114].

Throughout the years FTH featured several achievements from providing new insights into the magnetic properties of nanostructured materials [115] to reaching higher-resolutions in combination with iterative phase retrieval methods [27]. In 2015, a discrete frequency comb of high-order harmonics until the XUV range, yielding a train of attosecond pulses, has been used to record spatially and spectrally resolved images employing FTH [19]. The highest resolution ever reported with FTH was 34 nm, achieved with a tabletop HHG source in 2018 [37].

FTH was also subject to several modifications throughout the years, leading to new techniques based on Fourier Holography.

Some examples are Fourier holography with uniformly redundant array (URA) as reference [116]; with a customizable reference [117]; or with an additional membrane containing a pupil and apertures in transmission [118] and reflection geometry [119]. One of the most important examples was holography with extended reference by autocorrelation linear differential operator (HERALDO), whose first experi-

mental demonstration was reported in 2008 [120] and have allowed single-shot 20-femtosecond imaging with LUCA's HHG source performed by our group in 2010 [12]. Recently, the first X-ray holograms of free nano-sized viruses were demonstrated using a new holographic method called in-flight holography, also based on Fourier holography. This work also reported the highest lateral resolution so far achieved via single shot X-ray holography (below 20 nm) [11].

1.2 Thesis Outline

This manuscript is divided into six chapters. In Chapter 2 the reader is introduced to the concept of Coherent Lensless Imaging and its different schemes, particularly coherent diffraction imaging, Fourier transform holography and in-line holography. It is also in this chapter that a large part of the theoretical background of this thesis is provided, with references to relevant articles and textbooks.

In Chapter 3 some experimental studies of spatial coherence and Fourier transform holography implemented in the HHG beamline of LUCA are presented. The reader is firstly introduced to the concept of HHG and to the XUV beamline. Follows spatial coherence measurements on this source, where we will use a new method, which allows a single-shot characterisation of the spatial coherence of a beam. We report the first experimental demonstration of this technique in single-shot regime. Finally, employing this technique, we investigate the possibility of compensating the magnitude of spatial coherence in Fourier transform holography. The discussions are supported with experimental data.

In Chapter 4, we demonstrate a new approach, single-shot-compatible, to correct in-line holography reconstructions from the aberrations of the optical system. Firstly, a numerical approach for in-line holography with waves with aberrations is developed and discussed with simulation results. After verifying the presence of the twin image in the reconstructions, a new algorithm is proposed for simultaneous correction of in-line holograms from optical aberrations and twin image. Experimental validations with beams with and without aberrations are also provided, employing respectively a tabletop UV source and a HeNe laser.

In Chapter 5 we propose to extend the concept of Computer Stereo Vision to XUV and X-rays in the perspective of single shot 3D imaging. The reader will be firstly introduced to the concepts of Computer Stereo Vision and to the different reconstruction steps which lead to the implementation of X-ray stereo imaging. We then explore practical cases by means of a simulation and by reconstructing experimental data from different types of samples. We demonstrate nanoscale 3D stereo imaging of a pure amplitude sample from a single dual-diffraction pattern acquisition, using XUV radiation from LUCA's beamline. Samples with predominantly-curved topography are also analysed to explore the limitation of the technique. Finally, we implement the technique in X-rays, showing that nanoparticles used as labels further extend the applicability of the technique to complex 3D samples.

In Chapter 6 we present the general conclusions of this manuscript along with some future perspectives. A brief description of some developed work, which requires significant further efforts with the aim of creating an XUV spatial light modulator is presented.

Chapter 2

Basics in Coherent Lensless Imaging

This chapter provides a theoretical overview of Coherent Lensless Imaging, the central topic of this thesis. The theoretical models as well as the formalisms used in this manuscript are presented.

2.1 Fourier Relationships in Optics

The Fourier transform is a powerful mathematical tool to describe and analyse periodic profiles. In signal processing, for instance, it is frequently used in the time and temporal frequency domains. Although these domains are intuitive for our perception, due to our ability to detect sound and understand its frequency, the interest of this manuscript lies in a less obvious domain - the domain of space and spatial frequencies. Analogous to the temporal case, the one-dimensional Fourier transform in space is defined by

$$G(f_X) \equiv \mathcal{F}\{g(x)\} = \int_{-\infty}^{\infty} g(x)e^{-i2\pi x f_X} dx, \quad (2.1)$$

where $g : \mathbb{R} \rightarrow \mathbb{C}$ is a function of x in real space and f_X is the respective frequency coordinate in the reciprocal space. The capitalisation of the function, G , and the operator \mathcal{F} both denote Fourier transform.

The field of Fourier optics employs the mathematical formalisms of linear systems, typically applied in the time domain for signal processing, to the spatial domain, providing both analog and numerical approaches to image processing. While analog image processing emerged as a powerful tool in the 1960s, nowadays, digital acquisition and processing prevail. The work developed throughout this manuscript exploits this latter case.

In a digital approach, the continuous Fourier transform is approximated by the discrete Fourier transform (DFT), computed using fast Fourier transform (FFT) algorithms. Considering N the array dimensions, with m and p the integer pixel coordinates in object and Fourier domains, respectively, ($m, p \in \{0, 1, \dots, N - 1\}$), the FFT of $g \in \mathbb{C}^m$ in one dimension is written [29]:

$$G(p) \equiv \text{FFT} \{g(m)\} = \frac{1}{\sqrt{N}} \sum_{m=0}^{N-1} g(m) e^{-i2\pi \frac{mp}{N}}. \quad (2.2)$$

Function G and, as well, the operator FFT both denote fast Fourier transform.

Let's now consider that $g(m)$ represents the discrete sampling of a continuous function $g(x)$ at a step Δ_x . For a numerical calculation of the analytical transform by means of FFT, the distribution $g(x)$ has to be sampled in x coordinates. Assuming that the centre of the coordinate system x is the centre of the distribution of $g(x)$, the sampling occurs at the points [39]:

$$x(m) = \left(m + 1 - \frac{N}{2}\right) \Delta_x, \quad m = 0, \dots, N - 1, \quad (2.3)$$

which in the Fourier domain gives

$$f_X(p) = \left(p + 1 - \frac{N}{2}\right) \Delta_p, \quad p = 0, \dots, N - 1. \quad (2.4)$$

Here Δ_p is the corresponding pixel size in the Fourier domain, which has a relation with Δ_x given by [121]:

$$\Delta_p = \frac{1}{N\Delta_x}. \quad (2.5)$$

As we will see in the next sections a huge portion of the formalism used in diffraction, and consequently coherent imaging techniques, relies on the application of two-dimensional (2D) Fourier transformations. The diffraction signals measured will be sampled digitally and, therefore, a numerical treatment will be used through the application of 2D FFTs.

2.2 Principle of Image Formation in Coherent Lensless Imaging

Coherent lensless imaging is a technique for imaging objects in which conventional image-forming optics (such as lenses, mirrors or holographic optical elements) are replaced by free-space propagation, an array for intensity detection and computational image reconstruction.

In conventional imaging systems, such as optical microscopes and photographic cameras, a single lens or assembly of lenses are generally employed to form the image of the target object (Fig. 2.1 (a)). More complex imaging systems can additionally include other optical elements, such as mirrors, filters, beam splitters or windows. In any of the configurations, the image quality is generally limited by this image-forming system, particularly by the ensemble of aberrations induced by all the optical elements. Specially in the X-ray spectral range, this imposes strong constraints on the manufacturing of these elements and, likewise, on the design of the optics system itself.

The penetrating nature of the X-rays allow imaging objects much thicker than those that can be inspected in a transmission electron microscope (e.g. 10 μm), at resolutions much better than those of visible microscopes [122]. However, the constraints on optical elements become more critical for these

wavelengths. The highest spatial resolution in X-ray microscopy, to date, was obtained using zone plate Fresnel optics [123]. The resolution of such image-forming optics is limited by the smallest outer feature of the zone plate, which raises a real manufacturing challenge, specially when targeting nanometric resolutions. Moreover, the strong photon absorption of materials in this range limits these optics efficiency to typically less than 10%, and often as low as few percent [124]. This efficiency of photons is critical for high resolution imaging, specially for specimens that are sensitive to radiation damage [125, 126]. With all these constraints, lensless imaging techniques present a remarkable solution for high resolution imaging, with applications ranging from biology to materials science.

In a lensless imaging system, no optics are required after the sample (Fig. 2.1 (b)). Thus, in principle, aberration-free, diffraction-limited images can be obtained. The object is illuminated by a coherent wave, ideally monochromatic, and its diffraction induces changes in amplitude and phase of the incident wave, containing all the information on the object. The resulting diffraction pattern is, then, measured in the near or far field by a pixel-array detector, typically a charge-coupled device (CCD), which is only sensitive to the intensities of the electromagnetic wavefield. Even though this diffraction pattern has all the information on the object, the phase information is lost in the detection process. This so-called *phase problem* constitutes the main obstacle in the extraction of object information from the measured diffraction pattern. To address this problem, different configurations of coherent lensless imaging have been proposed, all resorting to computational data treatments to avoid optical elements.

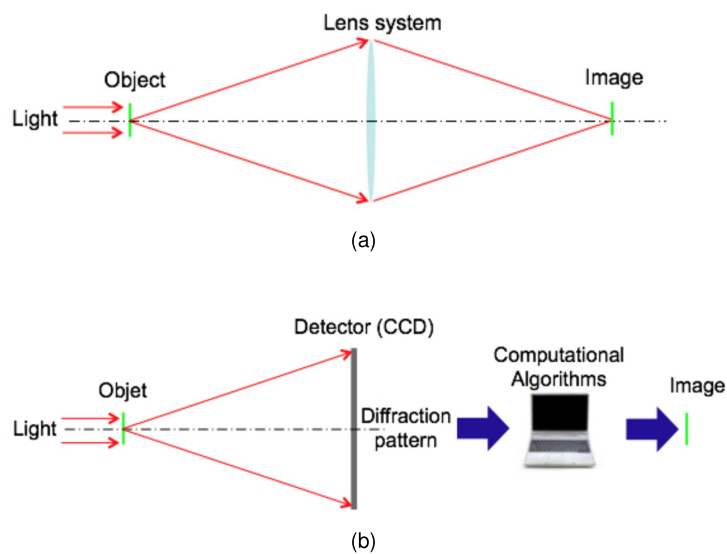


Figure 2.1: **Schematic comparison between conventional and lensless imaging systems.** (a) Schematic of a conventional imaging system. The image of the object is formed by a lens system. (b) Schematic of a coherent lensless imaging setup. The array for intensity detection and the computation algorithms replace the conventional lens system. Images from Ge [127].

There are different schemes and configurations of lensless imaging. According to the reconstruction principle used to retrieve the object's image, they can be classified into two main categories. The first, called coherent diffraction imaging (CDI), uses phase retrieval algorithms to reconstruct the phase lost during detection. The second, called holography, uses holographic modulations to record and encode

this phase. In this manuscript these two different approaches will be used, with two different variations of the second one: Fourier transform holography (FTH) and in-line holography. The image formation for these three configurations is based on the same principles, including formalisms of diffraction, object transmittance and digital detection. The main distinction occurs during data analysis and reconstruction. The coherent diffraction imaging (CDI) configuration is based on the iterative and non-deterministic reconstruction of the phase with a *phase retrieval* algorithm [2, 13, 73, 100, 122, 128]. The Fourier transform holography (FTH) and in-line holography schemes are based on a principle of non-iterative and deterministic reconstruction (analytic solution) by *phase demodulation* recorded in the hologram [19, 27, 37–39, 119, 129].

To account with the conceptual differences, the experimental implementation of these three techniques have as well some small particularities. While CDI and FTH have the same experimental setup, varying just in the sample design, in-line holography requires a different positioning of the sample and CCD in the setup. While in the first two cases the sample is placed at the focal spot of the coherent beam and the CCD in the far field, in in-line holography the sample is placed after the focus and the diffraction pattern can be collected in the near field. This will be explored later on when these techniques will be presented and their reconstruction formalisms discussed. But before, the formalisms behind image formation in lensless imaging will be introduced.

2.2.1 Diffraction

When a coherent light wave encounters an obstacle, comparable in size with its wavelength, it exhibits a characteristic behaviour. Instead of exhibiting a profile similar to the obstacle, as our intuition could suspect, the light distribution forms a pattern of dark and bright regions in a phenomenon called diffraction. Diffraction can be explained with the Huygens' principle, which states that every point of a wavefront can be considered as a point source for secondary spherical wavelets. The coherent superposition of these wavelets define the propagated wavefront at any other point in space. A schematic of the phenomenon is illustrated in Fig. 2.2.

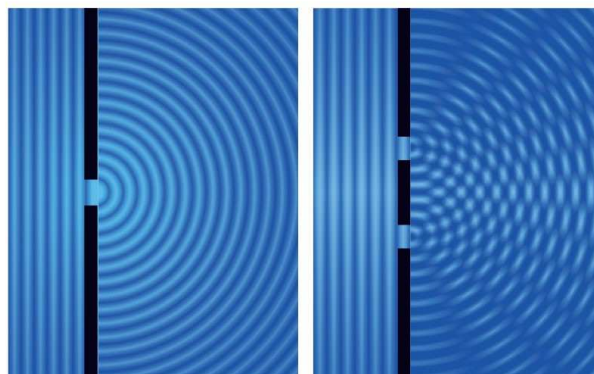


Figure 2.2: **Phenomenon of diffraction through a single slit (left) and double slit (right) [130].**

2.2.1.1 Helmholtz equation and *diffraction limit*

Diffraction theory is treated in depth by a large number of authors [131, 132]. The approach followed in this manuscript begins with the Helmholtz wave equation. Considering a monochromatic wave, represented by the wave vector $k = \frac{2\pi}{\lambda}$ and described by the scalar function $\psi(x, y, z)$, the wavefield transmitted by the object has a behaviour given by the Helmholtz equation:

$$\nabla^2 \psi(x, y, z) + k^2 \psi(x, y, z) = 0 \quad (2.6)$$

where ∇^2 is the Laplacian.

The amplitude of the wavefield is described in space as a plane transverse to the direction of propagation, z . Separating both Cartesian components, transverse ($(x, y) = r_\perp$) and longitudinal (z), the Helmholtz equation is written in the form:

$$\nabla_\perp^2 \psi(r_\perp, z) + \frac{\partial^2}{\partial z^2} \psi(r_\perp, z) + k^2 \psi(r_\perp, z) = 0 \quad (2.7)$$

Applying a Fourier transform to this equation for the transverse coordinate r_\perp we have:

$$-k_\perp^2 \tilde{\psi}(k_\perp, z) + \frac{\partial^2}{\partial z^2} \tilde{\psi}(k_\perp, z) + k^2 \tilde{\psi}(k_\perp, z) = 0 \quad (2.8)$$

with $\tilde{\psi} = \mathcal{F}(\psi)$ and k_\perp the spatial frequencies. The general solution of this equation yields

$$\tilde{\psi}(k_\perp, z) = \tilde{\psi}^+(k_\perp, 0) e^{i\kappa z} + \tilde{\psi}^-(k_\perp, 0) e^{-i\kappa z}, \quad (2.9)$$

with the two terms representing respectively the propagation solutions towards a positive (+) and negative (−) z - forward and backward scattering. In our case, back-propagating terms can be neglected and, therefore, only the first term applies. Inserting this term into Eq. (2.8) we obtain

$$(k^2 - \kappa^2 - k_\perp^2) \tilde{\psi}(k_\perp) = 0. \quad (2.10)$$

This formulation gives us directly two solutions: $\tilde{\psi}(\vec{k}) = 0$, which is the trivial solution; or $\tilde{\psi}(\vec{k}) \neq 0$, with $\kappa = \sqrt{k^2 - k_\perp^2}$. In the Fourier space the set of non-trivial solutions consists, thus, of a sphere of centre $O = (0, 0, 0)$ and radius $|k|$. This sphere is known as *Ewald's sphere* and is schematized in Fig. 2.3.

The initial condition is given by the Fourier transform of the transverse dimension of the complex amplitude in $z = 0$ and, finally, the solution in the direct space is given by the inverse Fourier transform of $\tilde{\psi}(k_\perp, z)$ written:

$$\psi(k_\perp, z) = \mathcal{F}^{-1} \left\{ \tilde{\psi}^+(k_\perp, 0) e^{i\kappa z} \right\}. \quad (2.11)$$

This solution does not use any simplification and takes into account all the frequencies k_\perp of the angular spectrum. Eq. (2.11) allows two situations:

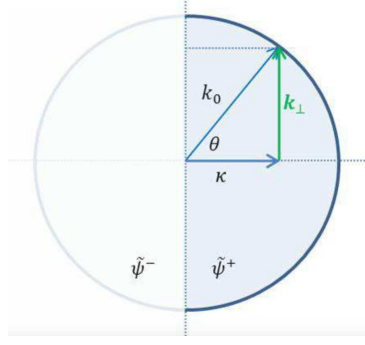


Figure 2.3: **Representation of the wave vector in Ewald's sphere [121]**. Angular spectrum, represented in Ewald's sphere, which describes the angular distribution of the "diffracted" wave vector of modulus value $|k|$ in reciprocal space. The Ewald's sphere allows a representation of the "diffracted" wave vector in agreement with the conservation of energy (elastic scattering).

1. $k^2 - k_{\perp}^2 > 0$: where κ is real and therefore the wave propagates;
2. $k^2 - k_{\perp}^2 < 0$: where κ is complex; the term $\pm i\kappa z$ is then real and the amplitude of the wave decreases exponentially with z . This type of wave is called *evanescent* and is particularly exploited by near-field microscopy.

From here one can deduce that the waves having a frequency content greater than k (corresponding to a wavelength smaller than λ) can not propagate. This corresponds to the so-called *diffraction limit*, which explains why in a coherent diffraction imaging experiment the maximum resolution is limited by the wavelength of the source.

2.2.1.2 Fresnel and Fraunhofer Diffraction

A widely adopted integral solution of the scalar Helmholtz equation is the Rayleigh-Sommerfeld diffraction integral [133]. Its derivation can be found in detail in Goodman's book [131]. Assuming an aperture lying in a plane (x, y) and illuminated in the positive z direction, the wavefield across a (X, Y) plane, parallel to the (x, y) , at a normal distance Z from it, is given by

$$U_{\text{diff}}(X, Y) = e^{-ikZ} \iint U_o(x, y) \times \frac{e^{ikr}}{i\lambda Z} dx dy \quad (2.12)$$

with $k = 2\pi/\lambda$ and $r = \sqrt{(X-x)^2 + (Y-y)^2 + Z^2}$. Here $U_o(x, y)$ represents the field in the aperture plane, while $U_{\text{diff}}(X, Y)$ is the field of the diffraction pattern, following the coordinate convention defined in Appendix A. Assuming now that the diffracting object is significantly small in comparison with the propagation distance, i.e. $(X-x)^2 + (Y-y)^2 \ll Z^2$, one can carry out a binomial expansion of the square root for r and keep only the first two terms, so that:

$$r \simeq Z + \frac{(X-x)^2 + (Y-y)^2}{2Z}. \quad (2.13)$$

This constitutes the Fresnel approximation, which introduced in Eq. (2.12) yields the Fresnel diffrac-

tion equation:

$$U_{\text{diff}}(X, Y) = \frac{e^{ikZ}}{i\lambda Z} \iint U_o(x, y) e^{i\frac{k}{2Z}[(X-x)^2 + (Y-y)^2]} dx dy. \quad (2.14)$$

The accuracy of Fresnel approximation is guaranteed from what is called the near field, if $Z^3 \gg \frac{\pi}{4\lambda} [(X-x)^2 + (Y-y)^2]_{\text{max}}^2$ [131].

Developing the factorizations in the exponential of equation 2.14, the Fresnel diffraction equation takes the form:

$$U_{\text{diff}}(X, Y) = \frac{e^{ikZ}}{i\lambda Z} e^{i\frac{k}{2Z}(X^2+Y^2)} \iint \underbrace{e^{i\frac{k}{2Z}(x^2+y^2)}}_{\text{Fresnel Phase}} U_o(x, y) e^{-i2\pi(\frac{1}{\lambda Z})(xX+yY)} dx dy. \quad (2.15)$$

In Equation 2.15 the quadratic phase exponential term labelled *Fresnel Phase* will approach unity over the entire aperture if $Z \gg \frac{\pi}{\lambda}(x^2 + y^2)_{\text{max}}$ - known as the Fraunhofer approximation. This leads us to a limiting case of the Fresnel diffraction, called Fraunhofer diffraction, which occurs in what is called the far field.

With the Fraunhofer approximation, the diffraction field at a distance z from the object yields

$$U_{\text{diff}}(X, Y) = \frac{e^{ikZ}}{i\lambda Z} e^{i\frac{k}{2Z}(X^2+Y^2)} \iint U_o(x, y) e^{-i2\pi(\frac{1}{\lambda Z})(xX+yY)} dx dy \\ \propto \mathcal{F}\{U_o\}\left(\frac{X}{\lambda Z}, \frac{Y}{\lambda Z}\right) \quad (2.16)$$

which is recognised (aside from the multiplicative factors) to be the Fourier transform of the complex field $U_o(x, y)$. Since it is the intensity, and not the field, that is detectable, our Fraunhofer diffraction pattern is, then, the squared magnitude of the two dimensional Fourier transformation of the aperture field:

$$I = |U_{\text{diff}}|^2. \quad (2.17)$$

Comparing the above equation with 2.1, one can identify the spatial frequencies f_X and f_Y as given by $\frac{X}{\lambda Z}$ and $\frac{Y}{\lambda Z}$, respectively. It is, therefore, the scaling factor:

$$F_{\text{scaling}} = \frac{1}{\lambda Z}, \quad (2.18)$$

which transforms the "real" space coordinates in a Fraunhofer diffraction pattern (measured in $[m]$) into the space of spatial frequencies (measured in $[m^{-1}]$).

The Fraunhofer diffraction approximation is valid when $F \ll 1$, with F denoting *Fresnel number*, which is defined by

$$F = \frac{a^2}{\lambda Z}. \quad (2.19)$$

Here a represents the characteristic dimension of the (diffracting) object. Small and large Fresnel

numbers correspond to, respectively, the far field and near field regimes. From Eq. (2.19), one can consider far field at $Z \gg \frac{a^2}{\lambda}$.

In this manuscript both types of diffraction described here will be addressed. In-line holography will be treated in the Fresnel regime, while coherent diffraction imaging and Fourier transform holography require far field regimes, where Fraunhofer approximation takes place.

2.2.2 Transmittance of an Object in Projection Approximation

It has been shown in Eqs. 2.14 and 2.16, for near field and far field, respectively, the relation between the diffracted wave at the plane of detection (note that the intensity of the measured diffraction pattern constitutes the squared magnitude of this wavefield) and the wave transmitted by the object in the transverse plane. It is now relevant to find the relation between the image of the object and this reconstructed transmitted wave.

When imaging an object, one can describe it by means of a transmission function, typically called object's *transmittance*. The transmittance of an object describes the passage of rays through its structure by defining a nominal surface/plane, in which all the transverse phase and amplitude changes are imprinted. This notion implies that the object's modification to the complex amplitude of an incident wave is independent of the properties of the incident wave and that it is only a function of the two dimensions transverse to the direction of propagation. When in far field, this is accomplished in what is called the *projection approximation* [134, 135]. The projection approximation assumes negligible diffraction within the scattering volume, so that all scattering within the object is fully described by one single exit wave. This way, the transmitted wave, $U_o(r_{\perp}, \omega)$, is simply expressed as the product of an incident wave, $U_{inc}(r_{\perp}, \omega)$, by the object's transmittance function:

$$U_o(r_{\perp}, \omega) = U_{inc}(r_{\perp}, \omega) t(r_{\perp}, \omega), \quad (2.20)$$

where this transmittance $t(r_{\perp}, \omega)$ is defined in a nominal plane localised immediately after the object.

If one can consider that the incident wave is a monochromatic plane wave, Eq. (2.20) is even more simplified. A plane wave propagated along the optical axis, z , is described by $U_{inc}(r_{\perp}) = e^{ikz}$. By defining an axis, with $z = 0$ at the object location, one can reduce $U_{inc}(r_{\perp}) = 1$. Consequently, the spatially transmitted field yields

$$U_o(r_{\perp}, \omega) = t(r_{\perp}, \omega). \quad (2.21)$$

In the projection approximation, the object should be considered *optically thin* so that the diffraction within its thickness is negligible when compared to the propagation distance. If e is the object thickness and δ_{lat} is the lateral resolution of the reconstruction, the condition for an *optically thin* object is described as [122]:

$$e < \frac{2\delta_{lat}^2}{\lambda}. \quad (2.22)$$

Hence, to reach a resolution of λ , it is, thus, necessary to have a thickness of less than 2λ . The term $\frac{2\delta_{iat}^2}{\lambda}$ in Eq. (2.22) describes the *depth of field* (DOF), which is also a function of the diffraction angle θ_{max} :

$$DOF = \frac{2\lambda}{\theta_{max}^2}. \quad (2.23)$$

When the object thickness is smaller than the DOF, the exit wave is associated to a single object plane, which corresponds to the reconstruction plane visualized with computational algorithms. Otherwise, there will be more than one object plane, thus more than one possible phase associated to the measured diffraction pattern. This can prevent the convergence of iterative algorithms. Indeed, one may need additional constraints on the object support to associate only one object plane for the reconstruction. Other methods are more suited to image "optically thick" specimens, such as ptychography [136–139] or holography with back-propagation functions [38, 119, 129, 140]. In holographic experiments (FTH, HERALDO, in-line and off-axis holography,...), the phase information is encoded in the hologram. Thus, there is a unique solution obtained in the plane of the object and the reference. All these concepts will be explained later on in this chapter.

2.2.2.1 Transmittance and Complex Refractive Index

As discussed, the transmittance of an object describes the passage of rays through its structure, by defining a nominal exit surface, in which all the transverse phase and amplitude changes are imprinted. This imprinted changes can be described in terms of the sample's complex refractive index, \tilde{n} , yielding:

$$t(r_{\perp}, \omega) = e^{ik\tilde{n}(r_{\perp}, \omega)z}. \quad (2.24)$$

In general, an object is defined by a refractive index, which is a macroscopic representation of the radiation-matter interaction. The complex refractive index, $\tilde{n}(r_{\perp}, \omega)$, is a unitless quantity, corresponding to the ratio of the speed of light in vacuum to the speed of a given electromagnetic wave in a particular medium. In the UV-X spectral range, this index deviates only slightly from unity, being for convenience commonly written in the form:

$$\tilde{n}(r, \omega) = 1 - \delta(r, \omega) - i\beta(r, \omega) \quad (2.25)$$

with

$$\delta(r, \omega) = \frac{r_e \lambda^2}{2\pi} n_e(r) f_1(\omega) \quad (2.26)$$

$$\beta(r, \omega) = \frac{r_e \lambda^2}{2\pi} n_e(r) f_2(\omega) \quad (2.27)$$

where ω denotes the radiation frequency, r_e is the classical electron radius and n_e the electron density [28]. The factors $f_1(\omega)$ and $f_2(\omega)$ define the real and imaginary parts of the atomic scattering factor, whose values are tabled for the spectral range of interest [141].

Substituting equations (2.24) and (2.25) in Eq. (2.20), we obtain

$$U_o = U_{inc} e^{iknz} e^{-k\beta z} \quad (2.28)$$

with $n = (1 - \delta)$, such that $\tilde{n} = n + \beta i$. From Eq. (2.28) one can notice that the real part of the complex refractive index, $\Re\{\tilde{n}\} = n$, accounts for refraction, describing the phase, $\varphi = knz$, accrued by the wave as it propagates across the medium. In turn, the imaginary part, $\Im\{\tilde{n}\} = \beta$, accounts for the absorption of light in the medium, describing the attenuation of the wave as it is absorbed. This formalism is commonly used in the IR, visible and UV spectral ranges where the real part, n , is the familiar index of refraction that appears in Snell's law and the Fresnel equations [142].

2.3 Detection and Reconstruction of Fraunhofer Diffraction Patterns

In this section we will introduce far-field detection techniques obeying to the formalisms of Fraunhofer approximation.

2.3.1 Coherent Diffraction Imaging

Coherent diffraction imaging or coherent diffractive imaging (CDI) is a type of coherent lensless imaging in which a beam is focused on an isolated object, reflective or transmissive, and the produced diffraction pattern is measured with an intensity detector array in the far field. This diffraction pattern is then inverted with *phase retrieval algorithms* to overcome the *phase problem* and recover the image of the object [35, 128, 143].

The technique of CDI is particularly used in the XUV and X-ray spectral ranges. Based on an imaging system of easy implementation, that is devoid of image-forming optical elements, CDI promises spatial resolutions that are limited, in principle, only by the wavelength of the incident light. Besides these aspects, this technique offers a large number of other significant advantages including the possibility of retrieving amplitude and phase information of the sample; the versatility of the processing techniques that can be applied to the digitally acquired data; the diversity of the samples it can image, which generally require no preparation; and the compatibility with single pulse illumination.

Amongst its limitations one can find the need to have an isolated sample; the restrictive two-dimensional object reconstructions; the use of a complex algorithm, whose performance requires some time; and the possibility of failure or ambiguity in the convergence of this algorithm as, in some specific cases, different objects can have identical diffraction patterns (*homometric structures*) [144]. When not applied in single pulse illumination regime, radiation damage is also a practical limitation of this technique for dose-sensitive samples [145].

2.3.1.1 Coherent Diffraction Imaging: the Principle

The procedure to perform CDI is illustrated in Fig. 2.4. For a typical transmissive sample, the object is positioned in a plane perpendicular to the optical axis and is illuminated by a highly coherent beam. The light scattered from it is then detected in the far field. Assuming a paraxial approximation, the diffraction pattern is exactly the squared magnitude of the two-dimensional Fourier transformation of the field's spatial profile at the object plane, as discussed in Section 2.2.1. For a plane wave, one can assume that this spatial profile, apart from constant factors, is given by the object's complex-valued transmittance, i.e.

$$I(X, Y) = |\mathcal{F}\{t(x, y)\}|^2 \quad (2.29)$$

(see Sections 2.2.1 and 2.2.2).

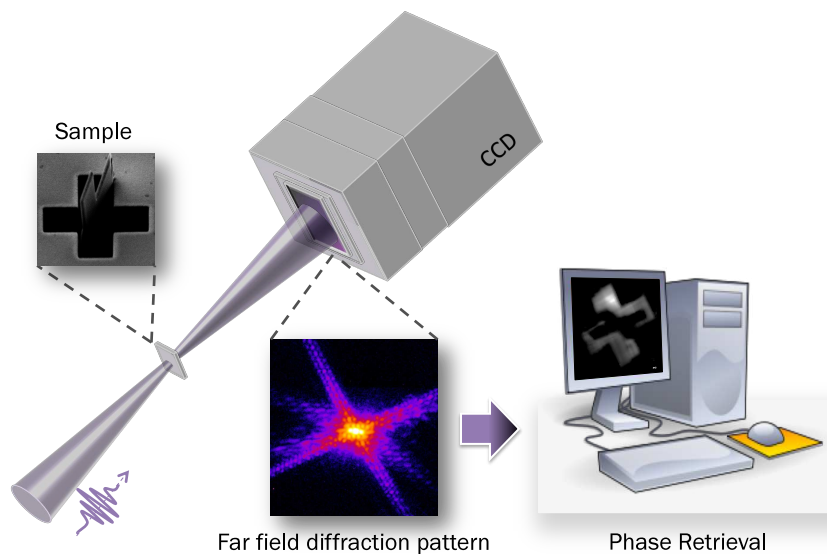


Figure 2.4: **Typical setup for coherent diffraction imaging.** In the typical implementation of CDI in transmission, a highly coherent beam is focused onto the sample, gaining modulations from its phase and amplitude. The resultant diffraction pattern is, then, collected in a CCD detector placed in the far field. Finally, computational phase retrieval algorithms are implemented to retrieve the “lost phase” and reconstruct the image of the object.

As introduced before, the problematic of the reconstruction consists in finding the object without phase detection on the reciprocal space. In CDI, this phase is recovered through an iterative process. Iterative phase retrieval algorithms converge to the spatial phase in the diffraction plane using constraints in both real (object plane) and reciprocal (diffraction plane) spaces. In the reciprocal space, the diffraction pattern recorded by the detector allows building our constraint, substituting the iterated version of $I(X, Y)$ in Eq. (2.29). In the real space, the object is contained in a finite dimension, called “support”. An example of a commonly-employed first constraint to this support is the object's autocorrelation. Follow-

ing Fraunhofer's approximation, this autocorrelation is defined as the Fourier transform of the measured diffraction pattern, i.e. $\mathcal{F}\{I(X, Y)\}$. This way, a simple Fourier transform links the two constraints between real and reciprocal spaces. During the detection of the diffraction patterns, the coherence of the incident wave plays an important role. CDI requires an illuminating beam with a transverse coherence that is at least as large as the object is wide. This coherence creates a characteristic *speckle pattern* in the diffraction plane, which constitutes the *phase signature* of the diffraction pattern. In general, most phase retrieval algorithms use these two kinds of constraints to reconstruct, simultaneously, the "lost phase" in the reciprocal space and the object image in the real space. The solution is generally unique for problems that have more than one dimension [146, 147].

2.3.1.2 Coherent Diffraction Imaging: Iterative Phase Retrieval Algorithms

The phase reconstruction algorithms are inspired by that of Gerchberg-Saxton, originally used in crystallography in 1972 [148].

The Gerchberg-Saxton (GS) algorithm relies on two intensity measurements - one captured in the Fourier space and one in the near field - to reconstruct the object. The process is described in Fig. 2.5. Let's consider the two planes of measurement called image plane and diffraction plane, with measured intensities $|F_i|^2$ and $|F_d|^2$, respectively. The first step of the GS algorithm consists in generating a random phase to perform a first image, denoted g . The following steps are:

1. apply a Fourier Transformation to the image g and obtain the phase term ϕ from $G = |G| e^{i\phi}$, where $G = \mathcal{F}\{g\}$;
2. impose the first amplitude constraint: the squared modulus of G has to be equal to the intensity pattern in the diffraction plane, which leads to $G' = |F_d| e^{i\phi}$;
3. perform an inverse Fourier Transformation to the image G' and obtain the phase term ϕ' from the obtained complex image $g' = |g'| e^{i\phi'}$;
4. impose the second amplitude constraint: the square modulus of g' has to be equal to the intensity pattern in the image plane, which leads back to the image $g = |F_i| e^{i\phi'}$;
5. iterate this process.

The GS algorithm gives the phase distributions in the two detection planes. As one can see, these are reconstructed by propagating the complex-valued wavefield between the two planes, back and forward, and replacing the updated amplitudes at each iteration with the measured amplitudes. This back and forward propagations are ensured with Fourier transformations, according to Fraunhofer approximation.

In CDI, however, only one intensity measurement is available – the diffraction pattern. Similarly to the GS algorithm, CDI's method also relies on back and forward propagations of the complex-valued wavefield, but this time, between the object and detector planes. To ensure the convergence of the algorithm and compensate for the "missing plane" information, CDI restricts the solutions space by using constraints. These constraints are:

- in the detector plane (reciprocal space): the amplitude of the updated wavefield is replaced by the square root of the measured intensity;

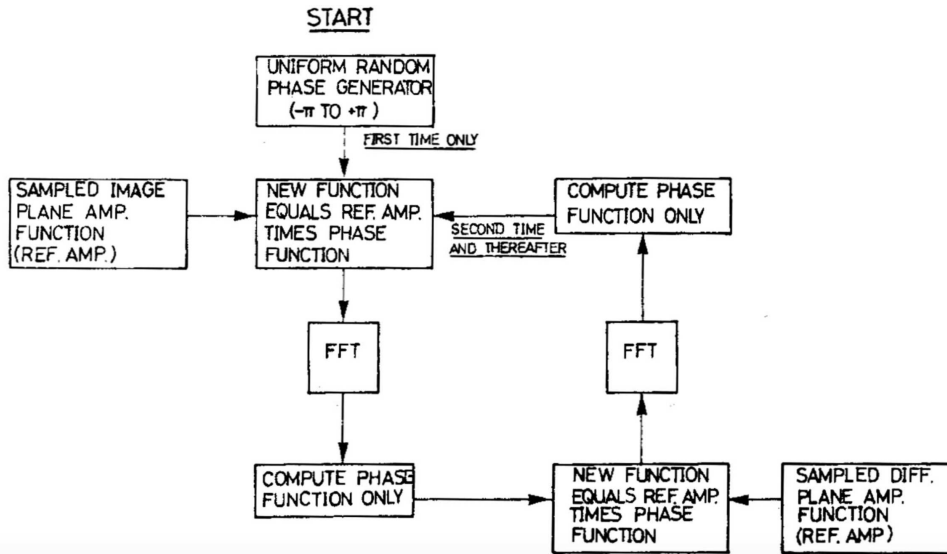


Figure 2.5: **Schematic drawing of the Gerchberg-Saxton phase determining algorithm [148].** This algorithm allows retrieving the phase distributions in the two detection planes, receiving as input the measured intensity patterns.

- in the object plane (real space): the object "support" of the reconstruction is defined. For the support, the object distribution must be surrounded by known values, typically zeros, in accordance with the oversampling conditions (which will be discussed later on). Depending on the experiments, this support may or may not be precisely known. In all cases, one knows that the object is supported by its autocorrelation, corresponding to twice its dimensions. The autocorrelation is, thus, a commonly used first input support. This constraint can also be combined with other requirements, as for instance, the real and positive nature of the object distribution.

This algorithm approach was proposed in 1978 by Fienup [35], upgrading the GS algorithm by allowing to reconstruct the object using only the intensity constraint in the reciprocal space. Fienup's hybrid input-output algorithm (HIO) is a significant contribution to the imaging community and is probably the most popular phase retrieval algorithm nowadays, inspiring as well several variations. The steps of the algorithm are summarised in Fig. 2.6. It starts by generating a random phase and performing a first reconstruction, denoted g . Follows to:

1. apply a Fourier Transform to the object g and obtain the phase term ϕ from $G = |G| e^{i\phi}$;
2. impose the reciprocal space constraint: the square modulus of G has to be equal to the experimental diffraction pattern $|F|^2$, which leads to $G' = |F| e^{i\phi}$;
3. perform an inverse Fourier Transform to G' and recover the object g' ;
4. apply the finite object support constraint in order to obtain the new iteration of the reconstruction g ;
5. iterate this process.

Note that the notation follows the one of Fig. 2.6. During the iterative process, an error function based on the satisfaction of the constraints is computed (an example will be provided later). A final

reconstruction is achieved once this measured error is minimised or below a specified threshold.

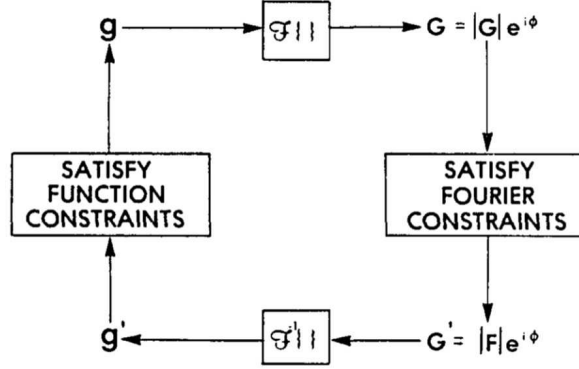


Figure 2.6: **Schematic drawing of a general algorithm for iterative phase retrieval [143].** This algorithm allows a simultaneous reconstruction of the phase of the diffraction pattern and the wavefield in the image plane (reciprocal plane to the detection plane).

Several types of CDI algorithms exist [34, 149] and the choice of one of them over another depends closely on the experimental conditions. In this work, we use the GS algorithm (Future prospects, Section 6.1) and the algorithm developed by P. Thibault based on the *difference map* technique [36] (Chapter 5), which is a generalisation of Fienup’s HIO algorithm. This algorithm consists in projecting the solutions on a set of *constraints spaces* [127], denoted C_1, C_2, \dots, C_n , defined as subsets of a finite-dimensional Hilbert space, \mathcal{E} . This *set of constraints* concern real physical constraints, such as the measured diffraction pattern, the object support in real space, phase positivity, etc. The goal of the reconstruction algorithm is then to find the solution (reconstruction) $x \in \mathcal{E}$, which satisfies:

$$x \in C_1 \cap C_2 \cap \dots \cap C_n. \quad (2.30)$$

For all $x \in \mathcal{E}$ and $i \in [1, N]$, we define the *projection operator* $P_{C_i} : \mathcal{E} \rightarrow P_{C_i}$ as [127, 150]:

$$P_{C_i} : x \rightarrow P_{C_i}(x) = y, \text{ such that } y \in C_i \quad (2.31)$$

which minimises $\|x - y\|$.

The solution resulting from all the projections on the constraints then verifies [127]:

$$\forall i \in [1, N], P_{C_i}(x_{sol}) = x_{sol}. \quad (2.32)$$

In our case, we have $N = 2$: a support constraint and an intensity constraint, for which we define the corresponding projectors P_1 and P_2 . Thereby, the iteration loop $(x_n)_{n \in [1, \dots, N_{iter}]}$ can be written in the form:

$$x_{n+1} = x_n + \beta \times d(x_n), \quad (2.33)$$

with

$$d(x) = y_2 - y_1, \quad (2.34)$$

and

$$\begin{cases} y_1 = P_2[(1 + \gamma_1)P_1(x) - \gamma_1 x] \\ y_2 = P_1[(1 + \gamma_2)P_2(x) - \gamma_2 x] \end{cases} \quad (2.35)$$

where γ_1 , γ_2 et β are complex parameters. The diagram presented in Fig. 2.7 illustrates the principle of projections on both spaces.

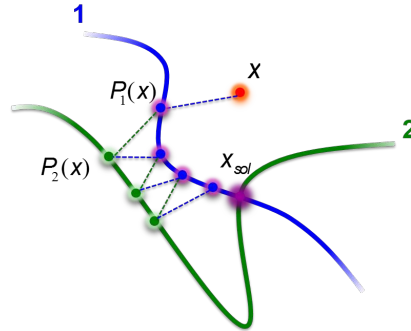


Figure 2.7: **Illustration of successive projections applied to x between two spaces of constraints [140].**

At each iteration, an error function is computed, measuring the similarity of the reconstruction to the "true" solution. A final reconstruction is achieved once this error function is minimised or below a specified threshold. Here, it is given by:

$$\epsilon_n = \sqrt{\sum_{i=1}^{N_s} |d_i(x_n)|^2} \quad (2.36)$$

where N_s is the number of constituting elements of the solution x . This error falls sharply during the first iterations to then fluctuate around a minimum. Typically, from a few hundred iterations originating from the same initial condition, one retrieves a dozen reconstructions that minimise the error function ϵ . In the approach followed in this work, these reconstructions are, later, summed coherently to improve the signal-to-noise ratio (see Section 2.5.2.3).

2.3.2 Fourier Transform Holography

As a holographic technique, Fourier Transform Holography (FTH) is built upon an interference phenomenon between a reference wave and a scattered wave from a sample [19, 27, 37, 74]. In its most standard implementation, FTH uses a well characterised aperture (such as a pinhole) as a reference, generated in plane with the unknown specimen, commonly called the object. This lensless imaging technique exploits the convolution of object and aperture to encode the object information in a hologram, recorded in the far field, as a Fraunhofer diffraction pattern.

In this manuscript will be exploited the technique of digital Fourier transform holography (DFTH), in which the hologram is electronically recorded and stored, while all the reconstruction is retrieved computationally. Amongst the advantages of this digital detection one can find the ability to acquire fast

images, the possibility of retrieving both, amplitude and phase data of the optical field, and the versatility of the processing techniques that can be applied to the complex field data.

DFTH (from now on generalised as FTH) is a scheme which is usually applied in the XUV and X-ray spectral ranges, where efficient lenses are difficult to produce. It also offers a large number of other significant advantages such as its simplicity, speed and accuracy; high spatial resolutions, not limited by detector's pixel size; and its compatibility with single pulse illumination. The disadvantages of its use are mainly the compromise signal-resolution given by the reference wave; the required sample preparations; the restrictive two-dimensional object reconstructions; and the limitations attributed to the micro and nano-fabrication abilities of the equipments used to manufacture the holographic masks. Reaching wavelength-limited spatial resolutions will thus require innovative approaches such as the use of nanoparticles, atoms or molecules as references, besides extremely intense coherent light.

2.3.2.1 Fourier Transform Holography: the Principle

The first procedure to perform Fourier Transform Holography is the recording procedure, illustrated in Fig. 2.8 (a) and (b). The object and reference are placed in the same plane, perpendicular to the optical axis, and both are illuminated by a highly coherent beam. The light scattered from the reference and object interfere and is detected in the far field. The recorded intensity distribution is called hologram (see Fig. 2.8 (b)). Assuming a paraxial approximation, the hologram is exactly the squared magnitude value of the two-dimensional Fourier transformation of the field's spatial profile, at the object/reference plane, as discussed in Section 2.2.1.

With the detection of the intensity pattern alone, the phase information from the Fourier transform is lost leading to the before-mentioned "phase problem". FTH addresses this problem with the use of a reference wave, encoding the phase information in the form of fringes inside the hologram. Reconstructing a real space image of the object, the last procedure of FTH, involves recovering this encoded phase information. This is accomplished from the autocorrelation of the object, recovered through the extraction of the two-dimensional Fourier transform of the recorded hologram. This 2D FT can be implemented by optical means or by the numerical implementation of a Fast Fourier transformation. The real space image of the object, the one recovered in the reconstruction process, corresponds to the spatial convolution of the "real" object with the reference (whose size should be comparable to the wavelength to ensure that it acts as a Dirac delta point), Fig. 2.8 (c).

To understand the physical sense behind the phase encoding, we first need to consider the waves emitted from both, reference and object, as spherical waves of matched curvature. At any given detection point on the hologram, the phase of the waves differ only by the path length difference between their respective points of origin at the sample (object and reference) and any additional phase induced by the object. Interference fringes arise from the modulation of this phase across the spatial extent of the detector. The spatial frequency of those fringes is inversely proportional to the separation between the reference and the points on the object.

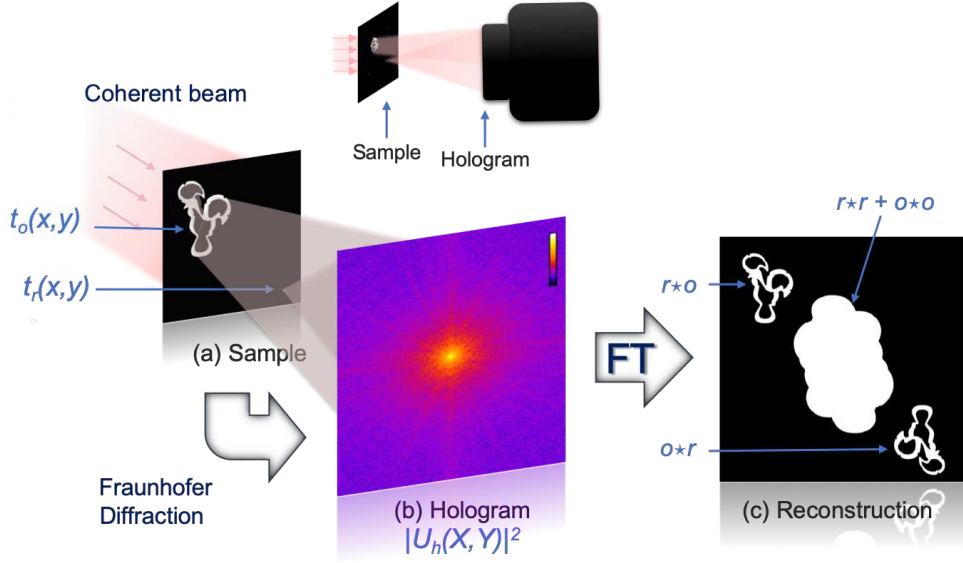


Figure 2.8: **Schematic of Fourier Transform Holography.** (a) A sample with an object - rooster - and a reference - pinhole -, both in the same plane, is coherently illuminated. (b) A hologram is recorded in the far field as a Fraunhofer diffraction pattern. (c) A Fourier transform of the hologram allows the object reconstruction from the cross-correlation of the sample.

2.3.2.2 Fourier Transform Holography: Mathematical Approach

After a conceptual explanation, a mathematical treatment is provided [142, 151].

The spatial amplitude transmittance function from a sample with coplanar reference and object, as illustrated in 2.8 (a), can be defined as

$$t(x, y) = t_r(x, y) + t_o(x, y), \quad (2.37)$$

where $t_r(x, y)$ is the amplitude transmittance function from the reference and $t_o(x, y)$ from the object. Let's now consider a spatially coherent monochromatic plane wave (i.e. light with infinite transverse and longitudinal coherence), propagated along the optical axis, illuminating the sample. The incident wave function is, thus, defined by $U_{inc}(x, y) = U_0(x, y)e^{ikz}$. By choosing the origin of the z -axis so that $z = 0$ at the object location, one can simply work with the incident amplitude distribution $U_0(x, y)$. Therefore, the spatially transmitted field, $U_o(x, y)$, yields

$$\begin{aligned} U_o(x, y) &= U_0(x, y)t(x, y) \\ &= U_0(x, y)t_r(x, y) + U_0(x, y)t_o(x, y) \\ &\equiv r(x, y) + o(x, y), \end{aligned} \quad (2.38)$$

with $r(x, y) = U_0(x, y)t_r(x, y)$ the reference contribution to the transmitted field and $o(x, y) = U_0(x, y)t_o(x, y)$ the field transmitted by the object. Note that $o(x, y)$ is the real space object reconstruction.

Applying equation 2.16 to equation 2.38, we find that the complex field amplitude in the far field is

given by

$$\begin{aligned}
U_h(X, Y) &= \mathcal{F} \{ U_o(x, y) \} (X, Y) \\
&= \mathcal{F} \{ r(x, y) \} (X, Y) + \mathcal{F} \{ o(x, y) \} (X, Y) \\
&= R(X, Y) + O(X, Y) \equiv R + O.
\end{aligned} \tag{2.39}$$

where the capital letters O and R denote Fourier transformations of $o(x, y)$ and $r(x, y)$, respectively, and X, Y are the coordinates of the hologram measured in a detector. In this step the linearity property of the Fourier Transformation was used (see Appendix C). More details on Fourier Transform properties can be found, for instance, on Appendix A of Schnars and Juepter book [104]. The detected intensity, $H(X, Y)$, which constitutes the hologram is, thus, given by

$$\begin{aligned}
H(X, Y) &= |R + O|^2 \\
&= RR^* + OO^* + OR^* + RO^* \\
&= |R|^2 + |O|^2 + OR^* + RO^*
\end{aligned} \tag{2.40}$$

The first two terms of equation 2.40 arise from each one of the apertures alone while the last two terms come from waves from both apertures, giving rise to the interference pattern, responsible for the fringes in the hologram. A simulated hologram, obtained from a simulated sample is illustrated in Fig. 2.8 (b).

The real space images are reconstructed by calculating the two dimensional Fourier transformation of the hologram as follows:

$$\begin{aligned}
\tilde{I}(u, v) &= \mathcal{F} \{ H(X, Y) \} (u, v) = \mathcal{F} \{ |R|^2 \} + \mathcal{F} \{ |O|^2 \} + \mathcal{F} \{ OR^* \} + \mathcal{F} \{ RO^* \} \\
&= \underbrace{r \star r + o \star o}_{\text{self-correlation}} + \underbrace{o \star r + r \star o}_{\text{cross-correlation}}.
\end{aligned} \tag{2.41}$$

with u and v the new real space variables and the \star denoting complex correlation. In the last step the correlation theorems of FT's were applied (see Appendix C). The cross-correlation terms of equation 2.41 correspond to the twin images in Fig. 2.8 (c), while the self-correlation ones correspond to the undifferentiated pattern in the middle. The reference used in the sample illustrated in Fig. 2.8 (a) is the conventional FTH reference: one single pinhole, which, mathematically, can be represented by a delta function. In that case, a similar image of o is returned in the cross-correlation since $r \star o = o$. Looking at Fig. 2.8 (c) one can see that both cross-correlation images are identical, differing only by a conjugate and their orientation. Since the reference is a real function, $OR^* = OR$, the term $o \star r$ can also be considered as a convolution $o \otimes r$, according to the convolution theorem of the FT.

For the approximation reasons stated before, in an ideal FTH, the reference should be a delta function with respect to the transmitted radiation intensity. However, in reality, the extent of the reference limits the spatial resolution of the reconstruction, thus blurring the image. Although a smaller pinhole leads to better resolution, it also implies a reduction of the reference signal intensity. This problem can be solved by an "enlargement" of the reference structures, as studied for instance by Schlotter and Guizar-Sicairos

in their PhD dissertations [29, 142]. This can be overcome by using

- multiple reference patterns - which consists of an arrangement of several pinholes;
- extended reference patterns - extended continuous references with corners or kinks, such as lines, rectangles or other shapes.

In the work presented here, only one reference pinhole is used, but the principle is the same for the other two types of references, differing only in some numerical treatment for the last case.

As one can see also in Fig. 2.8 (c), in order to ensure a valid reconstruction, the cross-correlation images should be spatially isolated from the self-correlation. Therefore, in order to perform FTH, one must respect some separation conditions. The limiting distance between the self-correlations and the cross-correlations depends on the size of the object as well as the distance between the object and the reference. The pinhole must be at least three times the radius of the object away from the centre of the object, in order to avoid overlapping. The existence of more than one pinhole adds the extra condition that the pinholes must be separated by a distance, at least, equal to the size of the object.

2.3.3 Detection and Sampling of Fraunhofer Diffraction Patterns

Even though the theoretical models presented in this manuscript are generalised with a Fourier notation \mathcal{F} , as discussed before, lensless imaging relies on a digital detection. Thus either simulations or reconstructions are based on discrete mathematics, often by means of FFT's.

The detection of the diffraction pattern occurs in an array, typically a CCD camera, which accumulates incoming photons (diffraction and noise) during the exposure time. The measured diffraction signal is then the photon flux, photons/m² or J/m², digitalised with a defined sampling ratio. This digitalisation and, particularly, the finite number of pixels of the detector, impose restrictions to the resolution and field of view (FOV) that are achievable for the reconstruction. For this reason, in this section, we will reveal some sampling notations required for the recovery of useful data from a diffraction pattern/hologram recorded in the far field.

Let's consider a diffraction pattern defined by $I_{\Delta_p}(p, q)$ and sampled at a step Δ_p , given by the pixel size of the detector. In the far-field, this magnitude is equal to the squared modulus of the two dimensional Fourier Transform of the exit field, $U_o(x, y)$, at the position of the sample (Eq. (2.17)). Assuming $U_{\Delta_r}(m, n)$ the discrete function of $U_o(x, y)$, at a step Δ_r , the intensity pattern at the detector takes the form:

$$I_{\Delta_p}(p, q) = |U_{\Delta_p}(p, q)|^2 = \left| \frac{1}{\sqrt{MN}} \sum_{m,n} U_{\Delta_r}(m, n) e^{-2\pi i \frac{pm+qn}{N}} \right|^2 \quad (2.42)$$

(note the 1D discrete FT definition from Eq. (2.2)).

If one can consider that the incident wave is a monochromatic plane wave, Eq. (2.21) applies, and the Fourier transform of the diffraction pattern of Eq. (2.42) gives:

$$\tilde{I}(m, n) = \text{FFT}\{I_{\Delta_p}(p, q)\}(m, n) = \sum_{p,q} I_{\Delta_p}(p, q) e^{2\pi i \frac{mp+nq}{N}} = [t_{\Delta_r} \star t_{\Delta_r}](m, n), \quad (2.43)$$

with $t_{\Delta_r}(m, n)$ the sampling function of $t(x, y)$ and the \star denoting complex correlation. In the last step the correlation theorems of FT's were applied. Indeed, as discussed before, the Fourier Transform of the diffraction pattern is the autocorrelation of the object's transmittance function and is defined in a support equal to twice the size of the object [121, 140]. This autocorrelation function is the basis of our reconstruction procedures for the far-field techniques used in this manuscript.

According to Eq. (2.5), one can extract from Eq. (2.43) the relation between both sampling steps, which is given by:

$$\Delta_r = \frac{1}{N\Delta_p}. \quad (2.44)$$

Here, Δ_p is the pixel size of the CCD, which is a matrix of $N \times N$ pixels, and Δ_r is the pixel size of the discrete representation of the transmittance autocorrelation, i.e. the reciprocal space of the plane of the detector (given in $[m^{-1}]$).

For an object with size $a \times a$, sampled in $N_o \times N_o$ pixels in its reconstruction plane, the relation between the real physical dimensions of the object and the sampling of this reconstruction plane is given by:

$$\frac{a}{\lambda Z} = N_o \Delta_r, \quad (2.45)$$

with Z the distance between the object and the detector array and $\frac{1}{\lambda Z}$ the scaling factor (Eq. 2.18), which defines the transition from the real space to the reciprocal space of the plane of detection (space of the reconstructed image) [121, 127]. Remark that in FTH a corresponds to the longest spacing between object and reference.

From here one can extract the effective pixel size of the reconstruction, given in object dimensions (in $[m]$), which occurs for $a = N_o \Delta_{obj}$:

$$\Delta_{obj} = \Delta_r \lambda Z, \quad (2.46)$$

which in function of the CCD pixel size (substituting Eq. (2.44)) yields:

$$\Delta_{obj} = \frac{\lambda Z}{N\Delta_p}. \quad (2.47)$$

The field of view (FOV) of the reconstruction, defined as $FOV = N\Delta_{obj}$ is then given, in terms of the experimental parameters by:

$$FOV = \frac{\lambda Z}{\Delta_p}. \quad (2.48)$$

To allow a reliable reconstruction of the object, the sampling ratio is a key factor. When the sampling interval is too large, frequencies higher than the *Nyquist* frequency will be wrapped and will appear as lower frequencies [150]. This phenomenon is called *aliasing*.

Since the sample has a finite size, reconstructing its entire field of view must satisfy the Nyquist-

Shannon sampling theorem, which states that the diffraction pattern/hologram must be sampled at, at least, twice the maximum spatial frequency of its fringes. In other words, each fringe period must be sampled by, at least, two pixels in the detector, in order to be distinguishable for reconstruction [152, 153]. This way, the sampling interval Δ_p of the diffraction pattern should obey

$$\Delta_p \leq \frac{1}{2\sigma_{max}}, \quad (2.49)$$

where σ_{max} is the Nyquist frequency, corresponding to the maximum frequency in the diffraction figure. Since in the reciprocal space of the diffraction pattern, the maximum frequency is given by the size of the autocorrelation of the object, which in turn is twice the object size, we have that

$$\sigma_{max} = \frac{2N_o\Delta_r}{2} = N_o\Delta_r. \quad (2.50)$$

Therefore, from Eqs. (2.49), (2.50) and (2.45):

$$\Delta_p \leq \frac{\lambda Z}{2a}. \quad (2.51)$$

The treatment described above suits both the lensless techniques implemented in this work, whose detection process occurs in the Fraunhofer regime: coherent diffraction imaging and Fourier Transform Holography. All of these considerations should be taken into account with the purpose of achieving the optimal sampling conditions and field of view, for a detector with a finite number of pixels. Carefully dimensioning these characteristic distances, successful reconstruction of diffraction patterns/holograms are achieved, even in cases with multi-coloured or broadband illumination [18, 19].

2.3.3.1 Nyquist sampling of the intensity pattern in CDI

During the phase retrieval reconstruction process the sampling ratio is particularly important. Indeed, a diffraction pattern suitable for reconstruction in CDI should be Nyquist sampled - or, as often generalized, *oversampled*. The notion of oversampling was first proposed by D. Sayre in 1952 [154], which applied the Shannon sampling theorem to crystallography. One commonly used parameter of CDI is the oversampling ratio, which measures the oversampling of a diffraction pattern [155]. One can define this ratio as a relation between the size of the diffraction figure (N pixels) and the size of the object (N_o pixels) as:

$$O = \frac{N}{N_o}. \quad (2.52)$$

From Eqs. (2.52), (2.44) and (2.45) we can write O as:

$$O = \frac{\lambda Z}{a\Delta_p} \quad (2.53)$$

where, taking the Shannon sampling condition applied to Δ_p (Eq. (2.51)) yields:

$$O \geq 2 \rightarrow N \geq 2N_o. \quad (2.54)$$

This last equation has a simple explanation: in fact, since the object transmittance is a complex function, there are $2N_o$ equations in each dimension. However, the total representation is contained in N pixels. Thus, for the problem to be solvable, at least as many equations as unknowns are required, therefore: $N \geq 2N_o$, i.e. $O \geq 2$. This condition is necessary but not always sufficient, especially in the unidimensional case. In the multidimensional case (our case), oversampling is generally sufficient [146, 147].

2.4 Detection and Reconstruction of Fresnel Diffraction Patterns

In this section we will introduce the technique of in-line holography, which obeys to the formalism of Fresnel diffraction, admitting a detection in the near field.

2.4.1 In-Line Holography

In-line holography refers to the original holographic scheme, introduced as *A new microscopic principle* by Dennis Gabor, in 1948 [103]. This setup constitutes the simplest realisation of the holographic method, requiring no lenses between object and detector, and no sample's special treatment. The application of this lensless imaging technique has been however limited until recently, owing to the non-practicality of the object's image reconstruction with another wave. With the emergence of digital imaging devices and their application to the topic, this was no longer a problem. Ever since, the versatile in-line scheme has been employed in numerous experiments using different types of waves, from electrons to X-rays [38, 39, 104, 129, 156].

The technique explored in this section is the digital in-line holography which, alike previous techniques, involves digital recording and a numerical reconstruction process. Amongst the advantages of this holographic method one can find its simplicity: the setup required is usually only a coherent source and a CCD camera (sometimes a pinhole is used as well); the speed: intrinsic changes in the object can be followed at the capture video rate of the CCD chip; maximum information: a single 2-D hologram contains all the information about the three-dimensional structure of the object; high resolution: optimal resolutions, of the order of the wavelength of the laser, can be achieved; and, finally, the simplicity of sample preparations: no sectioning or staining is required - feature valued especially in the imaging of biological samples, where living specimens can be viewed [129]. As for drawbacks, the main ones are the requirement of a high numerical aperture and the superposition, on the reconstruction, of an out-of-focus virtual twin-image of the object, due to the symmetry of the in-line setup. Also, with the full incoming beam acting as a reference wave, this coherent technique is particularly vulnerable to the aberrations of the source.

2.4.1.1 In-Line Holography: the Principle

By definition, in in-line holography, the reference and object waves share the same optical axis. In a typical setup, a wave passes by an object, located nearly in a central position related to the beam illumination. Part of the wave is scattered by the object, thus creating the object wave O , and the unscattered part of the wave forms the reference wave R . The interference of this two waves is captured by a detector, placed perpendicularly to the optical axis, at a distance Z from the object. If the scattered wave from the object is small compared to the unscattered reference wave, the recorded interference pattern constitutes a hologram.

Figure 2.9 illustrates the two typical in-line holography schemes utilising, respectively, plane and spherical waves. In the first case (Fig. 2.9 (a)), an incident plane wave is illuminating the sample, with a diameter considerably high with respect to the sample's size. In the last scheme (Figs. 2.9 (b)-(c)), a highly coherent beam illuminates the sample after being focused with proper optics. This focal spot, which can be filtered resorting to a pinhole, acts as a "point source" of spherical waves. In both cases, the diameter of the reference beam in the plane of detection will set the interference area, in which the fringes encode the phase induced by the sample to the beam. Analogously to FTH, this interference pattern constitutes the hologram. In-line holography with spherical waves is also called Gabor holography [103] and is the one which most suits the wavelength range of interest, due to the requirement of high numerical aperture of the technique and, as well, the possibility of retrieving reconstructions with magnification.

After the recording process, a numerical reconstruction takes place. The reconstruction in in-line holography contains 3D information of the object encoded in the 2D hologram measured by the detector. The numerical procedure recovers the object reconstruction through back-propagation calculations.

2.4.1.2 In-Line Holography: Mathematical Approach

In this section, simple methods for simulation and reconstruction of holograms, with both plane and spherical waves, will be summarised [39, 131, 157, 158]. Before proceeding, we remark that all the reasoning follows the coordinates convention defined in Appendix A.

General Approach: Separation of Contributions

Let's begin, similarly to Section 2.3.2.2, with the spatial amplitude transmittance function of the plane (x, y) where our object is located. One particularity of in-line holography is that the object covers only a part of the illuminated plane and, where there is no object, the distribution of the incident wave remains undisturbed (see Fig. 2.9). This allows the plane transmittance function to be defined as

$$t(x, y) = 1 + t_o(x, y), \quad (2.55)$$

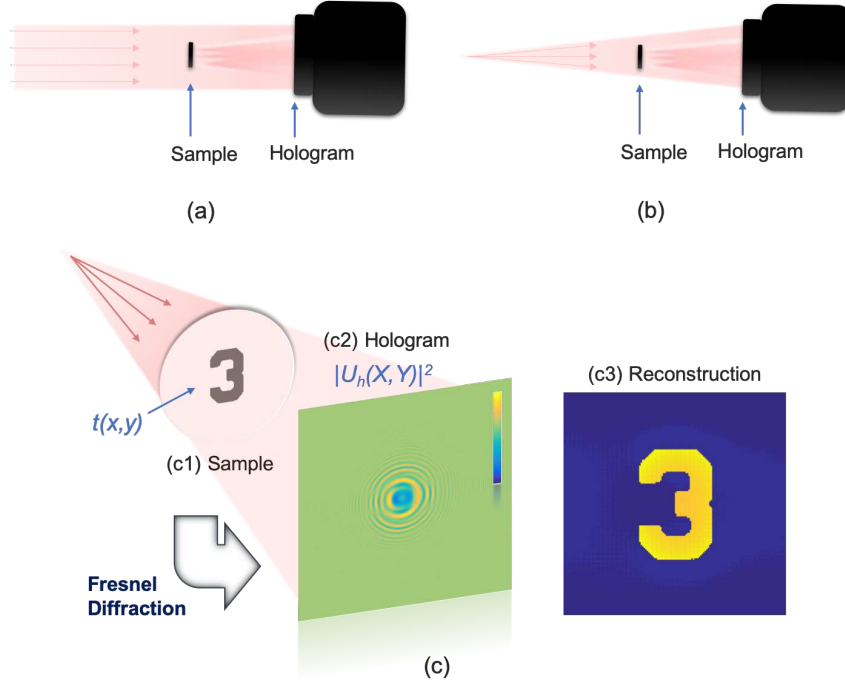


Figure 2.9: **In-line holography schemes.** Schematic of in-line holography with respectively (a) plane and (b-c) spherical waves. (c1) An object "3" is coherently illuminated by a reference spherical wave. (c2) A hologram is recorded as a Fresnel diffraction pattern. (c3) A reconstruction of the original object can be accomplished by a back-propagation algorithm.

where the reference wave has a transmittance of value 1 all over the plane and the object imposes a perturbation $t_o(x, y)$ to this reference wave. As a remark, this transmittance definition allows the separation of both contributions, by defining the object perturbation $t_o(x, y)$ in the interval $[-1, 0]$. This way, the actual object transmittance is given by $t_o(x, y) + 1 \equiv t(x, y)$ and not $t_o(x, y)$, like in the FTH case.

Illuminating the sample with an incident wave $U_{inc}(x, y)$, the wavefront distribution in the plane of the object, immediately after it, is given by

$$\begin{aligned}
 U_o(x, y) &= U_{inc}(x, y)t(x, y) \\
 &= U_{inc}(x, y) + U_{inc}(x, y)t_o(x, y) \\
 &\equiv r(x, y) + o(x, y),
 \end{aligned} \tag{2.56}$$

where $r(x, y)$ describes the reference and $o(x, y)$ the field transmitted by the object. The wave propagation from this point, towards the detector, is described by Fresnel diffraction equation 2.14. Considering a detector positioned in the plane (X, Y) , the field distribution in this plane, denoted $U_h(X, Y)$, can be described, separately, for both contributions, $R(X, Y)$ and $O(X, Y)$. With this notation, the recorded

hologram is

$$\begin{aligned}
H(X, Y) &= |U_h(X, Y)|^2 \\
&= |R(X, Y) + O(X, Y)|^2 \\
&= |R|^2 + |O|^2 + OR^* + RO^*,
\end{aligned} \tag{2.57}$$

where the first term is the constant background, originated by the reference wave alone; the second term comes from the object alone; and the last two terms give rise to the interference pattern, responsible for the fringes in the hologram. The second term is assumed to be substantially small when compared to the strong reference wave term [39].

To retrieve the reconstruction of the object from the resultant hologram, one must normalise it in a first step to remove the dependence on external factors such as the intensity of the reference wave and detector's sensitivity. This can be accomplished by dividing the hologram into the background image:

$$B(X, Y) = |R(X, Y)|^2. \tag{2.58}$$

This background corresponds to the image recorded under the exact same experimental conditions as the hologram, but without the object in the setup. The normalised hologram is, therefore, given by

$$\begin{aligned}
H_0(X, Y) &= \frac{H(X, Y)}{B(X, Y)} - 1 \\
&\approx \frac{OR^* + RO^*}{|R|^2},
\end{aligned} \tag{2.59}$$

where the subtraction of 1 allows the calculations to proceed only with the interference terms, assuming $\frac{|R|^2}{|R|^2} + \frac{|O|^2}{|R|^2} \approx 1 + 0$.

The reconstruction of the digital hologram consists of multiplying the normalised hologram, with the reference wave $R(X, Y)$, followed by a back-propagation of the Fresnel diffraction pattern to the plane of the object. This is given by the integral

$$U_r(x, y) = -\frac{e^{ikZ}}{i\lambda Z} \int_{-\infty}^{\infty} \int_{-\infty}^{\infty} R(X, Y) H_0(X, Y) e^{-i\frac{k}{2z}[(X-x)^2 + (Y-y)^2]} dX dY. \tag{2.60}$$

Since this reconstructed wavefront corresponds to $t_o(x, y)$, to obtain the object transmission function $t(x, y)$, the value 1 needs to be added to the result [39].

In-Line Holography with Plane Waves

A plane wave propagated along the optical axis, z , can be simplified by $U_{inc}(x, y) = 1$, with choice of proper axis (Appendix A). Consequently, the spatially transmitted field at the object plane, illuminated by

such wave yields

$$\begin{aligned} U_o(x, y) &= t(x, y) \\ &= 1 + t_o(x, y) \equiv r(x, y) + o(x, y). \end{aligned} \quad (2.61)$$

Propagated in the Fresnel regime, up to the detector position Z (equation 2.14), the corresponding hologram field becomes

$$U_h(X, Y) = \frac{e^{ikZ}}{i\lambda Z} \int_{-\infty}^{\infty} \int_{-\infty}^{\infty} t(x, y) e^{i\frac{k}{2Z}[(X-x)^2 + (Y-y)^2]} dx dy. \quad (2.62)$$

According to the convolution definition (see Appendix B), neglecting the constant phase factor e^{ikZ} , equation 2.62 can be rewritten in the form of a convolution between the object transmission function $t(x, y)$ and the Fresnel function $s(x, y)$ defined by

$$s(x, y) = \frac{1}{i\lambda Z} e^{i\frac{k}{2Z}(x^2 + y^2)}. \quad (2.63)$$

Thus, $U_h(X, Y)$ becomes

$$U_h(X, Y) = t(X, Y) \otimes s(X, Y) \quad (2.64a)$$

$$\begin{aligned} U_h(X, Y) &= [1 + t_o(X, Y)] \otimes s(X, Y) \\ &= \underbrace{1}_{R(X, Y)} + \underbrace{t_o(X, Y) \otimes s(X, Y)}_{O(X, Y)}, \end{aligned} \quad (2.64b)$$

where $R(X, Y) = 1$ due to $1 \otimes s(X, Y) = 1$. As a remark, in Eq. (2.64b), $t(x, y)$ was again split into the two contributions: object $o(x, y) = t_o(x, y)$ and reference $r(x, y) = 1$, according to Eq. (2.55). Being a convolution, $O(X, Y)$, according to the convolution theorem [104], can be expressed by Fourier transformations. Therefore, $U_h(X, Y)$ can be rewritten in the form:

$$U_h(X, Y) = 1 + \mathcal{F}^{-1} \{ \mathcal{F} \{ t_o(x, y) \} (u, v) \cdot \mathcal{F} \{ s(x, y) \} (u, v) \} (X, Y), \quad (2.65)$$

with (u, v) the spatial frequency coordinates in the Fourier plane and \cdot denoting usual multiplication. The hologram recorded with plane waves is, therefore,

$$H(X, Y) = |1 + \mathcal{F}^{-1} \{ \mathcal{F} \{ t_o(x, y) \} (u, v) \cdot \mathcal{F} \{ s(x, y) \} (u, v) \} (X, Y)|^2. \quad (2.66)$$

The reconstruction of the object transmission function is given by equation 2.60, which can also be expressed in the form of a convolution by

$$\begin{aligned} U_r(x, y) &= R(x, y) H_0(x, y) \otimes s^*(x, y) \\ &= \mathcal{F}^{-1} \{ \mathcal{F} \{ H_0(X, Y) \} (u, v) \cdot \mathcal{F} \{ s^*(X, Y) \} (u, v) \} (x, y). \end{aligned} \quad (2.67)$$

where $R(X, Y) = 1$ was substituted in the last line.

In-Line Holography with Spherical Waves

A spherical wave propagated from a point source, located at a distance z_0 from the object, is described by

$$U_{inc}(x, y) = \frac{e^{ikr_1(x, y)}}{r_1(x, y)}, \quad (2.68)$$

with $r_1(x, y) = \sqrt{x^2 + y^2 + z_0^2}$. Consequently, the spatially transmitted field at the object plane, illuminated by a wave in the form of Eq. (2.68) becomes

$$U_o(x, y) = \frac{e^{ikr_1(x, y)}}{r_1(x, y)} \cdot t(x, y). \quad (2.69)$$

Assuming a Fresnel propagation of this field (Eq. (2.14)) until a detector position Z , Eq. (2.69) yields

$$U_h(X, Y) = \frac{e^{ikZ}}{i\lambda Z} \int_{-\infty}^{\infty} \int_{-\infty}^{\infty} \frac{e^{ikr_1(x, y)}}{r_1(x, y)} \cdot t(x, y) e^{i\frac{k}{2Z}[(X-x)^2 + (Y-y)^2]} dx dy, \quad (2.70)$$

which developed in a paraxial approximation, where $r_1(x, y)$ follows the approximation of Eq. (2.13), gives:

$$U_h(X, Y) \propto \int_{-\infty}^{\infty} \int_{-\infty}^{\infty} t(x, y) e^{i\frac{k}{2z_{eff}}[(\frac{X}{M}-x)^2 + (\frac{Y}{M}-y)^2]} dx dy, \quad (2.71)$$

with

$$M = \frac{Z + z_0}{z_0} \quad (2.72)$$

and

$$z_{eff} = \frac{Z}{M}. \quad (2.73)$$

Indeed, this spherical geometry, apart from constants and factors of unit modulus, relates to a plane wave illumination (see equation 2.62) through an equivalent propagation distance z_{eff} and a magnification factor M , given by the simple relations (2.72) and (2.73) [158].

Eq. (2.71), similarly to the plane-wave case, can be written in the form of a convolution between the object transmission function $t(x, y)$ and the Fresnel function $s(x, y)$ for a spherical-reference wave:

$$s(x, y) = \frac{1}{i\lambda z_{eff}} e^{i\frac{k}{2z_{eff}}(x^2 + y^2)}. \quad (2.74)$$

The hologram recorded with spherical waves is, therefore, calculated from equation (2.66), with a wavefield given by (2.64a), and its size corresponds to the size of the object area, multiplied by the magnification factor M . Likewise, the reconstruction of the object transmission function is given by equation (2.67), where the size of the reconstructed object area is equal to the size of the hologram, divided by the magnification factor M .

2.4.2 Sampling Considerations in In-Line Holography

Alike the far-field techniques, the hologram captured in in-line holography is a discrete representation of the phase-modulated intensity profile, digitalised with a specific sampling ratio. Therefore, again, even though the theoretical models presented in this section are generalised with a Fourier notation \mathcal{F} , the implementation is made through two-dimensional FFT's (see Sections 2.1 and 2.3.3 for reference).

As implicit in the mathematical approach presented earlier on, in in-line holography, both the hologram and reconstruction are sampled in "real space", contrasting with the previous far-field techniques. Indeed, the field of view and pixel size of the reconstruction are given by the dimensions and pixel size of the detector, apart from the magnification factor if a spherical wave is used as reference. When using plane waves, the reconstruction is achieved in a field of view $FOV = N\Delta_{obj}$, where N is the number of pixels of the detection array and $\Delta_{obj} = \Delta_p$ is the pixel size in both object and reconstruction planes. As well, from Section 2.4.1.2, we know that the pixel size in the hologram recorded with spherical waves, Δ_p , corresponds to the pixel size of the plane wave illumination case, multiplied by the magnification factor M . Therefore, in in-line holography with spherical waves, our field of view is given by $FOV = N\Delta_{obj}$ where $\Delta_{obj} = \frac{\Delta_p}{M}$, with M given by Eq. (2.72). This means that the smaller the pixel sizes on the detector, the better the detection of the fringes with higher spatial frequencies in the hologram, and the better the sampling of the reconstruction. However, this parameter should be optimised along with the available field of view, which should be extended enough not to lose essential information in the reconstruction.

In order to ensure proper sampling of the hologram, there is a condition which should be considered, given the process's intermediate passage through the Fourier domain. Indeed, during the reconstruction procedure, the Fourier transform of the normalised hologram is multiplied by the spherical phase term $\mathcal{F}\{s^*(x, y)\}$ (see equation 2.67). This term is only correctly simulated with $N \times N$ pixels when

$$N\Delta_p^2 \leq \lambda z_0. \quad (2.75)$$

The deduction and discussion of this condition can be found in Latychevskaia's work [39].

2.5 Image Quality in Coherent Lensless imaging

In order to analyse the quality of the reconstructions achieved from coherent lensless techniques, two characteristic quantities must be highlighted: the resolution and the signal-to-noise ratio (SNR). In this section, these two concepts are exploited with three main purposes: evaluation of the image quality; discussion of the limitations to this quality; and identification of means and strategies to improve it.

2.5.1 Resolution

The fidelity of an image, representative of some real sample, is a very important concept in imaging. It can be categorised by several distinct and measurable criteria, with a special emphasis on one: the resolution.

Multiple criteria have been suggested for determining the resolution of an image. One of the most commonly accepted is the Rayleigh criterion [28]. The Rayleigh criterion defines resolution as the shortest distance required to discern two point sources, as schematized in Fig. 2.10.

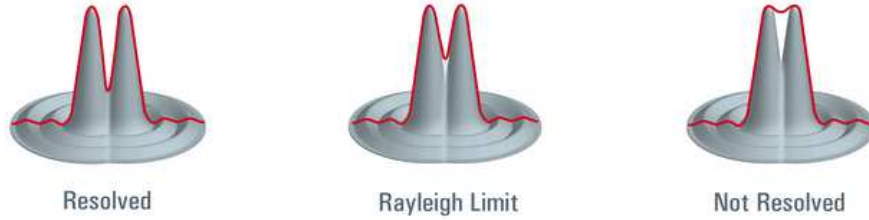


Figure 2.10: The limit of resolution, according to the Rayleigh criterion, shown by the overlapping diffraction patterns of two single Airy Disks. Left: well resolved; middle: just resolved; right: not resolved. Image from [159].

2.5.1.1 Resolution Evaluation in Reconstructions

Quantitatively, the Rayleigh criterion can be described as the distance between the 10% and 90% points of a rising edge [28]. Therefore, the resolution \mathcal{R} of an image, which, by definition is a two-dimensional discretized space, can be expressed as

$$\mathcal{R} = N_{10\%-90\%} \Delta_{obj}. \quad (2.76)$$

Here $N_{10\%-90\%}$ is the number of pixels that constitute the 10%-to-90% rising (or falling) edge, in intensity, and Δ_{obj} the image pixel size. This criterion is the one adopted in this manuscript for the evaluation of the resolution of the achieved experimental reconstructions.

2.5.1.2 Achievable Resolution of a Setup

The resolution one can expect from a coherent lensless imaging experiment is directly related to the value of the accessible frequency components at the detection plane.

In CDI, as the detection occurs in the far field, the mapping of the diffraction pattern represents the spatial frequencies of the diffractive object, which makes the low frequencies located in the centre and the high frequencies on the extremity areas. Similarly, in digital FTH and in-line holography, the fringes that encode the phase of the smallest features in the object are formed by the interference between reference and object wave, scattered at large diffraction angles. The achievable resolution is, thus, limited by the detection of the finest interference fringes in the hologram, given by the *numerical aperture* (NA) of the reference beam at the detector. Therefore, in all cases, increasing the NA of the beam will allow detecting the high frequencies, leading to a better final resolution. The latter writes, by Abbe's criterion [160]:

$$\delta_{lat} = \frac{\lambda}{2 NA}, \quad (2.77)$$

with NA the numerical aperture of the beam, which can be defined by the ratio:

$$NA = \frac{D}{2L}. \quad (2.78)$$

Here L is the "source"-detector distance and D the beam diameter at the detector.

In CDI and FTH, $L = Z$ and the diameter D can be written in terms of the number of pixels extending the diffraction figure, N_{signal} . Assuming a pixel size in the detector given by Δ_p yields:

$$\delta_{lat} = \frac{\lambda Z}{N_{signal} \Delta_p}. \quad (2.79)$$

The achievable lateral resolution in digital in-line holography with plane waves also follows Eq. (2.79) noting that, in this case, N_{signal} is the number of pixels which samples the hologram, usually limited by the reference wave aperture. In digital in-line holography with spherical waves, because it induces a magnification M , this achievable resolution is reduced by $1/M$ [38, 39]:

$$\delta_{lat} = \frac{\lambda Z}{N_{signal} \Delta_p M}. \quad (2.80)$$

If M is large enough, though, the resolution is limited by the NA of the optical system (Eq. (2.77)) [38], which can be written:

$$\delta_{lat} = \frac{\lambda(z_0 + Z)}{N_{signal} \Delta_p}, \quad (2.81)$$

with Z the distance detector-sample and z_0 the distance from the latter to the point source.

Thus, in order to optimise the achievable resolution, the object-detector distance must be reduced, while ensuring that the sampling conditions are fulfilled. In CDI, one must also ensure that the over-sampling condition is valid. Increasing too much the (over)sampling, without binning the intensity on the detector pixels, can though decrease the number of photons per pixel and, consequently, the signal-to-noise ratio (SNR) of the recorded diffraction pattern. As the distribution of the signal in a diffraction pattern decreases in the extremities, the influence of noise is always greater on the high-frequency components of the image. Thus, a low SNR can decrease the diameter of the reconstructible signal, downgrading the achievable resolution of the apparatus.

2.5.2 Signal-to-noise Ratio (SNR)

As briefly mentioned in the earlier section, the *signal-to-noise ratio* (SNR) is a key factor for quality reconstructions, restricting the useful signal, and therefore, the achievable resolutions. This quantity is defined by the ratio between the respective signal and noise powers [140]:

$$SNR = \frac{P_{signal}}{P_{noise}} = \left(\frac{RMS_{signal}}{RMS_{noise}} \right)^2 \quad (2.82)$$

with RMS the *root mean square* value.

The lensless configurations described in the previous sections are susceptible to *white noise* arising from the experiment (deficient filtering, unintended reflections/transmissions in the setup components...); *photon noise*, which is directly related to the diffraction signal (follows a Poisson distribution); *readout noise*, intrinsic to the detection device; and finally *dark noise* (dark current).

Even though one can not completely get rid of the noise, we can reduce it by adopting proper actions. Indeed, one can add light shields and additional filters in the setup to avoid parasite white noise, which also entails a decrease of the signal. One can also increase the SNR associated to the photon noise by increasing the total number of coherent photons. Experimentally, this can be achieved by an effective optimisation of the beamline-output (photon flux, coherence...) and focusing, for instance. As well, one can perform the imaging acquisition with the CCD camera closer to the object plane to have higher photons/pixel ratio and, thus, enhance the SNR associated to the photon noise. Note again that the object-CCD distance should always fulfil the sampling requirements for the holographic techniques or the oversampling condition for CDI. To reduce the readout noise, one can, if there is the option, decrease the readout frequency of the CCD or use techniques such as hardware binning, which combines the charge from adjacent pixels into a single large pixel during the readout process. Finally, to reduce the dark noise, techniques such as cooling down the CCD camera can be employed (for example, -40° are used in LUCA beamline described in the next Chapter).

2.5.2.1 Interest of Signal Accumulation

Often, in XUV/X-ray coherent lensless imaging experiments, the sources have short pulse duration, in the order of a few tens of femtoseconds. This is the case, for instance, of the LUCA beamline (described in the next Chapter and used for some of the experiments of this manuscript), which is based on the generation of high-order harmonics. The high-photon flux beamline of CEA allows to work in single-shot regime and to resolve temporal dynamics of the same order of magnitude as the pulse's temporal width [161]. However, when no temporal dynamics are involved, it is possible to integrate the photon flux over a few seconds to improve the signal-to-noise ratio, essentially limited by the readout noise.

Nevertheless, when detecting a diffraction pattern resultant from accumulation, it is important not to saturate the camera, to avoid incorporating artificial data into the reconstruction. On the other hand, an unsaturated image might not detect enough signal in the high spatial frequencies areas, which decreases the SNR and substantially degrades the resolution. To overcome these issues, one can resort to the *High Dynamic Range* (HDR) technique.

2.5.2.2 High Dynamic Range (HDR)

The *High Dynamic Range* (HDR) technique is widely used in photography to improve the contrast and dynamics of images, intrinsically limited by the camera. This post-acquisition processing technique involves recording two images with two different exposure times - one long and one short - and assembling them, in order to artificially increase the detection dynamics. This method applied to diffraction patterns has several advantages. Firstly, by acquiring a high gain image, we are able to detect with high SNR

the less intense high spatial frequencies, which are located in the peripheral regions of the diffraction pattern. Additionally, accessing a second image recorded at the limit of saturation allows, in turn, to have all the acquisition dynamics in the centre of the pattern, where the previous image is saturated. The advantages associated with each of the input images are thus exploited: one can get an effective detection of both high and low frequencies, thus increasing the acquisition dynamics. The steps for HDR post-processing are as follows:

- the area of saturated pixels is delimited by a rectangle;
- a binary mask is constructed from this rectangle: it will be applied to the saturated image, while its negative will be used on the unsaturated image;
- a Gaussian filter is applied to these masks in order to smooth out the binary boundaries - not to introduce parasite high frequencies into the inverse Fourier Transforms of the signals;
- a multiplying coefficient - found by calculating the average value of pixels located just outside the saturated area, in both images - is applied to the unsaturated image in order to level both images;
- the unsaturated image, inside the rectangle, and the saturated image, outside the rectangle, are finally assembled.

Even though several input images can be exploited for both exposure times, the diffraction patterns post-processed with HDR in this thesis use only one for each.

2.5.2.3 Coherent Superposition of Image Reconstructions

The technique of coherent superposition of image reconstructions constitutes another strategy for the improvement of the SNR, when several reconstructions of the same object are obtained. This method will be introduced briefly as it is used in the work presented in this manuscript [162].

In coherent diffraction imaging, since the algorithm starts from a random phase, slightly different constructions are obtained from one algorithm launch to another, even with the same input diffraction pattern. Moreover, for each new reconstruction, the position of the object fluctuates in the loose support allocated to the reconstruction. In order to improve the contrast and the signal-to-noise ratio of the final reconstruction, several reconstructions resulting from independent launches of the algorithm can be superimposed coherently. This coherent superposition also allows any possible inconsistent features to be averaged out, ending up in the reduction of the high-frequency noise that cannot be reliably reconstructed. It should be performed in amplitude and phase. Indeed, particularly with binary objects, the phase plays a crucial role in the contrast: note that it is well defined within the object but random outside it.

The CDI reconstructions presented in this manuscript are coherently superimposed from some runs of the phase retrieval algorithm. To sum up the reconstructions efficiently and accurately, we resort to a *DFT (discrete Fourier Transform) sub-pixel registration* algorithm, developed by Guizar-Sicairos [163],

which computes an upsampled cross correlation between the two images and locates its peak. The algorithm uses a matrix multiplication implementation of the 2D DFTs to refine the initial peak location estimate, achieving subpixel registration.

This technique can also be used in FTH with multiple or extended references, which involve the reconstruction of several versions of the same object. Applying a coherent superposition of all the obtained reconstructions, besides improving the SNR, allows improving the spatial quality of the reconstructions. Indeed, one can get rid of different experimental conditions at the level of the reference apertures, such as non-uniform illumination or partial coherence.

2.6 Summary of Beam Requirements for Ultrafast Coherent Lensless Imaging

To summarise, CDI, FTH and in-line holography are three important types of lensless imaging techniques, allowing high-resolution imaging at ultrafast time scales. As we have seen along this chapter, even though their reconstruction procedures are distinct, they all rely on high-quality diffraction patterns. Therefore, in order to obtain high-resolution reconstructions, the imaging beam must fulfil some requirements. They are:

- high coherence;
- high photon flux;
- ultrashort pulse duration;
- short wavelength;
- non-aberrant wavefront.

High-resolution lensless imaging requires high coherence. The treatment of diffraction and, consequently, lensless imaging described above assumes fully coherent illumination [131]. In real experiments, however, samples are usually illuminated with partially coherent waves. The lack of coherence of the illuminating beam affects the contrast of the fringes in the diffraction pattern/hologram and, consequently, the reconstruction is altered [47]. This way, with an SNR reduced, as discussed in Section 2.5, the achievable resolution is also affected.

Another restrictive factor for coherent lensless imaging is the beam flux. As discussed along Section 2.5.2, the number of photons is crucial to ensure a high quality diffraction pattern with a satisfying SNR. Moreover, a high flux of photons is critical for high resolution imaging of specimens that are sensitive to radiation damage [125, 126].

Free Electron Laser facilities, synchrotron facilities and high-order harmonics beamlines are examples of qualified sources for high-flux coherent XUV photons (see Section 1.1.1). FELs and HHG sources can provide coherent radiation with ultrashort pulse durations (typically in the femtosecond scale or even down to the attosecond scale).

Ultrashort pulse durations have allowed the concentration of huge amounts of energy in a really short time period. This concentrated photon flux is responsible for high-resolution imaging, overcoming the time scales of most damaging processes. Moreover, combined with short wavelength radiation it allows performing dynamic studies on femtosecond-resolved scales (or even attosecond-time scales in a near future). Indeed, the short wavelengths, as presented in Sections 2.2.1 and 2.5.1, are an intrinsic requirement to achieve high-spatial resolutions specially when seeking nanometric or even atomic scales.

Finally, high-resolution lensless imaging requires a high-quality wavefront. Even though coherent lensless techniques are in principle aberration-free, as they dispense any type of optics between the sample and the detection plane, they still require a focusing system to focus the beam onto the sample. As XUV and X-ray radiation have short absorption lengths in materials, the production of focusing systems involve high technological requirements, which makes the optics very limited and expensive. Very often, reducing the high photon absorptions at the level of the optics implies lenses configurations which induce strong aberrations [28], imposing a limitation to coherent imaging techniques.

Collecting all these requirements, coherent lensless imaging can be implemented as a powerful imaging tool for users in a large variety of scientific domains. In all its variations, it offers a remarkable solution for high resolution imaging, with current applications ranging from medicine to solid-state physics.

Chapter 3

Experimental Studies of Spatial Coherence and Fourier Transform Holography in LUCA's High Harmonic Generation Beamline

3.1 Introduction

As presented in the previous theoretical chapter, in order to perform ultrafast nanoscale coherent lensless imaging a key requirement is a high-quality diffraction pattern. Therefore, a beam with high spatial coherence, strong photon flux, short wavelength, good wavefront and ultrashort pulse duration is needed. High harmonic generation (HHG) beamlines can generate XUV radiation which meets these criteria [8, 13, 14, 17, 26].

In this thesis, we use HHG to generate the XUV beam for the lensless imaging experiments. The HHG beamline of LUCA, developed by the ATTO group of the LIDYL laboratory of CEA Saclay, provides an intense source of coherent XUV photons (a few tens of nanometres) with ultrashort pulse duration (20 femtoseconds). Its features have allowed to carry out single-shot experiments of different natures: from coherent diffraction imaging (CDI) [13] to holography [12] and, more recently, single-shot spatial coherence characterisation [82]. Such a beamline provides a cheaper and easy-to-access alternative to large laser installations such as FELs and synchrotrons. In addition, the almost complete control of the properties of the harmonic beam allows a wide spectrum of applications, from biomolecular studies to developments in solid-state physics.

XUV/ X-ray sources, whether HHG, synchrotrons or XFELs, present partial spatial coherence [26, 40, 41, 164, 165]. Moreover, these sources exhibit shot-to-shot variations of this parameter along with other spatial properties, including beam-pointing. The ultrashort pulse duration of such sources requires

single-shot consistent characterisation methods to address these phenomena, which can affect the lensless imaging techniques.

Most optical devices used to characterise the coherence of conventional laser beams do not work in the XUV and X-rays ranges [166–168]. On the other hand, the techniques available either require parallel intensity measurements [169–171], either the use of sequential measurements [41, 168, 172–175], being incompatible with single-pulse characterisation. In addition, beam-pointing instabilities, which strongly affect HHG and XFEL sources, have been reported to be critical in coherence studies based on sequential single-shot measurements [41]. Besides the challenge of measuring this parameter with temporal resolution and beam-pointing instabilities, the use of characterised XUV/X-ray sources improves the quality of the results in multiple applications [15, 42, 43, 46, 176, 177].

The characterisation of the spatial coherence of a source has different uses. Firstly, knowing the coherence of a source helps to understand the physics behind the generation process [41, 169], opening the way to XUV beam shaping [178]. On the other hand, both temporal and transverse coherence effects play an important role in the now accessible field of non-linear excitations of atoms and molecules [176]. Furthermore, diffraction depends on the spatial coherence of the source [131], making the knowledge of this parameter important for applications based on interferometric techniques. This is the case, for instance, of lensless imaging where the quality of the reconstruction strongly depends on the degree of coherence of the illuminating beam [42, 43, 46]. By having a knowledge of the partial coherence of the source, some authors have already input this information in CDI algorithms to improve the image quality of 2D or even 3D reconstructions [42, 43, 46, 177]. The effects of partial coherence have been as well reported in holography [12, 44, 45], even though no correction was tried so far.

This chapter is divided into three main parts. Firstly, the concept of high harmonic generation will be addressed and a presentation of the LUCA's XUV beamline, will be provided. Follows some spatial coherence measurements on this source, where we will use a new method, which allows a single-shot characterisation of the spatial coherence of a beam while being compatible with beam-pointing instabilities. The mathematical formalism of this method was partially developed in previous theses at CEA [178] and experimentally implemented here. The method is based on the interferometry through a 2D non-redundant array (NRA) of apertures, designed in a strategic configuration to disentangle the degree of spatial coherence from the intensity distributions of a beam. We report the first experimental demonstration of this technique in single-shot regime, using an XUV beam generated at LUCA's beamline. Finally, employing this technique, a compensation of the magnitude of spatial coherence in Fourier Transform holography will be investigated. Spatial coherence corrections will be tested on experimental data from Fourier Transform holography.

3.2 High Order Harmonics Generation in Gases

In this section, the process of high-order harmonics generation (HHG) in gases will be briefly introduced. The aim is to provide some foundations to better understand the concept and, as well, the parameters

that allow its optimisation as a source of XUV radiation. The HHG process will not be discussed in detail, but a more extensive approach can be found for instance in the thesis of W. Boutu [179] and the book of R. W. Boyd [180].

3.2.1 Principle of HHG in Gases

When a highly intense laser pulse (with optical intensities on the order of $10^{13} - 10^{15} \text{ Wcm}^{-2}$) is focused into a noble gas, strong non-linear interactions occur. If phase-matching conditions are ensured, this can lead to the generation of several high-order odd harmonics of the fundamental laser frequency. This phenomenon is called *high-order harmonics generation*, or simply *high harmonic generation* (HHG) [181, 182]. A typical setup is shown in Fig. 3.1.

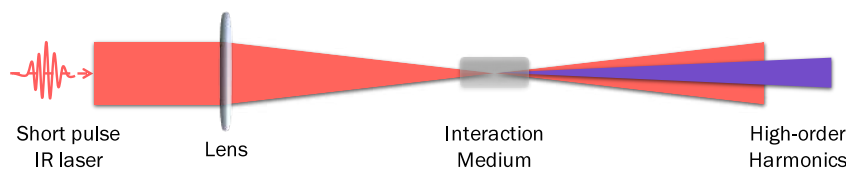


Figure 3.1: **Schematic of a setup for HHG.**

HHG is characterised by a very typical spectrum, presented in Fig. 3.2. It includes a *plateau* constituted by several orders, presenting an approximately equal number of photon counts, followed by a cutoff order after which the harmonic signal decreases sharply.

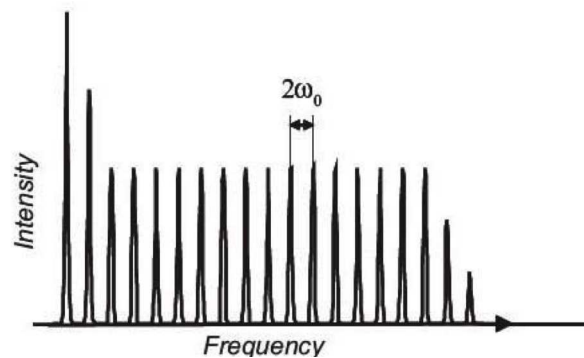


Figure 3.2: **Typical spectrum of high-order harmonics.** A typical spectrum of high harmonics displays a regular decrease of the harmonic intensity for the first few orders, followed by a fairly uniform intensity spectral range, known as the *plateau*. It, then, abruptly falls off in the cutoff. The harmonics are separated by two times the fundamental laser frequency ω_0 and correspond to odd multiples of it, due to an inversion symmetry of the gas media [183].

High harmonic generation from rare gases is one of the most prominent sources of XUV radiation nowadays [8, 13, 20, 22, 184, 185]. Besides the laboratory-scale apparatus and wide tunability ensured by its specific spectrum, this source provides bright ultrashort pulses with a high degree of spatial coherence. For more information on the state-of-the-art features and applications of HHG-based XUV radiation please refer to Section 1.1.1.

3.2.2 Microscopic Effects: Three Step Model

The first theoretical breakthrough of HHG came in 1992, when Krause *et al.* showed that the cutoff energy (i.e. total maximum photon energy) in a high-harmonics (HH) spectrum is given by the universal law:

$$h \cdot \nu_{\text{cutoff}} = I_p + 3.2U_p. \quad (3.1)$$

Here h is the Planck's constant, ν_{cutoff} the cutoff frequency, I_p the ionization potential of the gas and

$$U_p = \frac{e^2 E_o^2}{4m\omega_o} \quad (3.2)$$

is the ponderomotive energy, i.e., the cycle-averaged kinetic energy of an electron in the laser electric field [184].

HHG can be understood using the semi-classical three-step model proposed by P. Corkum in 1993 [80]. According to this model, the physical processes that lead to the generation of high harmonics in a gas follow a sequence of three steps, illustrated in Fig. 3.3. What happens is that, for a high-intensity laser, the laser-electric field becomes comparable to the atomic-electric field felt by outer shell electrons of the noble-gas atom. This leads to a perturbation of the atom potential which allows the electron to tunnel through the potential barrier to the continuum, according to the first step of Corkum's model, Fig. 3.3 (b). While in the continuum, the electron is accelerated by the oscillating laser field, Fig. 3.3 (c), until the inversion of the electric field direction brings the electron back to the nucleus. Here it occupies its original ground state, upon recombination and high-energy photon emission, Fig. 3.3 (d). This three-step process repeats at every half-cycle of the driving laser. The ionization potential and the acquired kinetic energy from distinct ionization/recombination times are, then, emitted as a single, very broad continuous light spectrum. Spectral interferences lead to the appearance of the harmonics as shown in the profile of Fig. 3.2.

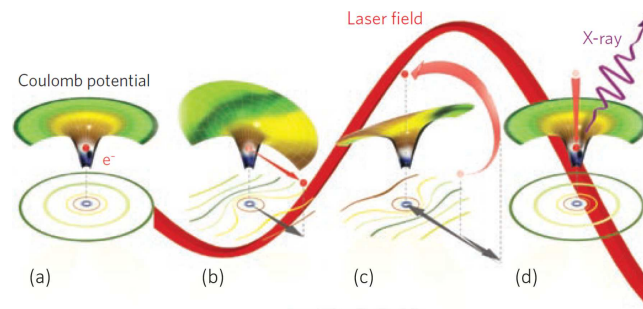


Figure 3.3: **Schematic of the three-step model [20]**. According to this model, HHs are generated from a process of tunnelling, acceleration (in the laser field) and recombination of the electrons in the atoms, which occurs at every half cycle of the driving laser.

In 1994, Lewenstein *et al.* proposed a "Strong Field Approximation" model to analytically solve the time-dependent Schrödinger equation. This model:

- assumes a "Single Active Electron" approximation, i.e. only one electron in the outermost shell is involved in HHG (all the others remain "frozen");
- adopts a two-level system, consisting of a ground state and a continuum state;
- ignores the ground-state depletion due to ionization;
- assumes the electron wave packet is not affected by the Coulomb potential, when in the continuum state.

The "Strong-Field Approximation" theory did not only successfully derive the cutoff law, but also showed that there are several relevant electron paths which bring the electron back to the nucleus after the tunnelling, propagation and recombination processes. Thus, at every half cycle of the driving laser, a valence electron can leave the parent atom at different times and upon recombination, also at different times, some of the electrons may have the same energy, contributing to the same harmonic [81]. Experimentally, it is possible to modulate the laser field to confine the emission to a single optical half-cycle, thus generating isolated attosecond pulses [186].

3.2.3 Macroscopic Effects: Phase Matching

Harmonic signals depend not only on microscopic response (single-atom response), but also on macroscopic phenomena. These include the propagation in a partially ionized medium, phase-matching and gas absorption.

Generating bright, fully coherent HH beams requires macroscopic phase matching. The driving laser and the high-order non-linear polarization must propagate in phase throughout the medium, in order to ensure that the HHG light, emitted by many atoms, adds coherently [23, 187] (see Fig. 3.4). This can be achieved by balancing the neutral gas and free-electron plasma dispersion, experienced by the laser, and is only possible up to some critical ionization level, which depends on the gas species, radiation wavelength and experimental conditions [23]. Overall, this balance is not straightforward to reach:

- The transverse illumination is needed of high intensity to ionize the noble-gas atoms and allow HH emission. However, an ionization beyond a few percent degrades the phase matching due to the strong presence of free electrons, which induce a "blue shift" of the fundamental frequency and strong refraction of the laser beam.
- A high atomic density of the gas reflects in a higher number of harmonic transmitters (maximum dipole density). However, the high density of free electrons on the axis acts as a diverging lens, modifying the phase-matching properties of the HHs. In addition, the gas density increases the reabsorption of the harmonic radiation in the generation medium.
- A loose-focusing geometry (lens with long focal-distance) provides a large cross-section of the interaction volume in the focal region and, as well, gently varying spatial properties of the laser field at the focus, which favour phase-matching conditions. This is the configuration used at CEA.

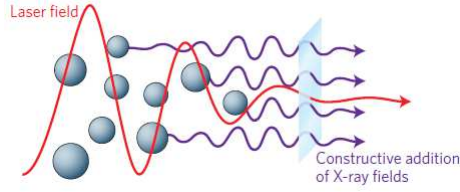


Figure 3.4: **Macroscopic phase matching [20]**. The driving laser and the high-order non-linear polarization must propagate in phase throughout the medium, in order to ensure that the HHs, emitted by many atoms, add coherently.

The optimisation of an HHG source is indeed a complex process, both theoretical and experimentally, due to the number of parameters that regulate this physical phenomenon. Moreover, optimising different features generally requires different parameters. For instance, increasing the number of generated photons is sometimes at the expense of the overall quality of the harmonic beam (spatial profile, wavefront, spatial coherence, beam-pointing stability...). Experimentally, we will mainly optimise the coherent flux and the wavefront. This will be detailed in the next section.

3.3 LUCA's Harmonic Beamline

The imaging experiments described in this Chapter and in Chapter 5 of this manuscript were carried out on the harmonics beamline of LUCA (for Laser Ultra Court Accordable) at the CEA research centre in Saclay, France. This beamline delivers a high-flux femtosecond XUV harmonic source generated from the tabletop LUCA's infrared femtosecond laser. The history of the HHG beamline can be found in the thesis works of Gauthier and Ge [121, 127].

3.3.1 Setup

LUCA is a Ti: Sapphire laser system that can deliver 60-fs pulses with energy up to 50 mJ at a wavelength of 800 nm and a repetition rate of 20 Hz.

The beamline comprises a lens stage in air, followed by three experimental chambers in vacuum, where the HHG and XUV interactions take place (see Fig. 3.5). At the lens stage, a long focal-length lens ($f = 5.6$ m) is used to focus the IR beam into the adjustable gas cell, mounted in the first chamber. A loose-focusing geometry is employed to target high-flux HH, by enlarging the interaction volume in the focal region, with a focus diameter of about half a millimeter [181]. This scheme also promotes a uniform phase-matching, which is further enhanced using a fiber spatial filter, thus increasing the HHG efficiency [21]. To optimise the generation, the focusing lens is mounted on a motorised translation stage, offering an easy control of the beam-focus position with relation to the gas cell. The Rayleigh range is about 13 cm. Finally, the IR beam aperture and flux can also be adjusted by a diaphragm placed just before the lens.

The experimental chambers of the beamline, which enclose the vacuum part of the experimental arrangement, are shown in Figs. 3.5 (a) and (b). In the direction of propagation of the IR beam, they

constitute the HHG chamber, the optics chamber and the diffraction (or imaging) chamber.

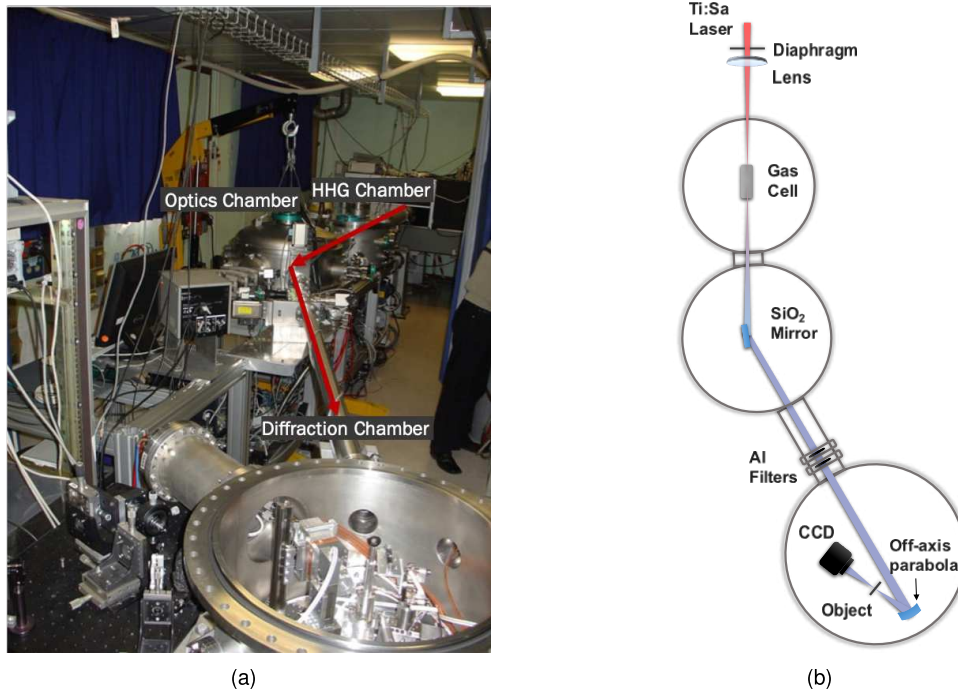


Figure 3.5: **LUCA's harmonic beamline.** (a) Photograph of LUCA's harmonic beamline. The image shows the three experimental vacuum chambers, with a red arrow pointing to the direction of propagation of the HH beam. All the setup is around 5 m long. (b) Scheme of the setup in (a) with the elements at each chamber.

The HHG chamber contains the gas cell, a cylindrical tube with a hole of 500 μm at each end. The length, orientation and position of the vacuum cell can be adjusted by means of an assembly of motors. Its dimensions can vary from 0 to 15 cm in the IR beam propagation-axis and its position in the lateral direction can be adjusted with precision thanks to a motorised translation stage. Additionally, the orientation of the cell can be regulated by tilting it in the transverse directions. Finally, one can also control the pressure of the noble gas inside the cell. Note that the parameters of cell length and gas-pressure are essential to control the macroscopic effects of the generation, in order to maximise the flux and optimise the spatial properties of the harmonics beam (e.g. stability, coherence, intensity profile) [121, 127, 162].

In the optics chamber, the harmonics beam and the incident IR beam, which are collinear at the output of the cell, are separated. For the purpose, an IR-treated anti-reflective fused-silica plate (SiO_2) is used to transmit the IR, while directing the HHs to the diffraction chamber in grazing-incidence geometry to increase the reflectivity for XUV radiation. Alternatively, this SiO_2 plate can be replaced by a toroidal mirror and a diffraction grating to study the harmonics spectrum, although this was not needed for this thesis. Two LUXEL 150-nm thick aluminium filters are then placed between the optics chamber and the diffraction chamber to filter the residual IR. The filters are continuously pumped to prevent from oxidation.

In the diffraction chamber (Fig. 3.6) an off-axis parabola (OAP) at 22.5° with a focal length of 20 cm focuses the beam into the sample. This OAP has a multilayer treatment designed to select the 33rd

harmonic (wavelength of 24 nm). Another OAP with a focal length of 10 cm is alternatively used for selecting harmonic 25th ($\lambda = 32$ nm). Note that, besides the parabola, the noble gases used in each HH generation also differ. In these cases particularly, we generate H33 from neon (*Ne*) and H25 from argon (*Ar*). The harmonic photon number generated in *Ne* is, in general, about one order of magnitude less than in *Ar* [127]. Nevertheless, H33 is already located in the cutoff region of *Ar*, thus presenting a much lower photons/pulse number than in a *Ne*-generation case. Note that this latter gas has a higher ionization potential than the first (energy of 21.6 eV required for the first ionization of *Ne* against 15.8 eV for *Ar* [162]) so, from Eq. (3.1), his cutoff takes place at higher energy.

The setup used in the experiments of this Chapter is presented in Fig. 3.6 (a), inside its respective chamber. This constitutes a typical imaging setup for CDI and FTH, Fig. 3.6 (b), where the sample is positioned in the focal spot of the focusing optics (in this case the OAP) and a CCD camera in the far field, to record the diffracted beam. The camera used for the measurements is an XUV PI-MTE CCD from Princeton Instruments, with a sensor of 2048×2048 pixels and a pixel pitch of $13.5 \mu\text{m}$.

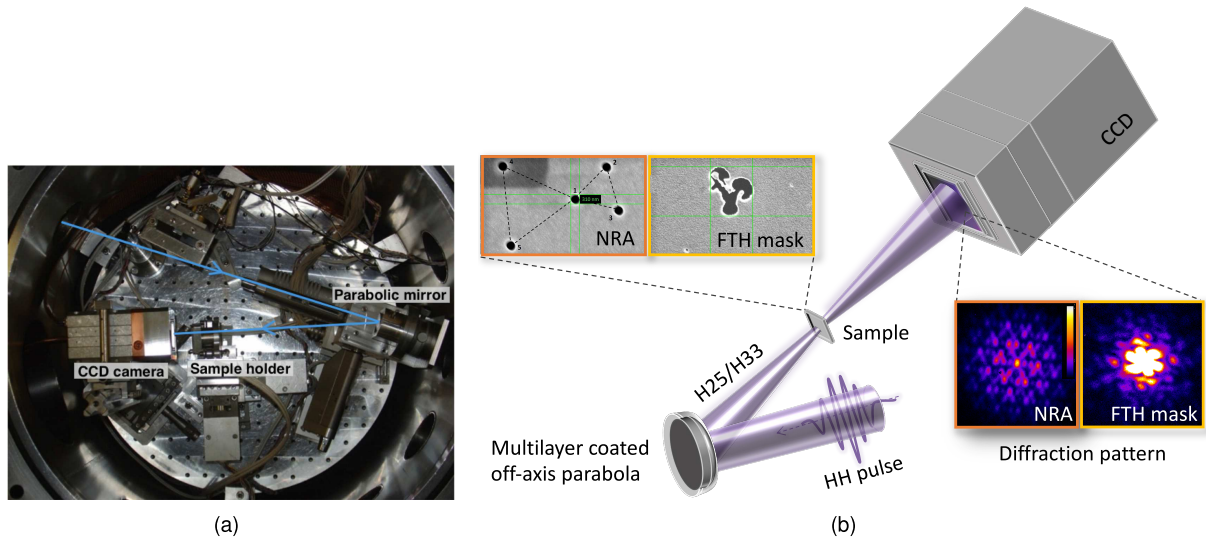


Figure 3.6: **LUCA's diffraction chamber.** (a) Photograph and (b) scheme of the setup used for the measurements of the magnitude of spatial coherence and Fourier Transform holography. A multilayer-coated off-axis parabola is used to focus the beam while selecting the wavelength used for the imaging experiments. The XUV beam is focused onto the imaging sample, mounted in a suited all-motorised sample-holder. Finally a CCD camera, positioned in the far field, records the diffraction pattern resulting from the interaction.

3.3.2 Optimisation of the Harmonics Signal

In order to find the macroscopic conditions for the generation process, which most suit our experimental purpose, a source optimisation step is required before each experimental run. Generally, this means to find the best compromise between photon flux, spatial coherence, wavefront and beam-pointing stability. In LUCA's experimental scheme, the parameters affecting these properties are the length of the generating medium (gas cell), the medium density (regulated by the gas pressure), the diameter of the IR beam at the cell (regulated by the opening of the IR diaphragm before the focusing lens) and the

position of the IR-beam focus with respect to the gas cell (more rarely adjusted due to setup-practical limitations).

Concerning the optimisation of the length of the gas cell, studies performed on the source showed that the variation of this parameter influences significantly the photon flux while having a much smaller effect on coherence. Some quantitative information about these measurements can be found for instance in Ge thesis [127]. This way, an optimisation based on a beam intensity maximisation is suited for this parameter.

The same intensity-based optimisation can be adopted for the parameters of gas pressure and the opening of the IR diaphragm before the focusing lens. Indeed, when modifying these generation parameters, for both H25 and H33, the spatial coherence generally presents the same behaviour as the average intensity of the harmonic beam [162]. This means that optimising the average intensity of the harmonic flux generally implies optimising its spatial coherence. This property is particularly interesting for lensless imaging, for which we have seen (Chapter 2) that photon flux and spatial coherence are two critical parameters for obtaining a diffraction pattern with good SNR and a faithful object's reconstruction.

For most of the experiments carried out in this thesis work, it was necessary to accumulate laser pulses in order to get a diffraction pattern with a sufficient SNR for a satisfying object reconstruction. Typically, more than 100 and up to 4800 laser pulses were accumulated for the experiments of this manuscript (Chapters 3 and 5). This makes the beam pointing another property to consider when dealing with the beam optimisation. The effect of accumulation can be detrimental to the quality of the diffraction pattern if the beam pointing is not stable [162]. In such scenario, the wave transmitted by the object is recorded in the far field as an incoherent superposition of different shifted contributions, resulting in a decrease of the fringes visibility at the diffraction pattern. This is particularly critical for CDI, which depends on the convergence of an iterative algorithm for the reconstruction. The possibility of obtaining or not a satisfying reconstructed image of the object will depend directly on the number of accumulated shots and the stability of the beam. Therefore, in experiments which require high accumulation times, an optimisation based on the beam-pointing stability at the expense of some beam-pulse energy might sometimes be more adequate. In the experiments of this thesis work, which did not seek for a single-shot measurement, we concentrated on optimising the compromise beam-pointing stability *versus* intensity, rather than obtaining the maximum energy possible out of a laser pulse.

In order to account with all these issues when optimising the HH beam, the intensity and beam-pointing stability of the harmonic beam were observed and optimised in real time. This inspection was possible by recovering the image of the HH beam in the far field with the CCD camera and using this information as input for further adjustments.

The optimal properties obtained for the harmonic beams H25 and H33, achieved after full-system optimisation are summarized in tables 3.1 and 3.2. A typical value for each of the optimisation parameters is also presented, for each case, in table 3.3.

Wavelength	32 nm
Pulse energy in the focal plane	10^9 photons/pulse
Pulse duration	20 fs
Intensity at the focus	10^{12} Wcm ⁻²
Diameter of the focal spot	$4.5 \mu\text{m} \times 7 \mu\text{m}$
Spatial coherence at the focus (in fringes visibility)	0.8
Spectral bandwidth ($\lambda/\Delta\lambda$)	50

Table 3.1: Optimal experimental properties and respective parameters used for the generation of H25 from Ar at LUCA's harmonic beamline. Some values were obtained from previous theses at CEA [127, 162].

Wavelength	24.24 nm
Pulse energy in the focal plane	10^7 photons/pulse
Pulse duration	20 fs
Intensity at the focus	10^{10} Wcm ⁻²
Diameter of the focal spot	$5 \mu\text{m} \times 7 \mu\text{m}$
Spatial coherence at the focus (in fringes visibility)	0.85
Spectral bandwidth ($\lambda/\Delta\lambda$)	120

Table 3.2: Optimal experimental properties used for the generation of H33 from Ne at LUCA's harmonic beamline. Some values were obtained from the thesis [162].

	H25 (from Ar)	H33 (from Ne)
Diameter of the IR diaphragm	~ 19 mm	~ 24 mm
Gas pressure	~ 2.1 mbar	~ 5.8 mbar
Gas cell length	~ 5.2 cm	~ 5 cm
Laser energy	20 - 40 mJ	20 - 40 mJ
Pulse duration	60 fs	60 fs

Table 3.3: Optimal experimental parameters used for the generation of both H25 and H33 at LUCA's harmonic beamline.

3.4 Fabrication of the Test Samples

In order to be able to reconstruct the object in a single plane, the sample needs to be considered "optically thin", as explained in Section 2.2.2. Assuming a sufficient resolution of 100 nm, we would need to draw an object thinner than 625 nm and 833 nm, respectively, for experiments with H25 and H33 (Eq. (2.22)). For the HHG experiments of this manuscript, the samples were patterned on 75-nm silicon-nitride (Si_3N_4) membranes, where a 150-nm layer of gold (Au) and a 4-nm layer of chromium (Cr) were deposited, this latter one to achieve adhesion between the other two materials. The objects were etched by a gallium focused ion beam (FIB) (see Fig. 3.7) at the Center for Nuclear Science and Material Sciences (CSNSM) in Orsay. This system was coupled to a scanning electron microscope (SEM), which allowed to observe the patterning step in real time and take images of the final samples. The process of etching removes all the thickness of Si_3N_4 , Cr and Au with an accuracy of about 10 nm.

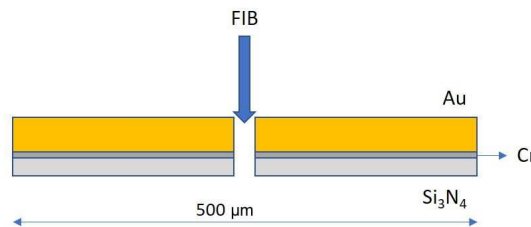


Figure 3.7: **Diagram of the etching of 2D samples with FIB.** The gold, chromium and silicon nitride membranes are 150 nm, 4 nm and 75 nm thick, respectively. Adapted from [162].

The 150-nm layer of gold has a virtually zero transmission, making the object contour opaque to our illumination source ($t = 2.8 \times 10^{-9}$ for H25 and $t = 1.8 \times 10^{-7}$ for H33 according to the CXRO database [188]), resulting in an object of purely binary amplitude (transmission of 0 for the membrane and 1 for the object).

The patterned membrane containing the test samples can be observed in Fig. 3.8. For the work described in this Chapter two types of objects were used. One consisted of a non-redundant array (NRA) for spatial coherence measurements, see Fig. 3.9 (a). The other depicted a sample for Fourier Transform holography (FTH), see Fig. 3.9 (b). The pattern chosen was a rooster for being a symbol of both Portugal and France. This FTH sample was designed to have several pinhole references, with different sizes, to test at the same time the compromise time-dose/features size. However, the smaller projected holes were not fully drilled, so only single-pinhole FTH samples were produced.

3.5 Single-Shot Characterisation of the Spatial Coherence of an XUV Source

There are several methods to characterise the spatial coherence of a beam. The standard technique is based on the double-aperture interferometer (Young experiment). Zernike observed that the visibility

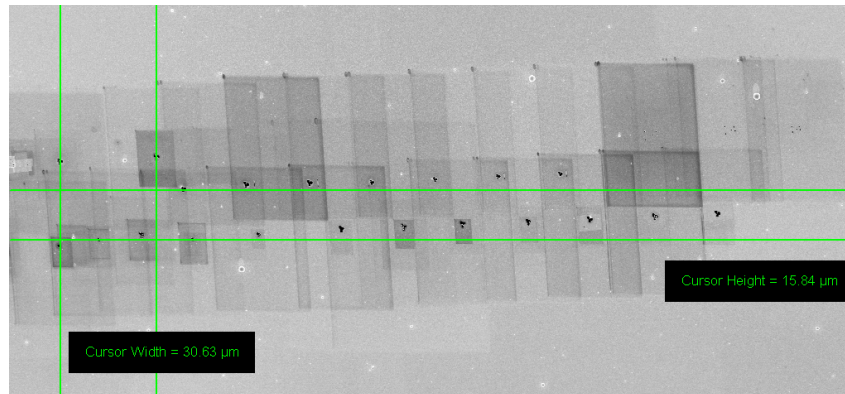


Figure 3.8: **SEM image of the membrane with the fabricated samples.**

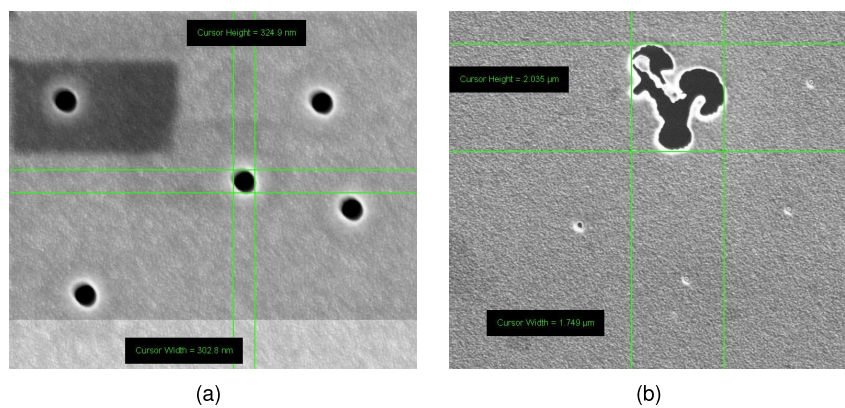


Figure 3.9: **Example of a fabricated NRA and FTH test samples.** (a) NRA of 5 apertures fabricated with FIB for measurements of the degree of spatial coherence in LUCA's beamline. (b) Example of a rooster test object with 5 reference apertures (only one fully etched) to perform Fourier Transform holography. The fully drilled pinhole has a diameter measured from the front face of the membrane of approximately 139 nm.

of Young's interference fringes [189] reveals the spatial coherence between the fields at the two apertures positions [190]. Therefore, when both apertures are illuminated with the same intensity function, by varying the double-aperture separation, one can map out the spatial coherence [41, 172]. The tediousness of this process has led to the development of several alternative approaches. For instance, some authors reported the use of a lateral-shearing Sagnac interferometer for the purpose [166, 167]. Alternatively, a fixed double-slit separation can be exploited by laterally shifting the slits across the field, along with a reversed copy of this field created by a cube beam splitter, which is also shifted laterally. This method consists of the so-called "reversed-wavefront" Young interferometer [168]. However, these two techniques use several optics restraining their application to XUV and X-ray radiation. Moreover, the methods based on the two-source interference [41, 166–168, 172] are not suitable for single pulse characterisation, since the separation distance between the sources must be changed for each interferogram. Other approaches rely on phase-space methods that exploit the propagation of the partial-coherent field as described by the Wigner function [173, 174]; make use of a pair of non-parallel slits for multiplexing one-dimensional interferograms [191, 192]; or exploit wavefront sensors [193]. However,

they all require several measurements.

Strategies for acquiring the spatial coherence function with one-single interferogram have been already proposed. One relies on the use of non-redundant arrays (NRA) of apertures to measure the spatial coherence at different distances [170, 171, 175]. Other shows that by using only one interferogram it is also possible to measure the spatial coherence of XUV sources, as a function of the vectorial separation for a fixed magnitude of separation [169]. In both cases, though, separate intensity measurements are needed to retrieve the spatial coherence function.

The method presented in this section is based on a multiple aperture interferogram [170, 171, 175] generated by an NRA of apertures. The two dimensional NRA has been designed to generate a set of equations that allows calculating the spatial coherence and the intensity at the position of each aperture. It can be applied for Gaussian Schell-model beams [43, 46, 168, 171, 175, 194], where the magnitude of the spatial coherence is shift invariant, i.e. is a function of the separation between the fields at the positions of the apertures. The mathematical formalism of this method was developed at CEA by Gonzalez in her thesis works [178]. According to simulations, the error induced by this technique is smaller than the one induced by the Young interferometry technique, which works under the supposition of equal intensity at each aperture. In addition, this technique shows good results under beam-pointing instability scenarios, which strongly affect HHG and XFEL sources and were reported to be critical with other methods [41].

3.5.1 Spatial Coherence

When the light from two light bulbs is directed towards a same target, a uniform brightness appears, given by the sum of their individual intensities. If instead two beams from the same laser source are used, the outcome is a sequence of dark and bright fringes. The property responsible for this phenomenon is called coherence.

A light field is called coherent when there is a fixed phase relationship between the electric field values at different locations or at different times (see Fig. 3.10 (a)). Two types of coherence are typically considered: spatial and temporal. Spatial coherence describes the mutual correlation of different parts of the same wavefront (Fig. 3.10 (b)), while temporal coherence depicts the correlation of a wave with itself, at different instants (Fig. 3.10 (c)) [104]. In this work, our attention will be given to the first type.

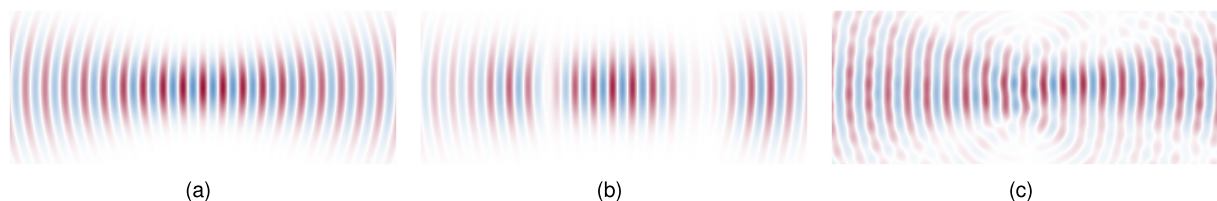


Figure 3.10: **Spatial vs temporal coherence.** (a) Electric field distribution around the focus of a Gaussian laser beam with perfect spatial and temporal coherence. (b) Laser beam with high spatial coherence, but poor temporal coherence. (c) Laser beam with high temporal coherence, but poor spatial coherence. Images from [195].

Quantitatively, the coherence is a statistical measurement of the correlation between the field oscillations at two different positions, at two different times $V(\vec{r}_n, t_n)$ and $V(\vec{r}_m, t_m)$. For a statistically stationary and ergodic field [131], the second order coherence is given by the cross-correlation function:

$$\Gamma(\vec{r}_n, \vec{r}_m; t_n, t_m) = \langle V^*(\vec{r}_n, t_n)V(\vec{r}_m, t_m) \rangle_T \quad (3.3)$$

where $\langle \rangle_T$ denotes the temporal average, and $\vec{r} = (x, y)$ is the spatial coordinate of each of the points where the coherence function is measured [196]. $\Gamma(\vec{r}_n, \vec{r}_m; t_n, t_m)$ is generally called *mutual coherence function*. Note that the notion of stationary and ergodic field specifies that the ensemble averages are independent of the origin of time and, therefore, the ensemble average in Eq. (3.3) can be given by a temporal average [131].

Both the spatial and temporal coherence contributions can be isolated from Eq. (3.3) by setting to zero either the temporal delay $\tau = t_n - t_m$ or the spatial separation $\vec{d}_{nm} = \vec{r}_n - \vec{r}_m$, respectively. One could attribute the first case to an amplitude splitting interferometer (Michelson interferometer) and the second case to a wavefront splitting interferometer (Young's double-aperture).

In the particular case where $\tau = 0$, one can define Eq. (3.3) as the *mutual intensity*, $J(\vec{r}_n, \vec{r}_m) = \Gamma(\vec{r}_n, \vec{r}_m; \tau = 0)$. The *complex degree of spatial coherence*, here denoted μ_{nm} , can be written in terms of this mutual intensity in the form:

$$\mu_{nm} \equiv \mu(\vec{r}_n, \vec{r}_m) = \frac{J(\vec{r}_n, \vec{r}_m)}{\sqrt{J(\vec{r}_n, \vec{r}_n)}\sqrt{J(\vec{r}_m, \vec{r}_m)}} \quad (3.4)$$

with $\sqrt{J(\vec{r}_{n,m}, \vec{r}_{n,m})} = I(\vec{r}_{n,m})$ the intensity value at the point n, m . This complex degree of spatial coherence, from now on called simply spatial coherence, is defined in the interval

$$0 \leq \mu_{nm} \leq 1. \quad (3.5)$$

These two limits represent, respectively, the incoherent case, $\mu_{nm} = 0$, and the fully coherent, $\mu_{nm} = 1$ [131]. Any value in between is a case of partial spatial coherence.

3.5.2 Description of the Method

As have been discussed, the spatial coherence is a function of four variables: $\mu(x_n, y_n; x_m, y_m)$. As the diffraction is related to the spatial coherence, the intensity of the diffracted beam after propagation is as well a four-dimensional function. Following the description given by Goodman in his book [197], one can calculate the field intensity at a plane $z > 0$ as the superposition of all the interference fringes generated by the different pairs of punctual sources of the field at $z = 0$. One can then relate the diffraction intensity at a far-field plane z to the mutual intensity $J_0(\vec{r}_n, \vec{r}_m)$ at a plane $z = 0$ in the form:

$$I(\vec{\rho}, z) = \frac{1}{\lambda^2 z^2} \int \int \int \int J_0'(\vec{r}_n, \vec{r}_m) e^{\frac{i2\pi}{\lambda z} [\vec{\rho}_n \cdot \vec{r}_n - \vec{\rho}_m \cdot \vec{r}_m]} d^2 \vec{r}_n d^2 \vec{r}_m, \quad (3.6)$$

where $\vec{\rho} = (X, Y)$ denotes positions in the plane of detection, parallel to the plane $z = 0$ with points given by $\vec{r} = (x, y)$.

This four-dimensional integral is, however, hard to use in practice. Firstly, because the problem not always has an analytical solution and the numerical calculation can be, as well, not trivial. Secondly, it implies that a four-dimensional characterisation of the spatial coherence has to be done. Consequently, the Gaussian Schell-model beam approximation is often employed by researchers in the field [43, 46, 168, 171, 194]. For a Gaussian Schell-model beam, the magnitude of the spatial coherence is *shift invariant*, i.e. is only a function of the magnitude of the separation vector $|\vec{d}_{nm}| = \|(\vec{r}_n - \vec{r}_m)\|$ [171, 178]. This reduces the spatial coherence to a 2-dimensional problem. Note that his approximation is generally only valid for the magnitude of the spatial coherence, not always applying to its phase [168, 178].

It has been shown that the use of an NRA of apertures allows the measurement of the spatial coherence between all its aperture-pairs $\{n, m\}$ ($n, m = 1, 2, \dots, N$) [170, 171, 175]. The concept can be understood as an extension of the Young double-aperture interferometer, but in this scheme, a series of double-pinhole interferograms, corresponding to different separation distances and orientations, are acquired simultaneously. The degree of spatial coherence is, then, retrieved from the Fourier transform (FT) of the interferogram generated by the diffraction of the field through the NRA. This Fourier spectrum takes the form:

$$\tilde{I}(\vec{r}, z) = \Lambda(\vec{r}) \otimes \left[\sum_{n=1}^N I_n \delta(\vec{r}) + \sum_{n=m+1}^N \sum_{m=1}^{N-1} \sqrt{I_n I_m} \times \left\{ \mu_{nm} \delta(\vec{r} - \vec{d}_{nm}) + \mu_{nm}^* \delta(\vec{r} + \vec{d}_{nm}) \right\} \right], \quad (3.7)$$

where \otimes denotes the convolution operation; I_n and I_m are the individual beam intensities at the correspondent apertures $\{n, m\}$ and μ_{nm} is the complex degree of spatial coherence. Here $\Lambda(\vec{r})$ is the autocorrelation of the function that describes the geometry of each aperture $h(\vec{r})$, i.e., $h(\vec{r}) = \text{circ}(\vec{r}/a)$ for circular apertures of radius a .

For an NRA, the autocorrelation of Eq. (3.7) consists of a distribution of peaks centred at the different separation vectors, $\vec{d}_{nm} = \vec{r}_n - \vec{r}_m$, between the apertures of the array. The magnitude of the spatial coherence for each pair of apertures $\{n, m\}$ is, then, estimated from

$$|\mu_{nm}| = \frac{|C_{nm}|}{\sqrt{I_n I_m}} \frac{S_0}{|C_0|}, \quad (3.8)$$

with $S_0 = \sum I_n$ the total intensity of the field thought the NRA and $|C_0|$ and $|C_{nm}|$, respectively, the magnitudes of the central peak of the Fourier spectrum and the peak centred at \vec{d}_{nm} [171].

One can now generate an NRA of $N = 3$ apertures in a configuration where $|\vec{d}_{nm}|$ is constant for all the aperture-pairs $\{n, m\}$ (see Fig. 3.11 (a)). The autocorrelation of such array comprises six peaks

located at each separation vector \vec{d}_{nm} , Fig. 3.11 (b). From Eq. (3.8) we have a set of 3 equations:

$$\begin{aligned} |\mu_{12}| &= \frac{C_{12}}{\sqrt{I_1 I_2}} \frac{S_0}{|C_0|} \\ |\mu_{13}| &= \frac{C_{13}}{\sqrt{I_1 I_3}} \frac{S_0}{|C_0|} \\ |\mu_{23}| &= \frac{C_{23}}{\sqrt{I_2 I_3}} \frac{S_0}{|C_0|}. \end{aligned} \quad (3.9)$$

For a shift-invariant magnitude of spatial coherence: $|\vec{d}_{12}| = |\vec{d}_{23}| \Rightarrow |\mu_{12}| = |\mu_{23}|$. The solution for

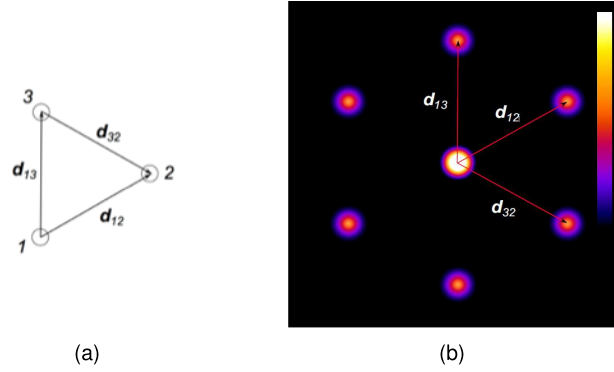


Figure 3.11: **NRA's elementary block for achieving intensity-independent measurements and respective autocorrelation.** (a) Array composed by 3 pinholes, with equal separation distances $|\vec{d}_{nm}|$. This NRA-set constitutes the elementary block for NRA's construction, in order to achieve intensity-independent measurements. (b) Autocorrelation of the NRA of (a), featuring the different separation vectors $|\vec{d}_{nm}|$ of the pairs of apertures that constitute the array.

this set can be found in terms of the intensity of only one of the apertures. Considering this reference aperture I_1 , yields

$$\begin{aligned} |\mu_{nm}| I_1 &= \frac{C_{12} C_{13}}{C_{23}} \frac{S_0}{|C_0|} \\ I_2 &= I_1 \left(\frac{C_{23}}{C_{13}} \right)^2 \\ I_3 &= I_1 \left(\frac{C_{23}}{C_{12}} \right)^2. \end{aligned} \quad (3.10)$$

The multiplicative factors I_1 and $\frac{S_0}{|C_0|}$ can be normalised after interpolation of the magnitude of spatial coherence to $|\vec{d}_{nm}| = 0$, where the condition $\mu_{nn} = 1$ holds. This allows a simultaneous disentanglement of both coherence and intensity contributions in the 3 apertures of the NRA.

Using this scheme as basis, one can build NRAs with $N > 3$ apertures, generated by different elementary blocks with the structure of Fig. 3.11 (a). With such scheme, the degree of coherence is found directly for a set of $N(N-1)/2$ pairs of apertures, from one single interferogram and without intensity measurements. An example of an NRA of 7 apertures is presented in Fig. 3.12 (a) with its respective autocorrelation in Fig. 3.12 (b), showing the 21 pairs of apertures that compose the array.

The NRA of Fig. 3.12 (a) was associated with a Gaussian distribution of intensity ($I = I_0 e^{-2(\vec{r}^2/w_I^2)}$, with radius $w_I = 5.2 \mu\text{m}$) and a Gaussian degree of spatial coherence ($\mu_{nm} = e^{-2(\vec{d}_{nm}^2/w_c^2)}$, with radius

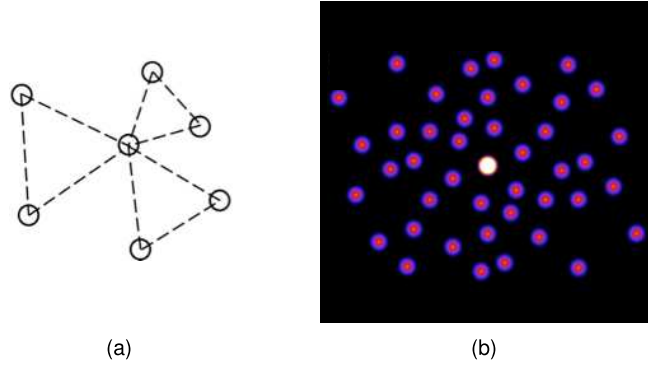


Figure 3.12: **Example of a 7-aperture NRA for spatial coherence measurements and respective autocorrelation.** (a) NRA composed of three sets of elementary blocks from Fig. 3.11 (a), highlighted with dotted lines. (b) Autocorrelation of the NRA from (a).

$w_c = 4 \mu\text{m}$). The Fourier transform of the respective interferogram was simulated employing Eq. (3.7). Two different beam pointings, Figs. 3.13 (a) and (c), were tested. Using the simulated values of C_0 and C_{nm} , and applying Eqs. (3.10), the degree of coherence was calculated, for both cases, assuming unknown intensity values.

The results of the simulation are presented in Figs. 3.13 (b) and (d). The graphics show the calculated values (black squares) and the degree of simulated coherence (red bold line), for the two different beam positions on the NRA. Despite the position-shift of the intensity profile with respect to the NRA, the coherence calculated presents the same behaviour and a good agreement with the simulation. From the calculated coherence values, the individual intensity values over all the apertures could as well be extracted.

These results show that single-shot measurements of the magnitude of spatial coherence employing this method are independent of the beam position and distribution of intensity. This way, the beam-pointing instabilities of XUV sources, which were reported to be critical for spatial coherence characterisations employing other methods [41], are not a problem with this technique.

Further simulations, including the study of the error induced in accumulation conditions, and respective comparison with the standard Young interferometer, can be found in Gonzalez thesis [178]. By simulating accumulation conditions, Gonzalez found that the error from beam-pointing instabilities induced with the NRA technique was smaller than the one induced with the Young interferometry technique (under the supposition of equal intensity at each aperture) [178].

3.5.3 Experimental Validation at LUCA's Harmonic Beamline

The setup employed for the measurement of the magnitude of spacial coherence of LUCA's harmonic beamline is shown in Fig. 3.6. In this experimental validation, harmonic 25 from Ar was used (see Table 3.1). The NRA was placed at the focus of the off-axis parabola and the far-field diffraction pattern was recorded 52-mm away from the sample. The harmonic beam was optimised to generate the maximum flux at the expense of the beam-pointing stability, observed in significant intensity-distribution and beam-

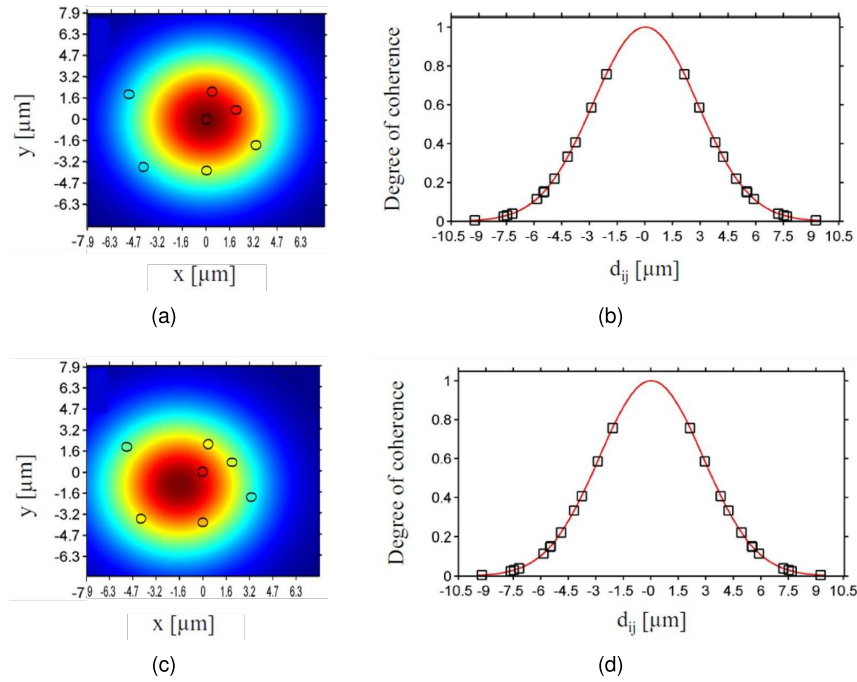


Figure 3.13: **Simulations of NRA measurements of the degree of spatial coherence with variation of beam pointing.** Gaussian intensity profile (a) centred at the NRA reference aperture and (c) displaced $(-1.6; -1.1)$ μm from it. The aperture positions are denoted with black circles. (b),(d) Simulation of $|\mu_{nm}|$ as a function of the separation distance (red bold line) and calculated values of the degree of spatial coherence (black squares) for the beam pointings of (a) and (c), respectively. The calculation of the degree of spatial coherence was achieved after normalisation of the intensity, without any assumption on its profile. Images from [178].

pointing fluctuations. The parameters used for this optimisation are detailed in Table 3.3.

To characterise the magnitude of spatial coherence of our source, the NRA of 5 circular apertures from Fig. 3.14 (a) was used. It has an overall size of $4.5 \times 3.2 \mu\text{m}^2$ with circular apertures of approximately 310 nm. The overall dimension was designed so that the sample would be smaller, but not too far from the H25 focal spot size, in order to measure the degree of coherence over all the spatial extent of the beam.

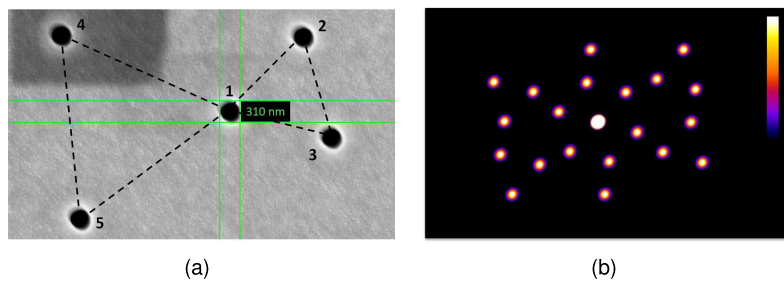


Figure 3.14: **SEM image of the NRA sample and respective simulated autocorrelation.** (a) SEM image of the NRA sample used for the measurements of the degree of spatial coherence of LUCA's harmonic beamline. The NRA has an overall size of $4.5 \times 3.2 \mu\text{m}^2$ with circular apertures of approximately 310 nm. The two elementary blocks are connected with dotted lines, to allow a better visualisation. (b) Simulation of the autocorrelation of an array with the structure of (a), assuming a uniform intensity profile and full spatial coherence. Note that all peak values of this autocorrelation image are equal. The color scale denotes arbitrary intensity units.

The magnitude of spatial coherence can be extracted from the autocorrelation of the NRA, employing Eqs. (3.10) for the two sets of tri-equidistant circular references, $(n, m) = \{1, 2, 3\}$ and $(n, m) = \{1, 4, 5\}$, with aperture 1 the common reference. The simulation of this autocorrelation can be found in Fig. 3.14 (b) for a case of uniform intensity and perfect coherence. Hence, solving the two systems of equations by the same method shown previously, yields for the intensities:

$$\begin{aligned} I_2 &= I_1 \left(\frac{C_{23}}{C_{13}} \right)^2, & I_3 &= I_1 \left(\frac{C_{23}}{C_{12}} \right)^2, \\ I_4 &= I_1 \left(\frac{C_{45}}{C_{15}} \right)^2, & I_5 &= I_1 \left(\frac{C_{45}}{C_{14}} \right)^2, \end{aligned} \quad (3.11)$$

which gives for the different aperture-pairs:

$$\begin{aligned} |\mu_{23}| &= \frac{C_{12}C_{13}}{C_{23}} B_0, & |\mu_{45}| &= \frac{C_{14}C_{15}}{C_{45}} B_0, \\ |\mu_{24}| &= \frac{C_{24}C_{15}C_{13}}{C_{23}C_{45}} B_0, & |\mu_{25}| &= \frac{C_{25}C_{14}C_{13}}{C_{23}C_{45}} B_0, \\ |\mu_{34}| &= \frac{C_{34}C_{15}C_{12}}{C_{23}C_{45}} B_0, & |\mu_{35}| &= \frac{C_{35}C_{14}C_{12}}{C_{23}C_{45}} B_0. \end{aligned} \quad (3.12)$$

The factor $B_0 = \frac{S_0}{C_0 I_1}$ can be found from the normalisation of the Gaussian function, obtained from the fit to the $|\mu_{nm}|$ values.

3.5.3.1 Experimental Results and Discussion

Fig. 3.15 (a) shows a single-shot experimental diffraction pattern of the 5-apertures NRA from Fig. 3.14 (a). The diffraction pattern was acquired in a 20-fs shot, with a reading frequency of 100 kHz, a binning factor of 4×4 and the CCD camera cooled down to -40° C. The Fourier transform of this diffraction pattern, i.e. the experimental autocorrelation of the NRA can be found in Fig. 3.15 (b).

Observing the autocorrelation image from Fig. 3.15 (b) one can notice the 10 peaks with respective conjugates, for the corresponding 10 aperture-pairs. From here, one can immediately conclude that the entire NRA was illuminated and that the entire spatial extent of the beam has non-zero coherence. Comparing with the simulation from Fig. 3.14 (b), achieved for a uniform intensity profile and full-spatial coherence, one can identify here amplitude variations of the autocorrelation peaks, given by the partial spatial-coherence and the non-uniform illumination of the NRA. Assuming a shift-invariant coherence magnitude, the amplitude variations exhibited at the same $|\vec{d}_{nm}|$ distances can have two causes: they can either be associated to diameter-differences at the level of the fabrication of the apertures; or to the non-uniform intensity-distribution of the beam at their positions. General intensity modulations affecting the harmonic beam profile could be directly observed on its footprint at the CCD. Indeed, we would like to recall that the H25 beam was optimised to generate the maximum photon flux at the expense of the beam stability, observed in significant intensity-profile and beam-pointing fluctuations. On the other hand, focusing on the peaks from the smaller elementary block (apertures $(n, m) = \{1, 2, 3\}$ from Fig. 3.14 (a)) and measuring the amplitudes of these peaks on 100 single-shot autocorrelations, it

was noticed that, in average, the peak associated with the pair of pinholes (2, 3) was 11% less intense than the one associated with the pair of pinholes (1, 2), in turn 9% less intense than the (1, 3) peak. These intensity variations are then possibly justified with apertures structural differences. In this scenario aperture 1 is probably better drilled (or has a larger diameter) than aperture 3, which is possibly also larger than that of 2. The SEM image presented in Fig. 3.14 (a) shows only the front-face of the NRA, being possible that, in the rear face, the apertures have a different diameter. Therefore, with these amplitude variations justified, the shift invariance of the single-shot spatial coherence distribution seems to be a good approximation to this source. This is also corroborated by the coherence function retrieved from these experimental data, Fig. 3.15 (c), which seems to fit extremely well a Gaussian distribution.

The data points from Fig. 3.15 (c) were calculated from Eqs. (3.12) and the curve of magnitude of spatial coherence, in red in the image, arises from a Gaussian fit to these points. The root-mean-square error of this fit was 2.5% and the estimated radius of the coherence function was $w_c = 3.85 \mu\text{m}$. Besides the good agreement of the experimental curve to the points, these results also report a source with extremely good magnitude of spatial coherence. One can highlight that the radius calculated for the coherence function is larger than the radius of the focal spot of the beam (see Table 3.1), where the measurement of coherence with the NRA was performed.

3.6 Case Study: Compensation of the Magnitude of Spatial Coherence in Fourier Transform Holography

As discussed in Chapter 2, the coherence of the source is a critical factor for lensless imaging. Indeed, the mathematical formalisms of diffraction and, consequently, lensless imaging techniques, assume fully coherent illumination. However, XUV/X-ray radiation from FELs, synchrotrons or HHG sources has been reported to possess only partial spatial coherence [26, 40, 41].

Several authors have shown the effects of partial spatial coherence in lensless-imaging reconstructions [15, 42, 43, 46, 198, 199]. Their works showed that in real-life experiments, an assumption of total coherence seems sometimes rather inaccurate.

The compensation of the spatial coherence effect in CDI has been the subject of several studies. Some authors reported that, in some cases, a phase curvature in the incident wavefield can compensate for the effect of the spatial coherence in the image reconstruction [46]. A modification of the CDI iterative algorithm has been proposed to improve reconstructions when a wavefield with a known spatial coherence is used [43]. In both approaches, a Schell-model beam approximation (which will be discussed later on in this section) was used, including the assumption of shift-invariance in the phase of the spatial coherence. Spatial coherence correction was also proposed for ptychographic imaging. In 2013, P. Thibault and A. Menzel developed a reconstruction technique to compensate for the effects of decoherence on ptychographic reconstructions, attributing it to mixed states in the illumination source [42].

The effects of partial coherence in Fourier Transform holography have been already reported by

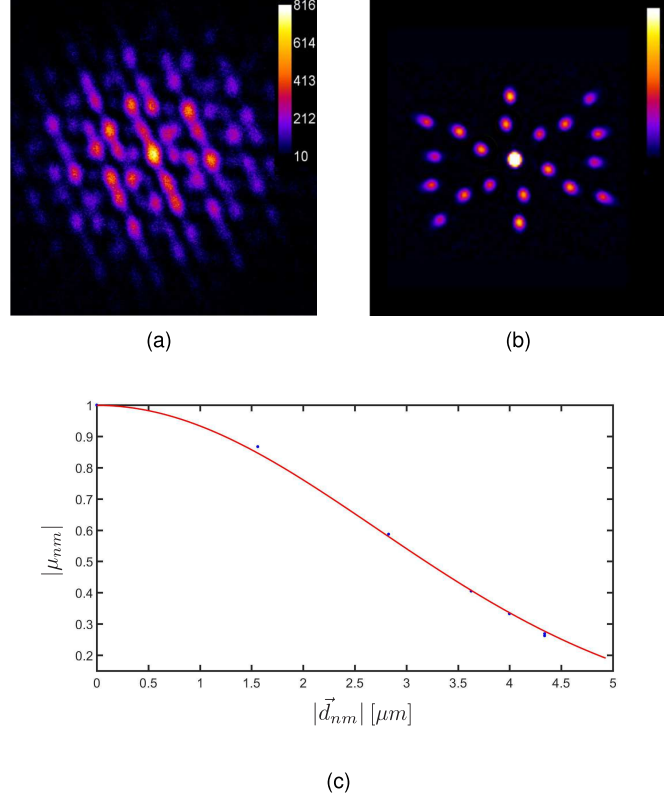


Figure 3.15: **Measurement of the magnitude of spatial coherence of a single H25 pulse from LUCA's harmonic beamline.** (a) NRA diffraction pattern with single-pulse acquisition. The scale bar denotes the intensity value measured at the detector. (b) NRA autocorrelation corresponding to the Fourier transform of the diffraction pattern of (a). The image is presented in logarithmic scale to allow a better visualisation of the magnitude-differences between the peaks. (c) Curve obtained for the magnitude of spatial coherence of the beam. The radius of the Gaussian distribution is $w_c = 3.85 \mu\text{m}$. The fit was obtained with a root-mean-square error of 2.5 %.

some groups [12, 44, 45]. To the best of our knowledge, a correction of this parameter has, however, not yet been experimentally studied. Moreover, no single-shot imaging compatibility was reported.

In this section, a possible correction of the spatial coherence in Fourier Transform holography will be investigated. The case study is performed at LUCA's harmonic beamline with measurements employing harmonic 33 of the IR HHG-driving laser. Spatial coherence measurements will be performed using the technique detailed in the previous section.

3.6.1 Fourier Transform Holography with partially coherent sources

Our treatment of FTH in terms of the spatial coherence of the illuminating field starts with Goodman's description of diffraction, given in Eq. (3.6) [197]. Assuming $J_0^I(\vec{r}_n, \vec{r}_m)$ the mutual intensity in the plane of the object, at the exit pupil of the system, one can write [197]:

$$J_0^I(\vec{r}_n, \vec{r}_m) = t(\vec{r}_n)t^*(\vec{r}_m)J_0(\vec{r}_n, \vec{r}_m) \quad (3.13)$$

where $t(\vec{r})$ is the object's transmittance function and $J_0(\vec{r}_n, \vec{r}_m)$ is the mutual intensity of the field before interaction with it. In an FTH sample, the transmittance function is given by the superposition of the object and reference transmittance, as given in Eq. (2.37). For a punctual reference, it can be written in the form:

$$t(\vec{r}, \vec{r}_r) = t_o(\vec{r}) + \delta(\vec{r} - \vec{r}_r), \quad (3.14)$$

with $\delta(\vec{r} - \vec{r}_r)$ the Dirac delta function centred at the reference position \vec{r}_r .

To reconstruct the object in FTH, a Fourier transform is applied to the diffraction intensity acquired in the far field (see Section 2.3.2). Taking the Fourier transform of Eq. (3.6) yields

$$\tilde{I}(\vec{\nu}, z) = \int \int J_0'(\vec{r}_n, \vec{r}_n - \lambda z \vec{\nu}) d^2 \vec{r}_n \quad (3.15)$$

where $\vec{\nu} = \Delta \vec{r} / \lambda z$, with $\Delta \vec{r}$ the distance between two points in the transmittance plane [197]. Inserting Eqs. (3.13) and (3.14) in Eq. (3.15), one can find an analytical expression of the holographic term for the object reconstruction as a function of the spatial coherence of the illuminating field:

$$\begin{aligned} \tilde{I}(\vec{\nu}, z, \vec{r}_r) = & \int \int J_0(\vec{r}_n, \vec{r}_n - \lambda z \vec{\nu}) [t_o(\vec{r}_n) t_o^*(\vec{r}_n - \lambda z \vec{\nu})] d^2 \vec{r}_n + \\ & \int \int J_0(\vec{r}_n, \vec{r}_n - \lambda z \vec{\nu}) [\delta(\vec{r}_n - \vec{r}_r) \delta^*(\vec{r}_n - (\lambda z \vec{\nu} + \vec{r}_r))] d^2 \vec{r}_n + \\ & \int \int J_0(\vec{r}_n, \vec{r}_n - \lambda z \vec{\nu}) [t_o(\vec{r}_n) \delta^*(\vec{r}_n - (\lambda z \vec{\nu} + \vec{r}_r))] d^2 \vec{r}_n + \\ & \int \int J_0(\vec{r}_n, \vec{r}_n - \lambda z \vec{\nu}) [\delta(\vec{r}_n - \vec{r}_r) t_o^*(\vec{r}_n - \lambda z \vec{\nu})] d^2 \vec{r}_n. \end{aligned} \quad (3.16)$$

In Eq. (3.16), the two first factors correspond to the object and reference self-correlations, respectively. The last two terms define the holographic image and its complex conjugate, as functions of the source-mutual intensity J_0 . After calculating the double integral in the third term of Eq. (3.16) we obtain the analytic expression that determines the object reconstruction, O_R , in terms of the mutual intensity of the source:

$$O_R(\vec{\nu}, z, \vec{r}_r) = J_0(\vec{r}_r, \vec{r}_r + \lambda z \vec{\nu}) t_o(\vec{r}_r + \lambda z \vec{\nu}). \quad (3.17)$$

This means that the FTH reconstruction retrieves, in fact, the object transmittance function modulated by the mutual intensity between the different pair of punctual apertures in the combination object-reference. Taking into account the relation between mutual intensity and spatial coherence (Eq. (3.4)), Eq. (3.17) can be written in the form:

$$O_R(\vec{r}_r, \vec{r}) = \mu(\vec{r}_r, \vec{r}) \sqrt{I(\vec{r}_r) I(\vec{r})} t_o(\vec{r}). \quad (3.18)$$

One can then see that in the particular case where the source is fully-spatially coherent, $\mu(\vec{r}_r, \vec{r}) = 1$, we obtain the same result as in standard FTH and the holographic term determines directly the object reconstruction. On the other hand, if the source is spatially incoherent, $\mu(\vec{r}_r, \vec{r}) = 0$, we do not have any interference and the holographic term is zero, $O_R(\vec{r}_r, \vec{r}) = 0$.

Eq. (3.18) also shows that for a partial-spatial coherence case, $0 < \mu(\vec{r}_r, \vec{r}) < 1$, the object reconstruction is modulated by the spatial coherence between the reference and the object. As all the combinations of distances $\vec{d}_r = (\vec{r} - \vec{r}_r)$ between the object and a punctual reference are different, the reconstruction problem is non-redundant. This means that one point sampled in the Fourier transform of the diffraction pattern (autocorrelation of the object) corresponds to only one pair of points object-reference. A consequence of this non-redundancy is that the phase of the spatial coherence can be neglected in the calculation of the amplitude reconstruction of the object [178]. We note that this principle was also subjacent in the measurements of the magnitude of spatial coherence with the NRA, allowing its separation from the phase contribution. Extending this comparison, one can also note that, in the autocorrelation image of the FTH sample, where the reconstruction is obtained, the configuration/distances are displayed similarly as discussed for the non-redundant array used in the earlier section. Only that despite having just pinhole-apertures, we have now one or more isolated pinhole-apertures, plus one more-complex structure - the object. This can be better visualised in Fig. 3.16 with the same \vec{d}_r vectors represented in the same colours in the sample and respective spatial autocorrelation. Several references were used to see the effect.

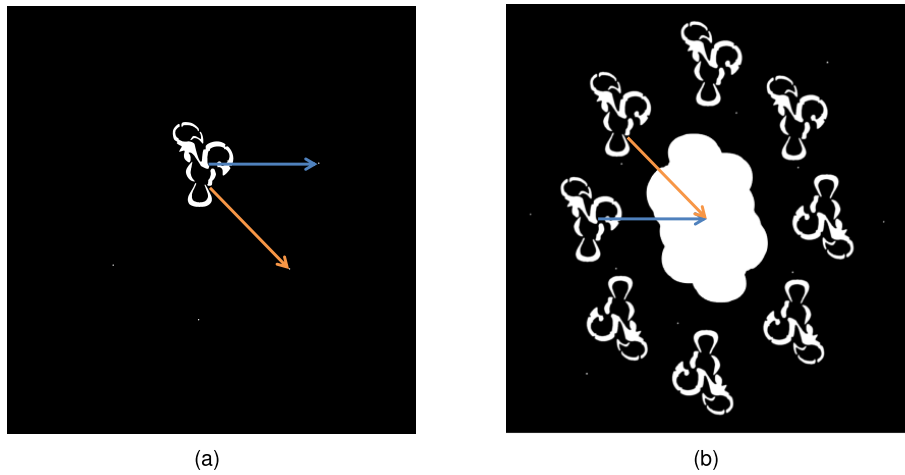


Figure 3.16: **Example of an FTH sample and respective reconstruction with corresponding separation vectors \vec{d}_r .** (a) FTH sample with four pinhole references. Two vectors denoting the separation between different object-points and distinct references are presented in different colours. (b) Autocorrelation of (a) given by the Fourier transform of the diffraction pattern generated by the sample. The image shows the same separation vectors of (a) displayed with the same colours. Note that in a multiple-punctual reference scheme, the same sample is reconstructed for each reference, along with its complex conjugate, which is located radially opposite to the origin. Therefore, in the image, we have four non-redundant complex reconstructions of the same object.

In turn, for the case of an extended reference, different pairs of points object-reference can have the same separation vector \vec{d}_r , i.e. our reconstruction will be redundant. The whole set of pairs of points with a separation vector \vec{d}_r will be sampled with only one point on the Fourier transform of the diffraction. Therefore, the modulation of the object reconstruction at \vec{d}_r , is given by the combined modulations induced by each pair of points with the same distance \vec{d}_r . If the phase of the spatial coherence for the different pairs in such a set is different (shift-variant phase), the total amplitude of the object reconstruction

at that position will be modulated by the phase of the spatial coherence.

In conclusion, from this description, one can see that any modulation in the object reconstruction induced by a shift-variant phase of the spatial coherence is avoided by using Fourier Transform holography with a punctual reference. In the case of an extended reference, shift variations of the phase in the spatial coherence may generate a superposition out of phase in the object reconstruction, which can degrade the object reconstruction.

3.6.2 Experimental Studies at LUCA's Harmonic Beamline

In order to test an experimental correction of the magnitude of spatial coherence in Fourier Transform holography, the setup of Fig. 3.6 was used. In this part, harmonic 33 was generated from *Ne* (see Table 3.2) and the second off-axis parabola was used to focus the beam. The harmonic beam was optimised for a good compromise between photon flux and beam-pointing stability with the parameters detailed in Table 3.3. Several samples from the produced membrane (Fig. 3.8) were tested. One example can be seen in Fig. 3.9 (b). The sample was placed in the focal spot of the parabola and the far-field diffraction pattern was recorded 40-mm away from it.

3.6.2.1 Experimental Results and Discussion

Figs. 3.17 (a) and (d) show two experimental diffraction patterns of two different fabricated samples. They will be addressed as sample 1 and 2, respectively. The diffraction patterns were acquired with an accumulation of 100s, reading frequency of 100 kHz, a binning factor of 2×2 and the CCD camera cooled down to -40° C. The Fourier transform of these diffraction patterns, with a zoom in the object reconstruction, can be found in Figs. 3.17 (b) and (e).

The reconstructions from Figs. 3.17 (b) and (e) were acquired with an average resolution of 90 nm and 86 nm, respectively (see Section 2.5.1.1). These values suggest that the diameter measured for the reference aperture (approximately 139 nm at the upper face of the membrane) is, in fact, larger than the actual diameter patterned over all the thickness of the sample.

Comparing now the reconstructions of Figs. 3.17 (b) and (e) with the pure-binary samples of Figs. 3.17 (c) and (f), one can notice considerable artefact-modulations. From Eq. (3.18), we know that they are given by the magnitude of spatial coherence and beam-intensity variations at the spatial extent of the sample. Comparing both Figs. 3.17 (b) and (e) one can also note that the modulations follow different profiles, depending on the case. While for sample 1 the amplitude distribution does not seem to follow a uniform tendency, having peaks of higher and lower counts in the body, tail and head of the rooster object; in sample 2 the amplitude seems to follow a close-to-linear (decreasing) profile from the head to the tail. This latter part seems to have not been sufficiently illuminated.

Under the consideration of different amplitude-profiles, a similar amplitude correction for both samples seems already not sufficient. However, we proceeded with the spatial-coherence correction study and performed NRA measurements under similar experimental conditions. Fig. 3.18 (a) shows the diffraction pattern obtained from the same 5-apertures NRA used in the earlier section (Fig.3.14 (a)).

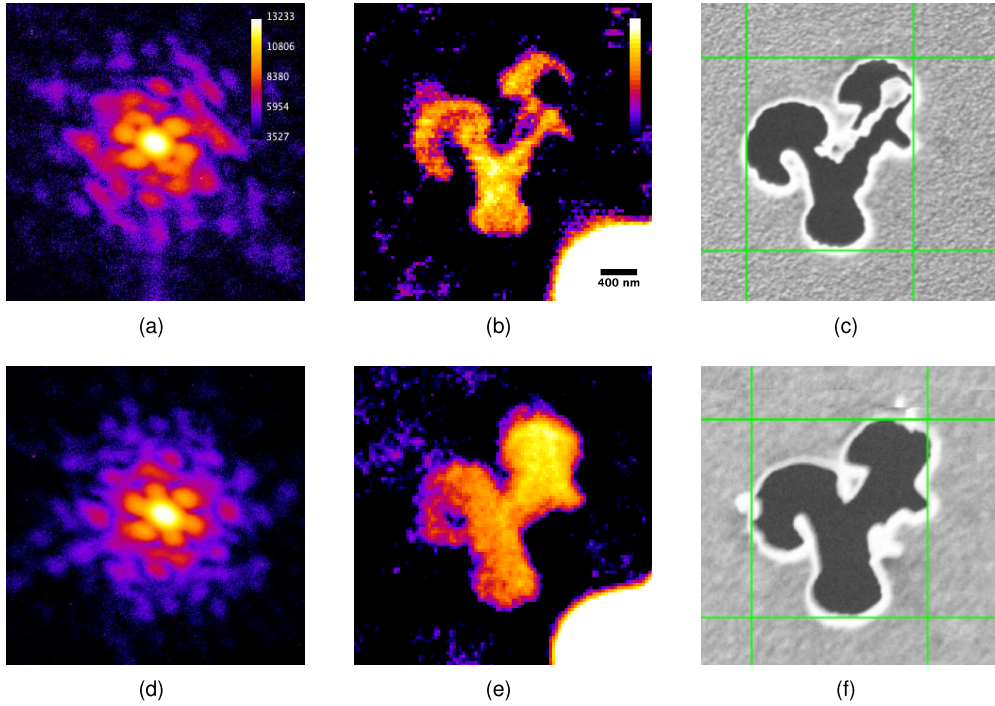


Figure 3.17: **Experimental diffraction patterns and respective reconstructions obtained for two different FTH objects.** (a),(d) Diffraction patterns resulting from an accumulation of 100s. The detected patterns were converted to a logarithmic scale to allow a better visualisation of the spatial dynamics. The colour scale is common to both images and denotes the intensity measured at the detector, after application of the logarithmic filter. (b),(e) Zoom in the object reconstruction, given by the Fourier Transform of the diffraction patterns from (a) and (d), respectively. The colour scale is arbitrary and common to both images. Also the scale bar is common to both. The images are presented in logarithmic scale to allow a better visualisation of the magnitude-variations of the reconstructions. (c),(f) SEM images of samples which seem to correspond to the objects imaged.

The diffraction pattern was acquired with an accumulation of 180s, with a reading frequency of 100 kHz and 2×2 binning factor. The Fourier Transform of this diffraction pattern, i.e. the experimental autocorrelation of the NRA can be found in Fig. 3.18 (b).

Observing the autocorrelation image from Fig. 3.18 (b) one can notice again the 10 peaks with respective conjugates, for the corresponding 10 aperture-pairs. The corresponding curve obtained for the magnitude of spatial coherence can be found in Fig. 3.18 (c). The data points were calculated from Eqs. (3.12) and the Gaussian fit to these points revealed a radius of the coherence function of $w_c = 3.7 \mu\text{m}$, with 4% root-mean-square error. This, again, reports a source with high-magnitude of spatial coherence.

In order to try a correction of this profile in the FTH reconstructions, according to Eq. (3.18), one must multiply the reconstruction by the 2D map $1/\mu(\vec{r}_r, \vec{r})$. This means that the autocorrelation of the sample must be multiplied by the Gaussian distribution displayed in Fig. 3.18 (d) (note that even though this map shows the right coherence radius, the colour scale used does not reflect well the effect of the multiplication, as it was chosen to allow a better visualisation of the profile and, therefore, is not the same used in Figs. 3.17 (b) and (e)).

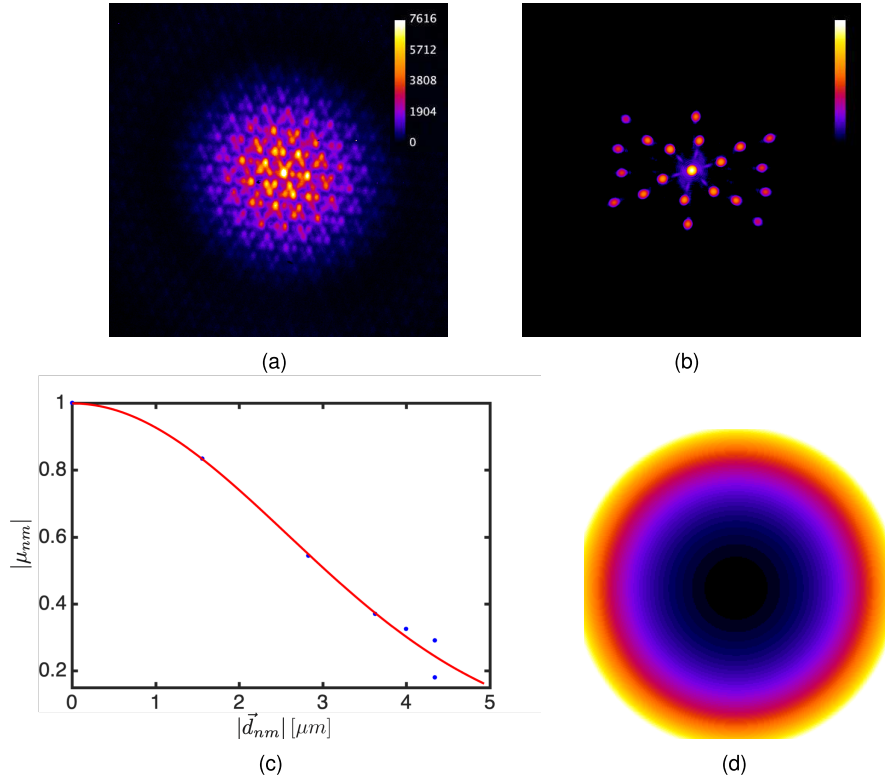


Figure 3.18: **Experimental diffraction pattern and respective NRA autocorrelation achieved with similar generation conditions to the FTH samples.** (a) NRA diffraction pattern resulting from an accumulation of 180s. The scale bar denotes the intensity measured at the detector. (b) NRA autocorrelation corresponding to the Fourier transform of the diffraction pattern of (a). The image is presented in a logarithmic scale to allow a better visualisation of the magnitude-differences between the peaks. (c) Curve obtained for the distribution of the magnitude of spatial coherence of the beam. The radius of the Gaussian distribution is $w_c = 3.7 \mu\text{m}$. The fit was obtained with a root-mean-square error of 4 %. (d) 2D Gaussian distribution of the magnitude of spatial coherence inverted, i.e. $1/\mu(\vec{r}_r, \vec{r})$. The multiplication of this profile by the autocorrelation of the sample must account for the effects of the magnitude of spatial coherence in the reconstruction. The colour scale is the same from image (b) and is arbitrary.

The result of the multiplication of the samples' autocorrelations with the Gaussian map from Fig. 3.18 (d) can be seen in Figs. 3.19 (b) and 3.20 (b) with respective versions prior to "correction" in Figs. 3.19 (a) and 3.20 (a). A zoom in the cross-correlation region (i.e. object reconstruction), before and after "correction", can be seen in Figs. 3.19 (c)-(d) and Figs. 3.20 (c)-(d), for samples 1 and 2 correspondingly. Analysing the set of images from Fig 3.19, corresponding to sample 1, one can see that the amplitude distribution, which before did not seem to follow any uniform profile (Fig 3.19 (c)), now follows the trend of the Gaussian map, with an induced gradient in the radial direction (Fig 3.19 (d)). In Fig 3.20, corresponding to sample 2, one can not see a relevant alteration in the amplitude modulations besides an increase of the signal in the tail, which is comparable in fact with the increase of the noise in that region. Indeed, in both sets of images from Figs. 3.19 and 3.20 one can see that the noise is accentuated after the multiplication of the Gaussian map, which is predictable as it gives more weight to features at larger radii. One could easily overcome this by limiting the Gaussian radius to the limits of the sample.

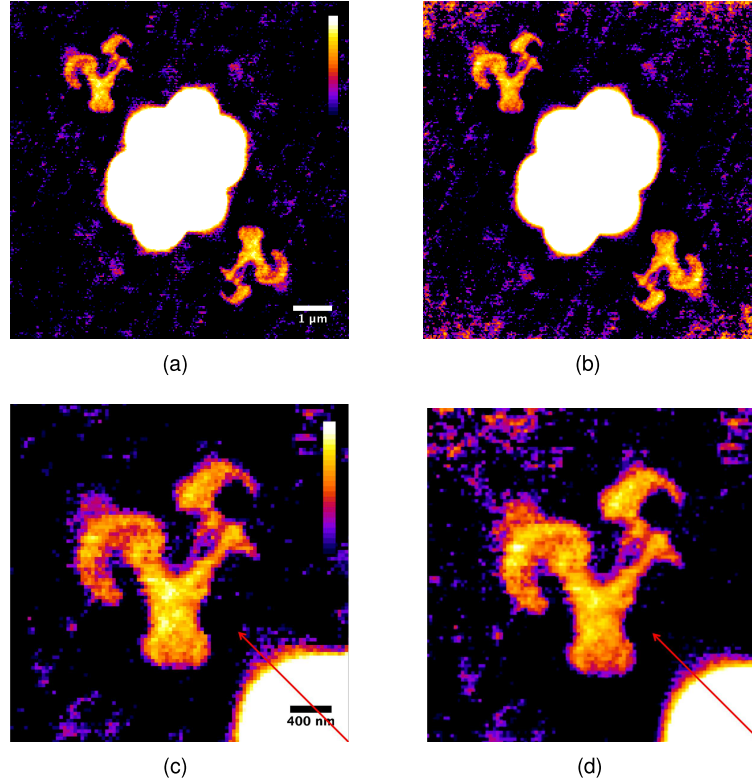


Figure 3.19: **FTH reconstructions before and after "correction" with the measured profile of $|\bar{\mu}|$.** (a)-(b) Autocorrelation of sample 1 before, (a), and after, (b), multiplication of the correction map for the effect of spatial coherence. The colour scale is arbitrary and common to both images. Also, the scale bar is common to both. (c)-(d) Zoom in the reconstruction of sample 1 before, (a), and after, (b), multiplication of the correction map for the effect of spatial coherence. The images are presented in logarithmic scale to allow a better visualisation of the structures. The red arrow indicates the gradient directionality that could be induced by partial coherence.

Considering the results, one can conclude that a Gaussian map correction does not make any clear positive impact in our FTH reconstructions. According to Eq. (3.18) this could have two reasons. One, the magnitude of spatial coherence does not follow a shift-invariant approximation, and therefore, the spatial-coherence profile would be more complex than just a Gaussian distribution. Two, strong intensity variations affect the illuminating beam at the spatial extent of the sample. Even though the first case could be true, we believe that it does not have a relevant influence here. Contrarily to the case of the NRA, where the autocorrelation peaks will have a distribution just given by the separations \vec{d}_{nm} , and therefore completely distinct from the original sample arrangement, here the distances of the reconstruction, \vec{d}_r , are measured in relation to the centre, as in the sample-plane to the pinhole reference. This structure preservation allows us to admit that a profile affected by the spatial coherence could only accuse an increase of signal for the structures as they approach the centre of the autocorrelation image (or reference in the sample) and, likewise, a decrease as they get further from it. This directional intensity gradient is illustrated by the red arrows in Fig. 3.20 (c)-(d). As this gradient is not visible in any of our reconstructions, we conclude that the intensity distribution of the beam under accumulation regime had strong modulations, which made the influence of the partial coherence negligible.

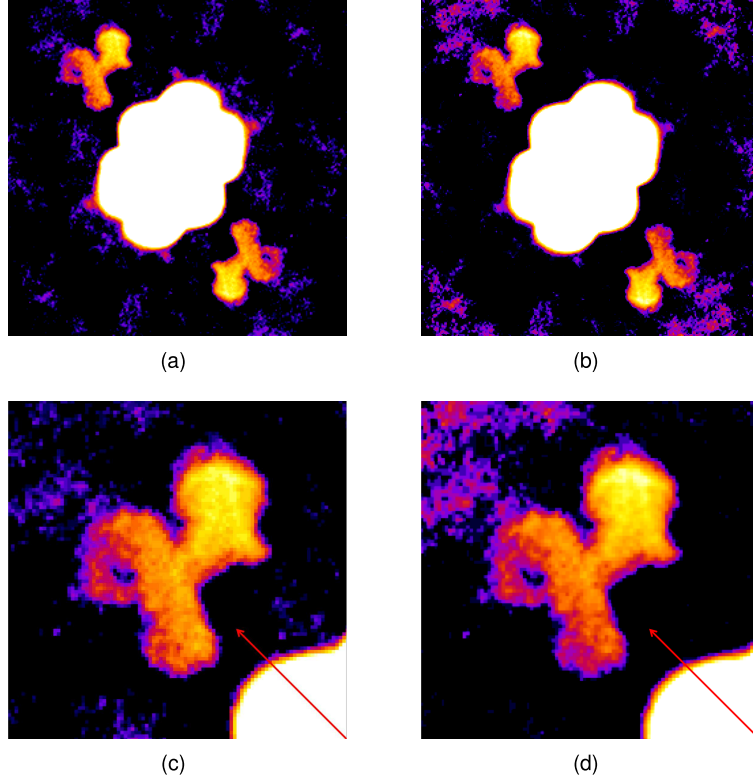


Figure 3.20: **FTH reconstructions before and after "correction" with the measured profile of $|\bar{\mu}|$.** (a)-(b) Autocorrelation of sample 2 before, (a), and after, (b), multiplication of the correction map for the effect of spatial coherence. (c)-(d) Zoom in the reconstruction of sample 2 before, (a), and after, (b), multiplication of the correction map for the effect of spatial coherence. The images are presented in logarithmic scale to allow a better visualisation of the structures. The scale and colour bars of all images are the same from Fig. 3.19. The red arrow indicates the gradient directionality that could be induced by partial coherence.

The effect of a non-uniform intensity profile was also observed for several NRA measurements. Figs. 3.21 show experimental diffraction patterns and respective autocorrelations, acquired with 180-s accumulation and three different gas-pressure values inside the generation cell. Each of them yields different intensity and coherence distributions. Observing the autocorrelation images - Figs. 3.21 (b),(d) and (f) - one can note that the peaks have different relative magnitudes for the different pressure values. In Fig. 3.21 (d) for instance, the peak in \vec{d}_{45} (notation from Fig. 3.14 (a), see red arrow showing \vec{d}_{45} in Fig. 3.21 (b)) presents extremely low counts, while all the peaks associated with aperture 5 in 3.21 (f) have lower counts than the remaining ones. This effect is explained by a different illumination of the NRA apertures, simulated in Fig. 3.22.

Fig. 3.22 shows a simple case where an NRA sample is illuminated by a perfectly coherent beam with a Gaussian-intensity distribution. The simulation was performed employing Eqs. (2.16), (2.20), and (2.17), with $U_{inc}(r_{\perp})$ given by the square-root of a Gaussian distribution. The autocorrelation was obtained from the Fourier Transform of Eq. (2.17). Observing the images one can see that, depending on the NRA positioning with respect to the beam, and consequently, depending on the different intensity values affecting the NRA apertures, the autocorrelation shows a different signal for the different

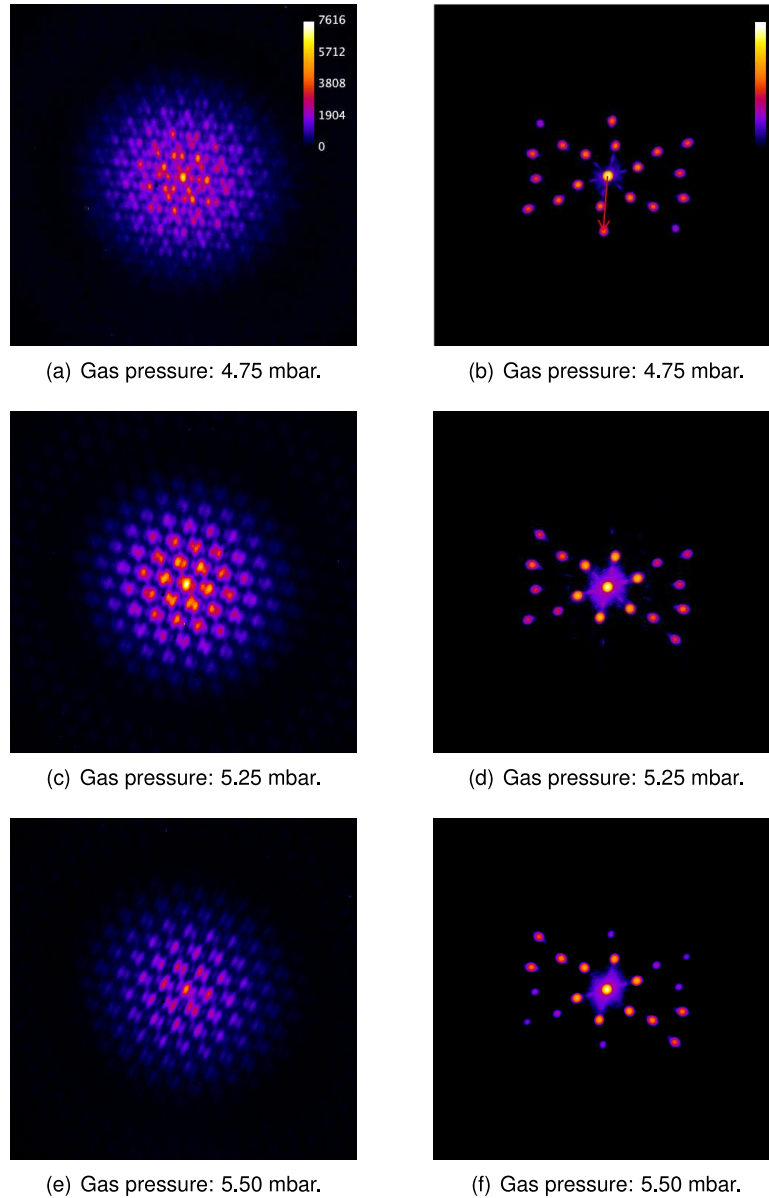


Figure 3.21: **Experimental diffraction patterns and respective NRA autocorrelations achieved from H33 for a scan of values of gas pressure inside the generation cell.** Left images: (a),(c) and (e) NRA diffraction patterns with an accumulation of 180 s for values of gas pressure of 4.75 mbar, 5.25 mbar and 5.50 mbar, respectively. The scale bar is common to all the patterns and denotes the intensity measured at the detector. Right images: (b),(d),(f) NRA autocorrelations corresponding to the respective left-sided diffraction patterns. The images are presented in logarithmic scale to allow a better visualisation of the magnitude-differences between the peaks. The red arrow in (b) represents \vec{d}_{45} . The scale bar is common to all the images.

autocorrelation peaks.

The curves of the magnitude of spatial coherence associated with each measurement of Fig. 3.21 are presented in Fig. 3.23. For gas-pressure values of 4.75 mbar, 5.25 mbar and 5.50 mbar, the radii of the Gaussian distributions found were $w_c = 3.9 \mu\text{m}$, $w_c = 5.0 \mu\text{m}$ and $w_c = 5.2 \mu\text{m}$, respectively. The fits were obtained with root-mean-square errors of 8 %, 11 % and 5 %. Comparing with the results from the single-shot regime, Fig. 3.15 (c), the high dispersion of the data points and the consequent increase of

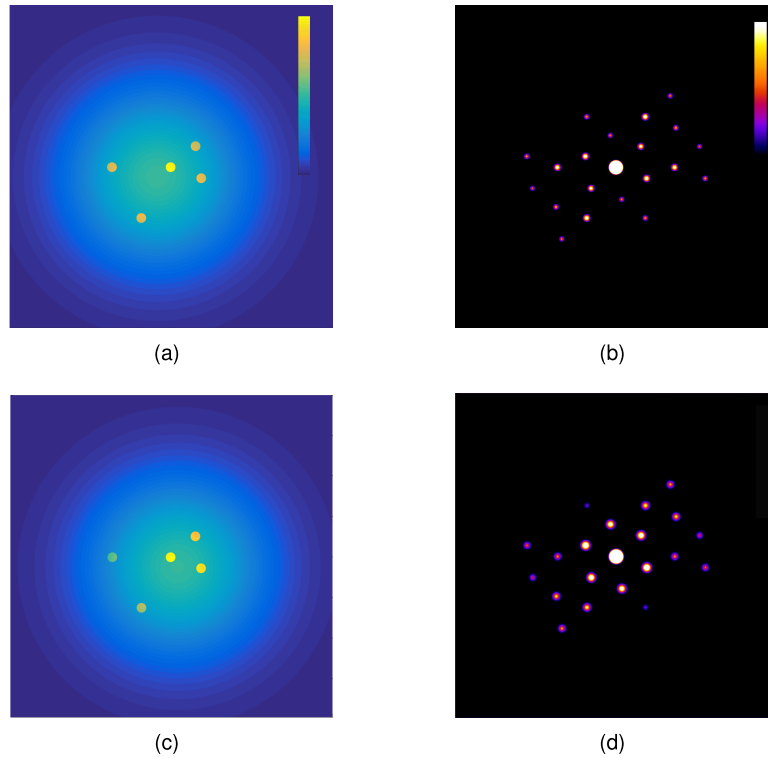


Figure 3.22: **Effect of the intensity profile of the illuminating beam in the NRA autocorrelation.** Left images: (a),(c) Visual representations of the NRA sample at different positions with respect to a beam with perfect coherence and a Gaussian-intensity distribution. The scale bar is arbitrary and common to both images. Right images: (b),(d) Simulation of the two NRA autocorrelations corresponding to the respective left-sided scenarios. The scale bar is again common to both images.

the error from the measurements are evident. This was predicted by Gonzalez simulations [178], arising from the accumulation of several pulses with different intensity distributions and beam-pointings.

In conclusion, according to the reconstructions obtained employing Fourier Transform holography in regime of accumulation, the intensity map $\sqrt{I(\vec{r}_r)I(\vec{r})}$ in Eq. (3.18) was seen to play a much larger influence in our reconstructions than the magnitude of spatial coherence. In the light of these results, a correction by means of a Gaussian distribution showed not only to be incomplete, but also to induce additional gradients in the reconstructions. Indeed, our attempt to compensate for the effects of spatial coherence in Fourier Transform holography would be more obvious with a lower partial coherence and a more intensity-homogeneous beam.

Looking into the actual parameters that affect the reconstruction in Eq. (3.18), one could also study FTH configurations with multiple apertures which could provide some additional and/or compensated information. An interesting configuration is an FTH mask where the object is placed in a central position with respect to several equally-separated punctual references. Besides allowing as many reconstructions as the number of references, such scheme has several particularities. Firstly, all the reconstructions carry different spatial-coherence profiles covering, with equal angular separations, 360° in the image of the autocorrelation of the sample (we recall that this autocorrelation needs to be non-redundant, i.e. the reconstructions must be separated from the self-correlation area and from the reconstructions - cross

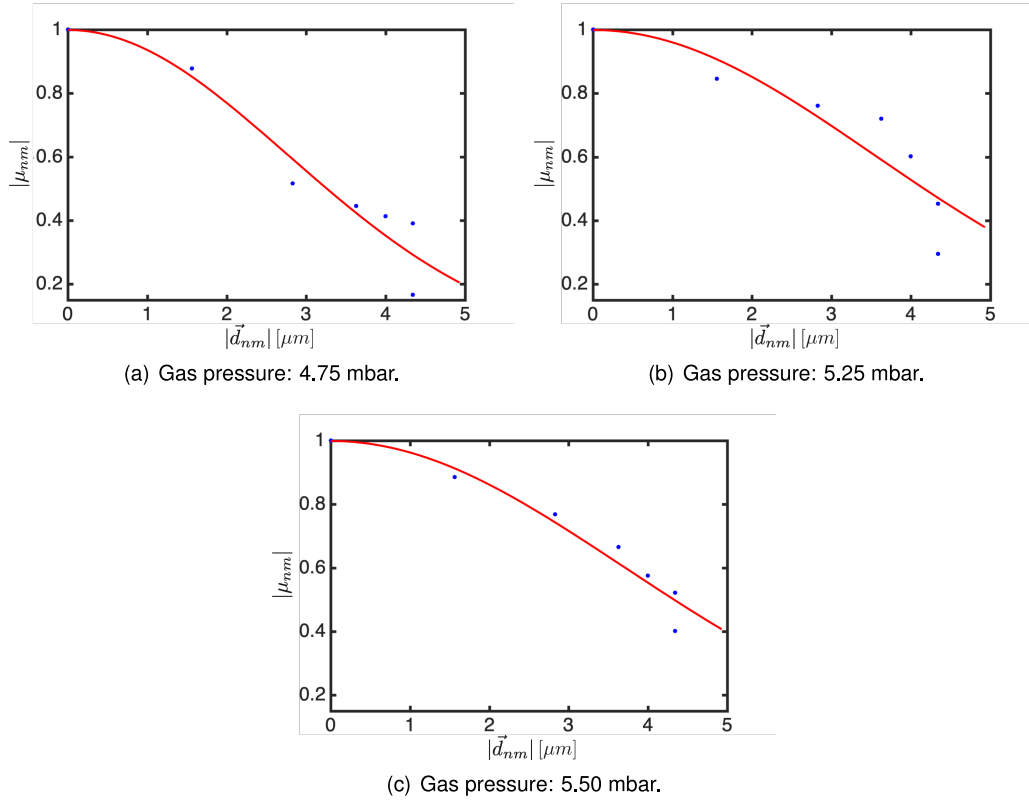


Figure 3.23: Calculation of the H33's degree of spatial coherence from the experimental data for different gas-pressure values, using the NRA of 5 apertures of Fig. 3.14. For the calculations, the aperture 1 from image 3.14 was used as reference for the intensity. In each case, the red line shows the Gaussian fit to the experimental values. (a) Curve obtained for a gas-pressure value of 4.75 mbar. The radius of the Gaussian distribution is $w_c = 3.9 \mu\text{m}$. The fit was obtained with a root-mean-square error of 8 %. (b) Curve obtained for a gas-pressure value of 5.25 mbar. The radius of the Gaussian distribution is $w_c = 5.0 \mu\text{m}$. The fit was obtained with a root-mean-square error of 11 %. (c) Curve obtained for a gas-pressure value of 5.50 mbar. The radius of the Gaussian distribution is $w_c = 5.2 \mu\text{m}$. The fit was obtained with a root-mean-square error of 5 %.

correlations - associated with all the reference-apertures). Secondly, for all the reconstructions, the beam-intensity map at the sample, $I(\vec{r})$, is the same (see Eq. (3.18)), varying just the contribution of the beam intensity at each reference position, $I(\vec{r}_r)$. As this $I(\vec{r}_r)$ is a simple factor, normalising each reconstruction allows to get rid of it and, this way, have reconstructions differing only by the coherence effects.

An example of such a sample was used by W. F. Schlotter *et al.* [200] and can be found in Fig. 3.24 (a). Extracting the reconstructions from Schlotter's article and readjusting the colour scale with *ImageJ* to a range where the variations in magnitude are visible, one can, in fact, directly see the spatial-coherence effects (Fig. 3.24 (b)). Analysing Fig. 3.24 (b), one can note the stronger reconstructed signal at distances in the object closer to the centre of the autocorrelation image (measured with relation to the pinhole reference in the sample) and weaker signal as it moves away from it. Note that the reconstructions are not normalised and thus the intensity value in their associated references, $I(\vec{r}_r)$, gives to some "F"s a general higher signal than to others. The respective reconstructions for each

pinhole reference are also presented in Fig. 3.24 (c) for better visualisation of the effect.

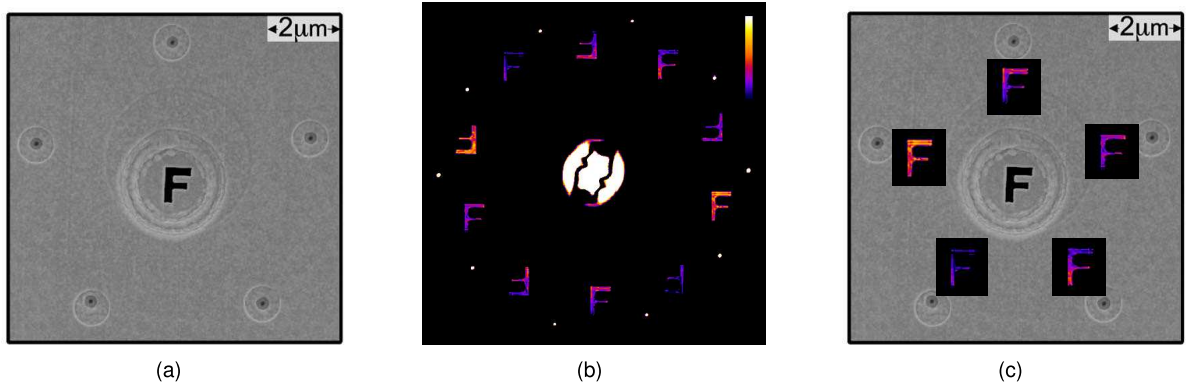


Figure 3.24: **FTH mask and holographic reconstructions with a clear effect of the partial spatial-coherence.** (a) SEM image of the FTH mask used by Schlotter *et al.* in [200]. (b) Reconstructed holographic images of the object, i.e., mask's autocorrelation. The colour scale was set to a range where the amplitude variations are visible. (c) Visualisation of the experimental reconstructions obtained for each reference pinhole in the FTH mask.

By averaging the 5 reconstructions of a Fourier Transform hologram recorded in the photon noise limit ($(2.5 \pm 0.3) \times 10^3$ detected photons, considerably less than the $\sim 7 \times 10^6$ measured for the data of Fig. 3.24 (b)-(c)), Schlotter departed from only-partial reconstructions to a full object reconstruction [200], reporting a considerable SNR enhancement. This SNR improvement is directly linked with the compensation of the spatial-coherence effects, given that:

$$\begin{aligned}
 O_R(\vec{r}) &= \frac{1}{N} \sum_{n=1}^N O_n(\vec{r}_n, \vec{r}) \\
 &= t_o(\vec{r}) \sqrt{I(\vec{r})} \frac{1}{N} \sum_{n=1}^N \sqrt{I(\vec{r}_n)} \mu(\vec{r}_n, \vec{r}), \tag{3.19}
 \end{aligned}$$

with O_n the reconstructed sub-image achieved for each of the $N = 5$ apertures and $I(\vec{r})$ the intensity distribution of the beam illuminating the sample. In fact, as we see in Eq. (3.19), this averaging process will actually average the $\sqrt{I(\vec{r}_n)} \mu(\vec{r}_n, \vec{r})$ contributions, which creates a composed image, O_R , more equilibrated from the effects of spatial coherence and intensity-variations between the references. The coherence profiles $\mu(\vec{r}_n, \vec{r})$ will complement some part of the effect of each other as they cover with equal angular separations, 360° in the image of the autocorrelation of the sample, while the $\sqrt{I(\vec{r}_n)}$ give more weight to sub-images with higher SNR, decreasing the influence of noise-related artefacts.

If now the individual reconstructions are normalised before the averaging process, one can get rid of the factors yielding:

$$\begin{aligned}
O_{norm}(\vec{r}) &= \frac{1}{N} \sum_{n=1}^N O_{norm_n}(\vec{r}_n, \vec{r}) \\
&= t_o(\vec{r}) \sqrt{I_{norm}(\vec{r})} \frac{1}{N} \sum_{n=1}^N \mu(\vec{r}_n, \vec{r}).
\end{aligned} \tag{3.20}$$

with $O_{norm}(\vec{r})$ the composed reconstruction achieved from the average of the normalised $O_{norm_n}(\vec{r}_n, \vec{r})$ reconstructions and $I_{norm}(\vec{r})$ the normalised intensity profile of the beam at the spatial extent of the sample.

If one could say that the average of the coherence values on the spatially-distributed sample reconstructions approximates to a situation where the coherence effect is negligible, i.e.

$$\frac{1}{N} \sum_{n=1}^N \mu(\vec{r}_n, \vec{r}) \simeq 1 \quad \forall \vec{r} \in \text{object} \tag{3.21}$$

one can obtain the value of the distribution $\sqrt{I_{norm}(\vec{r})}$ and extract individual coherence profiles for each individual reconstruction, given by:

$$\mu(\vec{r}_n, \vec{r}) = \frac{O_{norm_n}(\vec{r}_n, \vec{r})}{\sqrt{I_{norm}(\vec{r})} t_o(\vec{r})}. \tag{3.22}$$

Therefore, besides compensating for the coherence effects in FTH reconstructions, a well-characterised test mask with the format of Fig. 3.24 (a), could potentially be used to measure the 2D spatial coherence of the beam. Coherence maps of radial slices of the autocorrelation could be retrieved by fitting Gaussian-Schell profiles to the 2D coherence distributions of Eq. (3.22). As in Section 3.5.2, these Gaussian functions obey $\mu(\vec{r}_n, \vec{r}_n) = 1$ at the centre of the autocorrelation (i.e. at $|\vec{d}_r(\vec{r}_n, \vec{r}_n)| = 0$), allowing to recover, for each sub-image, the factor associated with the spatial coherence which was lost in the normalisation process. Interpolation functions could then be used to retrieve the magnitude of the spatial coherence of the regions between the reconstructions. Note that, as discussed before, contrarily to the case of the NRA, where the autocorrelation peaks have a distribution distinct from the original sample arrangement, here the distances of the reconstruction, \vec{d}_r , are measured radially with respect to the centre, as in the sample to the pinhole reference. This structure preservation, allied with the radial-regular distribution of references, seems to be able to avoid shift-invariant approximations, allowing for 2D measurements, which are sensitive to directional variations of the spatial coherence. Another consequence of this shift variance is that one could, in principle, have access to the phase of the degree of spatial coherence, in addition to the magnitude. Therefore, with a well-characterised simple shape as an object, and the full sample covering the biggest area possible of the beam at the focus, single-shot full-2D characterisation of the complex spatial coherence function could be potentially reached.

This example constitutes only a simple idea which requires further simulation efforts and could be developed for a future work in the topic. The case provided follows the approximation given by Eq.

(3.21), however, other more appropriate simplifications can be studied. As example, we can propose the separation of the coherence function between the two transverse directions of propagation, frequently used for the coherence characterisation of X-ray sources [41, 165]. Such approximation would retrieve an ellipse Gaussian distribution for the magnitude of spatial coherence, which would be itself the assumption to extract the optimal parameters from the fit. We note that, without approximation, for each autocorrelation image we directly have a system of N equations of the form of Eq. (3.22), with the same denominator $\sqrt{I_{norm}(\vec{r})} t_o(\vec{r})$. Therefore, by dividing the contributions from the different sub-images one can directly write the maps of the magnitude of spatial coherence, for all the sub-images, with respect to only one.

3.7 Conclusion Notes

This chapter presented some examples of experimental studies performed in the HHG beamline of LUCA, which provides an intense source of coherent XUV photons with 20-femtoseconds pulse duration.

Here, a typical setup for lensless imaging in the far field was successfully mounted. After the optimisation of the generation process and the overall beamline, the samples were positioned in the focus of an off-axis parabola, followed by an XUV CCD camera, located in the far field. Two types of objects were fabricated. One consisted of a non-redundant array (NRA) for spatial coherence measurements, the other a Fourier Transform holography (FTH) sample.

A new technique to characterise the magnitude of the complex degree of spatial coherence of Gaussian-Schell beams [178] was studied and implemented in LUCA's beamline. It is based on the interferometry through an NRA, with different separation distances and orientations, allowing for spatial characterisation of the entire light field in a single shot. Besides allowing single-pulse characterisation, this method is also independent of the intensity profile of the beam and the stability of its pointing, in contrast to other methods such as the Young double slits [41]. The measurement revealed a very good magnitude of spatial coherence with a radius $w_c = 3.85 \mu\text{m}$, fit with a root-mean-square error of 2.5% (larger than the radius of the focal spot). Overall, the simplicity and versatility of this method give it enormous potential as a tool for single-shot spatial coherence characterisation of the most varied sources, ranging from ultrafast laser-based sources to XFELs and synchrotrons.

Followed a study to compensate for the impact of partial-spatial coherence in Fourier transform holography. For the purpose, we showed that any modulation in the object reconstruction induced by a shift-variant phase of the spatial coherence is avoided by using FTH with punctual references. The same does not directly apply to holography with extended references, though. An extension of the study to these techniques would be interesting, as shift-variant phases of the spatial coherence may generate a superposition out of phase in the object reconstruction, which can degrade it.

In the FTH experiments, provided in Section 3.6, harmonic H33 of LUCA's beamline was used. We selected two examples of reconstructions of two different samples to perform the studies of this manuscript. By using the NRA method, a radius of the coherence function of $w_c = 3.7 \mu\text{m}$ was obtained,

with 4% root-mean-square error. Performing a compensation of the partial coherence no substantial improvement of the reconstructions was obtained and, inclusively, additional gradients were induced. The main explanation found is that strong intensity variations across the sample affect the image reconstruction, leading to a limited effect of the partial coherence in the experimental test. Indeed, a limited spatial coherence would induce a radial intensity gradient (as illustrated by the case of Schlotter *et al.* [200]), which is not observed. The modulations are thus mostly attributed to a non-uniform illumination of the sample.

A multi-directional Fourier transform hologram, as shown by Schlotter, can recover the information lost radially by the lack of spatial coherence. Based on this, we saw that single-shot full-2D characterisation of the complex spatial coherence function could be potentially reached, using a characterised extended object as probe. A consequence of this allowed shift variance is that one could, in principle, have access to the phase of the degree of spatial coherence, in addition to the magnitude obtained with the NRA.

In the same context, one could also propose as a future work perspective an extension of this study to imaging with extended references. Indeed, the effect of spatial coherence is also observed for holographic reconstructions employing the technique of HERALDO (i.e. holography with extended reference by autocorrelation linear differential operator), as presented in Fig. 3.25 [12]. A description of derivative algorithms for FTH imaging with extended references in terms of the spatial coherence would, thus, be of interest.

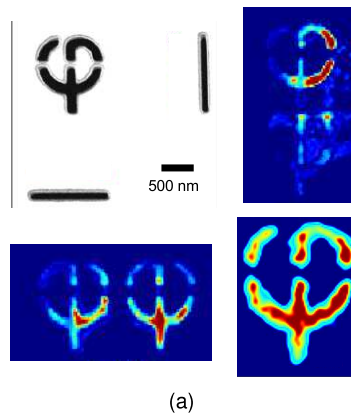


Figure 3.25: **Fourier transform holography based on the use of extended references with a clear effect of the partial spatial-coherence [12].** In the image, one can see the respective reconstructions achieved for each HERALDO reference. One can observe in the individual reconstructions the typical coherence profile, where the reconstructions show stronger signal at distances in the object closer to the reference, and weaker as they move away from it. The image presented in the bottom-right corner represents the sum of all the 4 contributions.

Chapter 4

Digital In-line Holography corrected from Aberrations by Resorting to Wavefront Sensor Measurements

4.1 Introduction

Future emerging applications of extreme-ultraviolet and X-ray imaging are directed towards the structure determination of single molecules, viruses and cells by resorting to ultrashort and extremely bright pulses, briefer than the timescale of most damage processes [1, 2].

In 2011, the 3-dimensional structure of a single protein was revealed to the world with the resolution of a few ångströms [1]. This was accomplished employing "diffraction-before-destruction" CDI, after spurring fully hydrated nanocrystals into the path of an ångström-wavelength FEL, in LCLS. Under similar conditions, diffraction data were collected from non-crystallized mimi-virus [2]. Nonetheless, this time, the reconstructions only reached nanometre-spatial resolutions. Behind these results are the limited photon flux - critical to ensure a reliable SNR in a single shot [2, 13]; some influence of the focal-spot quality [15, 38] -, particularly important, since no statistical analysis is achievable for such samples; and the low dynamic range of the detection [2]. Indeed, especially affecting measurements which can not be replicated, there is a clear need to achieve higher resolution in single shot [2].

The reduced photon flux, in the energy ranges of interest, is a major constraint in single-shot imaging. To reconstruct molecular structures from diffraction snapshots of random orientation, requires, by current proposals, ~ 1000 times more signal than the currently available in next-generation XFEL sources [201–203]. Single-shot imaging of complex biological samples with tabletop high-harmonic generation (HHG) sources is even more challenging [13]. In addition to the low efficiencies of the HHG sources [83], they intrinsically produce an ultra-broadband spectrum. Even though some progress is made towards the use of a broad part of this spectrum for imaging purposes [18, 19], current techniques require a spectrally

filtered beam, enclosing flux reductions of 3-4 orders of magnitude [204].

Another central condition for imaging with single-shot configurations is the beam quality. It has been demonstrated that the optimisation of the beam wavefront leads to significantly improved resolutions [15]. Indeed, the same object placed in different positions on the same wavefront with aberrations exhibits distinct diffraction patterns [48]. Nonetheless, wavefront optimisations are not always possible, or sufficiently satisfactory, and, often, the beam has to be spatially filtered [73]. This entails extra photon reductions, working as an experimental compromise between the two demanded conditions. In the XUV and X-ray ranges, this compromise is specially emphatic due to the limited available optics. Very often, better quality focal spots require extremely high photon absorptions [205]. Reducing these absorptions or achieving tighter focusings usually implies specific lenses configurations which induce strong aberrations [28, 38].

In-line holography, as originally proposed by Gabor [103], is the simplest and most versatile realisation of the holographic method, offering both absorption and phase contrast images, while requiring no lenses between object and detector, and no sample special treatment. This technique uses the full beam diameter, not requiring a particular photon filtering in the reference wave, as for instance in Fourier Transform holography or its extended-reference variants [37, 120]. Due to this configuration, it has, however, a particular vulnerability to the quality of the beam (Fig. 4.6).

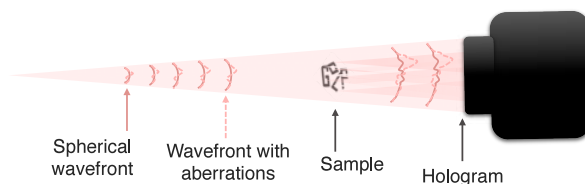


Figure 4.1: **Scheme of in-line holography with spherical waves versus waves with aberrations.**

In 2003, digital in-line holography was demonstrated using a fully coherent high-order harmonic source emitting at 32 nm [38]. The spatial resolutions achieved, however, did not go beyond 800 nm, even though setups with higher numerical apertures were tested. It was observed that, for these cases, the effect of the beam aberrations was non-negligible, originating strongly distorted holograms. Indeed, the presence of optical aberrations significantly affects the reconstructions, as usual algorithms always assume either a purely spherical, or a purely plane wave illuminating the sample [39]. Moreover, its high-numerical aperture requirements, makes it particularly dependent on tighter focusings, often requiring optics configurations with additional aberrations content. This has been limiting the application of this lensless technique to high-resolution XUV and X-ray imaging.

Recently, several methods have been proposed with the purpose of compensating the aberrations of digital holograms. Most of them are based on the computation of a phase map to be multiplied somewhere in the reconstruction process [206–209], others are based on adding extra physical components to the setup [210]. All these methods, however, present considerable drawbacks or, simply, show not to be suitable for single-shot configurations. For instance, they often require extrapolation of fitted polynomials in different areas, which can be deceiving for some objects [206], restricted object dimensions

[207, 208] or prior knowledge of the object diffraction pattern [209]. The great majority are actually designed to correct only one aberration type [211, 212]. Other physical approaches involve the use of extra optics as, for instance, deformable mirrors [210], entailing unnecessary photon absorptions.

In this Chapter, we propose and demonstrate a new approach, compatible with single-shot imaging, which uses the data collected on a wavefront sensor to correct in-line reconstructions from the aberrations of the optical system. By employing this technique one can achieve diffraction-limited reconstructions, without the need for a high-quality beam and, therefore, allowing for imaging processes using all the photons available. This method is particularly advantageous for coherent imaging in the XUV and X-rays, considering these energy-ranges often offer reduced photon fluxes. For the same reason, it can also have a crucial role in the expansion of digital in-line holography as a high-resolution single-shot imaging technique for these energy ranges, where its capability of 3D imaging from a single hologram can be of extremely high value.

This chapter is divided into five development sections. In Section 4.2 some theoretical overview is provided, introducing the concepts and formalisms of optical aberrations and *generalised pupil function*. Follows, in Section 4.3, the development of the approach for simulation and reconstruction of holograms generated from "in-line holography with waves holding aberrations". The approach proposed departs from the formalisms of in-line holography with spherical waves, in order to make use of the magnification in in-line configurations. The details for simulation of a hologram and respective object reconstruction, generated in this scheme, are then described in Section 4.4. After verifying the presence of the twin image in the reconstructions, a new approach is presented in Section 4.5, where an algorithm is proposed for simultaneous correction of in-line holograms from optical aberrations and twin image. A test with experimental data from a biological sample (phase and amplitude) illuminated by an aberration-free spherical-wave reference is also provided. Section 4.6 presents an experimental validation with an astigmatic wavefront employing a HeNe laser. The setup was assembled with a wavefront sensor, which allowed the caption of the phase map and respective Zernike coefficients in the conditions whereby the hologram was recorded. The object reconstructions are presented with respective resolution measurements.

4.2 Aberrations and Generalised Pupil Function

An optical aberration occurs when the performance of an optical system departs from paraxial optics predictions. It can be associated with different causes, ranging from a simple misalignment of the focusing optics, to inherent properties of perfectly spherical lenses. In the great majority of the cases, they arise from the simple fact that, in a real optical system, the incident angles can hardly be accounted as paraxial, what makes the paraxial theory not a completely accurate model [131]. In an image-forming optical system, the presence of aberrations leads to a blurring of the produced image.

Physically, aberrations are defined as wavefront modulations, representing path-length errors in a phase map. Assuming an effective path-length error at a point (ξ, η) , defined as $W(\xi, \eta)$, the phase

error at that point is represented by $k W(\xi, \eta)$, where $k = 2\pi/\lambda$. The complex amplitude transmittance associated with such perturbation is given by

$$\mathcal{P}(\xi, \eta) = \sqrt{I(\xi, \eta)} e^{ikW(\xi, \eta)}, \quad (4.1)$$

usually referred to as the *generalised pupil function* [131]. Often, it is more convenient to define $W(\xi, \eta)$ in units of wavelength (λ) and therefore Eq. (4.1) becomes:

$$\mathcal{P}(\xi, \eta) = \sqrt{I(\xi, \eta)} e^{i2\pi W(\xi, \eta)}. \quad (4.2)$$

The propagation of a wavefield affected by aberrations of the form $W(\xi, \eta)$, measured in a distinct plane from (ξ, η) , is equivalent to a Fresnel diffraction pattern of a point/aperture with complex transmittance $\mathcal{P}(\xi, \eta)$.

4.2.1 Main types of Aberrations

Astigmatism

Astigmatism is a very common type of optical aberration which occurs when rays, propagating in perpendicular planes, have different foci. Between the astigmatic foci, the image of a point is blurred and takes the shape of an ellipse. A tilted plate or lens, mounted in the way of a converging cone of light, induces astigmatism [213]. The creation process of the astigmatism aberration can be visualised in Fig. 4.2 (a).

Coma

Coma describes the aberration inherent to certain optical designs, or due to imperfections in the lenses or other components, which results in off-axis point sources. A plate or lens displaced from the optical axis constitute examples of systems that induce coma. The image of a point, formed by these kinds of systems, presents the shape of a comet [213]. The creation process of the coma aberration can be visualised in Fig. 4.2 (b).

Spherical aberration

Spherical aberration is another type of optical aberration, which occurs due to reflection, when some light rays strike a mirror, near its edge, in comparison with those that strike nearer the centre. It can also occur due to the increased refraction of light rays when they strike a lens. The process of creation of the spherical aberration can be visualised in Fig. 4.2 (c).

4.2.2 Zernike Polynomials

To interpret the optical output, it is convenient to express the wavefront data in a polynomial form. Zernike polynomials are often used for this purpose, being composed by terms, which are similar in

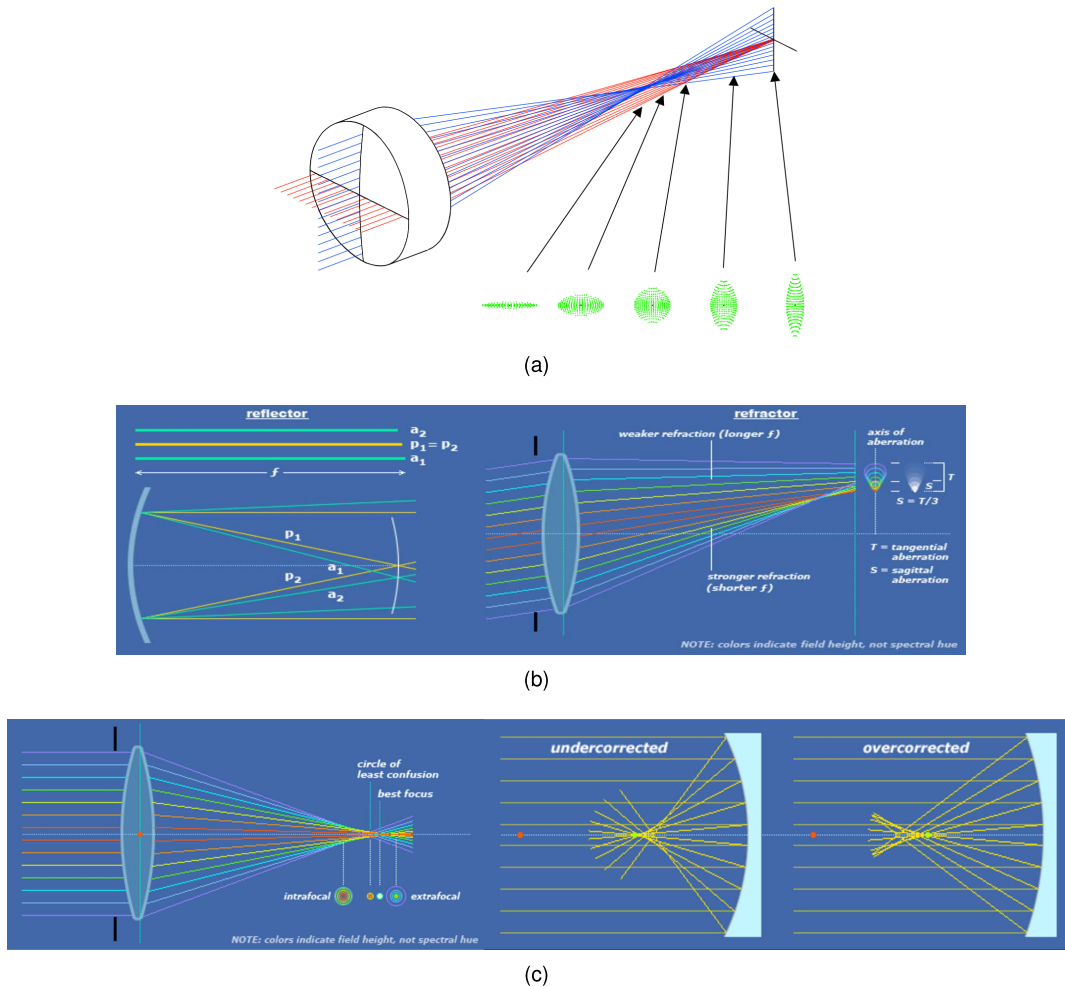


Figure 4.2: **Schematic of the main aberrations.** Schematic of the (a) astigmatism aberration [214], (b) coma aberration [215] and (c) spherical aberration [215].

form to the types of aberrations often observed in optical systems [216]. These polynomials, introduced by the Dutch scientist Fritz Zernike, in 1934, can be applied to mathematically describe 3D wavefront deviations from its *zero mean* plane. This plane is defined as a surface, for which the sum of deviations, on either side, - opposite in sign one to another - equals zero. The combined sum of the different Zernike polynomials - commonly referred to as terms - can produce a large number of complex surface shapes, capable of fitting the specific forms of aberrations. By including the sufficient polynomials, the degree of accuracy can be defined.

Zernike polynomials, by definition, describe wavefront deviations from its *zero mean*, in a pupil defined as an unit-radius circle. These deviations are represented as a function of the radial distance, ρ , and the angular circle coordinate θ , with $0 \leq \rho \leq 1$ and $0 \leq \theta \leq 2\pi$. Therefore, the wavefront profile, described by a series of Zernike wavefront modes, is given by

$$W(\rho, \theta) = \sum_{n=0}^{\infty} \sum_{m=0}^n C_n^m Z_n^m(\rho, \theta), \quad (4.3)$$

with C_n^m denoting the Zernike coefficient associated with the Zernike polynomial $Z_n^m(\rho, \theta)$. In turn,

$Z_n^m(\rho, \theta)$ is given by

$$Z_n^m(\rho, \theta) = \begin{cases} \overbrace{\sqrt{\frac{2(n+1)}{1+\delta_{m0}}}}^{\text{Normalization Factor}} \overbrace{R_n^{|m|}(\rho)}^{\text{Radial variable}} \overbrace{\cos(m\theta)}^{\text{Angular variable}} & \text{if } m \geq 0 \\ -\sqrt{2(n+1)} R_n^{|m|}(\rho) \sin(m\theta) & \text{if } m < 0. \end{cases} \quad (4.4)$$

The polynomials $R_n^m(\rho)$, $n \in \mathbb{N}$, $m \in \mathbb{Z}$, are defined such that

$$R_n^m(\rho) = \sum_{j=0}^{\frac{n-m}{2}} \frac{(-1)^j (n-j)!}{j! \left[\frac{n+m}{2} - j\right]! \left[\frac{n-m}{2} - j\right]!} \rho^{n-2j}, \quad \text{with } n \geq |m| \text{ and } n - |m| \text{ even.} \quad (4.5)$$

The wavefront modes for each Zernike polynomial are illustrated in Fig. 4.3.

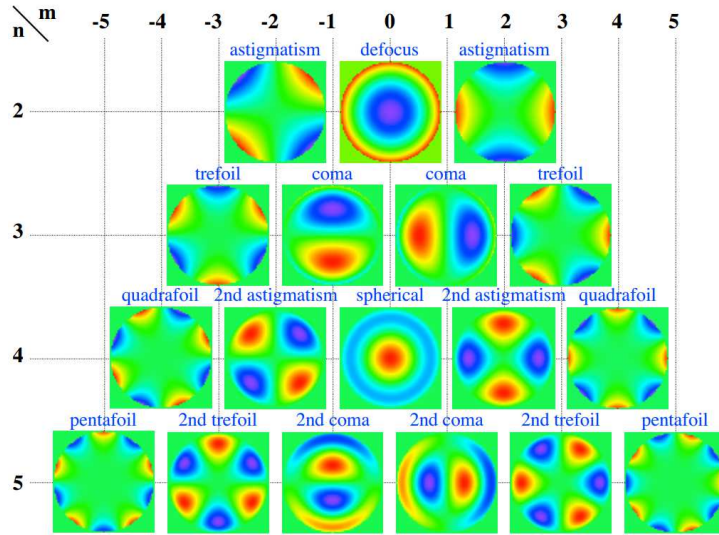


Figure 4.3: Wavefront modes associated with each Zernike polynomial [214].

The main types of aberrations, described in the previous section, can be determined by Zernike polynomials, as given in table 4.1. The normalization factors used in the table, are chosen so that its product

Z_n^m	n	m	Polynomial	Aberration Name
Z_1^1	1	1	$2\rho \cos \theta$	Tilt X
Z_1^{-1}	1	-1	$2\rho \sin \theta$	Tilt Y
Z_2^0	2	0	$\sqrt{3}(2\rho^2 - 1)$	Defocus
Z_2^2	2	2	$\sqrt{6}\rho^2 \cos 2\theta$	Astigmatism 0°
Z_2^{-2}	2	-2	$\sqrt{6}\rho^2 \sin 2\theta$	Astigmatism 45°
Z_3^1	3	1	$\sqrt{8}(3\rho^3 - 2\rho) \cos \theta$	Coma X
Z_3^{-1}	3	-1	$\sqrt{8}(3\rho^3 - 2\rho) \sin \theta$	Coma Y
Z_4^0	4	0	$\sqrt{5}(6\rho^4 - 6\rho^2 + 1)$	Spherical aberration

Table 4.1: Description of the main aberration with Zernike polynomials.

with the peak-to-valley (PtV) deviation equals the PtV-to-RMS wavefront error ratio for the aberration. This way, by multiplying this product with the expansion coefficient C_n^m - which equals the RMS error for a given aberration - yields the PtV wavefront error corresponding to the coefficient. Therefore, for any

value of the polynomial, for a given pupil coordinate ρ , the product of the normalization factor with C_n^m , yields the wavefront deviation from its *zero mean*, for that particular pupil coordinate [216].

4.2.3 Hartmann Wavefront Sensor

In a Hartmann wavefront sensor, a beam is sampled through an array of apertures and its projection captured in a 2D photon sensor - typically a CCD. This technique, as proposed by J. Hartmann in 1900 [217], allows tracking the directions of individual rays in a beam. Its basic working principle is illustrated in Fig. 4.4. First, a reference beam - usually a nearly-perfect plane or spherical wavefront - is allowed to pass through the aperture-array, called Hartmann plate. The positions of the pattern of the XUV/X-ray pulses, projected onto the detector, are then recorded and saved as reference (green dots in Fig. 4.4). When an unknown beam illuminates the Hartmann plate, the projected pattern (red dots in Fig. 4.4) deviates from this reference. By estimating the change in position for this pattern to that of a perfect wavefront, the wavefront errors can be estimated.

Thus, with this technique, every phase aberration is approximated with a set of discrete tilts, sampled in each aperture of the array. Since only tilts are measured, the Hartmann sensor cannot detect discontinuous steps in the wavefront. This type of wavefront sensor is often used in the XUV/X-rays ranges [15, 47, 218, 219] and was the one employed to measure the experimental values used in the simulations section (Section 4.4).

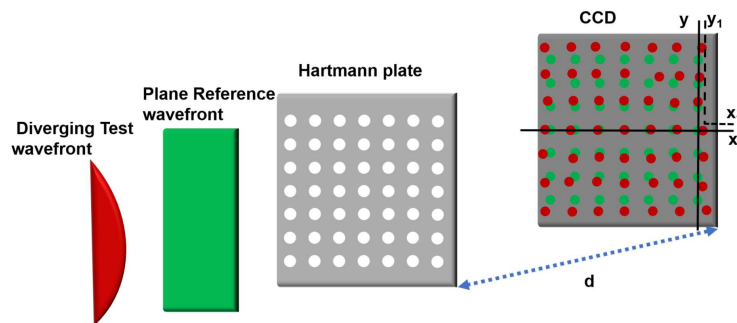


Figure 4.4: **Principle of operation of the Hartmann wavefront sensor.** To measure the wavefront-aberrations, the pattern generated by the unknown wavefront, after the Hartmann plate, on the CCD (red dots) is analysed with relation to a reference wavefront (green dots). Image from [220].

4.2.4 Quadriwave Lateral Shearing Interferometry Wavefront Sensor

In a quadriwave lateral shearing interferometry wavefront sensor, the incident light is diffracted by a complex amplitude diffraction grating, called a modified Hartmann Mask, which results in its replication into 4 beamlets. These replicas interfere on a CCD detector. The interferogram recorded is deformed by the wavefront gradients, which are recovered by Fourier analysis [221].

Due to the fact that the recorded interferogram is mostly sinusoidal, a small number of pixels is needed to recover a phase pixel. This leads to an increased resolution (at least by a factor 4), compared to all other gradient-recovery-based wavefront sensors, such as the Shack-Hartmann wavefront sensor

(similar to the Hartmann wavefront sensor, but with an array of lenses instead of an array of apertures) [222]. This type of wavefront sensor is used in the experimental validation presented in Section 4.6.

4.3 In-line holography with waves with aberrations

The first holographic setup proposed by Gabor in 1948 used a plane wave as the reference wave [103]. In this case, the sampling is limited by the detector pixel size as seen in Section 2.4.2, which is not satisfying for nano-scale imaging in the XUV and X-ray ranges. Digital in-line holographic microscopy (DIHM), which uses spherical waves as reference waves was developed as a new tool, yielding 3D images of objects with higher resolution [38, 156]. Because it induces a magnification, M , the sampling and achievable resolution are reduced by $1/M$ (see Sections 2.4.2 and 2.5.1.2).

In order to account with the best implementation for XUV and X-rays, the treatment described below is given for in-line holography with spherical waves. It can be easily transposed to in-line holography with plane waves ($Z \ll z_0$) by replacing $M = 1$, $z_{eff} = Z$ and including in the phase map definition any coefficient of defocus, C_2^0 , extracted from the wavefront sensor. Here, to make use of the magnification M , we define the aberrated wavefront discarding this coefficient and perform the simulation and reconstructions based on Section 2.4.1.2, accounting with a spherical-wave reference.

Assuming the same coordinates system as given in Section 2.4.1.2, a spherical wave propagated from a point source to an object, both separated in the optical axis by a distance z_0 , is given by Eq. (2.68). Considering now that, besides its divergent character, the beam is affected by optical aberrations, one can include a phase contribution in the form of Eq. (4.2). The spatially transmitted field in an object-plane with transmission function $t(x, y)$, illuminated by this wavefield then yields

$$\mathcal{P}(x, y) = \sqrt{I(x, y)} e^{i2\pi W(x, y)} \cdot \frac{e^{ikr_1(x, y)}}{r_1(x, y)} \cdot t(x, y), \quad (4.6)$$

with \cdot denoting multiplication.

The propagation of this pupil function at $z = 0$ towards a detector in $z = Z$ can be described by the Fresnel approximation of the Rayleigh-Sommerfield diffraction formula (Eq. (2.14)) [131]. Therefore, the field distribution in the plane of the detector $U_h(X, Y)$, assuming a distance Z from the object becomes

$$\begin{aligned} U_h(X, Y) &= \frac{e^{ikZ}}{i\lambda Z} \int_{-\infty}^{\infty} \int_{-\infty}^{\infty} \left[\sqrt{I(x, y)} e^{i2\pi W(x, y)} \cdot \frac{e^{ikr_1(x, y)}}{r_1(x, y)} \cdot t(x, y) \right] e^{i\frac{k}{2Z}[(X-x)^2 + (Y-y)^2]} dx dy \\ &\propto \int_{-\infty}^{\infty} \int_{-\infty}^{\infty} \left[\sqrt{I(x, y)} e^{i2\pi W(x, y)} \cdot t(x, y) \right] e^{i\frac{k}{2z_{eff}}[(\frac{X}{M}-x)^2 + (\frac{Y}{M}-y)^2]} dx dy. \end{aligned} \quad (4.7)$$

with M and z_{eff} given by Eqs. (2.72) and (2.73). Note that the last expression was obtained similarly to Eq. (2.71).

Eq. (4.7), similarly to the spherical-wave case can be written in the form of a convolution between the term $\sqrt{I(x, y)} e^{i2\pi W(x, y)} \cdot t(x, y)$, here denoted $U_o(x, y)$, and the Fresnel function $s(x, y)$ for

a spherical-reference wave, given by Eq. (2.74). One can separate this term into the object and reference contributions, considering the definition of the transmission function in the plane of the object as $t(x, y) = 1 + t_o(x, y)$ (Eq. (2.55)). We then obtain for a wave with aberrations, $U_o(x, y) = r(x, y) + o(x, y)$ with:

$$r(x, y) = \sqrt{I(x, y)} e^{i2\pi W(x, y)}, \quad (4.8)$$

and

$$o(x, y) = t_o(x, y) \cdot \sqrt{I(x, y)} e^{i2\pi W(x, y)}, \quad (4.9)$$

which allow us to define $U_{inc}(x, y)$ as

$$U_{inc}(x, y) = \sqrt{I(x, y)} e^{i2\pi W(x, y)} \quad (4.10)$$

from Eq. (2.56).

One can then write Eq. (4.7) in the form:

$$\begin{aligned} U_h(X, Y) &= [r(x, y) + o(x, y)] \otimes s(x, y) \\ &= \underbrace{r(x, y) \otimes s(x, y)}_{R(X, Y)} + \underbrace{o(x, y) \otimes s(x, y)}_{O(X, Y)}, \end{aligned} \quad (4.11)$$

with $R(X, Y)$ and $O(X, Y)$ denoting, again, the reference and object contributions to this field. Being two convolutions, $R(X, Y)$ and $O(X, Y)$ can be expressed in terms of Fourier transformations so that $U_h(X, Y)$ becomes

$$\begin{aligned} U_h(X, Y) &= \mathcal{F}^{-1} \{ \mathcal{F} \{ r(x, y) \} (u, v) \cdot S(u, v) \} (X, Y) + \mathcal{F}^{-1} \{ \mathcal{F} \{ o(x, y) \} (u, v) \cdot S(u, v) \} (X, Y) \\ &\equiv R(X, Y) + O(X, Y). \end{aligned} \quad (4.12)$$

In Eq. 4.12 the function $S(u, v)$ corresponds to the Fourier transform of the Fresnel function $s(x, y)$ of Eq. (2.74), which can be analytically solved yielding

$$S(u, v) = e^{-i\pi\lambda z_{eff}(u^2+v^2)}, \quad (4.13)$$

with (u, v) the spatial frequency coordinates in the Fourier plane.

The hologram recorded with waves with aberrations is, therefore, computed by the squared magnitude of Eq. (4.12) and its size corresponds to the size of the object area, multiplied by the magnification factor M .

The reconstruction of the object transmission function is given by Eq. (2.60), which can also be expressed in the form of a convolution by

$$\begin{aligned}
U_r(x, y) &= R(X, Y)H_0(X, Y) \otimes s^*(X, Y) \\
&= \mathcal{F}^{-1} \{ \mathcal{F} \{ R(X, Y)H_0(X, Y) \} (u, v) \cdot S^*(u, v) \} (x, y).
\end{aligned} \tag{4.14}$$

where $S^*(u, v)$ is the conjugate Fresnel function:

$$S^*(u, v) = e^{i\pi\lambda z_{eff}(u^2+v^2)}. \tag{4.15}$$

Note that, if no multiplication with the digital reference $R(X, Y)$ is performed, before the back-propagation process, the reconstruction follows the typical reconstruction procedure for in-line holography with spherical waves. In such case, the actual reconstruction retrieved includes amplitude and phase modulations given by the aberrations of the incident wavefront.

4.4 Simulation

The numerical implementation described below follows the model described in the previous section. The algorithm was tested for plane and spherical waves and as well for the individual aberrations, using different Zernike coefficients. Additional simulation results, without magnification, can be found in [223].

4.4.1 Transmittance of the Object-Plane

The sample used in the simulation was a totally opaque "3" (0 transmission function) drawn in a uniform background with 1-transmission function, as illustrated in Fig. 4.5. The object-plane was defined with a pixel size of $\Delta_{obj} = 0.2 \mu\text{m}$, so that the object represents a two-dimensional "3" with $14.8\text{-}\mu\text{m}$ height (see Fig. 4.5). These measurements correspond to image dimensions of 74 and 15 pixels, respectively.

The simulated plane was defined with a total of 3050×3050 pixels, corresponding to a FOV of $610 \times 610 \mu\text{m}$. Fig. 4.5 represents a zoom in the object area. The extended FOV ensures that the subsequent calculated planes (diffracted field and the reconstruction) are inside the window dimensions, avoiding numerical errors arising from backscattering phenomena on the window limits.

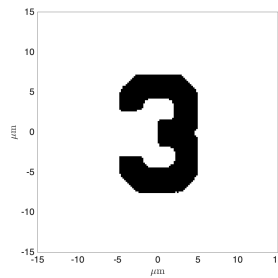


Figure 4.5: **Transmission function $t(x, y)$ used in the simulation.** The object consists of a pure amplitude "3" shape.

After a correct sample definition, the value 1 was subtracted to the sample's transmittance, in order to work with the object perturbation $t_o(x, y)$ separately from the reference contribution (see equation 2.55). This separation of contributions is helpful for a simulation with less numerical errors, allowing, if needed, for a separation of the amplitude and phase of the reference wave at the detector. Moreover, for the calibration of the code with plane wavefronts with no aperture definition, it was critical. By propagating directly the field transmission function $t(x, y)$, as defined in Fig. 4.5 - as a matrix of ones around the object -, we are incorporating an extra-object, with the finite dimensions of our matrix. As a consequence, our hologram is affected by non-real diffraction contributions through a square aperture. Thus, if the reference wave at the detector is known, by employing the linearity of the Fourier transformation, one can define t_o as the complex function describing the presence of the object and add the known reference wave after the propagation steps, plotted correctly in all the FOV considered (Eq. (4.11)).

4.4.2 Phase-Map Definition

The wavefront profile at the sample position was defined with the experimental Zernike coefficients presented in Fig. 4.6. These coefficients were measured with a Hartmann wavefront sensor from an XUV HHG-based source focused by a Kirkpatrick-Baez (KB) optics system (see Fig. 4.6 (a)). Details on the setup and experiment can be found in [223]. The KB system was composed of two fused silica spherical mirrors mounted perpendicularly to each other, at grazing angles between 10° and 15° . The focal lengths used were $f_1 = 1$ m and $f_2 = 0.5$ m (Fig. 4.6 (a)).

The wavefront profile at the sample position was defined with the Zernike coefficients from Fig. 4.6 (b). The point spread function associated with such XUV beam is shown in Fig. 4.6 (c) for reference. The phase plane, with cartesian coordinates (x, y) , was defined as a 3050×3050 matrix, with pixel size $0.2 \mu\text{m}$, so that it would correspond to the FOV used for the sample. As explained in Section 4.2.2, the function $W(x, y)$, describing the deviations from the wavefront *zero mean*, was defined in an unit-radius circle, in order to be determined by a linear combination of Zernike polynomials (Eq. (4.3)).

$W(\rho, \theta)$ was defined within a circular aperture of radius $200 \mu\text{m}$, centred in the sample. For the phase definition in an unit-radius circle, a new coordinate system was adopted. (x_1, y_1) were defined to represent discrete coordinates, derived from (x, y) , centred in the circular aperture, and chosen so that, inside it, they could be defined as regular increments in the $[-1, 1]$ interval. The Zernike polynomials were then represented as a function of the radial distance, $\rho^2 = x_1^2 + y_1^2$, and the angular circle coordinate $\theta = \arctg\left(\frac{y_1}{x_1}\right)$, with $0 \leq \rho \leq 1$ and $0 \leq \theta \leq 2\pi$. The polynomials were plotted in this aperture according to Table 4.1 and with the coefficients from Fig. 4.6 (b). The phase deviations outside this aperture were considered zero.

Having defined the wavefront profile, described by a series of Zernike wavefront modes (Fig. 4.6 (d)), the incident field at the object was defined by Eq. (4.10) with $W(x, y) = W(\rho(x, y), \theta(x, y))$ and the field amplitude, $\sqrt{I(\xi, \eta)}$, given by a simple matrix of 1s.

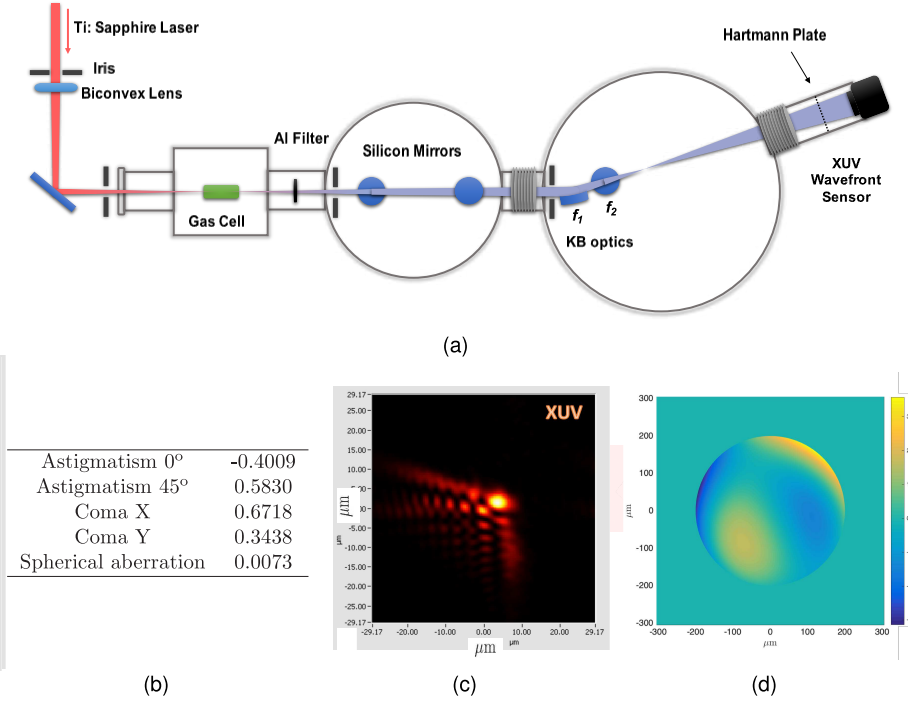


Figure 4.6: **Setup and phase map, with respective Zernike coefficients, obtained experimentally from the measurement of an XUV-HHG source with a Hartmann wavefront sensor.** (a) Setup and XUV beam ($\lambda = 32$ nm) focused by a Kirkpatrick-Baez optics system. The data were obtained in *Laboratoire d'Optique Appliquée* (LOA), employing a high-harmonic generation source set up by the focusing of a *Ti:Sapphire* laser in a gas cell filled up with argon [223]. (b) Zernike coefficients of the main aberrations, in RMS (root mean square) values, obtained from the analysis of the XUV wavefront with the Hartmann wavefront sensor, after focusing with the KB system. (c) Point spread function of the XUV beam measured at the wavefront sensor. (d) Computed phase map with the Zernike coefficients from (b).

4.4.3 Hologram simulation

The simulation followed the reasoning presented in Section 4.3, which is schematized in Fig. 4.7.

Having clarified in Section 4.4.1 the advantage of the separation of reference and object waves, the computed fields were defined as a sum of both contributions. The hologram, $H(X, Y)$, was then computed from $r(x, y)$ and $o(x, y)$, given by Eqs. (4.8) and (4.9) with $t_o(x, y)$ and U_{inc} defined according to Sections 4.4.1 and 4.4.2.

We remark that $S(u, v)$, in Fig. 4.7 (given by Eq. (4.13)) is defined in the Fourier domain. This way, the plane with spatial frequency coordinates u and v , where it is defined, has a pixel size inversely proportional to the sample's pixel size Δ_{obj} (see Eq. (2.5)):

$$\Delta_{\mathcal{F}} = \frac{M}{N\Delta_{obj}}. \quad (4.16)$$

In an illumination with magnification, it includes the factor M [158].

From Fig. 4.7, one can also see that to retrieve the digital reference wave at the detector, $R(X, Y)$, the reference contribution, $r(x, y)$, was propagated from the object position until the plane of the detector.

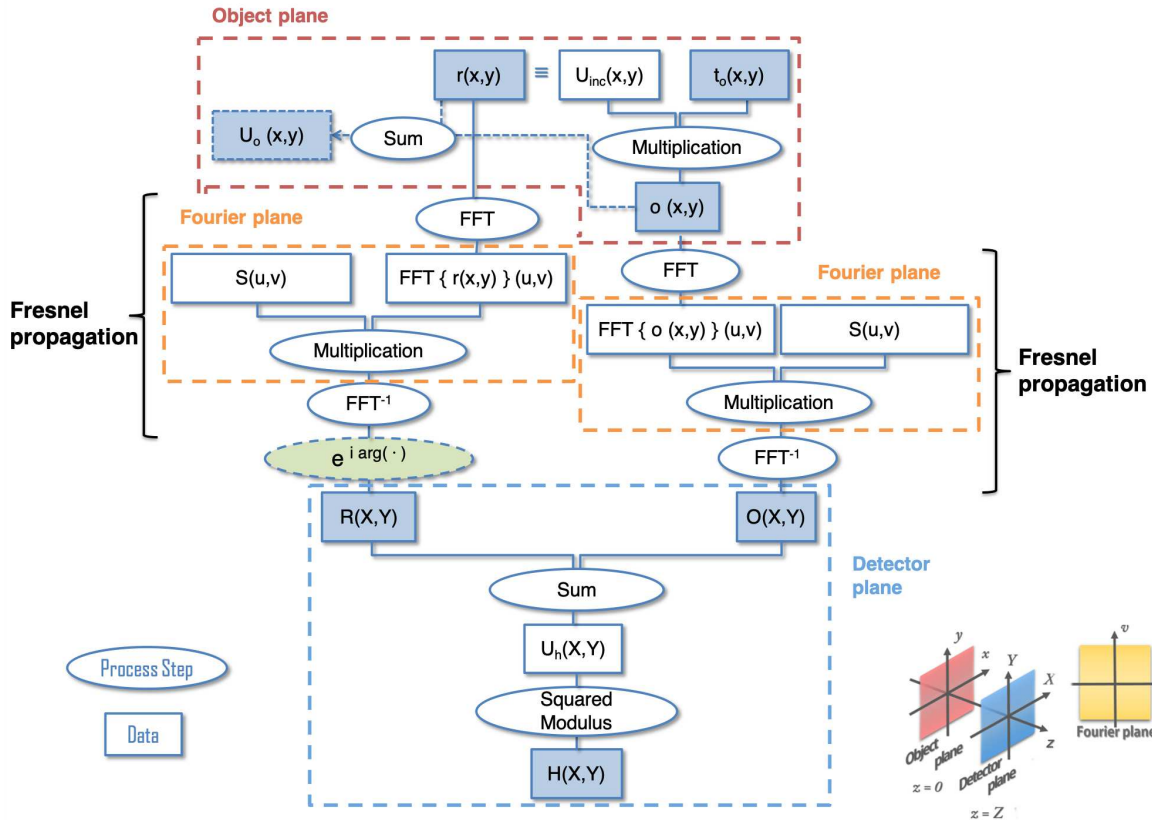


Figure 4.7: **Hologram simulation scheme for in-line holography with waves with aberrations.** Schematic of the Fresnel propagation processes applied to the object wave and reference phase map, from the object to the detector. At the bottom right, one can visualise the different propagation planes with respective coordinates system. For in-line holography with plane and spherical waves, all the left branch is nonexistent and the reconstructions follow $R(X, Y) = 1$.

In this process, one can choose to keep a uniform amplitude in the propagated reference wave and work just with the propagated phase. For the purpose, we can add the step in green in Fig. 4.7 and use only the propagated argument of the complex field as the new phase map. This was not used in the simulation results presented in this manuscript, however, it was seen to be useful to avoid numerical amplitude errors by simulating other setups.

As a last remark, we recall that the hologram generated from Fig. 4.7 has also a magnification given by M .

4.4.4 Object Reconstruction

The process used for the reconstructions is described in Fig. 4.8. It follows Section 4.3 and is based on the formalisms presented in Section 2.4.1.2.

Before reconstruction, the hologram was normalised, in order to remove the dependence on external factors. This was accomplished by dividing the hologram into the background image, defined by $B(X, Y) = |R(X, Y)|^2$, and subtracting the value 1, as explained in Eq. (2.59). After multiplication with the digital reference $R(X, Y)$, this field was then back-propagated until a distance z_{eff} , according to

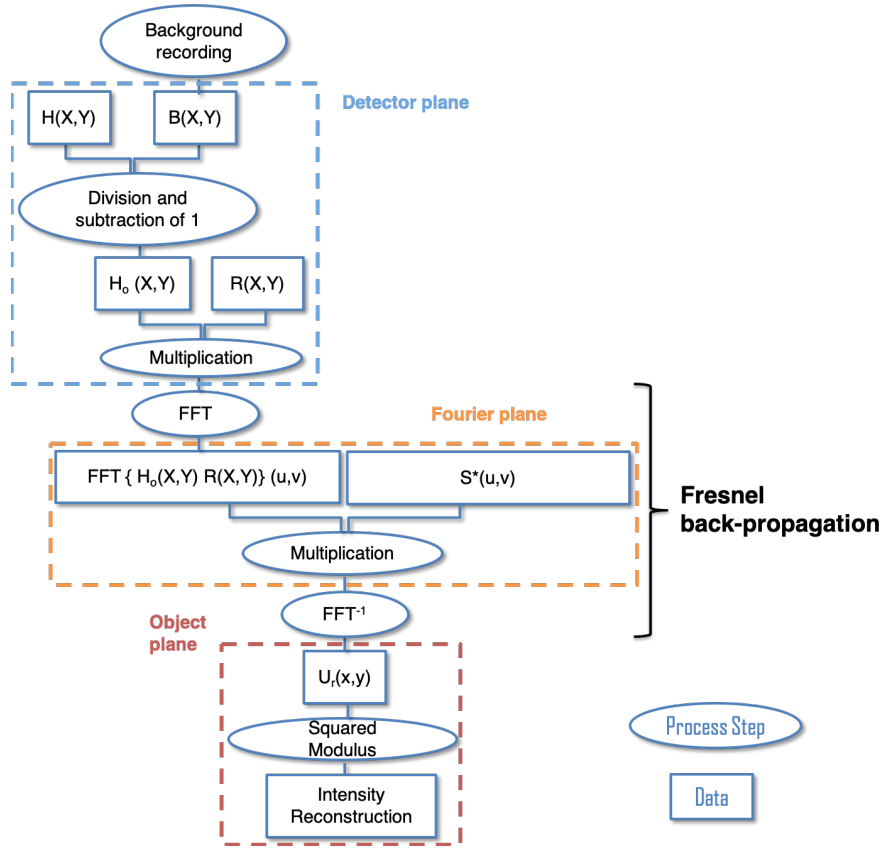


Figure 4.8: **Schematic of the reconstruction process.**

Fresnel (Eq. (4.14)). The reconstructed intensity at the object is then computed by taking the squared modulus of the reconstructed field at the object plane. Note that the reconstruction without correction of aberrations is achieved the same way, but without multiplication of the digital reference wave $R(X, Y)$, which is assumed to have a value 1.

4.4.5 Results and Discussion

The holograms simulated by the described process and respective reconstructions without and with aberrations correction are shown in Fig. 4.9. Each line corresponds to datasets extracted for different sample-detector distances, with values $Z = 4$ mm, 6 mm and 10 mm, respectively. The sample-point source distance was assumed $z_0 = 10$ mm.

The real space reconstructions with and without correction of the aberrations of the beam are presented in the central and right rows of Fig. 4.9. The images constitute the intensity reconstructions $|t_o(x, y)|^2$.

Observing the results, one can see a clear improvement of the reconstructions including the reference wave information, when compared to a standard reconstruction procedure (right-side images vs central images in Fig. 4.9). One can also see that the experimental phase map of the KB system analysis, which was employed for the simulation, induces strong aberration-effects on the reconstructions. Indeed, larger Z distances could not be reached as the reconstructions were too deteriorated when

employing the standard reconstruction method, without accounting with the aberrations. We would also like to point out that the phase-map was computed in a considerably large pupil when compared to the sample size (see Fig. 4.6 (d)), which also attenuated the general effects of the aberrations otherwise too strong to be able to obtain reconstructions without aberrations-correction.

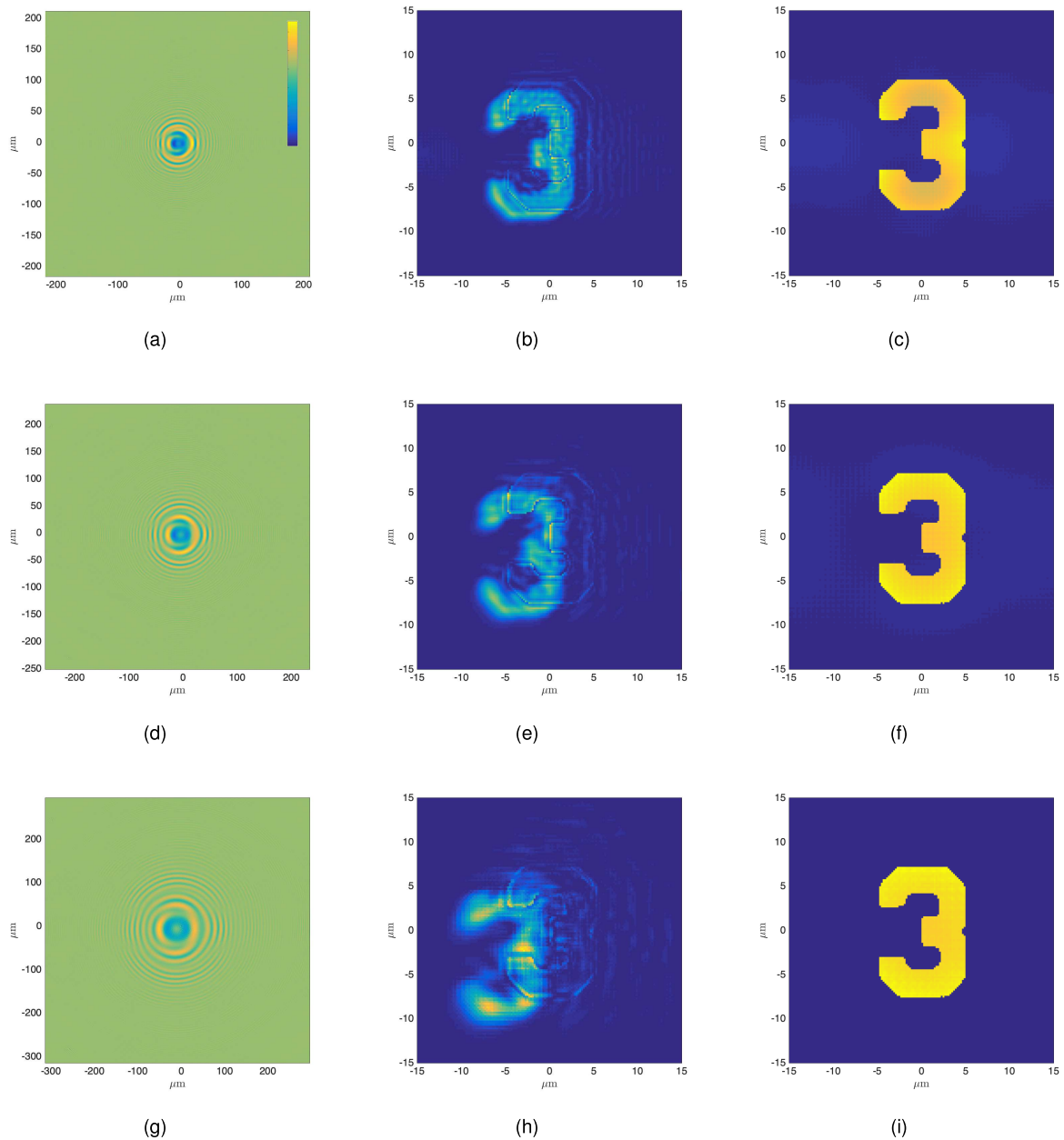


Figure 4.9: **Simulation results for in-line holography with waves with aberrations, using a phase map with Zernike coefficients measured experimentally from an XUV beam focused with KB optics.** (a)-(d)-(g) Normalised holograms achieved for sample-detector distances with values $Z = 4$ mm, 6 mm and 10 mm, respectively. (b)-(e)-(h) Reconstructions achieved from the respective left-hand holograms, assuming no aberrations on the reference beam. (c)-(f)-(i) The same reconstructions performed with aberrations correction, i.e., by including the aberrations phase-map in the propagation. The colour scale bar from (a) denotes arbitrary units and is common to all images.

Observing the reconstructions from Figs. 4.9 (c)-(f)-(i), one can identify some smooth magnitude

modulations, not included in the object's transmittance, which get stronger with the decrease of Z . These modulations are even more evidenced in the reconstructions from Figs. 4.9 (b)-(e)-(h) (due to the smaller contrast of the reconstructions), even though no comparison is possible with the object transmittance. Their cause can be attributed to the twin image problem, which occurs in the in-line configuration, due to symmetry reasons. Indeed, the reconstructions of in-line holograms suffer from the superposition of the hologram of a twin image of the object, with similar information content, but located at a distance $z = -2z_0$ from it. A compensation of this twin image problem will be addressed in the next Section.

4.5 In-line Holography with Correction of Aberrations and Twin Image

The existence of a twin image is a standard problem in in-line holography, which limits the information obtainable from a holographic record. Indeed, arising from the Hermitian symmetry of the complex field, there are always two images appearing in a hologram and affecting the reconstruction. The two images present mirror-symmetry with respect to the point source and thus, the twin image appears as an out of focus image in the reconstructed object-plane (see Fig. 4.10).

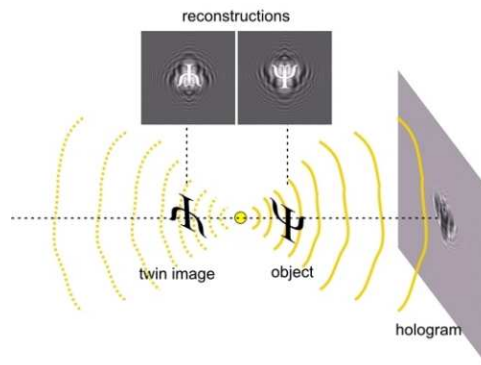


Figure 4.10: **Object with respective twin image [224].**

In visible light holography, the object and its twin image can be separated by using parallel beams and subtracting a second hologram from the reconstructed image [103, 225, 226]; by employing off-axis approaches with a beam splitter [227]; or introducing additional lenses into the recording and reconstruction schemes [228]. However, such approaches are not available for XUV and X-rays. Another widely employed approach to address the twin image problem is to record a set of holograms at different wavelengths [229, 230]. However, this method is experimentally difficult to implement, and particularly unsuited for fragile biological samples subject to radiation damage. Other numerical methods to reduce the effect of the twin image are restricted to holograms of purely absorbing objects [231–233] and later ones are based on iterative methods for phase retrieval [224, 234–236]. For the implementation of twin image correction presented in this Section, we base our approach in the iterative method developed by T. Latychevskaia and H.-W. Fink [224]. This method eliminates the twin image by numerical reconstruc-

tion of the phase of the hologram, without using assumptions or imposing any restrictions on the object to be imaged.

The aim is to reconstruct the distribution of the complex sum $U_h(X, Y) = R(X, Y) + O(X, Y)$. This is achieved by an iterative procedure consisting of the back and forth propagation between the detector and object-planes until all artefacts due to the twin image are removed. The procedure followed is described in Fig. 4.11 and includes the steps:

1. Creation of the input complex field as $R(X, Y) + O(X, Y) = |R(X, Y) + O(X, Y)|e^{i\Phi(X, Y)}$ where the amplitude is always given by the square root of the normalised hologram $|R(X, Y) + O(X, Y)| = \sqrt{H(X, Y)/B(X, Y)}$, and the phase $\Phi(X, Y)$ is initially set to $2\pi W_p(X, Y)$ - the phase of the known reference wave at the detector $R(X, Y)$. This phase evolves towards its true value during the iteration process.
2. Back-propagation to the object-plane, according to Fresnel diffraction formula applied to a distance z_{eff} .
3. The reconstructed complex field multiplied with the conjugated back-propagated incident wave $e^{-i2\pi W_{obj}(x, y)}$ and subtracted from its numerical amplitude, with the addition of the value 1, gives the complex transmission function in the object-plane $1 + t_o(x, y)$. The obtained complex transmission function describes the object's absorption and phase shift given by the relation:

$$1 + t_o(x, y) = (1 - a(x, y))e^{-i\varphi_{obj}(x, y)}, \quad (4.17)$$

where $a(x, y)$ describes the absorbing properties of the object and $\varphi_{obj}(x, y)$ the phase shift induced by the object to the incident wave [224]. This way, due to the presence of the reference wave, the absorption $a(x, y)$ and phase $\varphi_{obj}(x, y)$ of the object can be extracted. Here, the following constraints can be applied:

- If the object is perfectly opaque, then it is possible to discard the phase term to accelerate the convergence. This yields $1 + t_o(x, y) = (1 - a(x, y))$.
- $a(x, y) \geq 0$, which describes the basic physical notion of energy conservation, stating that, after a scattering process, absorption can not result in an increased amplitude. Thus, whenever negative values of $a(x, y)$ emerge, they arise from the interference between the twin image and the reference wave and are subsequently replaced by zero-absorption values, while the phase values remain unaltered. Based on this constraint of positive absorption values, we can derive a re-combined absorption and phase distribution for the object, creating a new transmission function in the form:

$$1 + t'_o(x, y) = (1 - a'(x, y))e^{-i\varphi_{obj}(x, y)}. \quad (4.18)$$

4. Next, without the reference wave with aberrations, we propagate the new transmission function $1 + t'_o(x, y)$, according to Fresnel, until the detector plane. We then recover the phase value from

this new complex field and use it as the input phase value for the next iteration, starting at step 1. We note that the first iteration already reconstructs the complex object with similar quality as the reconstruction routine described in Sections 4.3 and 4.4.4 and used for the simulation. Further iterations eventually lead to the elimination of the twin-image term.

The routine created imposes no limitations on the object properties or its surrounding. Moreover, it can be applied for in-line holography with waves with and without aberrations by proper definition of the reference wave.

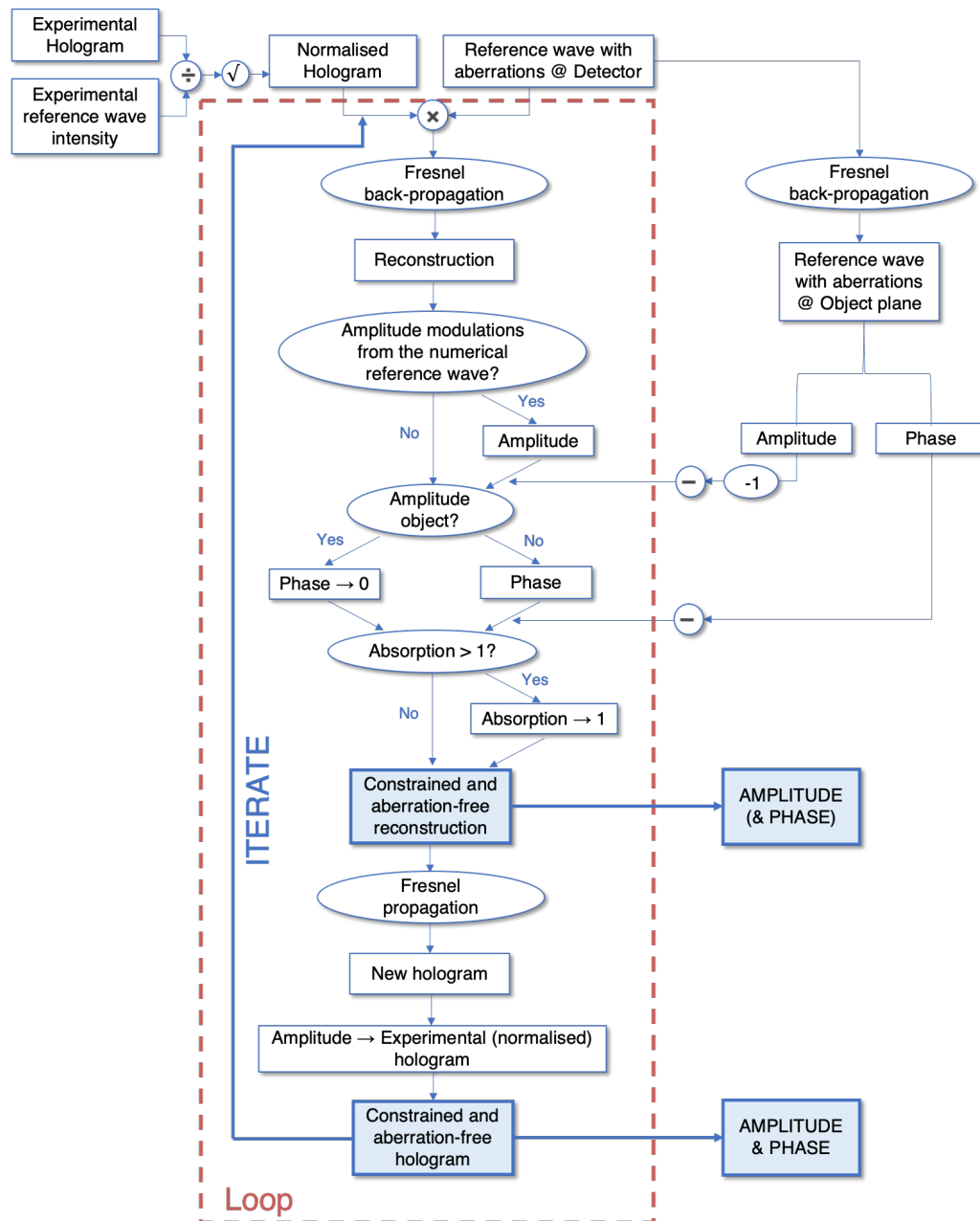


Figure 4.11: Schematic of the reconstruction process of in-line holography with correction of aberrations and twin image.

4.5.1 Experimental Test with a Phase Sample illuminated by an Aberration-free Spherical Wave Reference

The algorithm was tested first using data from in-line holography using waves without aberrations. The data were obtained at the NanoXim setup of CEA Saclay, employing a source of 405-nm wavelength [237]. The sample consisted of a zebrafish embryo, which was positioned at $|z_0| = 4.8$ mm from a 1- μm pinhole, aligned at the focus of a 3-mm focal-distance lens. The hologram was captured by a CCD detector, with 5.4- μm pixel size, positioned at $Z \sim 31.2$ mm from the sample (note that the sample has non-negligible thickness). Under these parameters, the magnification reached was $M = 7.5$, with $z_{eff} = 4.16$ mm. The hologram and respective background images can be observed in Fig. 4.12. They were provided by R. Corman [237] to the author, which in turn provided the algorithm for the data analysis of the system.

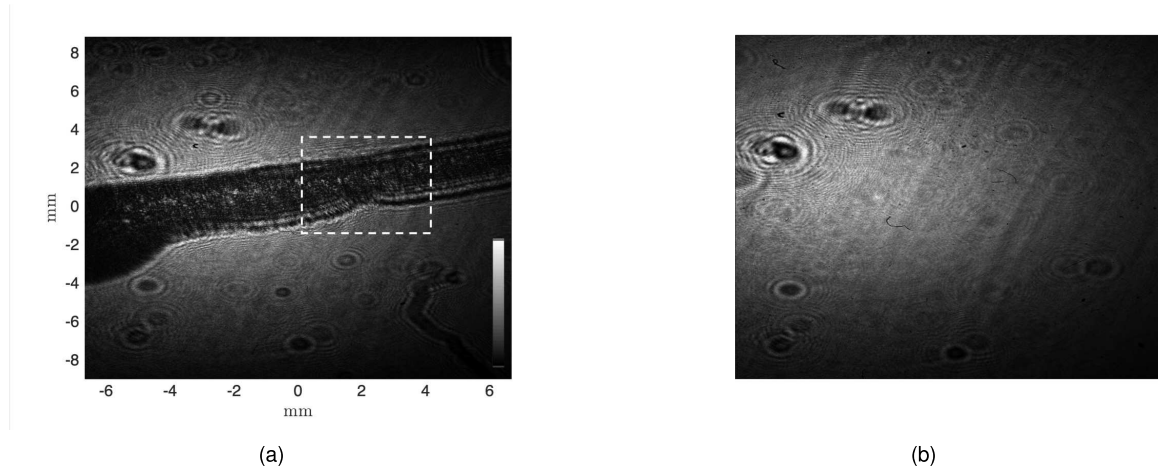


Figure 4.12: **In-line hologram of a zebrafish embryo and corresponding background image.** (a) Experimental hologram. The highlighted region shows the area where the reconstructions are presented zoomed in, in order to allow a better visualisation of the sample details. (b) Experimental background image. The colour scale presented in (a) is arbitrary and common to both images.

The reconstructions from Figs. 4.13 were obtained from the hologram and background image of Fig. 4.12. In the figure, one can see the amplitude and phase reconstructions obtained after 1, 5 and 20 iterations of the reconstruction code (Figs. 4.13 (a)-(b), (c)-(d) and (e)-(f), respectively). With the increase of the number of iterations, one can note a clear improvement of the reconstructions, cleaned from the twin image, with better visualisation of the sample details. One can also see these details changing as a scan in the reconstruction plane is made. In Fig. 4.14 (b) the reconstruction was achieved for a plane separated 100 μm from the one reconstructed in Fig. 4.14 (a), which is the same image of that of Fig. 4.13 (e). The new reconstruction parameters were then: $z_0 = -4.7$ mm, $Z = 31.3$ mm, which led to $M = 7.660$ and $z_{eff} = 4.086$ mm. Comparing both depth planes one can note that the sample's cross-section decreases slightly in size, from the first to the second image, and that different depth-structures are reconstructed. Some of these are highlighted with white arrows in the images. These results show good compatibility of the routine with 3D imaging using back-propagation functions

in free space and were crucial to set a trustworthy base, which allowed the increase of complexity for an implementation with aberrations correction.

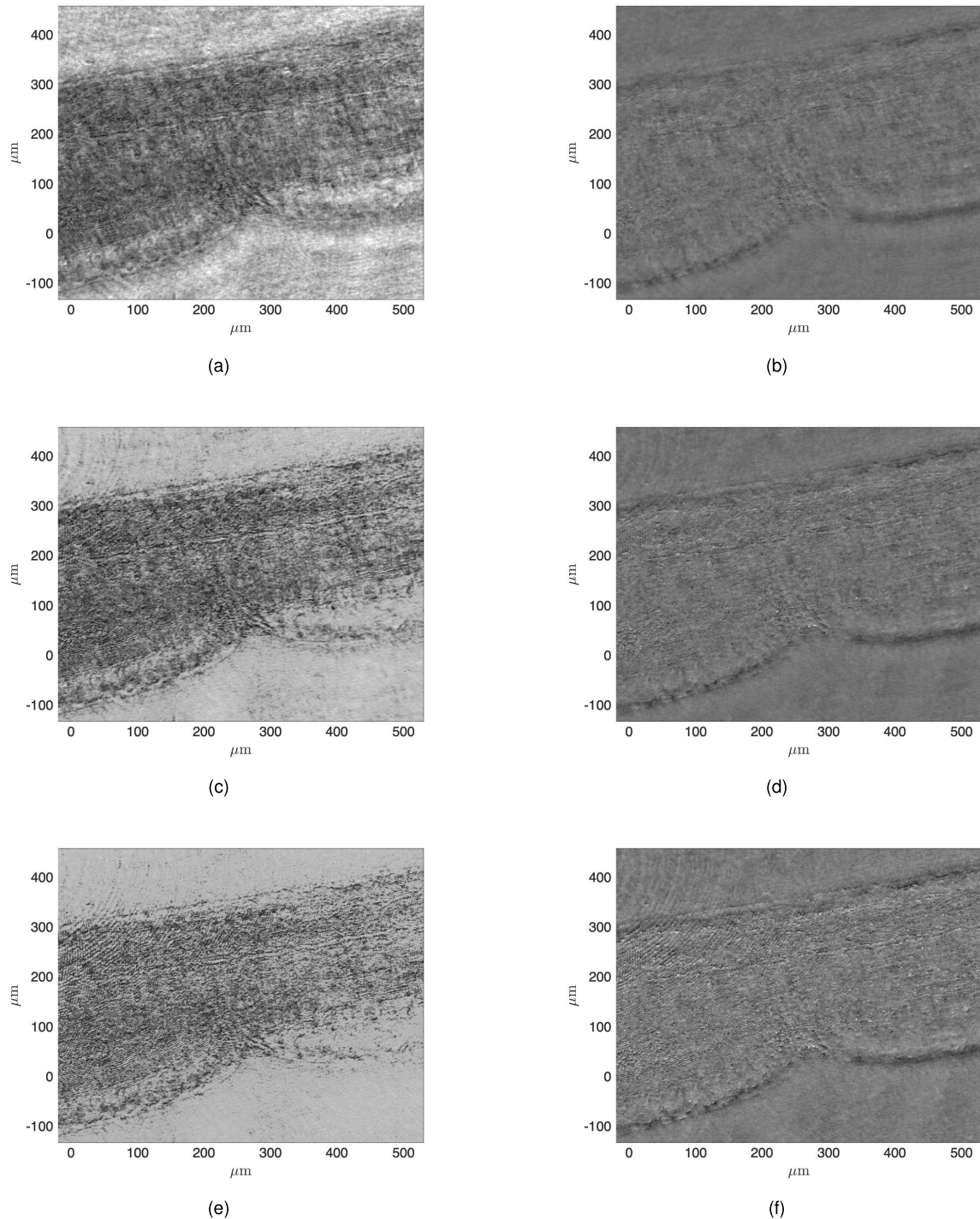


Figure 4.13: **Amplitude and phase reconstructions for 1, 5 and 20 iterations of the reconstruction algorithm.** (a) Amplitude and (b) phase reconstructions for iteration 1 of the twin-image correction algorithm. (c)-(d) The same as (a)-(b), but after 5 iterations. (e)-(f) Amplitude and phase reconstructions after 20 iteration of the twin-image correction algorithm.

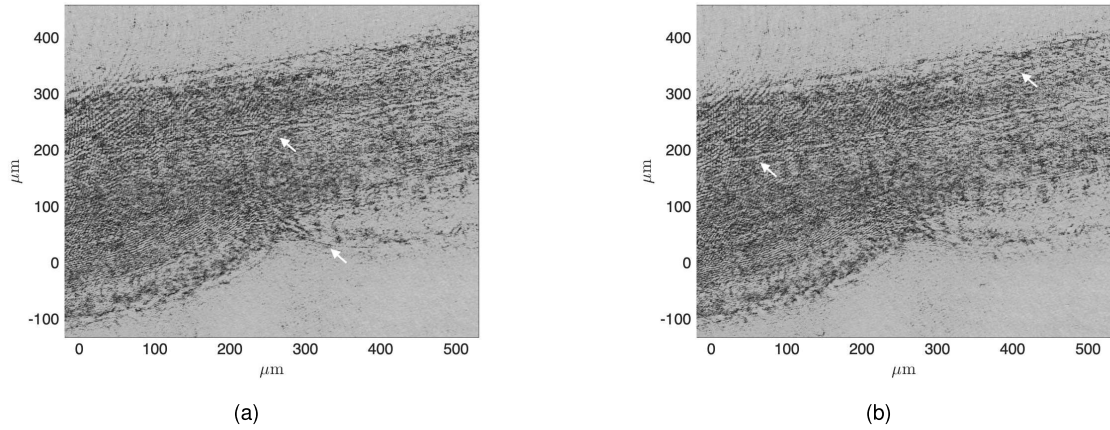


Figure 4.14: **Amplitude reconstructions for different depth planes of the sample, separated from $100 \mu\text{m}$.** (a) Reconstruction of the cross-section of the sample obtained with the parameters $z_0 = -4.8$ mm and $Z = 31.2$ mm. (b) Reconstruction obtained with the parameters $z_0 = -4.7$ mm, $Z = 31.3$ mm. Different reconstructed structures are highlighted with white arrows, for easier perception.

4.6 Experimental Validation with a HeNe laser

To implement the routine for correction of aberrations and twin image, an experimental test was performed in the visible range. The experiment was carried out at GoLP/Instituto de Plasmas e Fusão Nuclear installations of Instituto Superior Técnico (IST), Lisbon, Portugal. The setup, procedure and results are presented throughout this section.

4.6.1 Experimental Setup and Experimental Data

The setup employed a HeNe (helium–neon) laser, $\lambda_{\text{HeNe}} = 632.8$ nm and can be found in Fig. 4.15 (a). After magnifying the beam with a telescope (combination of two plano-convex lenses with a pinhole in between - magnification with a factor 3), the beam was focused with a 20 cm focal-length lens to create the Gabor configuration for in-line holography. A plano-concave cylindrical lens (focal length $f = -100$ cm) was placed before the focal-spot position to create an astigmatic beam. The hologram was captured by a 640×480 -pixels CCD, with $6 \mu\text{m}$ pixel size, positioned at $Z = 2.6 \pm 0.1$ cm from the sample. The intermediate focal-spot position of the astigmatic beam was estimated at $z_0 \sim -4.7$ cm, yielding a magnification $M = 1.56$ and $z_{\text{eff}} = 1.68$ cm. The sample consists of a ThorLabs Resolution test target, with a positive pattern. The illustration of the sample and respective hologram can be observed in Figs. 4.15 (b) and (c), respectively.

After the recording process, the sample and CCD were removed, and the beam was analysed by a PHASICS SID4 wavefront sensor. This device was fixed at $z_{\text{wfs}} = 6.2 \pm 0.1$ cm from the position of the sample. The Zernike coefficients measured are presented in Table 4.2. They were extracted from a circular aperture of diameter $2871 \mu\text{m}$, capturing the $1/e^2$ width of the beam at the sensor.

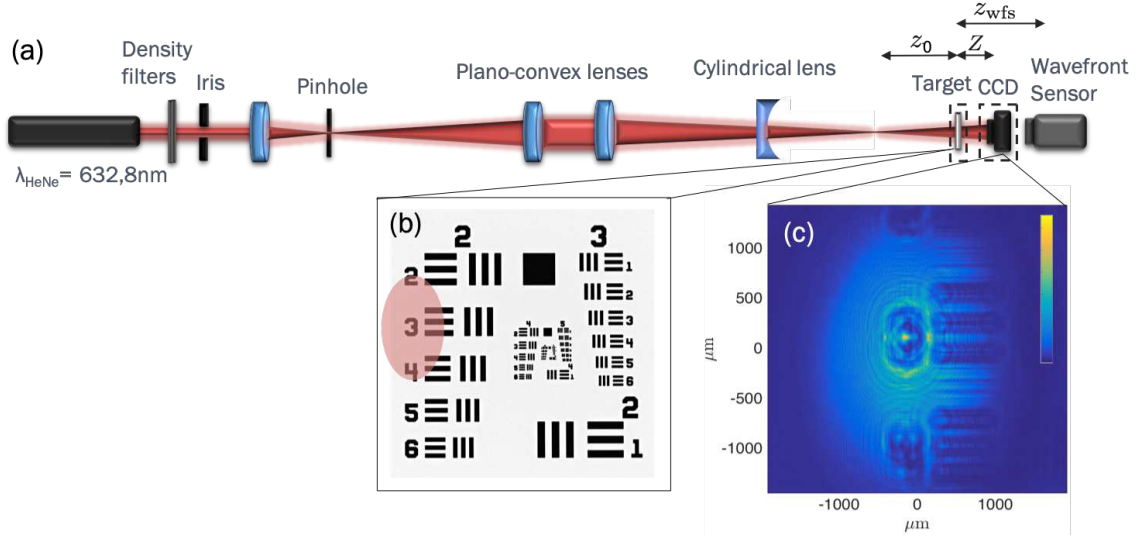


Figure 4.15: **Experimental setup used for testing the correction of aberrations by resorting to wavefront sensor measurements.** (a) Experimental setup implemented with a HeNe laser and a cylindrical lens, to create an astigmatic beam. (b) ThorLabs Resolution test target, used as sample. The illumination of the target is schematized by a red ellipse, which represents the astigmatic beam. (c) Experimental hologram.

Defocus	-4.579
Astigmatism 0°	-0.301
Astigmatism 45°	-0.009
Coma X	-0.018
Coma Y	0.001
Spherical aberration	0.017

Table 4.2: Zernike coefficients measured in the wavefront sensor. The measured RMS error was 4.873λ .

4.6.2 Data Analysis and Reconstruction Procedure

The different steps of the reconstruction procedure used in the experimental data are illustrated in Fig. 4.16. The process followed the routine of twin image and aberrations correction described in Section 4.5, after the proper definition of the reference wave at the CCD.

To obtain the reference wave at the CCD, the phase information extracted at the wavefront sensor had to be propagated until the CCD plane and correctly positioned with respect to the hologram. For the purpose, the phase map defined by the Zernike coefficients of Table 4.2 was plotted in a circular aperture of diameter $2871 \mu\text{m}$, as given in the experiment. The coefficient of defocus was discarded in order to provide reconstructions with magnification, as discussed in Section 4.3. The field at the wavefront sensor was then described, according to this phase map by

$$U_{\text{wfs}}(\xi, \eta) = e^{-2\pi W(\rho(\xi, \eta), \theta(\xi, \eta))}, \quad (4.19)$$

different of a minus sign in the phase with respect to Eq. (4.2). This correction of the direction of propagation was calibrated with the defocus term measured at the wavefront sensor.

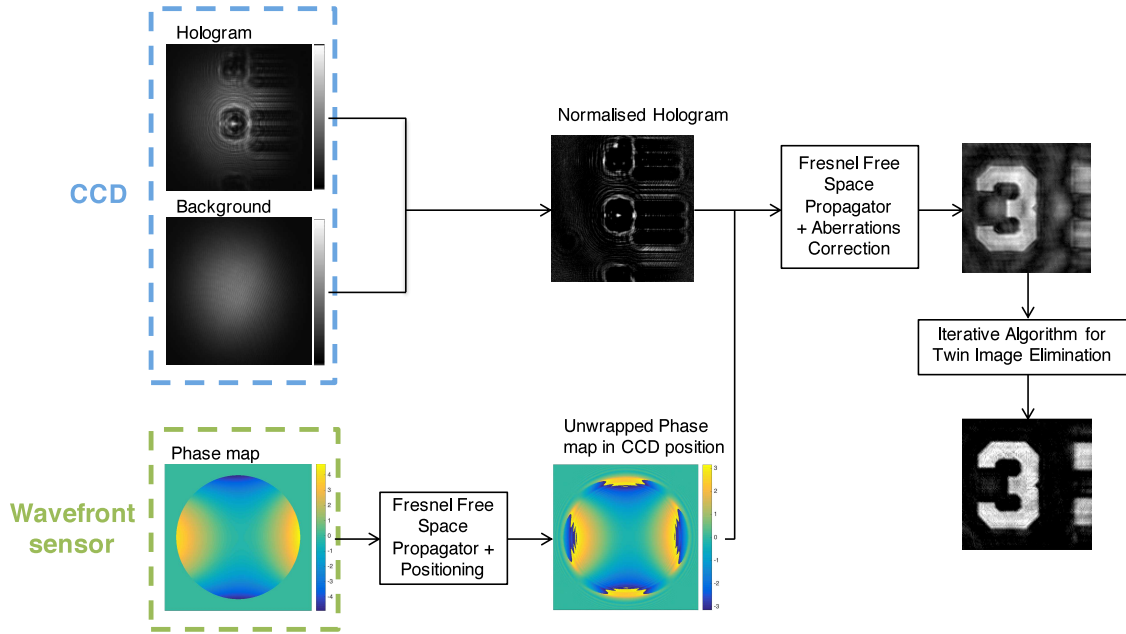


Figure 4.16: **Different steps of the reconstruction procedure used in the experimental data.** The hologram and background images, recorded at the CCD, together with the phase-map measured at the wavefront sensor, constitute the input data of our numerical routine. The first two are used to generate a normalised hologram which, associated with the phase map, propagated from the wavefront sensor until the detector, allow us to obtain reconstructions corrected from the optical aberrations of the illuminating beam.

The field from Eq. (4.19) was back-propagated as Fresnel diffraction until the detector position, as schematized in Fig. 4.17 (a), assuming a field with unitary amplitude. At the detector, the field amplitude resulting from propagation was filtered out and the propagated argument was used as the new phase map of the reference wave $R(X, Y)$.

In order to correctly perform the reconstructions, it is mandatory to define the phase map on its correct position with respect to the hologram. Indeed, the same object located in different positions on the same wavefront with aberrations was reported to exhibit distinct holograms [48]. Similarly, an incorrect positioning of the wavefront with respect to the hologram can induce additional propagation-artefacts in the reconstruction, instead of correcting them. The method developed to ensure the success of this step was to use the intensity-centroids of both detectors, CCD and wavefront sensor, as references. For this purpose, a Gaussian-intensity profile was centred at the position of the centroid of the intensity image at the wavefront sensor. This intensity map was then associated with the phase map at the wavefront sensor and propagated until the detector, in a parallel step illustrated in Fig. 4.17 (b). This process allowed to trace the intensity-centroid associated with the propagation of that specific phase map. By knowing its lateral displacement over a propagation through the experimental distance, the phase map achieved in the process of Fig. 4.17 (a) was re-centred so that the propagated intensity centroid matched the centroid of the background picture recorded at the CCD detector.

After the definition of the reference wave at the CCD, the reconstruction process followed the procedure of correction of aberrations and twin image described in Fig. 4.11. Note that, to reduce the

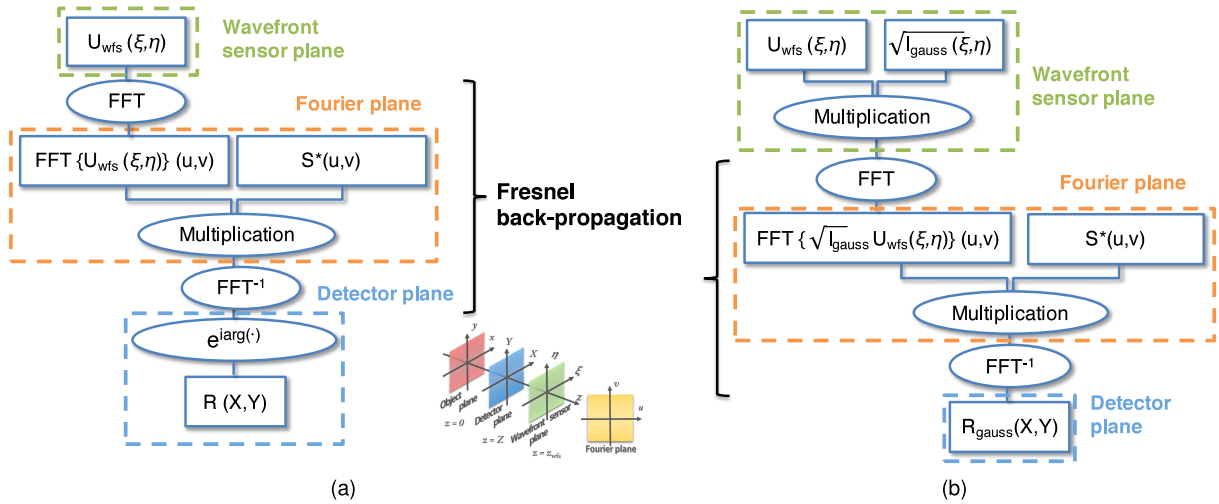


Figure 4.17: **Schematics of the process through which the experimental $R(X, Y)$ was obtained.** (a) Schematic of the phase map back-propagation, from the wavefront sensor to the detector. (b) Schematic of the parallel step, in which a Gaussian intensity profile is associated with the wavefront at the wavefront sensor and propagated, from its position until the detector. According to the lateral displacement of the intensity centroid associated with the propagation, the reference wave $R(X, Y)$ achieved in (a) is re-centred in a correct position with relation to the background picture, captured at the CCD.

numerical errors on the reconstruction process, a padding of zeros was made to the background and hologram images. The FOV used was 3048×3048 pixels.

4.6.3 Results and Discussion

The amplitude reconstructions (absorption maps) obtained by following the process described in the earlier section are presented in Figs. 4.18 (a) and (c), for 1 and 20 iterations of the twin-image correction algorithm respectively. The corresponding reconstructions achieved with the conventional method, i.e. without accounting with the phase map of the beam, are presented on the left, Figs. 4.18 (b) and (d). Looking first into the results from the twin-image correction, one can note a significant improvement of the reconstructions after running several iterations of the twin-image correction algorithm. In fact, the algorithm was seen to converge around the same 20 iterations for both datasets.

Considering now the impact on the reconstructions given by the corrections of the measured phase map, the results also reveal a significant success. Comparing Figs. 4.18 (c) and (d) one can see a clear improvement of the borders definition for the first case, which accounted with the experimental phase map measured at the wavefront sensor. This improvement can also be observed in the lineouts of Fig. 4.18 (e). Indeed, for the conventional reconstruction case (Fig. 4.18 (d)), the reconstruction showed different regions better "focused" at different Z positions sample-detector, consequence of the astigmatism and its inherent different experimental foci. The images shown were obtained for the best compromise between the vertical and horizontal resolution degradations, corresponding to an equivalent focal-spot distance of $z_0 = 4.68$ cm, optimized numerically. The object position also optimised numerically yielded a value of $Z = 2.62$ cm.

From the plots of Fig. 4.18 (e) and the opposite edges, it was obtained an average resolution

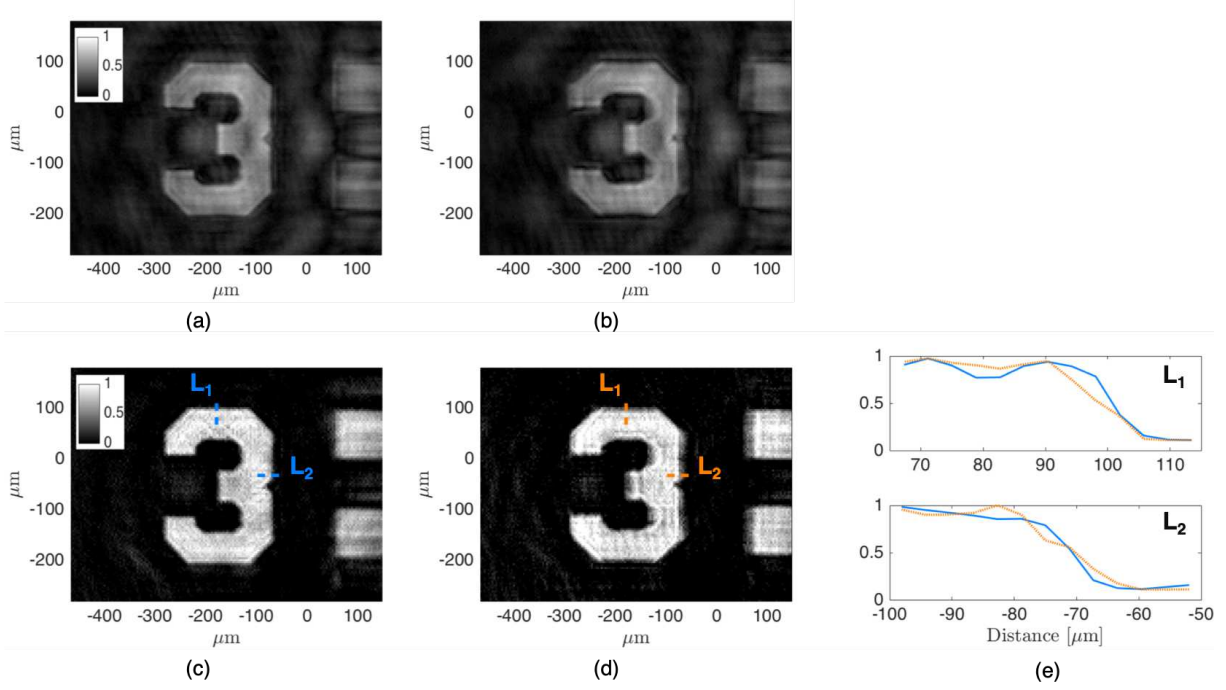


Figure 4.18: **Experimental in-line reconstructions with and without correction of the beam aberrations and twin image.** (a) In-line reconstructions with and (b) without correction of the beam aberrations for the first iteration of the reconstruction algorithm. (c) Reconstructions with removal of the twin image contributions with and (d) without correction of the beam aberrations. (e) Lineouts in two different positions, vertical and horizontal, of the images in (c) and (d) (blue and orange profiles, respectively).

(Rayleigh criterion) of $9.00 \mu\text{m}$ against $16.77 \mu\text{m}$, in the x -axis; and $8.27 \mu\text{m}$ against $11.20 \mu\text{m}$ in y ; both first values referencing to the case where the aberrations-correction was performed. The results show a significant improvement of resolution for the case where the correction of the aberrations was applied, when compared to the conventional approach.

The achievable (theoretical) lateral resolution for this experiment is estimated to be $\sim 7.14 \mu\text{m}$ in the x -axis and $\sim 6.13 \mu\text{m}$ in y , according to Eq. (2.80). These results point out diffraction-limited reconstructions when the proposed algorithm is used. Note that the values of achievable-lateral resolutions are different in both axes due to the astigmatism of the beam, which manifests in different numerical aperture values in both directions. All resolution values are organised in Table 4.3 for better visualisation.

Case	$\mathcal{R}_x [\mu\text{m}]$	$\mathcal{R}_y [\mu\text{m}]$
(c)	9.00	8.27
(d)	16.77	11.20
δ_{lat}	7.14	6.13

Table 4.3: Resolution values, \mathcal{R} , calculated from the experimental reconstructions and corresponding setup-achievable resolutions, δ_{lat} .

Concluding, this experimental section proves the validity of the algorithm proposed and, more importantly, shows that a correction of the wavefront aberrations in the reconstruction is possible and compatible with a twin-image correction. We would like to point out that even though the technique is exploited here with a commercial wavefront sensor, any other wavefront-sensing methods can be used

[238–240]. Indeed, the defocus term can be easily extracted from any wavefront measurement by fitting the respective Zernike polynomial to the measured map, limiting this analysis to a circular aperture [140, 206]. Moreover, the wavefront measurement can be performed at any position in the setup, making of this technique extremely versatile and easy to use.

4.7 Conclusion Notes

In this chapter, we proposed and demonstrated a new approach, compatible with single-shot imaging, which uses the data collected on a wavefront sensor to correct in-line reconstructions from the aberrations of the optical system.

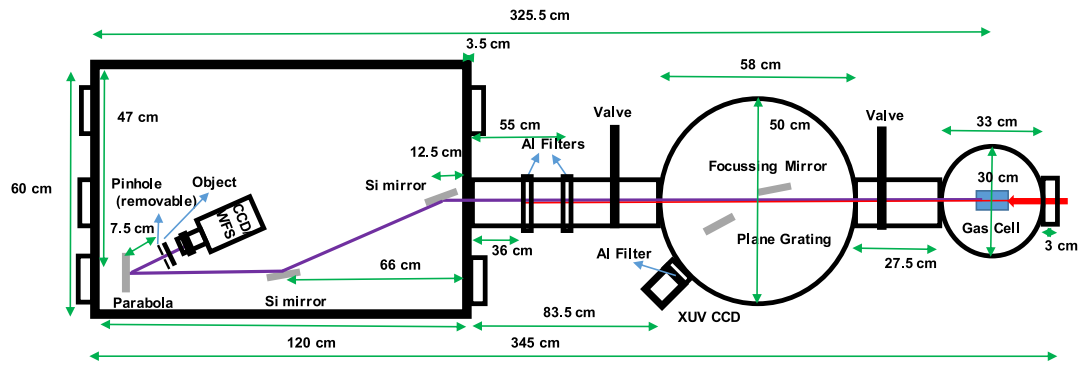
We started by developing a formalism, in Section 4.3, which allows for simulation and reconstruction of holograms generated from in-line holography with waves with aberrations. The proposed approach separates the measured phase map from the defocus term, allowing for in-line reconstructions with the resolution improvements of magnification. Applying this formalism, simulations were performed in Section 4.4. The phase map employed was based on the Zernike coefficients measured from an XUV HHG-based beam, focused by two fused-silica spherical mirrors in a KB configuration. We saw that the wavefront aberrations induced by that focusing system were enough to compromise the quality of in-line reconstructions. Accounting with the beam phase maps we were able to overcome the effects of aberrations, reaching accurate object reconstruction, only polluted by smooth amplitude and phase modulations arising from the twin image.

In order to clean the reconstructions from the twin-image effects, we proposed an algorithm in Section 4.5, which allows a simultaneous correction of in-line holograms from optical aberrations and twin image. A test with experimental data from a biological phase sample illuminated by an aberration-free spherical-wave reference was also provided. The results validated the twin-image correction without the aberrated phase-map, setting a trustworthy base. Moreover, by reconstructing different planes of the sample, with different focused details, the routine showed good compatibility with 3D imaging using back-propagation functions.

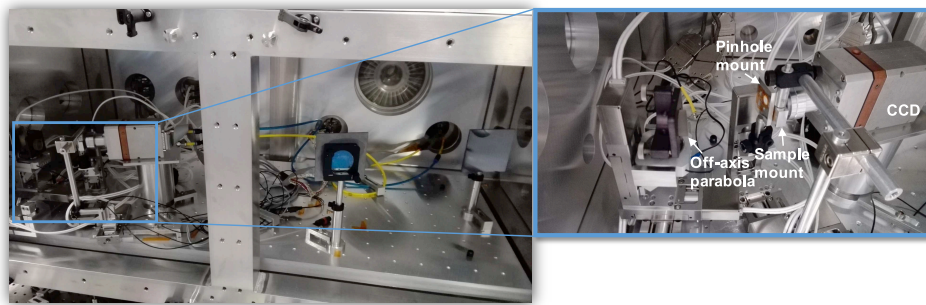
Finally, in Section 4.6, an experimental validation with an astigmatic wavefront was presented. The setup was assembled with a wavefront sensor and a HeNe laser, which allowed the caption of the phase map and respective Zernike coefficients in the conditions whereby the hologram was recorded. We have proven the validity of the algorithm proposed and showed that a correction of the wavefront aberrations in the reconstruction is possible and compatible with a twin-image correction. By employing this technique we achieved close to diffraction-limited reconstructions, without the need of a high-quality beam and, therefore, allowing for imaging processes using all the photons available, which is particularly advantageous for coherent imaging in the XUV and X-rays. Moreover, the technique presented is single-shot compatible and setup-versatile, allowing for aberrations correction, regardless of the wavefront-sensing method and its position in the setup.

Even though the proof of the technique was made in the visible range, the great impact would be in

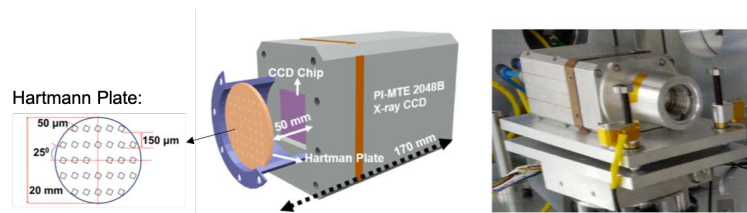
the XUV/X-rays as discussed in the introduction of this chapter. Therefore, a future prospect is the implementation of in-line holography in these spectral ranges. Here, diffraction-limited resolutions associated with higher-numerical aperture systems, which entail strong aberration effects [38], could really change the scenario of XUV/X-ray in-line holography, with possible extension to high-resolution 3D imaging. However, an implementation in these wavelengths faces practical difficulties. An attempt to perform such an experiment was realised at *Laboratoire d'Optique Appliquée* (LOA). The experimental implementation is illustrated in Fig. 4.19 and detailed at its legend. The experiment was however not successful due to equipment problems allied with beamtime limitations. For an experimental implementation in the XUV, in-line test samples were also fabricated at INESC–MN. Some examples are presented in Fig. 4.20. The fabrication process included the coating of two layers of PMMA; electron-beam exposure of the customized pattern; deposition of 5 nm of *Cr* and 50 nm of *Au*; and, finally, PMMA lift-off. The batch file of the fabrication process can be found in Appendix D, providing a strong basis for similar fabrications performed in the future.



(a)



(b)



(c)

Figure 4.19: **HHG beamline and setup implemented at LOA to perform XUV in-line holography, corrected from the aberrations measured with a Hartmann wavefront sensor.** (a) Schematic of the HH beamline at Salle Corail, *Laboratoire d'Optique Appliquée* (LOA). A commercial Ti:Sapphire laser system provides a beam with a central wavelength of 800 nm, pulse duration < 40 fs, pulse energy of 3.5 mJ (which can be increased up to 5 mJ) and repetition rate of 4 kHz (which can be increased up to 5 kHz). The IR laser is focused on a gas cell of length 15 mm, using a plano-convex lens with a focal length of 750 mm. The cell is centred in a first vacuum-chamber, and for this experiment was filled up with 60 mbar of Ar (optimised for the photon flux). The XUV beam generated at the gas-cell chamber travels through the diagnostics chamber (central chamber, which we did not use for the experiment) and two aluminium filters, of thicknesses 150 nm and 300 nm, which are placed before the experimental chamber to filter-out the residual IR. (b) Experimental chamber with respective imaging setup. A multilayer-coated off-axis parabola with 10-nm bandwidth and 32-nm central wavelength, focused at 20° after 75 mm, was positioned at the extremity of the chamber to select and focus H₂₅ ($\lambda = 32$ nm). A 0.5- μ m pinhole (possibility to increase to 1, 2 and 5 μ m) was aligned at the focus to allow an aberration-free image reconstruction for reference. This pinhole would be later removed to test configurations with aberrations. Parabola misalignments would be additionally induced. The sample was placed after the pinhole. Due to setup constraints the minimum separation distance sample-pinhole was 6 mm. An XUV CCD with 2048×2048 square pixels with a pixel size of 13.5 μ m was mounted after the sample, at a minimum experimental separation distance of 7 cm. Due to a problem with the CCD device allied with the reduced experimental time, we were unable to perform the experiment. (c) Scheme and image of the in-vacuum high-NA XUV Hartmann wavefront sensor [241], which would measure the aberrations of the beam in a later stage of the experiment, after replacing the imaging system. Image adapted from [220]. The device consists of a Hartmann plate attached to an in-vacuum detector (2048×2048 pixels; pixel size 13.5 μ m), mounted in an assembly of translation, rotation and tip/tilt stages for optimising its alignment during experiments.

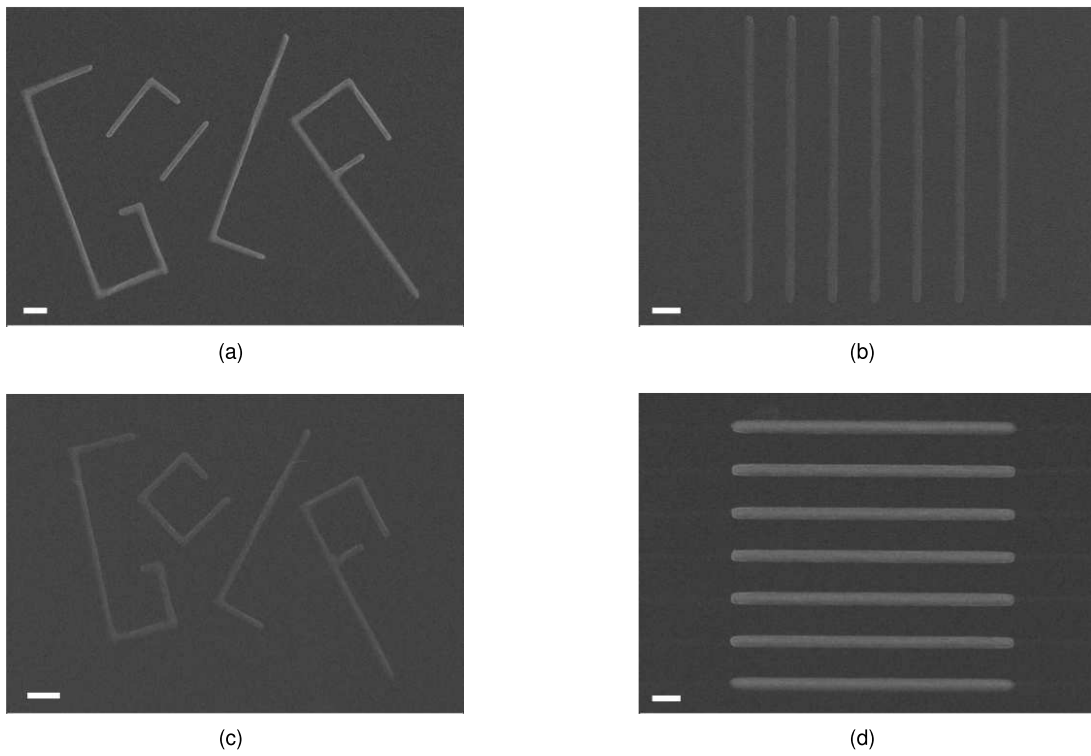


Figure 4.20: **In-line XUV test samples fabricated at INESC-MN.** (a)-(b) Patterned objects composed by lines of 300 nm-nominal width. (c) Object with lines of 200 nm-nominal width. (d) Lines with 400 nm nominal width. The scale bar in all images denote 1 μm .

Chapter 5

Computed Stereo Lensless X-ray Imaging

5.1 Introduction

In nature, most dynamic systems hold a complex 3D structure, whose deep understanding is crucial for several fields in medicine or biology. It is also relevant for many areas of research in academic science or applied physics such as semiconductor technology or nano-technologies. The wide development of ultrafast coherent X-ray sources on small-to-large-scale facilities has allowed 2D single-shot lensless imaging at nanometre-femtosecond scales [2, 8, 10–13, 242, 243]. Nevertheless, the expansion to ultrafast 3D imaging is showing some challenges. Nowadays, 3D nanometre-scale imaging techniques are mainly based on computed tomography. In this scheme, the sample is rotated with respect to the illumination source, while a full set of 2D projections is extracted and recombined to form a 3D image [122, 244, 245]. The number of views can exceed several hundreds [125]. To allow imaging extended objects, a new branch called ptycho-tomography has been proposed, combining concepts from tomography and ptychography [137–139]. Even though it leads to improved axial and transverse resolutions, this technique is also demanding in terms of number of projections, requiring large scanning times [246]. These approaches are, however, incompatible with single shot imaging of ultrafast processes or dose-sensitive samples, as many projections are required. The flash technique of "diffraction-before-destruction" of single nanospecimens, as proposed on X-ray FEL sources, overcomes this radiation-dose problem [1, 2, 49, 50]. However, to retrieve a 3D reconstruction, it requires an enormous number of identical samples, not allowing imaging of unique objects or non-reproducible processes. Moreover, it generates an extremely large amount of data that needs to be sorted, classified and combined to provide a full set of consistent 3D data [3].

There is an intensive work on decreasing the number of orientations in the direction of retrieving 3D information from a single acquisition. An extreme solution is imaging through *Computer Stereo Vision*. Although X-ray stereoscopy was discovered in the end of the 19th century [247], it did not find

wide scientific applications immediately. Recently, however, electron stereopsis microscopy has shown to produce unprecedented 3D perception of nanometre scale details [248]. The main drawback about this approach is that the 3D effect is purely physiological. Indeed, the human brain can attain a fast 3D perception of the sample by processing binocular disparities in the cortex region, but it cannot access quantitative depth information. Moreover, to allow the cognitive 3D reconstruction, the angle between the two stereo views has to be small, limiting the gain in structural information. Several experiments have taken place at synchrotron beamlines using stereo imaging, but none have achieved a 3D reconstruction stemming from a single-shot pair of images [249–251]. In 2008, Schmidt et al. [252] proposed a theoretical study of a method dividing an X-ray FEL beam into two sub-beams using a crystal. In 2014, Gallagher-Jones et al. [253] probed the 3D structure of an RNAi microsp sponge by combining *coherent diffraction imaging* (CDI) reconstructions from successive single-shot diffraction patterns from an X-ray FEL, and from X-ray diffraction at a synchrotron. However, this method requires several acquisitions to record multiple angles. Techniques to retrieve the 3D structure from a single diffraction pattern have also been proposed, but they work under limited circumstances and heavily rely on sample *a priori* knowledge [51–55]. To date, it has not been possible to obtain a 3D reconstruction from a single X-ray acquisition. Still, stereoscopic coherent imaging has been proposed as a future and promising technique for nanoscale fast-time-frame 3D imaging at XFEL sources [56].

In this chapter we propose to extend the concept of Computer Stereo Vision to XUV and X-rays. Instead of constructing a stereo anaglyph with only qualitative 3D perception, our approach retrieves depth information by computing disparity maps from two CDI stereo views. Using this method, we explore different types of samples to prove the applicability and the limitations of the technique.

This chapter is divided into six sections. In the theoretical section, 5.2, the concepts of Computer Stereo Vision are introduced, with a detailed description on the different reconstruction steps which lead to the implementation of X-ray stereo imaging. In Section 5.3, we explore this implementation by means of a simulation, while identifying the issues specific for pure amplitude and phase samples and proposing ways to overcome them. In Section 5.4, nanoscale three-dimensional stereo imaging of a pure amplitude sample from a single dual-diffraction pattern acquisition is demonstrated, using XUV radiation from a HHG source. In Section 5.5 the limitations of the implementation of this technique to samples with predominantly-curved topography are tested and discussed. In the last content section, 5.6, we implement the technique in X-rays. We show that nanoparticles used as labels further extend the applicability of the technique to complex 3D samples. The last section, 5.7, provides the conclusions of the chapter.

5.2 Computer Stereo Vision: Principle and Reconstruction Steps

The field of *Computer Vision* deals with the computational understanding of the 3D information present in two-dimensional representations of the real (3D) world [254]. In particular, *Computer Stereo Vision* consists in the extraction of 3D information from pairs of digital images of the same scene. This technique,

of great importance in the field of machine vision and robotics, allows retrieving depth information by analysing the relative positions of objects in each view, captured with well-known projective parameters.

Generally, the stereo reconstruction problem can be divided into four big processes:

1. Acquisition of the stereo image pair;
2. Pre-processing of the stereo images, which can require the procedure of image rectification;
3. Stereo matching and computation of the disparity maps;
4. Retrieval of depth information and 3D reconstruction.

In general lines, the first step of a stereo reconstruction scheme consists in the acquisition/generation of the stereo views. After pre-processing, if the images are not captured by a parallel camera system, they are projected onto a common image-plane to allow comparison with the pair-image. This step is known as image rectification. Follows a process in which the disparity map is created. This map encodes the difference in horizontal coordinates of corresponding image points, in the two views. Applying considerations on the configuration of the system, this disparity map can be converted into depth information and the 3D coordinates of the pixels can be projected into a 3D point cloud. From this arrangement, if needed, some additional intermediate points can be interpolated to achieve a more complete 3D scene. Finally, in case of knowledge of the textures/colours, this information can be, as well, added to achieve the ultimate representation of the 3D sample.

The sequence of steps used in this manuscript is schematized in Fig. 5.1, with distinction between simulation and experimental cases.

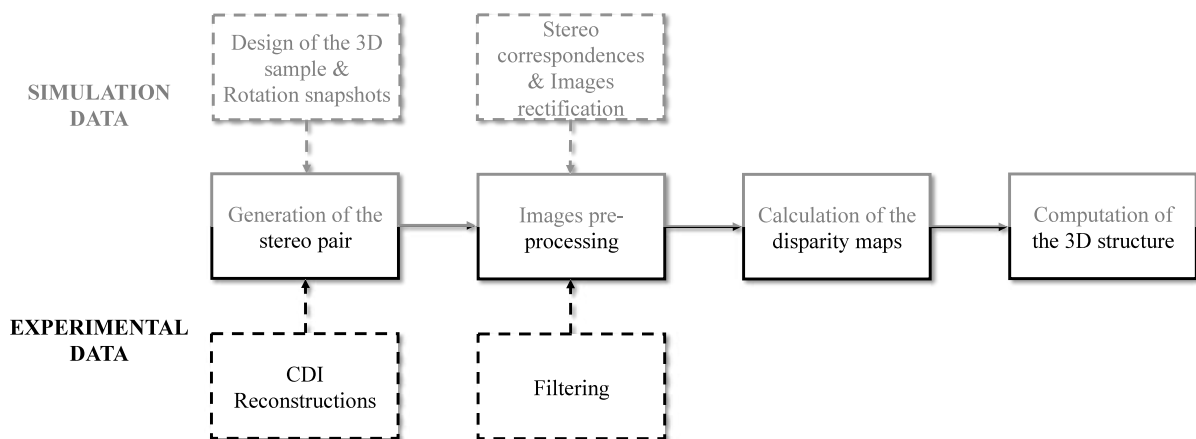


Figure 5.1: **Steps followed in the reconstruction of the 3D structure of a sample from stereo data.** In the block scheme, one can identify the main differences between the reconstruction process followed for the simulations (gray) and experimental data (black).

A resumed description of each of these steps is presented next, along with the presentation of the methods commonly adopted for all the studies, aiming a computed stereo imaging approach in transmission geometry. Note that this section introduces a global view over the adopted stereo reconstruction process. The particular path followed for each of the samples/cases studied in this manuscript will be detailed in its specific section.

5.2.1 Generation of the Stereo Image Pair

Computer Stereo Vision extracts 3D knowledge about a scene by comparing information from two vantage points. To these vantage points we call the stereo pair (Fig. 5.4).



Figure 5.2: **Example of a stereo image pair - "Man" - from Kim *et al.* [255].** (a) Left view. (b) Right view.

In order to make use of the nanometre-scale spatial resolution in an aberration-free system, the stereo pairs in this chapter result from coherent lensless imaging techniques. The views are generated by different beams with controlled incident (stereo) angles on the sample, which diffract and are collected in a CCD. These different beams can originate from the same beam, after split and redirection with proper optics. Such a system will be employed in this chapter for the generation of XUV stereo views in single acquisition (section 5.4).

5.2.1.1 Choice of the appropriate stereo angle

The choice of the angle between the stereo pair of images is a key factor in Stereo Vision. The optimal parallax between two view points results from a trade-off between the adequate depth resolution of significant details and the competent sampling of the same areas of the specimen. Indeed, inferring depth information is only possible by the presence of identical features in both views, which is improved by a reduction of the stereo angle. On the other hand, when the two views are separated by a very small angle, the disparities observed on the images are very small in comparison with the pixel size of the digital stereo views. This decreases the depth perception and, as well, the accessible depth resolution. Consequently, the proper choice of the stereo angle depends on the nature of the specimen's topography. Generally, if the sample has extremely rough topography, the angle separation between both images of the stereo pair should be low. Conversely, slight topography will produce a better stereo effect with a larger angle. For stereopsis, the typical range for the stereo angle is between 4° and 10° as usually the observers find stereo images achieved with an angle larger than 10° difficult to fuse [256]. In Computer Stereo Vision, however, this angle can considerably increase, since it is based on a digital treatment, thus overcoming the biological limitations of having the 3D perception captured by two eyes.

5.2.1.2 Stereo views in transmission

After digital detection of the diffraction-pattern pair, generated with a suited stereo angle, follows the reconstruction process. In this process our stereo images are formed as 2D projections of our sample since they are acquired in a transmission regime. The reconstruction procedures can vary from holographic methods to phase retrieval procedures, depending on the setup employed. All the experimental data presented in this chapter were collected in coherent diffraction imaging configuration, hence the reconstruction is performed using phase retrieval routines.

In the visible range, the standard imaging devices collect stereo views in reflection geometry, which, apart from an offset in intensity, should exhibit similar illumination conditions (if no transparent objects are present in the scene). In the XUV and X-ray spectral ranges, though, most of the samples are probed in transmission as reflectivity is quite poor. Additionally, one can make use of the penetrating nature of this type of radiation. This allows the imaging of objects much thicker than those which can be imaged by a transmission electron microscope, at resolutions much better than the ones achieved with visible microscopes [30]. The transmission geometry poses, however, a difficulty to the typical stereo approach, due to the superimposition of different structures/layers in the same pixel, which induces ambiguities in the stereo correspondence problem. As we will see later on, this is, however, not a limitation of the proposed scheme. In the next topics we present the different steps specific to treat a transmission stereo pair.

5.2.2 Stereo Correspondence and Image Rectification

If the stereo images are not captured in the same camera, or in a parallel camera system, they require a projection onto a common image plane in a first step, to allow comparison between them. This step is known as image rectification.

To understand the idea of rectification, it is helpful to firstly introduce some concepts of *epipolar geometry*. As shown in Fig. 5.3 (a), the centres of projection of the two cameras of a stereo setup and any point in their field of view define what is called an epipolar plane. The intersection of any epipolar plane with the left and right image planes generate two conjugate lines - called the epipolar lines -, defined in their respective 2D images space [257]. Naturally, each pair of corresponding points of the two images is mapped in conjugate epipolar lines (Fig. 5.3 (b)).

When the stereo images are acquired by a parallel camera system, the conjugate epipolar lines are collinear. In this arrangement, the cameras are assembled with their optical axes parallel and, thus, perpendicular to the line connecting their optical centres, the baseline. The images are, hence, separated by a simple horizontal shift, which enables each feature in one image to find its match in a 1D-horizontal search over the conjugate epipolar line of the second image.

The process of image rectification allows for the transformation of any stereo images pair, captured with a relative rotation, into a parallel camera system. This transformation consists, precisely, in projecting the initial stereo views onto a common image plane, such that their conjugate epipolar lines are

vertically aligned and, therefore, parallel to horizontal scan lines on the images (Fig. 5.3 (c)). It allows reducing the 2D stereo correspondence problem to 1D.

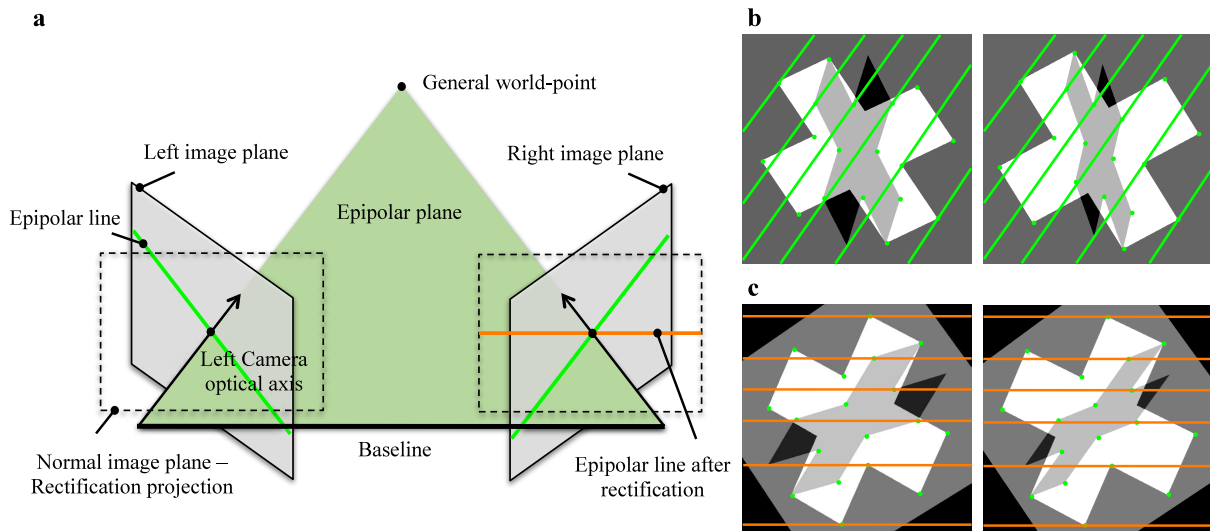


Figure 5.3: **Schematic representation of image rectification, by means of epipolar lines.** (a) Stereo camera system with concepts of epipolar geometry. The camera baseline intersects each image plane at its respective epipole, e and e' . Any plane containing the baseline consists of an epipolar plane and intersects the image planes in corresponding epipolar lines l and l' . As the position of the 3D world point varies, the epipolar planes “rotate” about the baseline so that all epipolar lines intersect at the epipole. (b) Example of a stereo image pair with representation of some epipolar lines. The images were acquired in a system as illustrated in (a). (c) Stereo image pair of (b) after the process of rectification. The rectification projects the original stereo images in a normal image plane so that the epipolar lines correspond to horizontal lines, and therefore, conjugate epipolar lines are collinear.

5.2.2.1 Stereo correspondence and fundamental matrix

In order to find the proper plane for re-projection of the stereo views, in a first stage, one needs to retrieve the fundamental matrix between the two views. In Computer Vision, the fundamental matrix F consists of the 3×3 matrix, which describes the relation between corresponding points in a pair of stereo images [258]. This way, considering x and x' image coordinates of matching points in a stereo pair, $l' = Fx$ describes the epipolar line of x on which the corresponding point x' , on the other image, must lay. In other words, $x'^T Fx = 0$ for all pairs of corresponding points.

The fundamental matrix can be computed from a set of corresponding points $x \leftrightarrow x'$ in the two views. The process of identification of matching points can be performed either manually or by combining feature detection [259–263] (e.g., corners, blobs) and feature matching [264–266] algorithms. Retrieving matching points manually requires a careful analysis of both images with visual identification of corresponding feature points, which is not optimal when several datasets are to be evaluated. While the resource to algorithms to identify interest points offers a more automatised process, the selection of the right combination of algorithms is not straightforward, as the results vary with the datasets. Moreover, these algorithms do not work for all stereo pairs, being particularly challenging for objects with slight topography or repeated pattern regions.

If the selected matching points are inliers, i.e. all matches are correctly done, one can compute the fundamental matrix employing the *Normalised Eight-Point Algorithm* [267]. As its name suggests, the *Normalised Eight-Point Algorithm* estimates the fundamental matrix from a minimum of eight corresponding-image points in the two views. The procedure is well documented in references [267, 268]. If, on the other hand, the matched input points are not all reliable, outlier points can be detected and excluded by using a robust estimation technique such as *RANdom SAMple Consensus* (RANSAC) [269]. RANSAC is an iterative method that estimates parameters of a mathematical model from a set of observed data, accounting with the presence of possible outliers, which must not contribute to the estimation.

5.2.2.2 Computation of the projective transformations

With access to the fundamental matrix, one can finally obtain the projective transformations that allow the rectification of the stereo images, as described by Hartley *et al.* [268]. Briefly, the rectification algorithm starts with the computation of the overall transformation for the right image. The image is rotated so that its epipole is translated to the line at $y = 0$ (see Fig. 5.3) and, after, warped in a way that the epipole is moved to a position at infinity. A synthetic camera matrix M is then computed for this view, from the factorization of F as $F = SM$, where S is a skew-symmetric matrix. Unfortunately, M cannot be computed using the usual factorization, where $S = [e]_{\times}$ and $M = [e]_{\times} F$, because then M would be singular. Instead, M should be computed using the singular-value decomposition (SVD) of F , which gives

$$F = UDV^T = UWZD'V^T = (UWU^T)(UZD'V^T) = SM \quad (5.1)$$

with

$$W = \begin{bmatrix} 0 & 1 & 0 \\ -1 & 0 & 0 \\ 0 & 0 & 0 \end{bmatrix}; \quad Z = \begin{bmatrix} 0 & -1 & 0 \\ 1 & 0 & 0 \\ 0 & 0 & 1 \end{bmatrix} \quad (5.2)$$

and if $D = \text{diag}(s, t, 0)$, then $D' = \text{diag}(s, t, (s + t)/2)$. On the other hand, $WZ = \text{diag}(1, 0, 0)$, so $WZD' = D$.

From M , which is the matrix representing the required homography, one can finally compute the transformation for the left image. This transformation is achieved so that the rows in this image correspond to the rows at the same location in the second image and, as well, so the input correspondent points have (approximately) the same column locations in the right and left images [268].

5.2.3 Stereo Matching and Computation of the Disparity Maps

From a pair of rectified stereo views one can compute two disparity maps (Fig. 5.4). Disparity refers to the distance between corresponding points in two images of the same scene taken under different viewpoints. By matching the pixels from one image to the other, one can produce a map where each pixel quantifies its disparity value, measured in relation to the corresponding pixel in the pair image (Fig.

5.5) [255, 270].

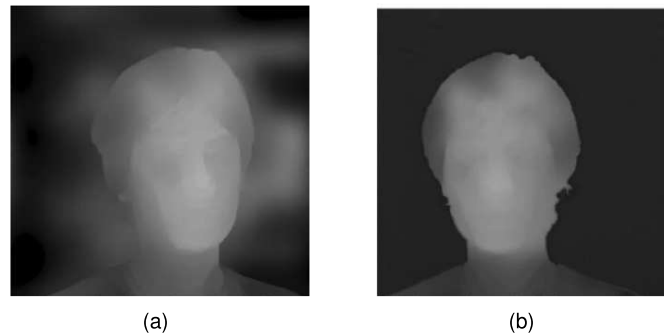


Figure 5.4: **Example of a pair of disparity maps of the "Man" - images from Kim *et al.* [255].** (a) Left map. (b) Right map, with background removal.

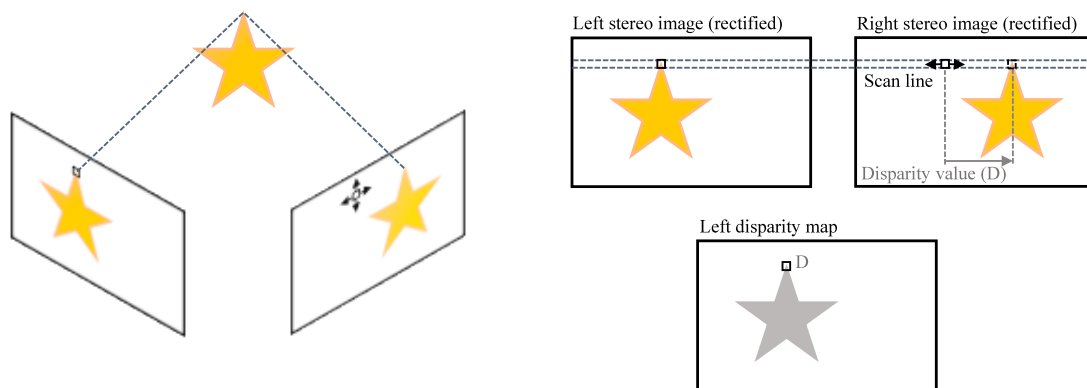


Figure 5.5: **Explanatory scheme of the disparity calculations.** From a rectified pair of stereo images, for each pixel in the left image, a scan is made over the horizontal scan line in the right one. Finding the corresponding match, the scan position is saved as a disparity value. This process is followed for all pixels in both images, creating two disparity maps, left and right map.

In order to properly retrieve disparity values, one needs to first identify the point matches in both images. The process of estimating corresponding points in a pair of stereo images, also known as stereo matching, has been one of the most fundamental and disputed topics in the fields of Computer Vision. Even though numerous routines have been proposed, it still remains a challenging task due to several factors including absence of texture in the objects, repeated-pattern regions, occlusions and photometric deficiencies incurred by camera variations and/or illumination problems [271–274].

5.2.3.1 Stereo matching constraints

To approach the stereo-matching problem, it is important to firstly identify and impose some matching constraints, in order to minimise the number of false matches. The most commonly used constraints in Computer Stereo Vision are:

- **Similarity** (or **Compatibility**) [275], which states that matching pixels must have similar intensity/magnitude values (i.e. differ only from a specified threshold) or the matching windows must

be highly correlated. In case of matching features (instead of intensities), they must have similar attribute values.

- **Uniqueness** [276]. According to this constraint, a feature/pixel from one image can match no more than one feature/pixel from the other image. This admits that some pixels or features can have 0 matches assigned if their corresponding pixel/ feature is occluded in the other image. This constraint may fail if transparent objects are present in the scene, as this often entails superposition of different structures in the same pixel.
- **Continuity** [276]. Continuity suggests that matching features should have nearly the same depth value as its neighbours. In other words, the disparity of the matches should vary smoothly almost everywhere over the image. Note that this constraint fails at depth discontinuities (e.g. object borders), as they cause an abrupt change in disparity.
- **Ordering** [277]. States that the ordering of features is preserved across images. If $m_1 \leftrightarrow m_2$ and $n_1 \leftrightarrow n_2$ and if m_1 is to the left of n_1 , then m_2 should also be to the left of n_2 and vice versa. The ordering constraint fails at regions known as *the forbidden zone*, Fig. 5.6.

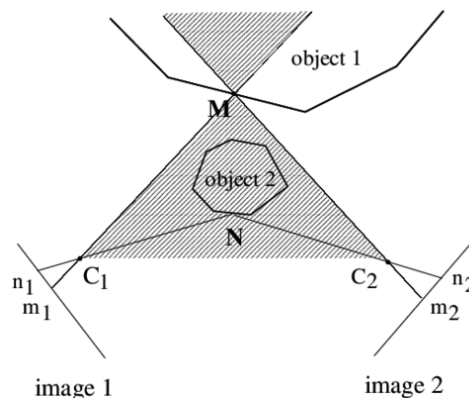


Figure 5.6: **Failure of the ordering constraint at the Forbidden Zone** [278]. The ordering constraint fails if a 3D point, N , falls onto the forbidden zone of another point M , represented in the image by the shaded area. In the image, the left image-plane shows n on the left of m , while in the right image this ordering is reversed.

- **Epipolar** [257]. For each feature point in the left image, the corresponding feature point must lie on the corresponding epipolar line. Lets recall that this constraint was explained in detail in the previous section 5.2.2, as it is implemented in the process of image rectification. Unlike all the other constraints, the epipolar constraint never fails once the epipolar geometry is known.
- **Relaxation** [279]. Consists in a global matching constraint, which is imposed by an iterative update process as follows. Firstly, a probability value is assigned to each match-candidate based on some quantitative “goodness-of-match” criteria. This probability value is then iteratively updated for each match-candidate. Finally, those matches whose probability value is below a specified threshold are discarded. One example of implementation of the update process, as proposed by Barnard and

Thompson [279], consists in increasing the probability of a given candidate match, in each iteration, by a value that is proportional to the number of neighbouring matches that have consistent disparity values with it. Other criteria may also be used as, for instance, the geometric support as proposed by Ayache and Faverjon [280].

5.2.3.2 Stereo matching algorithms

Conventionally, stereo matching algorithms are divided into two categories: aggregated and global algorithms [281–284]. In either of them, four steps are usually required: matching cost computation, cost (support) aggregation, disparity computation and disparity refinement (or post-processing) [281].

Local (window-based) stereo matching algorithms, such as sum of absolute differences (SAD) [255, 270, 285], sum of squared differences (SSD) [286], adaptive supported weight [287], guided filter [286], histogram aggregation [288], geodesic stereo [289] and accelerating cost filter [290] constitute an important part of the aggregated ones. In this type of algorithms the computation of the disparity at a given point depends only on intensity values within a finite window and generally make implicit smoothness assumptions by aggregating support. The fundamental behind them is the local disparity consistency assumption [291], which states that all of the pixels within a local supported window have constant disparity values. A typical non-local aggregated method is the non-local cost aggregation (NLCA) algorithm [292]. In this approach, cost volumes are aggregated on a minimum spanning tree. Based on the NLCA framework and with integration of additional features other non-local algorithms have recently risen [293–295]. Conceptually, aggregated algorithms implement a matching cost computation at first and then execute a cost-aggregation step with a local or non-local framework. A winner-takes-all (WTA) optimisation is then performed to select, for each pixel, the disparity value associated with the minimum aggregated cost value [281, 284, 291]. This strategy has been reported to provide fine and fast disparity estimation. A limitation consists in the fact that the uniqueness of matches is only enforced for one image (the reference image), while points in the other image might get matched to multiple points.

Global algorithms, also called energy minimisation algorithms, minimise a predefined energy function and omit the step of cost aggregation by directly formulating an explicit smoothness term. Even though some produce much improved results than those of the aggregated algorithms, they face the bottleneck of computational complexity. Indeed, minimising an energy function is a non-deterministic polynomial hard problem, thus former researchers have focused on several approximate optimisation approaches. The two most notorious optimisers are belief propagation [296] and graph cut [297]. Based on these optimisers, some significant progresses have been made [298–300].

Recently, some approaches integrating aggregated algorithms into the energy function model have also been investigated [301–304]. These algorithms, combining concepts from aggregated and global routines, have shown to provide generally better results. Nevertheless, they hold too much computational load.

All of the above-mentioned stereo matching algorithms resort to disparity refinement strategies for attaining a final refined disparity map. Techniques such as sub-pixel estimation [305], left–right

consistency-check [306], peak ratio [307] and occlusion filling [308] are widely employed. Recently, other learning-based [309–311] or convolutional neural network (CNN)-based [312–314] approaches have been proposed, boosting the performance of confidence estimation.

In the implementation of X-ray stereo imaging described in this manuscript, a local algorithm based on absolute intensity differences (AD) was used for stereo matching. Together with the squared intensity differences (SD), this pixel-based matching cost is one of the most commonly employed in Stereo Vision, requiring low computational load, while still offering fine disparity estimations [255, 270, 281, 285, 291]. After the matching-costs aggregation we resort to WTA optimisation to select the best match from the several candidates. For disparity refinement, sub-pixel registration [305] and left–right consistency-check [306] strategies are employed.

5.2.3.3 Detailed methodology

Following a local approach, the process of locating the corresponding pixels in both stereo images was achieved with a block-matching routine. In a block-matching routine, the images are divided into support windows/blocks and, for each block of the reference picture, a scan is made over blocks of the same size in the pair picture (Figs. 5.5 and 5.7). The scan is allowed to a number of pixels N to the left (negative disparity) and the same amount to the right (positive disparity) of the block central-pixel position. A cost function, which should be minimised, specifies which window is the best match from the set of candidate blocks. Expression (5.3) presents the cost function employed in this work, depicting a simple sum of absolute differences (SAD), added to a less weighted pixel proximity term [255, 270, 281, 285]:

$$C(x_o, y_o, d) = \sum_{(x_i, y_i) \in \text{Block}} |I_1(x_i, y_i) - I_2(x_i + d, y_i)| + \alpha d. \quad (5.3)$$

Here, (x_i, y_i) represents the coordinates of all the pixels in the evaluated block; I_1 and I_2 are the intensity values of the respective pixels in both images; α constitutes the weighting factor of the pixel-proximity term and d is the distance between the scanned pixel and the one under evaluation. $C(x_o, y_o, d)$ gives, therefore, the cost function of the block central pixel $(x_o + d, y_o)$ in the second image, which measures its matching potential with the pixel (x_o, y_o) from the first one (Fig. 5.7).

Note that in (5.3) no particular smoothness term is included in the function, since we preferentially deal with disparity measurements over edges and, for that reason, the final disparity maps do not necessarily follow a smooth-dense field of point correspondences. This will be explored along with the datasets in the next sections.

The cost function value of the best pixel match p is, therefore, given by

$$C_p(x_o, y_o, d_p) = \min_{d \in \Omega} C(x_o, y_o, d), \quad (5.4)$$

with d_p the disparity value of p , in pixels, and $d_p \in \Omega$, $\Omega \equiv \{-N, \dots, 0, \dots, N\}$. Selected the best match, the corresponding disparity value is stored and the scan is allowed to the next block.

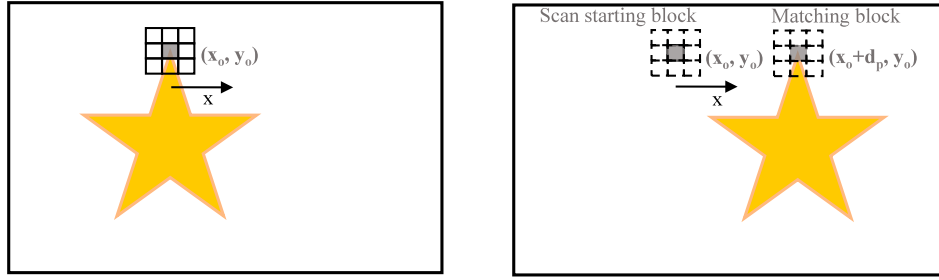


Figure 5.7: **Schematic representation of the block-matching routine employed in the disparity estimations.** To find the best match for the pixel with coordinates (x_o, y_o) in the left image, a window of pixels surrounding it is considered. By comparing each pixel in this window to the corresponding one in this window in each scanned window on the right image, the closest match is evaluated. This evaluation looks for the disparity value d_p , achieved through a minimisation of a cost function.

The final disparity values are obtained after refinement by second-order sub-pixel interpolation [305]. For the purpose, a quadratic estimator is applied over each disparity value arising from the sorting process. This estimator takes the form:

$$D = d_p + \frac{C_{p+1} - C_{p-1}}{2(2C_p - C_{p+1} - C_{p-1})}, \quad (5.5)$$

where, C_{p-1} and C_{p+1} are the respective cost function values of the left and right pixels of p . Here D is the maximum of the the second-order function that fits our cost distribution and corresponds, therefore, to the final disparity attributed to the block's central pixel of the reference image.

Resuming, breaking down the used methodology into the four stereo-matching pipelines [281], we have that:

1. The **matching cost** employed is based on the absolute difference (AD) of intensity values at a given disparity. This cost function guarantees the fulfilment of the similarity and continuity constraints (this last one only for the samples to which we allow the creation of a dense disparity map). Besides the AD, a less weighted pixel-proximity term is added to the cost function, whose main purpose is to follow the ordering constraint when computing disparity values just over edges.
2. **Aggregation** is performed by summing the matching cost over square windows, with constant disparity.
3. **Disparity computation** is achieved in a WTA optimisation, by selecting the minimal (winning) aggregated value at each pixel.
4. **Disparity refinement** is accomplished with sub-pixel interpolation [305] and left–right cross-check [306] strategies. As the latter states that reliable conjugate pairs are found with both direct and reverse matchings, it reinforces the uniqueness constraint. Even though this constraint can fail with the presence of transparent objects, which are predominant in a transmission apparatus like ours, we will avoid failing it by ensuring a separation of different superimposed structures/layers in a pre-processing step of the stereo images (more details are given later on).

5.2.3.4 Selecting an appropriate window size

In a block-matching routine, the images are divided into support windows/blocks, which are evaluated in the light of a stereo-matching metric. In this manuscript, blocks from 3×3 to 29×29 pixels were used, depending on the sample under study.

The choice of the appropriate block size is a crucial parameter in stereo matching, as it affects largely the quality of the disparity maps. A stereo-matching algorithm based on small support windows generally entails lower algorithm run times. However, it fails particularly in textureless and repetitive-image regions, as well as areas with only horizontal texture. Indeed, the drawback of blocks-reduced sizes is that they are often unable to capture enough texture variation to resolve matching ambiguities. On the other hand, they provide significantly better preservation of disparity/depth discontinuities [291].

A way to overcome the ambiguity problem is to use large support windows. For a large 23×23 window, for instance, the disparity map is considerably smoother, at the expense of the bad preservation of the object's borders. In fact, the issue is our implicit smoothness assumption, since pixels within the window are presumed to have constant disparity. This smoothness assumption is, yet, broken in the proximity of depth discontinuities, when the window captures a mix of foreground (object) and background disparities.

The classic problem of local algorithms is exactly the choice of the ideal window size such that the algorithm gives accurate results at the same time in low-textured areas and regions close to object borders. For that reason, a significant part of the work on local stereo matching focuses on the use of adaptive windows [306, 315, 316]. In this work, however, we use uniformly-sized windows in each dataset, along with complementary strategies to ensure the correct computation of the disparity maps. As will be discussed, the use of adaptive windows would not be justified for our datasets.

5.2.4 Retrieval of Depth Information and 3D Reconstruction

Having access to the disparity values, one can retrieve depth information on the object by employing camera geometry considerations (see Fig. 5.8). In the fields of Computer Vision and *Computer Graphics*, the *pinhole camera model* is widely used, offering a simple and reasonably accurate mathematical description to retrieve a 3D scene [257]. However, this approach does not suit the proposed case, since the original stereo views are acquired in a lensless setup. Hence, before proceeding to the description of the reconstruction process, it is important to understand the configuration of our system so that one can properly treat it.

5.2.4.1 From disparity to depth

The starting points of our stereo scheme are two 2D coherent diffraction imaging (CDI) reconstructions, from which we know exactly the pixel correspondence in terms of object dimensions. One can, thus, understand them as direct projections of our object at known angles, given by the geometry of our probes. In our experimental demonstration presented in section 5.4, the same CCD captures both



Figure 5.8: **Example of a 3D reconstruction originating from a pair of stereo images. The sample is the "Man" - images from Kim *et al.* [255].**

diffraction patterns, which corresponds to a direct parallel camera geometry. This setup, as well as any stereo pair stemming from a lensless system, after rectification, allows retrieving the depth values only from the geometric relations described in Fig. 5.9.

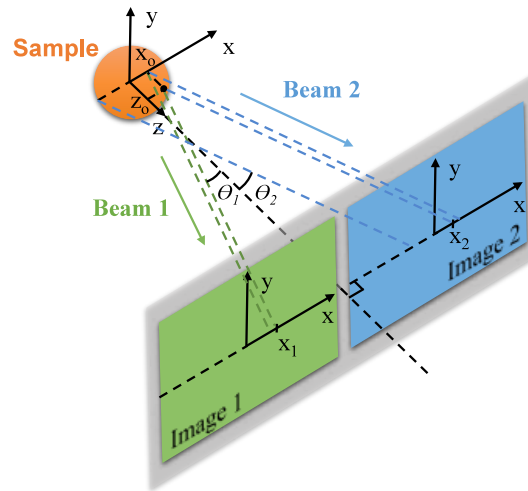


Figure 5.9: **Stereo system geometry.** The stereo images are captured by a parallel camera system, with the two diffraction patterns recorded simultaneously in the same CCD. The two stereo angles, θ_1 and θ_2 , are defined by the angles of the two incident beams on the sample. Note that after the rectification, the stereo images collected with different rotation angles, are as well converted into this geometry.

In the geometry of Fig. 5.9, the depth of a point in real space with spatial coordinates (x_o, y, z_o) is given by:

$$z_o(x_1, x_2, \theta_1, \theta_2) = \frac{(x_1 - x_2)}{\tan\theta_1 + \tan\theta_2} = \frac{-(x_2 - x_1)}{\tan\theta_1 + \tan\theta_2} \quad (5.6)$$

with $(x_1 - x_2)$ the disparity value of the left view picture with respect to the right view and $(x_2 - x_1)$ the inverse situation. From Eq. (5.6) one can notice that the voxel size on the depth axis decreases with

the angle between the two illuminating beams. As discussed before, there is however a physical limit for the increase of this angle, as identical features need to be identified in both views to allow disparity computations.

In order to match the information of the two disparity maps, it is necessary to correct the x_1 and x_2 coordinates, from the left and right disparity maps, respectively, to the object coordinate x_o . This conversion is obtained from the relations

$$x_o(x_1, z_o, \theta_1) = x_1 - z_o \tan\theta_1 \quad (5.7)$$

and

$$x_o(x_2, z_o, \theta_2) = x_2 + z_o \tan\theta_2. \quad (5.8)$$

After retrieving all the coordinates of the points in the 3D space, the stereo consistency of the two disparity maps is evaluated. Indeed, reliable conjugate pairs are found with both direct and reverse matchings. In this step, the 3D points extracted from each disparity map whose coordinates do not have a match for the second map are discarded. This bi-directional check was made with x_o , y and z_o values rounded to a defined number of decimal digits or, when not mentioned, to the unity (i.e. 1 μm precision). It is important to note that this precision is not meaningful, since an outliers removal routine is applied in a later stage.

From the left-right consistent points, a point cloud is created. At this moment, the 3D shape of the sample is already visible, with some structures partially/fully reconstructed. The next steps consist in crossing the information of the 3D point cloud to the direct stereo images if some final 3D renderings are requested. This part can change from sample to sample, and according to the approach followed in each case, but the general lines employed in our studies are described next.

5.2.4.2 Post-processing

Before proceeding, it is important to recall the transmissive nature of our stereo views. In fact, contrarily to the standard stereo setups, the images, arising from a transmission regime, are affected by a superimposition of different structures in the same (x_o, y) coordinates, positioned at different depths. The 3D points retrieved can, then, be attributed to different sample components. It is, therefore, necessary, when a 3D interpolation is aimed, to identify isolated sample components and address each component individually, in order to ensure no wrong connections are established in a surface rendering. Routines like image segmentation tools [317, 318] and gradient calculations [319, 320] are useful to automatise this process.

After identifying the structures, they are separated in different point clouds and the outlier points are removed from each of them. If their points are sparse, but following a well-defined profile, one can fit surfaces in each with topography according to their amplitude and phase variations. This was used, for instance, in our study of section 5.3 to obtain the point cloud of the simulated phase sample. These surfaces can be useful not only in the detection of outlier points, but as well, they can provide additional

points to the point clouds to help with the 3D interpolation of other intermediate values. If the structures are not clear, another algorithms can be used to perform the outliers removal, addressing the isolation of the 3D points from the cloud arrangement. In the terminology used for some of our case-studies, a point was considered an outlier if the average distance to its κ -nearest neighbours was above a specified threshold ζ [321]. For all datasets where this outliers-detection approach was used, $\kappa = 20$ or 80 points and $\zeta = 0.05$. This threshold ζ specified the number of standard deviations away from the estimated average distance.

When more points are needed, as for instance, when the extraction of the 3D coordinates occurs only on the edges, a 3D scattered interpolation can be performed over the resultant point cloud(s) to infer the intermediate values. The routine employed for the purpose in this work applies a *Natural Neighbour Interpolation* to the scattered sample points [322, 323].

Another consequence of the stereo transmission regime is the possibility of recovering information on the opaque and empty regions of the sample. Indeed, by identifying the areas of the stereo views where the transmission function is 1, one can have access to the empty volume of our sample. For instance in this manuscript, for both simulations and experiment presented in sections 5.3 and 5.4, this information was crucial. For such cases, additional point clouds are computed, composed by stacks of planar points, which are known to correspond to these empty regions. Excluding from the interpolated 3D meshes the neighbours of the empty region clouds, detected with a standard neighbours detection algorithm [265], one retrieves a final 3D rendering of the sample.

5.3 Simulations with a pure-amplitude *versus* phase sample

This section presents the results of a simulation applied in the study of two cases: stereo imaging with a pure amplitude sample; and with a phase sample. The two studies are presented together to foster the comparative analysis. While the pure amplitude 3D sample reproduces the experimental case of Section 5.4, the study with a phase sample was included to evaluate the advantages of adding this information to the reconstruction algorithm.

5.3.1 3D sample and Generation of the Stereo Views

The 3D object used for the simulation of a pure-amplitude sample, Fig. 5.10 (a), was drawn in AutoCAD, inspired by the sample used in the experiment. A symmetric cross was detached from a plane and rotated 90° about two contact points in opposite extremities. From a random starting position, two stereo views were captured, Figs. 5.10 (b) and (c), with a total separation angle of 12° .

In Fig. 5.11 one can observe the corresponding images for a phase sample. The same cross sample was used, but non-zero transmission was assumed to the probe beams. To simulate the different phase shifts, distinct absorption values were attributed to the central cross and to the membrane, resulting in stereo views composed by different grey tones. A transmittance of 60% was attributed to the lid-cross, contrasting with the 30% of the substrate plane that supports the cross-hole. As the object allows the

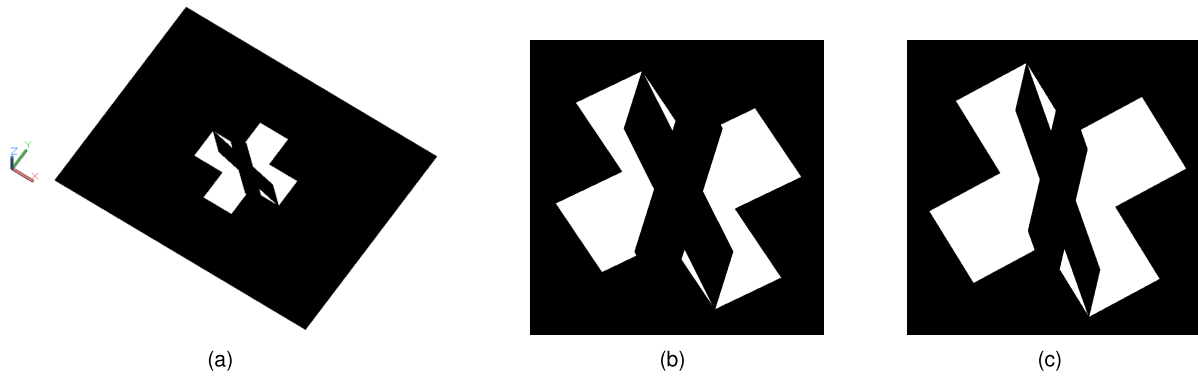


Figure 5.10: **Simulated pure-amplitude sample and correspondent stereo views.** (a) Sample designed in AutoCAD. (b)-(c) Pair of stereo images used in the simulation. In the images, the black areas correspond to the opaque parts of the object, while the white areas are empty regions. Stereo angles: (b) -6° , left view; (c) $+6^\circ$, right view.

transmission of the light in all its extent, one can "see" through the different planes.

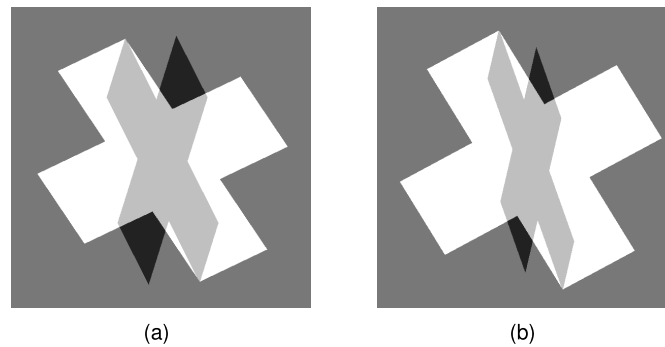


Figure 5.11: **Pair of stereo images used in the simulation of a phase sample.** In the images, the different grey tones denote the different phase values, in a range between 0 and 2π , from white to black. Stereo angles: (a) -6° - left view, (b) $+6^\circ$ - right view.

5.3.2 Stereo Correspondence and Image Rectification

Since the simulated views were obtained from a rotation of the sample, a rectification step was necessary. As explained in section 5.2.2, the process of image rectification requires a set of point correspondences between the two stereo views. In the dataset of Figs. 5.10 (b)-(c), for a pure-amplitude sample, the object presents an extremely symmetric binary shape. Although several feature detection and feature matching algorithms were tested [259–266], the retrieved results were ambiguous, due to the colour/topography similarities of all the features. Therefore, sixteen extremity-points were manually selected in the two images (Fig. 5.12 (a)). Applying the Normalised Eight-Point Algorithm to these points, the fundamental matrix between both views was computed and the images were finally re-projected onto a parallel camera system, following the procedure described in section 5.2.2. The images resulting from the rectification can be observed in Fig. 5.12 (b). They are shown superimposed to create an anaglyph.

Fig. 5.13 displays the corresponding cases of Fig.5.12, but for a phase sample. Note that the same matching points were used for the rectification process, since the images present exactly the same

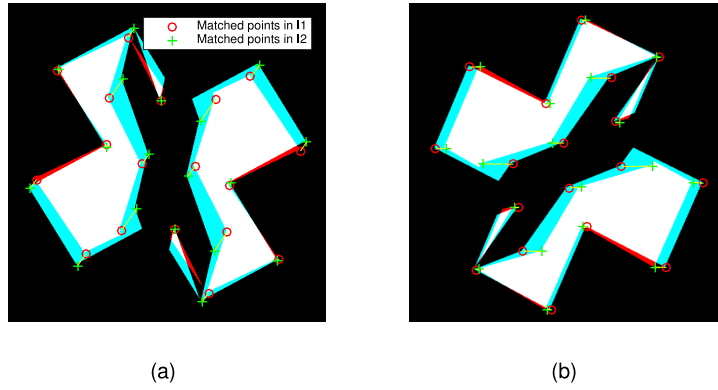


Figure 5.12: **Stereo images of a pure-amplitude sample, with corresponding point matches, before and after rectification.** (a) Original and (b) rectified stereo views, superimposed, with selected points and respective matches. In the images, the red/cyan areas correspond to the empty areas of the left and right stereo images, respectively. Empty areas which are common to both, are coloured white. Image (b) consists of an anaglyph, allowing for a 3D visualisation by the use of a proper pair of stereo glasses.

views.

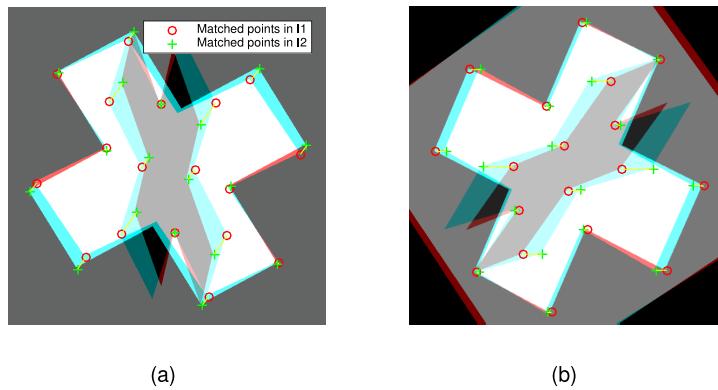


Figure 5.13: **Stereo images of a phase sample, with corresponding point matches, before and after rectification.** (a) Original and (b) rectified stereo views, superimposed, with selected points and respective matches. Image (b) is the stereo anaglyph.

5.3.3 Stereo Matching and Computation of the Disparity Maps

Using the method described in section 5.2.3, two disparity maps were generated for each simulated sample. Figs. 5.14 (a) and (b) represent, respectively, the disparity of the left image with respect to the right one (left map) and the reverse case (right map), stemming from the stereo views of the pure amplitude sample. Figs. 5.15 (a) and (b) present the similar images for the sample containing phase information.

The disparity range N was established to 65 pixels. This means that the scan was allowed 65 pixels to the left (negative disparity) and the same amount to the right (positive disparity) of the block's central-pixel position. The colour scale of the images encodes this range. The weighting factor α used for this

data (Eq. (5.3)) was defined as 0.01. Its effective purpose here is just to make sure the closer border is selected, in the case where more than one border is found within the range allowed.

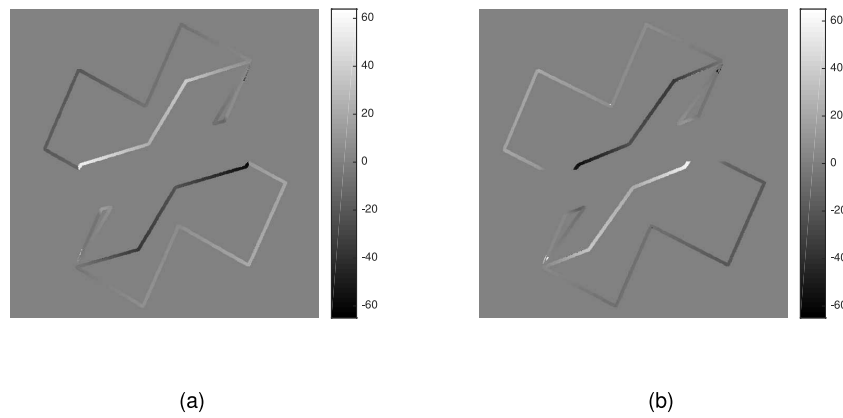


Figure 5.14: **Disparity maps obtained from the rectified stereo views of a pure-amplitude sample.** (a) Left map. (b) Right map. The disparity maps displayed were achieved from a scan with blocks of 5×5 pixels (in contrast to the 3×3 pixels used in the data analysis) to provide a better visualisation. The scale bar denotes disparity, in pixels.

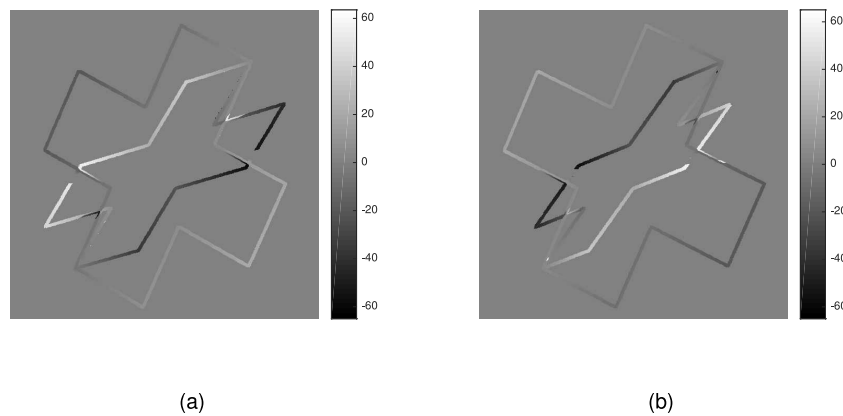


Figure 5.15: **Disparity maps obtained from the rectified stereo views of a phase sample.** (a) Left map. (b) Right map. The disparity maps displayed were achieved from a scan with blocks of 5×5 pixels (in contrast to the 3×3 pixels used in the data analysis) to provide a better visualisation. The scale bar denotes disparity, in pixels.

Observing both sets of images (Figs. 5.14 (a)-(b) and 5.15 (a)-(b)) one can note that the disparity values were only retrieved over the edges of the 3D structure. Indeed, it is ambiguous to find matching blocks in the uniformly-coloured regions. One way to overcome this ambiguity would be to allow really large windows in the scanning process, so that at least two edges are covered by it and therefore, the disparity values of the central region are well framed. However, this would lead to a bad preservation of the object borders, which are in fact our most unambiguous depth references. Thus, we opted for reduced matching-blocks, which favour the disparity over the borders, and restricted the disparity calculations to the border regions of our sample. Hence, blocks of 3×3 pixels were employed and, in the

computational routine, the disparity values were directly set to zero for homogeneous blocks. Besides avoiding disparity calculation errors, this helped reducing significantly the computational time (estimated average in a normal laptop of 18s, for 592×591 pixels images).

Comparing the images of the simulation without and with phase information, one can directly notice the presence of additional disparity data for the last case. The new structures with disparity values are, in fact, the regions of overlap of planes, which in the first case are hidden in the opaque sample. Analysing Fig. 5.15 with detail, one can identify, however, some lost connections in areas of the images which have different superimposition status in the different views. In fact, as the views are acquired in transmission, it happens that a same feature is imaged in a completely different colour tone in the two views, due to the effect of the other superimposed structures in the pixel intensity. In order to avoid the missing of disparity information in these areas, a new disparity estimation was realised, this time targeting specifically the discontinuity regions.

Therefore, a directional gradient [319] was applied to the rectified stereo views of the phase sample and two additional disparity maps were extracted from the resultant images, Figs. 5.16 (a)-(b) and 5.17 (a)-(b), respectively.

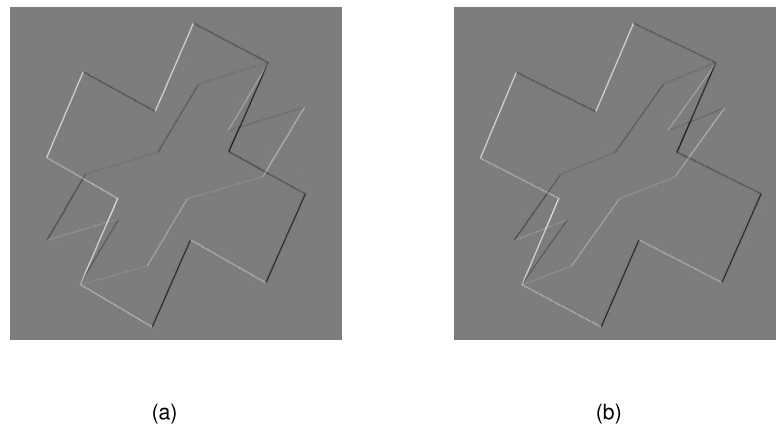


Figure 5.16: **Stereo images of a phase sample submitted to a directional gradient along the x -axis - direction of the disparities.** (a) Left view and (b) right view. The discrete differentiation operator (Sobel gradient operator) [319] computes, at each point, the norm of the gradient vector in x , providing the gradient of the image intensity function.

Observing the disparity maps of Fig. 5.17 one can see that, with the edges identified, the pixel correspondence is allowed in the regions which show superposition of different structures in different views. However, despite presenting more disparity information, these disparity maps present as well more errors. A final disparity estimation is, therefore, ensured by a combination of the four generated disparity maps, where an outliers removal routine gains special importance.

5.3.4 Retrieval of Depth information and 3D Reconstruction

In the reconstructions of the simulated samples, the procedure described in section 5.2.4 was followed.

For the pure amplitude sample, the disparity values of Figs. 5.14 (a)-(b), were first converted into

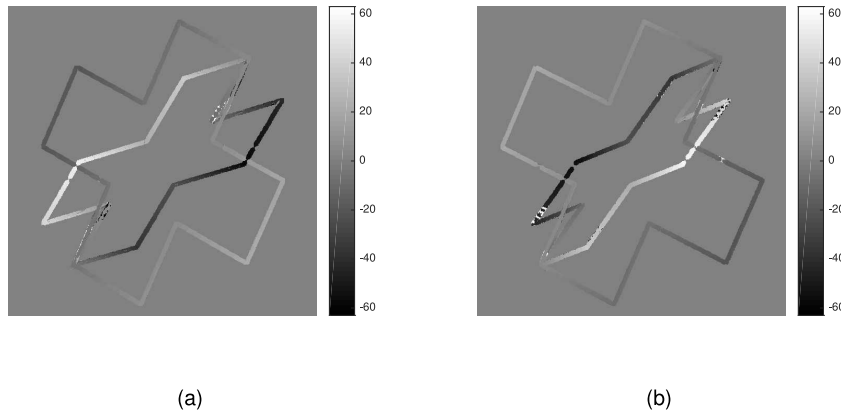


Figure 5.17: **Disparity maps obtained from the gradient-intensity stereo views of a phase sample.** (a) Left map. (b) Right map. The disparity maps displayed were achieved from a scan with blocks of 5×5 pixels (in contrast to the 3×3 pixels used in the data analysis) to provide a better visualisation. The scale bar denotes disparity, in pixels.

depth values, employing equations (5.6), (5.7) and (5.8). After retrieving all the coordinates of the points in the 3D space, the stereo consistency of the two disparity maps was evaluated and only the consistent points were kept. The outliers were then removed with the parameters $\kappa = 20$ points and $\zeta = 0.05$ (see Section 5.2.4), and a point cloud was created (Fig. 5.18 (a)). Due to the high quality of the stereo views, it was immediately possible to identify the existence of two planar structures in the resultant point cloud, each holding a respective cross shape. Noting that the stereo views present a uniform profile surrounding these borders, two plane surfaces were fitted to the 3D data. For the purpose, the *M-estimator Sample Consensus (MSAC) algorithm* [324] was employed. To make sure no false point would interfere with the interpolation, the point cloud was further cleaned to keep only a small amount of consistent points. Thus, points were discarded from a distance of $0.2 \mu\text{m}$ to the fitted surfaces, giving rise to the point cloud of Fig. 5.18 (b).

From the 3D planar surface containing the cross-shaped cut of the membrane, a square frame with three points of length was added to the point cloud (Fig. 5.18 (c)). These points set the limit within which the interpolation would be performed, defining the physical boundary of our 3D rendering. We note that this frame do not necessarily translate the physical extent of our sample, just of our representation. A 3D *Natural Neighbour Interpolation* was then applied to infer the intermediate values, whose depth information could not be retrieved from the disparity maps (Fig. 5.18 (d)) [322, 323]. These values were computed in a mesh of $0.2\text{-}\mu\text{m}$ pitch for all the extent defined by our frame of points.

Crossing the information on the white regions of the stereo views, one extra point cloud was computed, composed by stacks of planar points, which are known to correspond to the empty regions of the sample (Fig. 5.18 (e)). To compute this point cloud, only one stereo view was used. This way, from each coordinate x_2 from the right view, corresponding to an 'empty' pixel (amplitude value 0), the respective sample coordinate x_o was calculated employing Eq. (5.8). This was performed for 600 z_o values in the range of $[-4, 4] \mu\text{m}$. Excluding from the interpolated 3D mesh, the neighbours of this empty-region cloud

(from a 3D-separation distance smaller than $0.1 \mu\text{m}$), a final 3D representation of the simulated sample was reached (Fig. 5.18 (f)). Note that in the images of Fig. 5.18, the sample coordinates used in the textual explanations as (x_o, y, z_o) are denoted by (X, Y, Z) . For simplicity, this coordinate system will be adopted in figures, from now on.

Examining the 3D rendering of Fig. 5.18 (f), one can note that the cross-shaped structure is clearly visible, however it presents some artefact-connections to the membrane in the areas where the different planes superimpose. This stems from the fact that the sample is a pure-amplitude object. In fact, opacity to light induces shadow effects from the occulted areas in the projection geometry. When an interpolation is needed to retrieve a 3D rendering from sparse data points, as in our case, one must be aware of critical areas. Areas of depth discontinuities in the 3D cloud arising from the disparity maps information can reveal superposition of different elements in different depths. If these elements are in the areas where there is no light transmission, as in a pure-amplitude sample, one cannot trace their 3D profile and therefore surface orientation and borders are under-determined.

A similar process was followed for the disparity maps of Figs. 5.15 and 5.17, relative to the phase sample. After discarding the inconsistent points between right and left images, for both pairs of disparity maps, the resultant point clouds were merged. This was performed before the outliers removal process, so that the sample's structure would be more consistent and the outlier points could be more accurately traced. The parameters used for outliers removal were $\kappa = 20$ points and $\zeta = 0.05$ (see Section 5.2.4).

Due to the existence of superimposed structures, it was necessary to identify isolated sample components and to address each component individually. Hence, recognizing the existence of two crosses with different orientations in the achieved point cloud, and noting the flatness of the phase images, two planes were fitted to the 3D shape. Similarly to the previous case, a frame of edge points extracted from the fit to the cross-hole structure was added to the cloud (Fig. 5.19 (a)). Two new point clouds were, then, generated constituted by the inlier points of each fitted plane (inliers considered at distance smaller than $0.2 \mu\text{m}$ from each fitted surface).

The 3D interpolation and removal of the empty volumes for a phase sample followed the same lines of the pure-amplitude case. However, each step was performed for each component/point cloud individually. In fact, for the empty regions removal, each individual component at the sample - attributed to a different point cloud - had to be identified in one of the stereo views and separated in a new modified image, where 0's were attributed to its surroundings. Those images were, then, used in the 'empty-regions' removal for each structure/point cloud, ensuring the component was correctly isolated in the 3D treatment. Note that if the 3D interpolation was made directly for the full point cloud arising from the disparity maps, one would have wrong connections between structures, as the 3D scattered interpolant would treat all the data points as belonging to one single surface.

The final 3D reconstruction of the simulated phase sample can be found in Fig. 5.19 (b). It was reached by assembling together the two sample parts. Comparing with the reconstruction of Fig. 5.18 (f) one can see a clear improvement of the 3D structure, with the access to the phase information. The extremities of the cross, before occluded behind the opaque membrane structure, are now visible

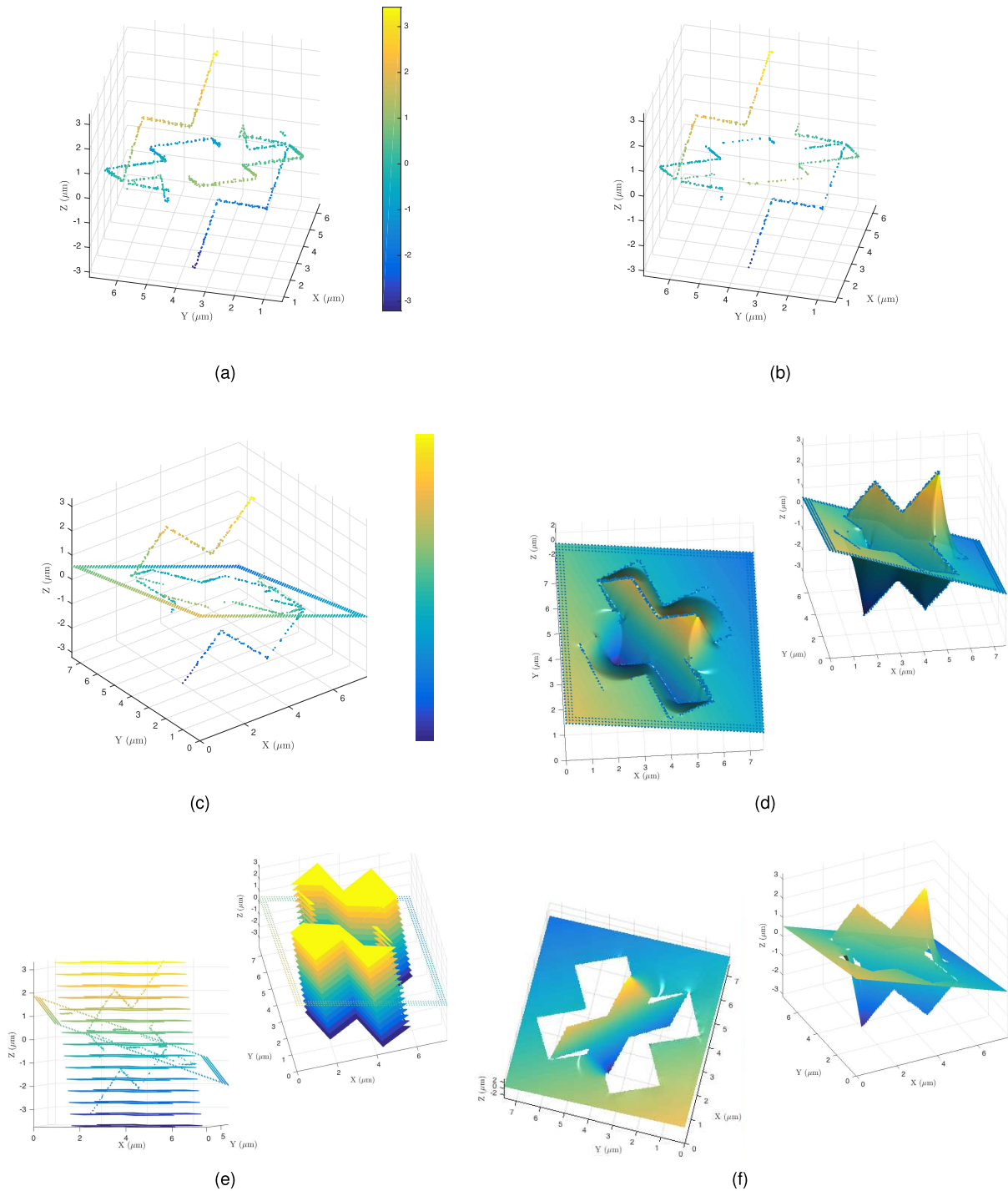


Figure 5.18: Different stages of the 3D reconstruction process of the simulated amplitude sample. (a) Point cloud with the depth information retrieved from the disparity maps. (b) Point cloud (a) after removal of the outlier points. (c) Structure of (b) with a frame of border points achieved from a plane fitting in the cross-hole profile. These will set the limit within which the interpolation will be performed. (d) Scattered interpolation over all the point cloud, from two perspectives. (e) Stack of planes in the 3D space corresponding to empty areas of the sample. Only a selection of 15 equidistant planes is shown, for better visualisation. (f) Final 3D reconstruction, from two perspectives. For a better understanding of the 3D structure, the colour scale of all figures represents the depth value, Z , in μm .

and their 3D orientation revealed. Indeed, the information on the phase shifts unveils the existence of superimposed planes, which allows retrieving 3D features otherwise hidden.

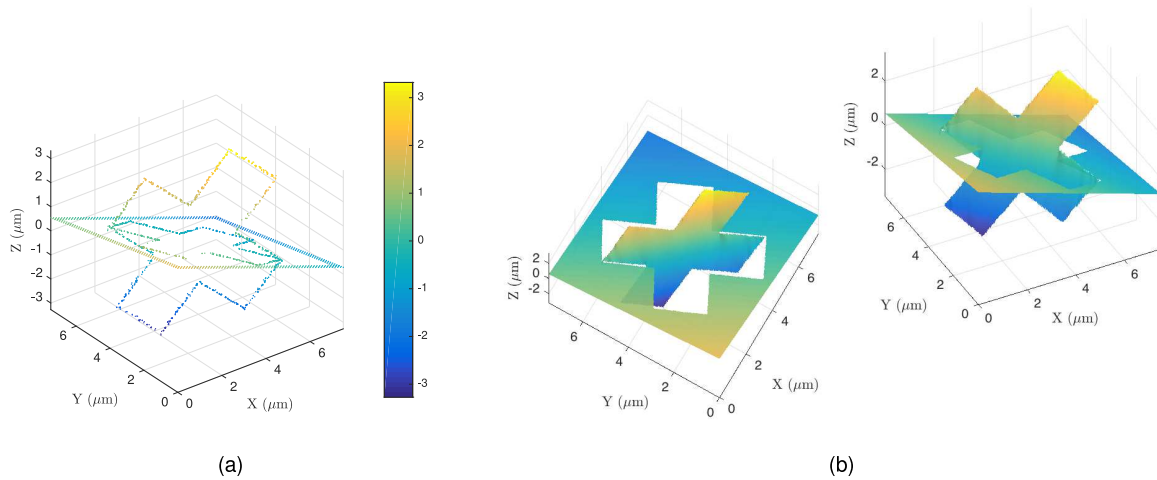


Figure 5.19: **Point cloud and final 3D reconstruction of the simulated phase sample.** (a) Point cloud with the depth information retrieved from the disparity maps with a frame of edges points achieved from a plane fitting in the cross-hole structure. (b) Final 3D reconstruction, from two perspectives. For a better understanding of the 3D structure, the colour scale of all figures represents the depth value, Z , in μm .

Overall, for a phase sample with clear edges we obtain a satisfying 3D rendering, with relevant depth content on the object. This simulation shows that ambiguities can be reduced by using the information on the phase of the object. In fact, investigating cooperatively the information of amplitude and phase of a sample gives us additional stereo views and, therefore, extra useful information to correlate for the 3D reconstruction. This is indeed one of the big advantages of exploiting this technique integrated with lensless CDI, where these reconstructions are retrieved simultaneously, if the object is not a pure-amplitude sample.

Phase contrast stereo imaging can be further exploited for multiple applications, having a special impact if 3D information is combined with femtosecond-temporal resolution.

5.4 Computer Stereo XUV Imaging in Single Acquisition Using a Pure-amplitude Sample

The present section describes our experimental implementation of single-acquisition stereo lensless imaging. In this first experimental study we demonstrate stereo imaging using an XUV optical setup, based on the separation of a high-order harmonics (HH) beam into two coherent sub-beams. These sub-beams are focused on the sample with a controllable angle, permitting the capture of two stereo diffraction patterns in single acquisition. The setup employed allows nanometre-transverse resolution in a femtosecond timescale.

5.4.1 Experimental Setup

The experiment was performed at LUCA's beamline of the SLIC laser centre in CEA Saclay, employing the imaging apparatus of Fig. 5.20. The high-order harmonics setup is described in section 3.3.

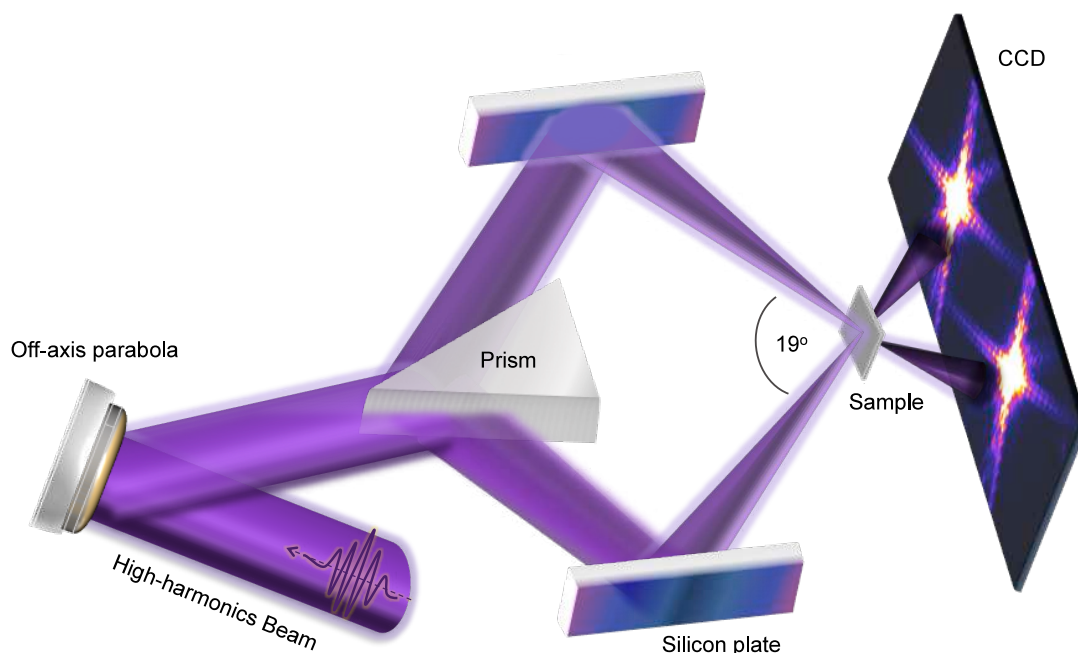


Figure 5.20: **Experimental setup for single acquisition 3D stereo imaging.** A multilayer coated off-axis parabola selects harmonic 33 from the laser beam ($\lambda = 24$ nm) and focuses it into the sample. A grazing-incidence prism inserted after the focusing optics splits the beam into two stereo halves. Controllable silicon mirrors are then used to reflect each sub-beam onto the sample. A single CCD camera is positioned in the far field and used to simultaneously record the two diffraction patterns, which constitute the input images to generate the two stereo views.

Briefly, the source is generated from an amplified Ti:Sa laser system, which delivers 30 mJ - 60 fs pulses, with a loose-focusing geometry. The harmonics are generated in a neon gas cell. A 22.5° off-axis-parabola of 20 cm focal length is employed to focus the harmonics beam into a $5 \times 7 \mu\text{m}$ focal spot (FWHM). This parabola also selects harmonic 33 ($\lambda = 24$ nm), thanks to a multilayer coating deposited on its surface. After optimisation, this apparatus provides 4×10^9 photons/pulse with the beam properties given by Table 3.2.

To generate the two sub-beams, a grazing incidence prism (6°) was inserted between the off-axis parabola and the sample, in order to increase the angle between the two sub-beams, otherwise limited by the parabola's aperture (Fig. 5.20). The sharp edge of the prism splits the HH beam into two halves. Two flat silicon mirrors were then adjusted such that the two-beams foci overlapped at the sample's position. The focus of each stereo spot was then enlarged (compared to the direct parabola's focusing) to $10 \times 7 \mu\text{m}^2$ at the sample's position. As the reflection angle in the parabola also limited the angle

between the two sub-beams in the experimental apparatus, the arrangement was implemented vertically in the vacuum chamber (note that, in Fig. 5.20, the setup is displayed horizontally to provide a better visualisation and to follow the standard stereo design, where the stereo pair renders right and left views).

After the two synchronised X-ray stereo-beams illuminate the sample, they are diffracted by it and detected, simultaneously, on a single CCD camera. From the average number of photons per pulse captured in the far field, the XUV transmission of the overall apparatus was estimated to about 75% for the operating wavelength.

To implement the synchronised stereo system, a first rough alignment was made with the incident infra-red (IR) beam to verify the superposition and the angle between the two sub-beams. At first, the height of the prism was corrected for a balanced division of the two sub-beams. After, the angle was set by aligning the top beam onto the sample. The next step consisted in adjusting the bottom beam at the symmetric angle by superimposing it on top of the top beam. To validate the temporal and spatial overlap of the stereo beams, a Beta-Barium Borate crystal (BBO) was employed. The second harmonic generated by phase matching the top and bottom beams was measured. The final alignment was then performed by visualising the XUV beam transmitted by the sample.

The positions and tilts of the two silicon plates were remotely controlled by vacuum compatible motors, offering the possibility to change the angle between the two optical lines. The position of the sample was controlled by piezo controllers to allow an effective search for the parabola's focus. Overall, this configuration enables a fine tuning of the time delay with sub-femtosecond jitter between the two pulses. It offers therefore a compatible alternative to perform femtosecond time-resolved X-ray-pump/X-ray-probe experiments.

5.4.2 3D Sample and Generation of the Stereo Views

The sample used in the experiment consists of a $6.9 \times 6.1 \mu\text{m}^2$ cross (Fig. 5.21), drilled on a membrane with a focused ion beam (see section 3.4). The composition of the membrane includes 75 nm of Si_3N_4 , a 150-nm Au layer and 4 nm of Cr for adhesion of the gold to the substrate. The outer edges of the cross were first patterned with a low gallium ion current. The soft patterning allowed to control the attachment of the inner cross to the edges. The 3D was then created by the natural rotation of this cross about two contact points.

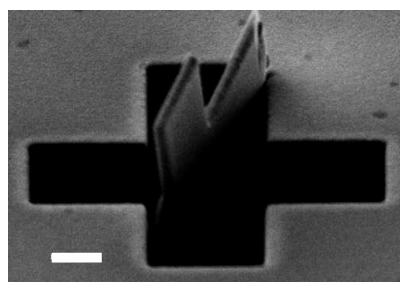


Figure 5.21: **SEM (scanning electron microscopy) image of the experimental sample, observed at a 60° angle.** The scale bar has a length of $1 \mu\text{m}$.

Due to the gold layer in its constitution, the membrane is totally opaque to high harmonic radiation. It depicts, therefore, a purely binary amplitude object (transmission 0 or 1), similarly to the homologous simulation in the previous section.

5.4.2.1 Stereo diffraction patterns

The two XUV beams provided by our stereo system were focused on the sample with an angle of 19° between them (see Fig. 5.20). Even though this angle is generally large for a stereo approach, this value choice ensured a good compromise between the aperture-size of the CCD (so that relevant high frequencies are not cut) and the overlap of the two diffraction patterns in the array.

The CCD detector was located 26 mm away from the sample, fulfilling the required conditions to perform two CDI reconstructions from the two resulting diffraction patterns. Indeed, these setup conditions place our sample in the far field, $Z \gg 1.5$ mm ($F \ll 1$, Eq. (2.19)), and lead to an oversampling ratio of $O = 8$ (Eq. (2.52)), with $a = 6$ μm .

A typical set of stereo diffraction patterns, acquired under these conditions, is shown in Fig. 5.22. The figure shows a logarithmic scale diffraction pattern, rotated by 90° clockwise, obtained for an acquisition of 180 s with 2×2 -pixels binning. The number of useful diffracted photons in each diffraction pattern is roughly equivalent, estimated in the order of 10^7 photons per shot. In the figure, the diffraction pattern on the left originates from the beam reflected by the top silicon plate (top view of the sample) and the right one from the beam reflected by the bottom plate (bottom view of the sample). From now on we will proceed with the data treatment with this notation, and therefore will address the bottom/top views of the sample as left/right views, respectively.

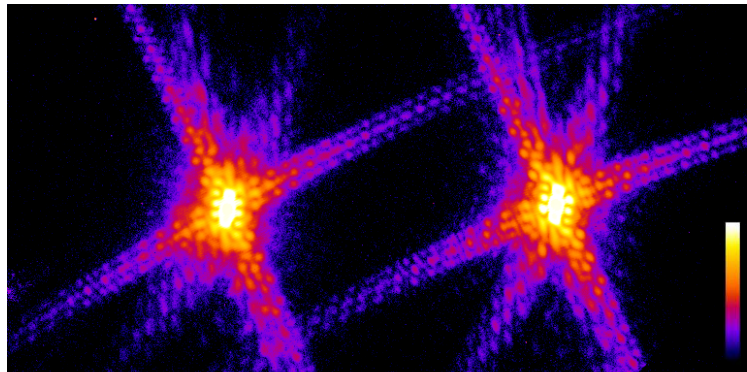


Figure 5.22: **Typical dual diffraction pattern of the pure-amplitude cross sample.** Diffraction patterns, achieved from the two stereo beams, recorded on a single X-ray CCD. The image is shown in logarithmic colour scale, with arbitrary units. The accumulation time was 180 s.

Still exploring Fig. 5.22, one can notice that the two patterns exhibit an overlap in the high-spatial frequency regions originated by the mutual detection in a single CCD. This is, however, not a problem of our system as this part of the diffraction pattern can be excluded without deteriorating the resolution of the reconstruction. In fact, the overlap occurs for spatial frequencies higher than 6.6 μm^{-1} , which correspond to a theoretical resolution of 75 nm at the sample.

To compensate for the limited photon flux and the low dynamic-range of the CCD, the diffraction patterns that originated from our stereo views were post-processed with *high dynamic range* (HDR) techniques [325]. Hence, the diffraction data were recorded for different acquisition times ranging from 30 s to 240 s. These acquisition times correspond to patterns fully acquired close to the CCD saturation and with maximal exposure time (saturated diffraction pattern), respectively. After selecting the two extreme cases for each stereo figure, these two were merged. The process was as follows. At first, the two stereo patterns were isolated by cropping slightly before the overlapped part, in order to work individually with each projection. The central part of the short-acquisition pattern was then recombined with the higher frequencies of the one with the large-integration time. A Gaussian filter ($\sigma = 2$) was used on the edge of the non-saturated area of this last, to stitch it smoothly to the respective area of the low-range diffraction pattern. A ratio, extracted from both corresponding non-saturated regions, was then applied to appropriately rescale the intensity values. The resulting diffraction figures can be observed in Fig. 5.23. Note that the two patterns were achieved with different acquisition times for the low-exposition images, in order to optimise the dynamics for each case. Hence, the HDR diffraction pattern from the right view merged the integration times of 30 s and 240 s (Fig. 5.23 (a)), while the left view was achieved with a combination of 35 s and 240 s (Fig. 5.23 (b)).

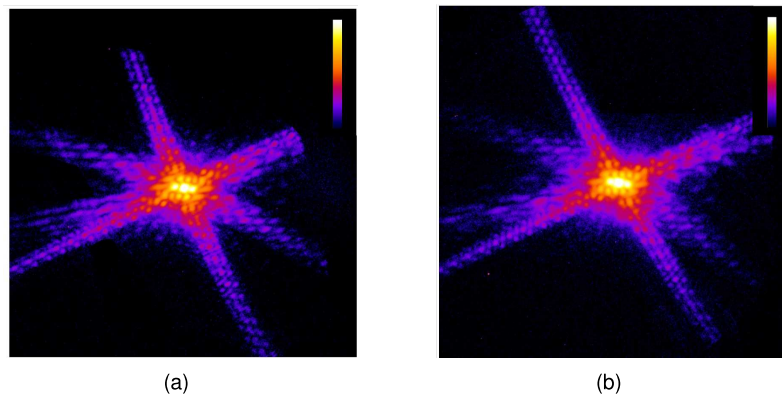


Figure 5.23: **Pair of diffraction patterns, from the pure-amplitude cross sample, after post-processing with HDR.** (a) Diffraction pattern from the top beam (right view after rotation) isolated and treated with HDR, with integration times of 30s and 240s. (b) Diffraction pattern from the isolated bottom beam (left view) processed with HDR with integration times of 35s and 240s.

5.4.2.2 Stereo views from coherent diffraction imaging

After the HDR post-processing, both diffraction patterns of Fig. 5.23 were reconstructed using a phase retrieval algorithm [36]. The iterative routine used to reconstruct the two diffraction patterns was the *difference map* algorithm, with support and Fourier magnitude as the two constraints (see Section 2.3.1). An initial support was generated by thresholding the autocorrelation of the HDR diffraction patterns at 5% of their peak intensities.

For each projection, we launched 45 independent runs of the algorithm and selected, for each run, the iteration that minimised the error function of Eq. (2.36). In our case, the algorithm converged after

roughly a hundred iterations. The *DFT image registration* algorithm [163] was then used to superpose the reconstructions with sub-pixel precision and average them to neutralise some of the amplitude fluctuations in the reconstructions.

Figures 5.24 (a)-(b) show the 2D amplitude reconstructions of the two diffraction patterns achieved experimentally, corresponding to the left and right views of the sample, respectively. The spatial resolution of each view was estimated to be 127 nm, by the 10-90% criteria. Differences between the two views are clear: all the edges of the cross-lid structure are visible in Fig. 5.24 (b), whereas some of them are hidden in Fig. 5.24 (a). Indeed the 19° angle showed relevant view differences, including some regions of major occlusions.

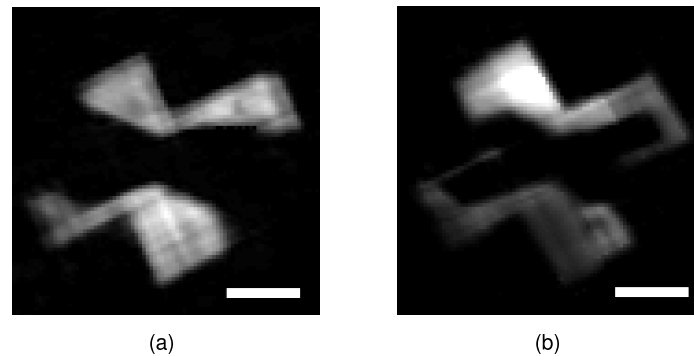


Figure 5.24: **Pair of experimental stereo images from the pure-amplitude cross sample.** 2D-amplitude reconstructions, corresponding to the (a) left (stereo angle -9.5°) and (b) right (9.5°) views of the sample, respectively. They are obtained from HDR diffraction patterns and correspond to the coherent average of 45 reconstructions from independent runs of the CDI algorithm. Each view reaches a spatial resolution of 127 nm. The scale-bar length is 2 μm .

As we see, qualitative 2D structural and spatial information from two observation angles can be achieved in a setup compatible with single femtosecond acquisition. It is even possible to go further and recover depth information from those images as we will disclose in the next steps.

5.4.3 Pre-processing of the CDI Stereo Views

One of the fundamental requirements of Computer Stereo Vision is similar illumination conditions in both views. This happens because the stereo technique is based on pixel/features matching and, therefore, is extremely sensitive to pixel magnitude variations. In the current configuration, the stereo views, arising from a CDI reconstruction routine, are affected by strong intensity modulations. Those can have their cause either in algorithm-related artefacts inherent to the CDI technique (specially critical in low-photon-flux regimes), either in experimental issues as for instance the beam non-uniform intensity profile and partial coherence. Moreover, in a transmission configuration, intensity variations can be ambiguous. Strong intensity attenuations can either arise from refractive-index variations within the sample (e.g. crossing different materials) or same refractive-index structures with longer thicknesses along the imaging axis. Consequently, depending on the quality of the data and the shape of the features present in the sample, additional pre-processing may be mandatory. To minimise depth calculation errors due to

all these phenomena, the followed approach relies on identifying non-ambiguous features to retrieve the depth information. In the cases where these features are too sparse as, for instance, objects with spherical structures or smooth gradients, the intermediate depth values are retrieved through 3D interpolation methods, upon crossing the information of the achieved 3D shape with the stereo views.

For the stereo images of Fig. 5.24, because of the limited SNR, a first step of binary conversion was required. This helped highlighting the edges of our 3D sample in order to use them as unambiguous depth references. Therefore, first, the images were resized by a factor 4, with a *bicubic* interpolation in the intermediate pixels (in a *bicubic* interpolation, the output pixel value is given by the weighted average of the pixel-values in the nearest 4-by-4 neighbourhood). A Gaussian low pass filter was then applied to both images to reduce the effect of the noise (standard deviation $\sigma = 1.9$). After filtering, the images were turned binary by defining suited binary thresholds. In left and right images, respectively, in a 0-to-1 scale, the thresholds used were 0.40 and 0.25. These differentiated values intended to reproduce as accurately as possible the limits of our sample in both images. Finally, to avoid errors in the binary conversion, the isolated regions constituted by less than 400 aggregated pixels, with no correspondence in the pair image, were removed.

Since both views were recorded with the same CCD, the parallel camera system is satisfied and no rectification was required. The images needed, however, to be centred with respect to each other. Thus, in the stereo views of Figs. 5.24 (a)-(b), thirteen edge points were manually selected (see Fig. 5.25 (a)). Using the four extremity points of the hole-cross in both views, both images were re-centred according to the central position obtained from these points. All the remaining selected points were used to refine this central position.

The final stereo anaglyph, generated from this process, can be observed in Fig. 5.25 (b). Note that with the rotation accounted in the earlier section for the diffraction patterns (and respective reconstructed stereo views), the epipolar lines should be already horizontal and, therefore, coincide with the image rows.

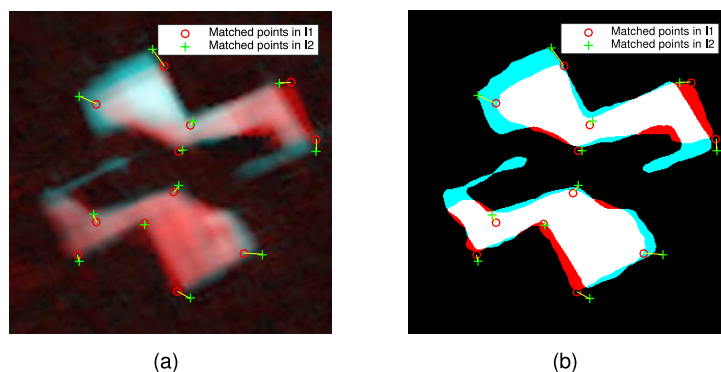


Figure 5.25: **Stereo anaglyphs of the experimental pure-amplitude cross sample.** (a) Before pre-processing. (b) After pre-processing. In the images, the red/cyan areas correspond to the empty areas of the left and right stereo images, respectively. Empty areas, which are common to both, are coloured white.

From a fast analysis of Fig. 5.25 one can directly see that the epipolar constraint is not flawlessly

fulfilled by our rectified stereo images. Observing the points which should match in both views, one can easily realise that most of them present more than just a horizontal offset. A process of image rectification was, thus, performed to the images in order to evaluate if it was a rectification problem. Note that, in principle, this could only be the case if there was an angle in the stereo system, namely in the diffraction patterns at the CCD, which made the epipolar lines with an angle with respect to the horizontal reference. With this additional rectification, however, the resultant images were too distorted and led to a completely deformed 3D reconstruction. This made us believe that the epipolar mismatches derived from artefacts in the experimental CDI reconstructions, due to the low SNR or beam aberrations; or due to the projection angles of the diffraction patterns on the CCD. Discarding this rectification test, the further steps of the reconstruction process used the stereo images of Fig. 5.25 (b).

5.4.4 Stereo Matching and Computation of the Disparity Maps

Using the method described in section 5.2.3, two disparity maps were generated. Figs. 5.26 (a)-(b) represent, respectively, the disparity of the left image with respect to the right one (left map) and vice-versa (right map).

In this part, blocks of 3×3 were used, and the disparity range N was established to 65 pixels. Similarly to the simulation case, we sought for disparity calculations along the object edges and, therefore, prioritised the borders accuracy over the (horizontal) disparity continuity, later compensated with a 3D interpolation. The weighting factor α was defined to 0.01, since its purpose was just to act as a tie-breaking criteria, in case more than one matching block was found with the SAD benchmark.

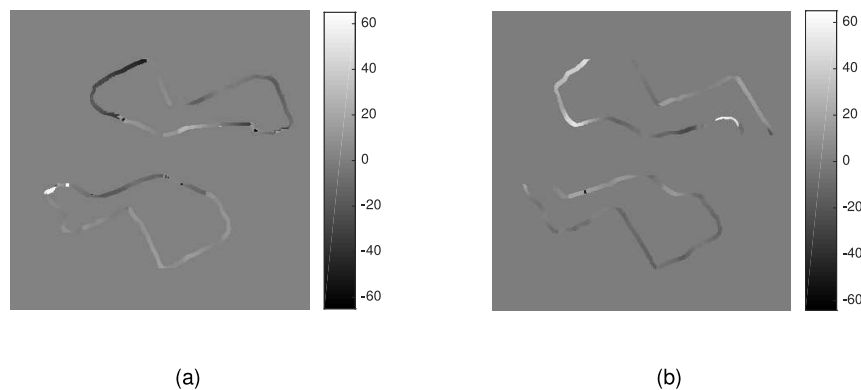


Figure 5.26: **Experimental disparity maps computed from the stereo views of the pure-amplitude cross sample.** (a) Left map. (b) Right map. The disparity maps displayed were achieved from a scan with blocks of 5×5 pixels (in contrast to the 3×3 pixels used in the data analysis) to allow a better visualisation. The scale bar denotes disparity, in pixels.

Observing the images of Fig. 5.26, one can see that no disparity values were found for the internal borders of the cross. In fact, inspecting the stereo images (Fig. 5.25 (b)) only one has these borders defined, which implies no relative position can be traced and, consequently, no depth information can be achieved in those areas. Moreover, one can note recurring discontinuities in the disparity values, contrasting with the smooth disparity contour achieved in the simulation with a pure-amplitude sam-

ple (compare with Fig. 5.14). This may reveal some depth errors in the measurements, which were somehow predictable due to the deficient fulfilment of epipolar constraints, as discussed in the previous step.

5.4.5 Retrieval of Depth Information and 3D Reconstruction

The 3D rendering of the experimental sample was achieved similarly to the simulation case of a pure-amplitude sample. After depth computations employing equations (5.6)-(5.8), the disparities consistency was evaluated likewise. This time, however, due to the worst quality of the point cloud achieved from the disparity estimations, the constitution by plane surfaces was not straightforward to observe. The post-processing was, thus, followed with the whole undefined structure, without outliers removal by fitted surfaces. The outliers removal routine consisted just of a simple detection of isolated 3D points from the cloud arrangement ($\kappa = 80$ points and $\zeta = 0.05$). A single plane fitting was, though, performed to the data points, but merely to retrieve the frame of points that would set the limit of the 3D interpolation in the membrane. The final point cloud is presented in Fig. 5.27 (a).

Similarly to the simulation, the 3D Natural Neighbour Interpolation was applied to infer the intermediate values. Those were computed in a mesh of 0.05- μm pitch for all the (x_o, y) extent defined by our frame of points. The empty-region cloud of the experimental sample was retrieved from the right stereo view, which provided additional information concerning the borders of the internal cross. This was performed for 150 z_o values in the range of $[-3.7, 3.7]$ μm . Excluding from the interpolated 3D mesh, the neighbours of this empty-region cloud (from a 3D-separation distance smaller than 0.05 μm), a final representation was reached. The 3D rendering of the experimental amplitude sample can be found in Fig. 5.27 (b). A surface was plotted in the data points to allow for a better visualisation.

Analysing the depth representation of Fig. 5.27, one can see that while the cross shape of the hole in the membrane is clearly visible, the reduced signal quality makes the reconstruction of the cross-lid more difficult. Furthermore, the reconstruction obtained presents some artefact connections to the membrane in the areas where the different planes superimpose. This effect, arising from the pure-amplitude nature of the sample, is not new and it was also observed and discussed for the simulation.

Indeed, the depth map retrieved does not seem to be the most accurate representation of our sample. As discussed in the previous sections, the epipolar constraint is not clearly fulfilled in our CDI stereo views, which points out some issues. These issues can have their cause in the signal quality (low signal-to-noise ratio); beam aberrations; and, as well, in the high angle used. That high angle induces some projection of the diffraction patterns on the detector, which was not taken into account. Additionally, the 19 $^\circ$ -angle employed, besides providing better theoretical depth-resolution, originated a left view without details on the internal-cross edges, precluding depth estimations in those areas.

The geometry of our system leads to a voxel size of $49 \times 49 \times 146 \text{ nm}^3$ and an estimated 3D spatial resolution of $127 \times 127 \times 379 \text{ nm}^3$. The voxel size was calculated by combining the xy pixel size, Δ_{obj} , obtained from each phase retrieval reconstruction and its corresponding projection on the z axis given

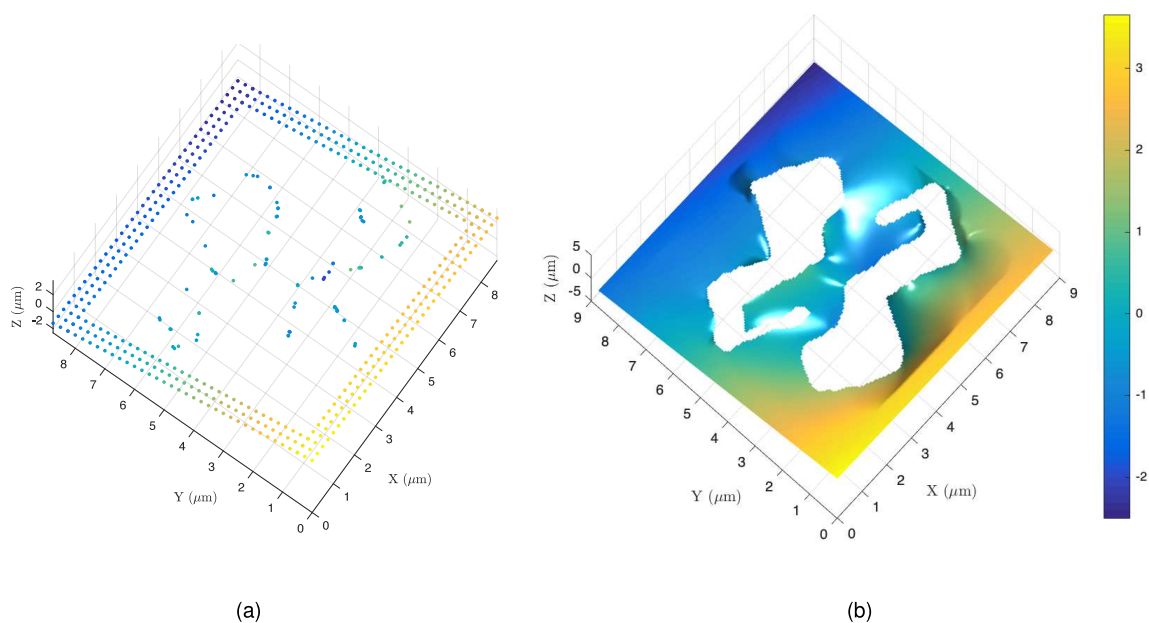


Figure 5.27: **Point cloud and final 3D rendering of the experimental sample of a pure-amplitude cross.** (a) Point cloud with the depth information retrieved from the disparity maps, after consistency check and outliers removal. It contains as well a frame of edges points achieved from a plane fitting in the structure. These will set the limit within which the interpolation will be performed. (b) Final depth representation of the experimental sample of a pure-amplitude cross. The colour scale is common to both images and represents the depth value, Z , in μm , for a better visualisation.

by:

$$\Delta_z = \frac{\Delta_{obj}}{\tan\theta_1 + \tan\theta_2} \quad (5.9)$$

The spatial resolution was estimated by combining the xy spatial resolution obtained for each stereo scene (using 10-90% Rayleigh criterion) and the respective z -depth resolution estimated using Eq. (5.9). We would like to note that this estimation does not account for resolution degradations arising from the numerical processing.

In this experimental study we made the first proof-of-principle of computed CDI-stereo imaging with a HH source. We were able to retrieve depth insights of a pure amplitude sample in a stereo X-ray setup compatible with single acquisition. This technique, developed with more photon flux, allows the imaging of dynamical processes in 3D with a sub-100-nm voxel, at temporal resolutions in the femtosecond range. With a huge impact in 3D structural imaging of single macromolecules, for instance, this technique finds important applications in materials science, medicine and biology.

5.5 Computer Stereo X-ray Imaging Applied to Curved Biological Samples

In this section, we discuss the application of computed X-ray stereo vision to biological samples with predominantly-curved topography. This demonstration exploits two projections from tomographic data

published and made available by Nishino *et al.* [244].

5.5.1 3D Sample and Generation of the Stereo Views

The sample used for this study was an unstained human chromosome. A set of CDI data from this sample was collected at a photon energy of 5 keV, from a coherent X-ray diffraction microscope, using the BL29XUL hard X-ray undulator beamline at SPring-8. The schematic of the setup is shown in Fig. 5.28 (a) and the procedure is described in detail in Nishino *et al.* [244].

The analysis of coherent X-ray diffraction data, acquired from 38 incident angles, originated the chromosome reconstructions of Fig. 5.28 (b). The sample, as one can see in the schematic figures, possesses a highly smooth structure, with no edged-borders or few-pixel-resolved features.

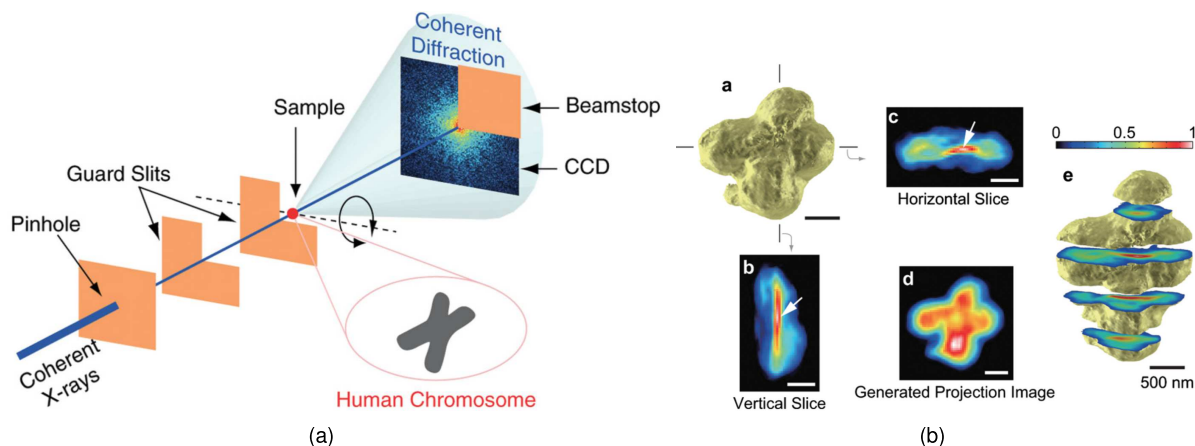


Figure 5.28: **Coherent hard X-ray diffraction microscopy of an unstained human chromosome and reconstructed 3D electron-density map.** (a) Schematic of the experimental setup. A 20- μm -diameter pinhole defined the illumination for a single chromosome, while two guard slits carefully aligned reduced the amount of missing data near forward-scattering angles. An X-ray CCD detector was used to acquire the coherent diffraction data. A beam stop blocked the unscattered direct X-ray beam, and shaded nearly a quadrant area of the CCD. The sample was rotated for 3D image reconstruction. (b) Reconstructed 3D electron-density map of an unstained human chromosome. One can observe, in **a**, the isosurface of the chromosome drawn with a threshold value at 15% of the highest density. In **b,c** two planes of the cross-sectional images are presented, including the position of highest electron density near the centromere (indicated by arrows). A projection image generated from the 3D reconstruction is shown in **d**, while **e** provides cross-sectional images of the chromosome at 409 nm intervals. All images were extracted from Nishino *et al.* [244].

In this work, only two 2D CDI reconstructions were exploited, recorded at a separation angle of 5° . Figs. 5.29 (a)-(b) show the respective left and right stereo-views of the sample. The spatial resolution of each view is estimated to be 38 nm [244].

5.5.2 Pre-processing and Image Rectification

Since the stereo views from Fig. 5.29 were acquired from a rotation of the sample, a rectification step was necessary.

In order to find a set of point correspondences between the two stereo views in a systematic way, several feature detection and feature matching algorithms were, at first, tested in the images of Fig.

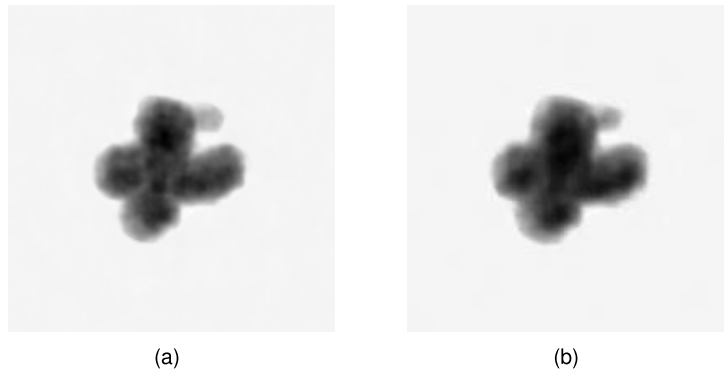


Figure 5.29: **Pair of CDI stereo images from an unstained human chromosome sample.** Stereo angles: (a) 10° - left view, (b) 15° - right view.

5.29 [259–266]. The matching points achieved with this approach were, however, not correct due to the ambiguity of the object features in transmission geometry. A manual approach was then followed and, therefore, ten corresponding points were manually selected in the two images (see Fig. 5.30 (a)). Applying the Normalised Eight-Point Algorithm to these points and allowing the exclusion of outlier points in a confidence level of 80%, the fundamental matrix between both views was computed. The images were then re-projected onto a parallel camera system, following the procedure described in section 5.2.2. The images resulting from the rectification can be observed in Fig. 5.30 (b). They are presented superimposed to create an anaglyph.

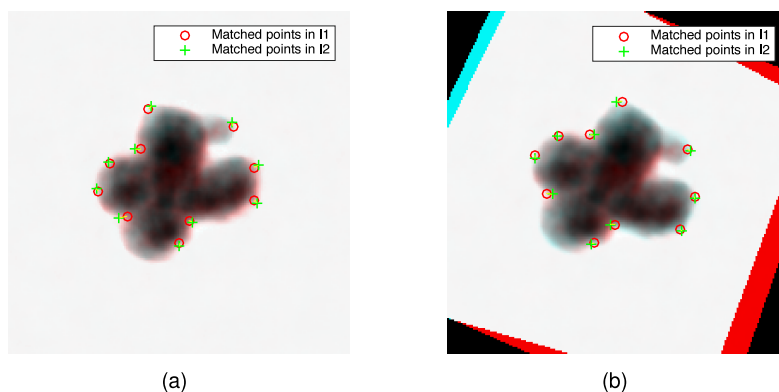


Figure 5.30: **Stereo images of the human chromosome sample, with corresponding point matches, before and after rectification.** (a) Original and (b) rectified stereo views, superimposed, with selected points and respective matches. Image (b) consists of an anaglyph.

In order to avoid disparity calculations errors due to the background noise, the images of Fig. 5.30 (b) were pre-processed with a background filtering. For the purpose, binary masks including the object areas were extracted from the stereo views and multiplied by it in order to provide a uniform background before the disparity analysis. The masks used for this part are shown in Figs. 5.31 (a)-(b) with a black colouration for better visual contrast. The chromosome reconstructions were included in the allowed area for reference. The final stereo images can be seen in Figs. 5.32 (a)-(b).

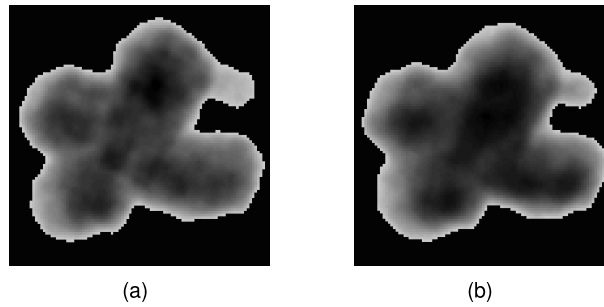


Figure 5.31: **Masks employed for background removal in the human chromosome stereo views.** Mask (represented in black) which was multiplied by the rectified (a) left view (b) right view in order to remove the background noise. Note that in the final stereo images, the background is white.

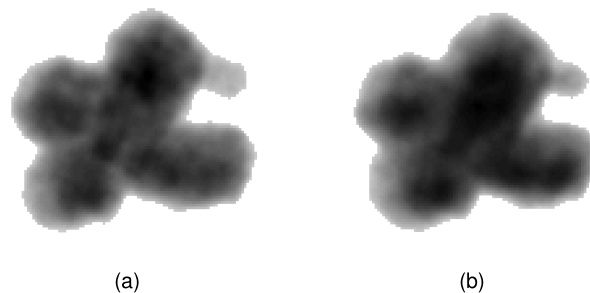


Figure 5.32: **Final stereo views of the unstained human chromosome, after rectification and pre-processing.** (a) Left view. (b) Right view.

5.5.3 Stereo Matching and Computation of the Disparity Maps

Using the method described in section 5.2.3, two disparity maps were generated from the stereo images of Figs. 5.32 (a) and (b). Figs. 5.33 (a) and (b) present, respectively, the disparity of the left image with respect to the right one (left map) and the reverse case (right map) achieved for the human chromosome sample.

In the disparity maps presented, the disparity range N was allowed to 12 pixels, the weighting factor α was defined to 0.01 and the block-matching process was performed with blocks of 29×29 pixels.

Several smaller sized windows were tested before arriving to the block dimensions presented in the figures. For this sample, particularly textureless, smaller support windows were constantly finding random values, full of sharp disparities, originating a completely non-smooth map. Indeed, the drawback of blocks-reduced sizes, in these types of samples, is that they are often unable to capture enough texture variation to resolve matching ambiguities. For that reason, a scan of windows sizes was made, and the smaller value, from which the disparity profiles were giving the same results, was kept. This value corresponded, as well, to the threshold from which the disparity profiles became smooth.

The problem of larger windows is, however, that they fail in the preservation of disparity/depth discontinuities, something evident in the images of Figs. 5.33 (a)-(b). In our configuration, this is, nonetheless, not a limitation. One can, in fact, consider that the object has a clear border line, actual requisite for the CDI algorithm to converge (in other words, the object must be contained inside a finite support). This

support/ border line was actually identified in the previous step and used as a binary mask for background filtering. Therefore, the final disparity maps of the human chromosome sample are shown in Figs. 5.33 (c) and (d), resulting from the multiplication of the disparity values of Figs. 5.33 (a)-(b) by the masks of Figs. 5.31 (a) and (b), respectively. As one can see, they present a smooth disparity profile, while preserving the sample border lines.

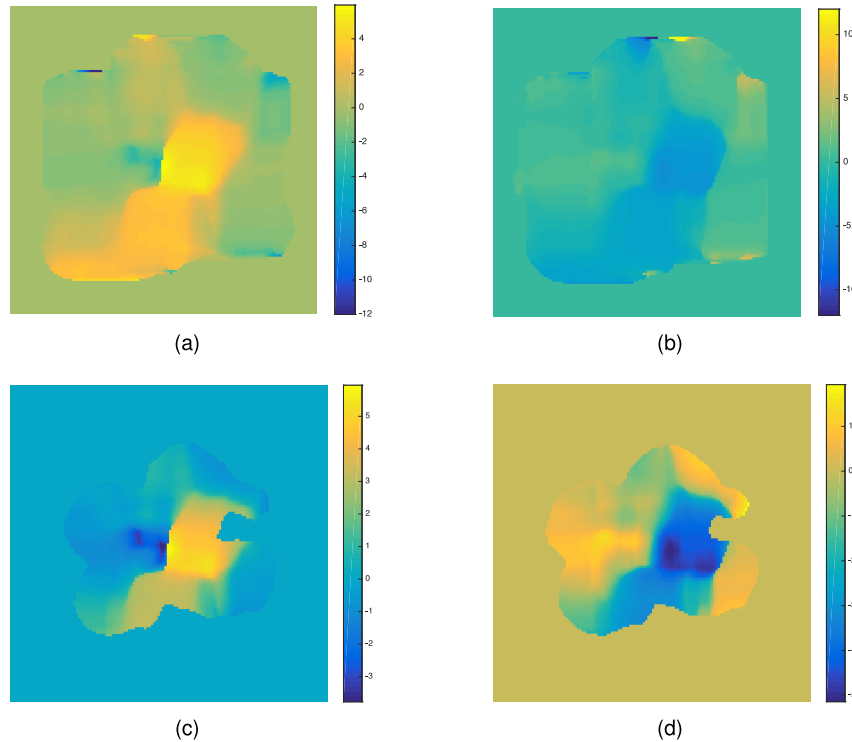


Figure 5.33: **Disparity maps obtained from the rectified stereo views of the human chromosome sample.** (a) Left map without borders correction. (b) Right map without borders correction. (c) Left map with multiplication of background-removal mask. (d) Right map with multiplication of background-removal mask. The disparity maps displayed were achieved from a scan with blocks of 29×29 pixels. The colour bar denotes pixels.

5.5.4 Retrieval of Depth Information and 3D Reconstruction

The retrieval of depth information from the disparity maps of Figs. 5.33 (c)-(d) followed the steps described in Section 5.2.4.

After computing all the coordinates of the points in the 3D space, using the same methodology as before, the stereo consistency of the two disparity maps was evaluated. This bi-directional check was performed with x_o , y and z_o values rounded to one decimal digit, as the disparity range found was considerably smaller than in the previous cases.

From the consistent points, the outliers were removed. This was executed with the parameters $\kappa = 80$ points and $\zeta = 0.05$ (see Section 5.2.4). As this time the borders of the 3D cloud were properly defined and, as well, the data points did not obey a standard profile, no surface fitting was performed. In Fig. 5.34 (a) one can find the final point cloud containing the depth information computed with the

stereo approach. A surface was plotted in the data points to allow a better visualisation of the resultant structure. One can observe it in Fig. 5.34 (b).

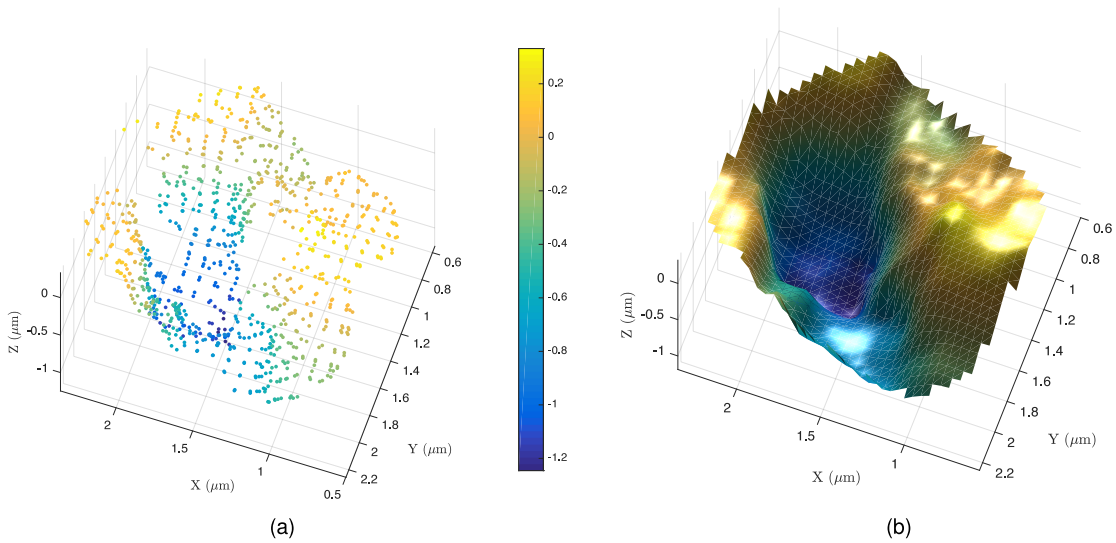


Figure 5.34: **Point cloud and surface plot of the experimental sample of an unstained human chromosome.** (a) Point cloud with the depth information retrieved from the disparity maps, after consistency check and outliers removal. (b) Surface plot in the data points to allow a better visualisation of the structure achieved. The colour scale is common to both images and represents the depth value, Z , in μm .

Comparing the depth-structure found in Fig. 5.34 with the reconstructed 3D electron-density map in Fig. 5.28 one can see immediate differences. In fact, the stereo approach found clear matching ambiguity and it is important to investigate why, in order to find the limitations of the technique. Coming back to the stereo images of Fig. 5.29 (a)-(b), they constitute electron-density projections of our sample. This means that each pixel magnitude encodes the density of electrons affecting the beam propagation along that specific optical path. When we use such images as input for a stereo-matching approach, the pixel matching do not translate the difference in relative positions of features from two well known viewpoints. Instead, it translates a correspondence between the sample's thickness *versus* constitution/density, which varies with the imaging axis. Such correspondence between two viewpoints has, hence, no physical meaning and absolutely no relation with depth. Consequently, equations (5.6), (5.7) and (5.8) do not apply, and the images of Fig. 5.33 are incorrectly called disparity maps.

The phenomenon described above affects both, amplitude and phase projection images, from samples with curved morphologies and non-negligible thickness. Indeed, both amplitude and phase CDI reconstructions vary with the sample's refractive index along the beam path, discretized in each pixel value. Hence, similar pixel magnitude variations can stem from refractive-index changes within the sample (e.g. crossing different materials/densities), or same-refractive-index structures with different thicknesses along the imaging axis. Therefore, computed stereo CDI in transmission can only provide reliable depth estimations over non-ambiguous features. By non-ambiguous features, we mean structures whose relative positions in both stereo views can be effectively traced. Examples of such profiles

are borders, edges, sharp structures or small localised features within the object. In the images of Fig. 5.29, for instance, this could only happen in the borders of the sample, providing some insights over the orientation of the arms of the chromosome. This information comes, though, with an associated error, which must be taken into account. Its origin is schematized in Fig. 5.35.

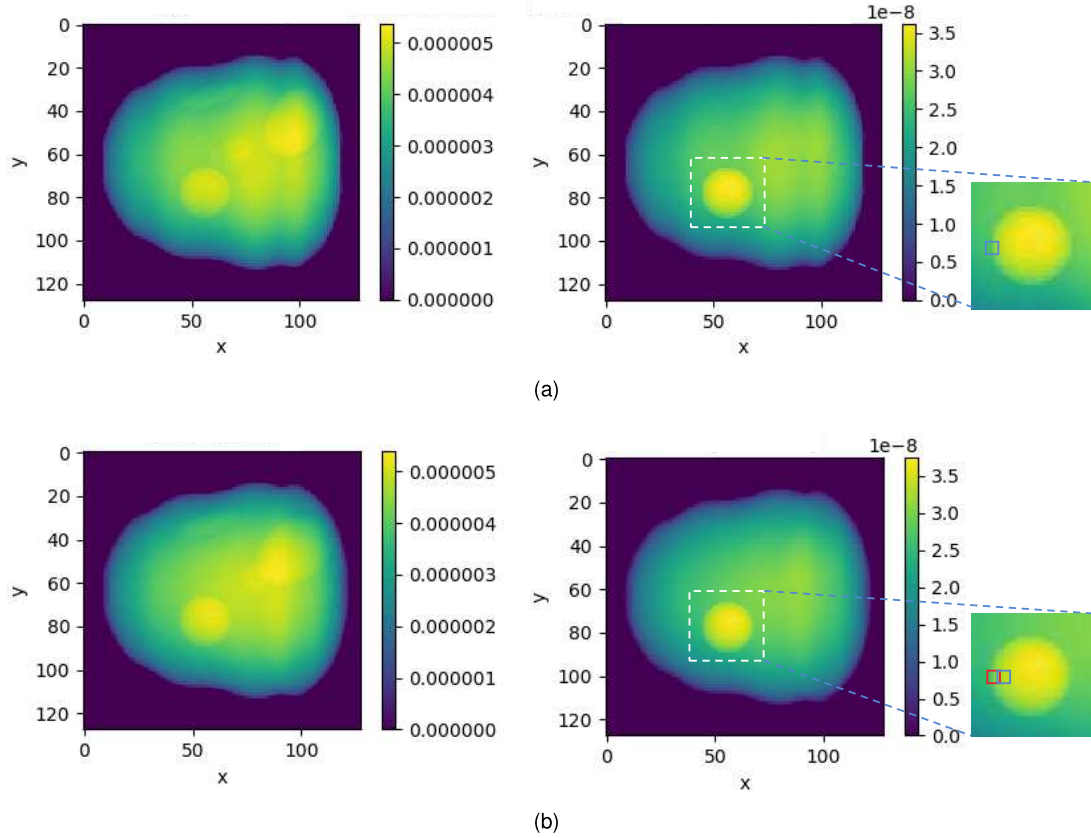


Figure 5.35: **Volume projections of the refractive index real and imaginary parts of a simulated cell, at 6 keV.** (a) Real (left) and imaginary (right) parts of the refractive index at 0° . The inset shows a zoom in the referenced area, with a selected region denoted by the blue square. (b) Real (left) and imaginary (right) parts of the refractive index rotated 22° around the y -axis. The inset shows a zoom in the referenced area, with the region corresponding to the blue square in (a) denoted by the same blue square. The red square shows the region which would be attributed as the corresponding match by the stereo block-matching routine.

Fig. 5.35 shows the real and imaginary parts of the refractive index for a simulated biological sample at two angles 0° and 22° . Note that the real part relates to the phase, while the imaginary part relates to the amplitude, describing the attenuation of the electromagnetic wave in the propagation through the material (see Section 2.2.2.1). The insets show a zoom in the same spherical structure, with corresponding regions denoted by blue squares. By running a stereo-matching routine on the images, one can easily see that the block found as the corresponding match (in the second image) would be the red one, which reveals a direct matching error. And this would be consistent over the whole structure, due to its persistently curved composition, for both real and imaginary views. Indeed, borders of curved structures possess an intrinsic matching error, when in transmission, which increases with the angle with which the stereo views were acquired. Knowing the angle and the computed depth variations in the

sample, one can, though, arrive to an estimation of the error associated with such depth values.

Concluding, the method shows difficulties in measuring the depth of structures with spherical topographies and smooth composition gradients, which are ambiguous in transmission geometry. One way to overcome this issue would be to use non-ambiguous labels to track from one projection to the other the sample structure. Currently, labels are often used in different microscopy types such as confocal, deconvolution and multiphoton, to allow the imaging of specific structures. Even though such labelings work in fluorescence regimes, not compatible with our setup demands, some labels were found to be metal nanoparticles. Conveniently, metal have contrast for X-rays in transmission, making such labels extremely powerful for our purpose as well. Such nanoparticles, or clusters of them, if attached to the smooth surfaces of a sample, could allow us to trace their depth arrangement and, ultimately, have access to the sample's 3D shape. In the next section, we investigate this option by implementing CDI stereo imaging with a test sample composed by gold nanoparticles.

5.6 Computer Stereo X-ray Imaging Using Nanoparticle Labels

In this section we extend the computed stereo vision concept to X-rays and more complex samples, testing the concept of using nanoparticles as surface labels. This demonstration exploits two views from tomographic data published and made available by Chapman *et al.* [122].

5.6.1 3D Sample and Generation of the Stereo Views

The sample is composed by an arrangement of 50-nm-diameter gold spheres spread on a 1.8 μm -tall pyramid-shaped indentation of a Si_3N_4 membrane (Figs. 5.36 (a)-(b)). A complete set of tomographic coherent diffraction imaging data were collected at a photon energy of 750 eV (1.65-nm-wavelength) at an undulator beamline [326] of the Advanced Light Source (ALS). The procedure is described in detail in Chapman *et al.* [122].

In this work, only two 2D CDI reconstructions were exploited, recorded at a separation angle of 7° . Figs. 5.37 (a)-(b) show the respective left and right stereo views of the sample of Fig. 5.36, each with a reconstructed pixel size of 14.7 nm. The spatial resolution of each view is estimated to be 42 nm (10-90% Rayleigh criterion).

5.6.2 Pre-processing of the CDI Stereo Views

As the images provided by Chapman *et al.* were already rectified, the only pre-processing performed to Figs. 5.37 (a)-(b) was background filtering. Hence, binary masks selecting the object areas were extracted from each view, similarly to the process followed for the human chromosome sample. The respective left and right stereo masks are shown in Figs. 5.38 (a)-(b). These masks were then multiplied by Figs. 5.37 (a)-(b), respectively, originating two stereo views with uniform background for the disparity analysis. The final stereo images can be observed, in anaglyph form, in Figs. 5.39 (a)-(b).

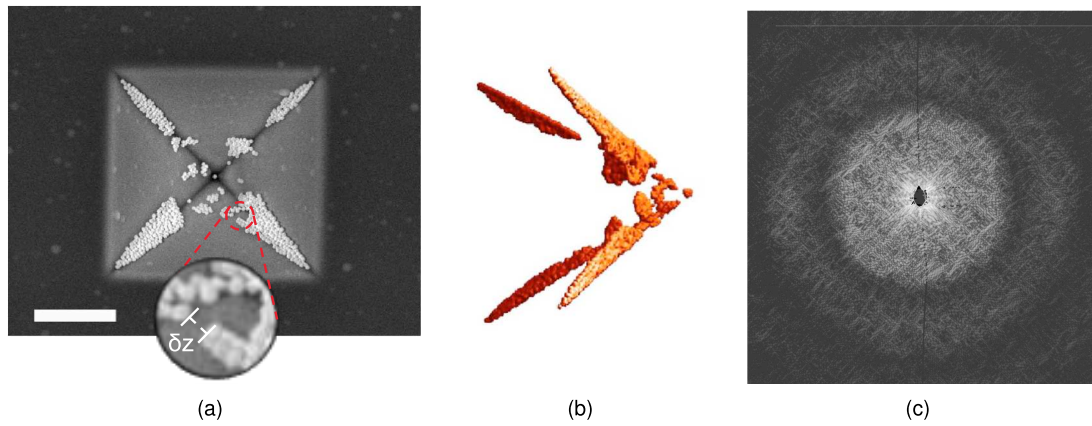


Figure 5.36: **3D pyramid sample and diffraction pattern acquired from a central view.** (a) SEM image of the 3D sample composed by an arrangement of 50-nm-diameter gold spheres lining the inside of a pyramid-shaped notch in a 100-nm-thick silicon nitride membrane. The pyramid base has a width of 2.5 μm and 1.8- μm height. The scale-bar length is 1 μm . The inset shows a zoom emphasizing a detail of 105-nm depth, δz . (b) Isosurface rendering of the 3D sample, reconstructed by Chapman *et al.*. (c) Diffraction pattern acquired from a central view of the sample. Images from [122].

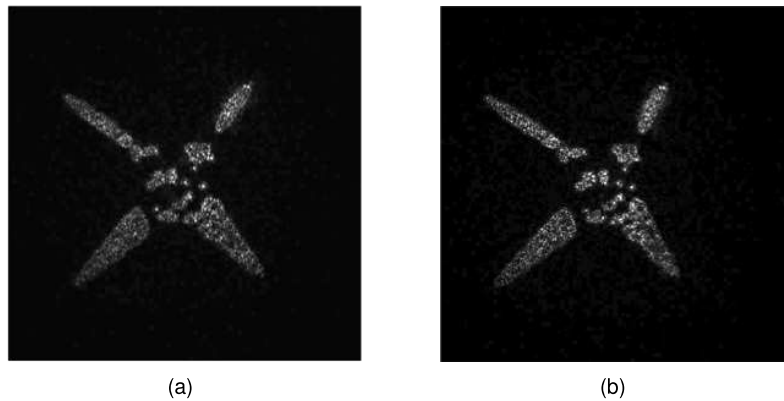


Figure 5.37: **Stereo image pair of the nanoparticles pyramid sample.** Pair of 2D CDI reconstructions, corresponding to 7° -apart views of the sample. (a) Left and (b) right views. Each view reaches a spatial resolution of 42 nm.

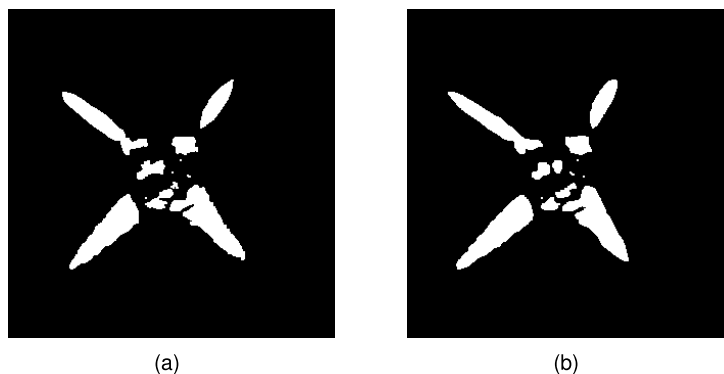


Figure 5.38: **Masks employed for background removal in the pyramid stereo views.** (a) Mask (represented in back) which was later multiplied by the rectified (a) left view (b) right view in order to remove the background noise.

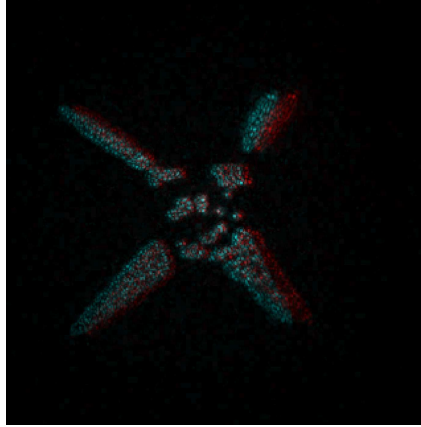


Figure 5.39: **Stereo anaglyph of the pyramidal structure of gold nanospheres.**

5.6.3 Stereo Matching and Computation of the Disparity Maps

Using the method described in section 5.2.3, two disparity maps were generated from the stereo images of Fig. 5.39. Figs. 5.40 (a) and (b) present, respectively, the disparity of the left image with respect to the right one (left map) and the reverse case (right map) achieved for the pyramidal structure with gold nanoparticles.

In the disparity maps presented, the disparity range N was allowed to 30 pixels, the weighting factor α was defined to 0.01 and the block-matching process was performed for blocks of 23×23 pixels.

Similarly to the human chromosome sample, the choice of the blocks size for the block matching routine was achieved after a scan, where this value was consistently increased. The final value constituted the smaller pixels-number from which the further disparity maps were providing the same results. This value allowed capturing enough texture variation to produce, as well, a smooth disparity profile.

To compensate the failure in preserving disparity/depth discontinuities, consequence of the large windows used, the images were multiplied by the masks of Figs. 5.38 (a) and (b), respectively. Again, the required support for the CDI views allowed a clear definition of the sample borders. The final disparity maps of the pyramid sample are shown in Figs. 5.40 (c) and (d). As one can see, they present a smooth disparity profile, whereas preserving the sample border lines.

5.6.4 Retrieval of Depth Information and 3D Reconstruction

Similarly to all the previous cases, the retrieval of depth information from the disparity maps of Figs. 5.40 (c)-(d) followed the steps described in Section 5.2.4. After computing all the coordinates of the points in the 3D space (equations (5.6)-(5.8)), the stereo consistency of the two disparity maps was evaluated. This bi-directional check was performed with x_o , y and z_o values rounded to one decimal digit. From the consistent points, the outliers were removed (parameters $\kappa = 80$ points and $\zeta = 0.05$).

Fig. 5.41 (a) shows the final point cloud containing the computed 3D stereo depth-map. Our geometry leads to a voxel size of, approximately, $15 \times 15 \times 120 \text{ nm}^3$ and an estimated 3D spatial resolution of $42 \times 42 \times 343 \text{ nm}^3$ (Eq. (5.9)). The inset highlights a feature corresponding to a z -depth value of 105

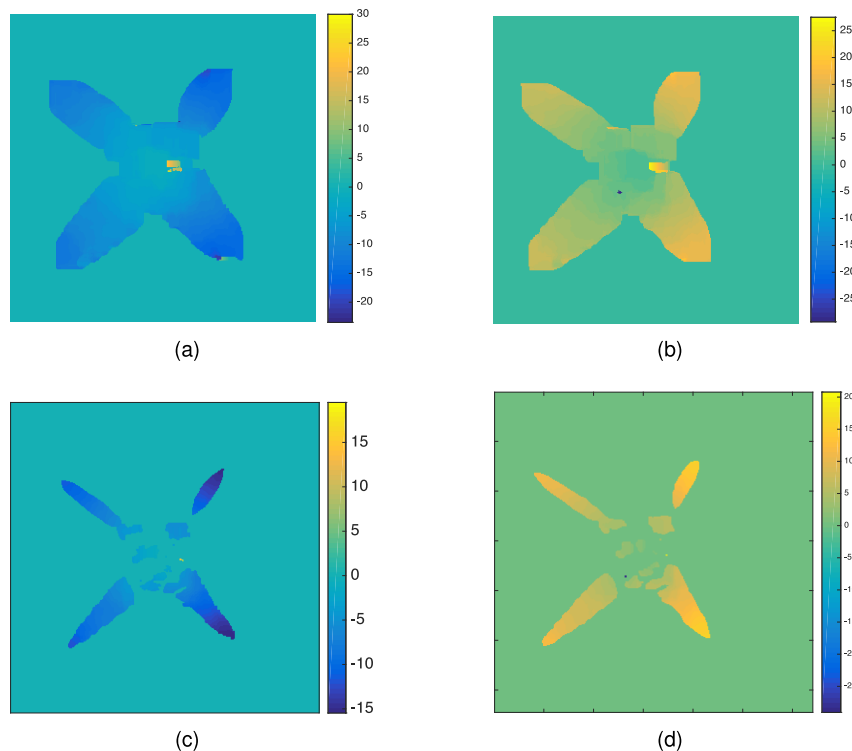


Figure 5.40: **Disparity maps obtained from the rectified stereo views of the nanoparticles pyramid sample.** (a) Left map without borders correction. (b) Right map without borders correction. (c) Left map with multiplication of background-removal mask. (d) Right map with multiplication of background-removal mask. The disparity maps displayed were achieved from a scan with blocks of 23×23 pixels. The scale bar denotes disparity values in pixels.

nm (see corresponding inset of Fig. 5.36 (a)). As one can see, such small feature was achieved even though representing dimensions below the estimated resolution value.

To allow a better visualisation of the resultant structure, a surface was plotted in the data points. One can observe it in Fig. 5.41 (b). This surface was acquired with a 3D Natural Neighbour Interpolation from the point cloud values of Fig. 5.41 (a). It was computed in a mesh of $0.01\text{-}\mu\text{m}$ pitch for all the extent defined by the extremities of our sample. The borderline was defined by discarding from this 3D surface-mesh the regions with a separation distance larger than $0.01\ \mu\text{m}$ from the data points.

The 3D structure from Fig. 5.41 reproduces quite well the pyramidal distribution of nanoparticles shown in Fig. 5.36. One can see that the arrangement follows a pyramidal shape with dimensions matching the dimensions of the reference SEM image. From the separation between the most extreme data points (voxels) we measured $2.49\ \mu\text{m}$ of base-width (comparing with the $2.5\ \mu\text{m}$ -notch value) and $1.73\ \mu\text{m}$ of z -depth (comparing with the $1.8\text{-}\mu\text{m}$ pyramid's height). One can note, though, by observing the SEM image of Fig. 5.41 (a), that the nanoparticles are not filling completely the indent and, therefore, the nominal-notch values correspond to slightly upper values than the actually measured depth.

Analysing carefully the profiles of Fig. 5.41 one can also notice that the overall structure does not follow straight pyramidal walls. In fact, in this experimental scenario, the gold nanoparticles are not exactly labels attached to the sample's surface. Instead, the 2D-CDI reconstructions, used as input stereo

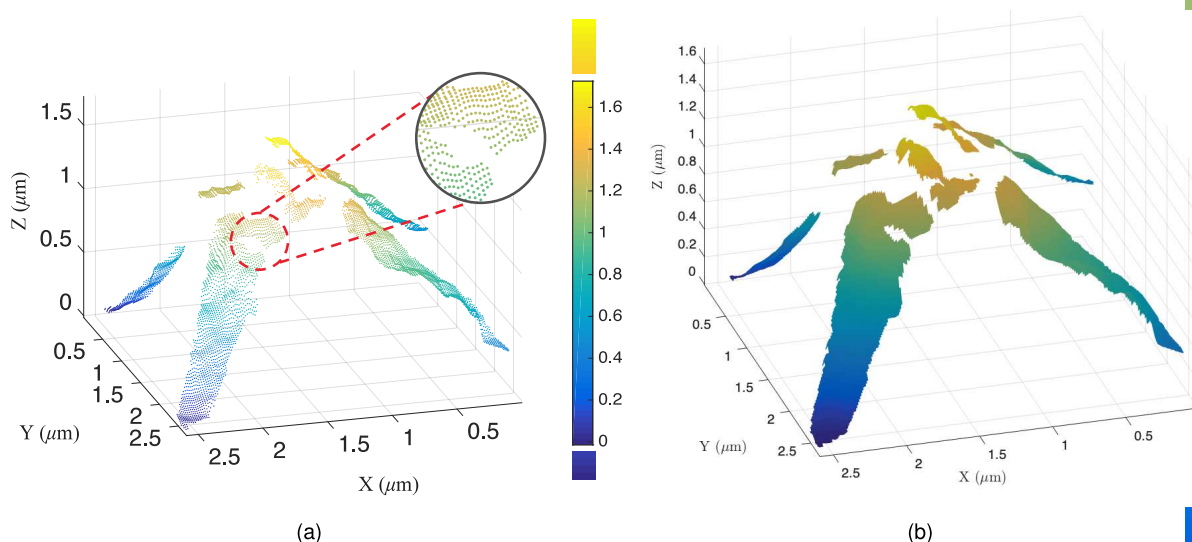


Figure 5.41: **Final depth reconstruction of the pyramidal arrangement of gold nanoparticles.** (a) Point cloud with depth information on the sample retrieved from the disparity maps, without 3D interpolation for surface rendering. The circle displays a zoom of the detail corresponding to the inset of Fig. 5.36 (a) (105-nm depth). The colour bar is common to both images and denotes the depth value, Z , in μm . (b) Surface rendering of the structure in (a).

views, correspond to “views from the top” of the set of nanospheres collected inside the pyramidal indent (see again Fig. 5.36 (a) for reference). Thus, the profile imaged do not follow flawlessly the pyramidal walls, due to the existence of regions where there is superposition of several layers of nanospheres in depth. Moreover, individual nanospheres can not be spatially distinguished in the reconstructions of Fig. 5.41. Indeed, the stereo reconstruction was achieved with a voxel size and estimated spatial resolution in depth larger than the size of the nanoparticles. It is important to note though, that their reduced dimensions are beneficial for the accuracy of our measurements. In order to be able to neglect the depth errors arising from their curved structure (see Fig. 5.35 and respective discussion), the nanosphere labels should have, indeed, significantly-reduced dimensions with respect to the object size.

The stereo reconstruction of this section was obtained without any *a priori* knowledge, employing just a simple background removal. This step was facilitated by the high signal-to-noise ratio of the reconstructed views, provided by the high-scattering factors of the gold nanoparticles. With the present demonstration we proved that metallic nanoparticles can be used as surface labels to trace the 3D profile of complex and non-trivial objects. This is particularly impactful for biological samples, which could have ambiguity in the direct implementation of the computed X-ray stereo method, allowing to overcome the limitations of the technique.

5.7 Conclusion Notes

In this chapter, we demonstrated the technique of computed stereo lensless X-ray imaging and extended its application to several types of samples, while discussing about their advantages and limitations.

In the implementation of X-ray stereo imaging described in this manuscript, we developed a local al-

gorithm for stereo matching, based on absolute intensity differences (AD) [281, 285]. Together with the squared intensity differences (SD) [286], this pixel-based matching cost is one of the most commonly employed in Stereo Vision, requiring low computational load while still offering fine disparity estimations. Further developments of the technique could use more complex algorithms, where a comparative analysis with the present results could be of interest.

The case studies of this chapter started with a simulation in Section 5.3. We demonstrated that quality 2D projections of a sample, captured from well known angles, effectively allow retrieving depth information. We showed that, having samples with non-ambiguous 3D features, as for instance edges (or labels), allows overcoming the problems inherent to the transmission geometry in X-ray stereo imaging. Indeed, even if one can not have conclusive depth information along all the object area, directly from the disparity calculations, we saw that we can follow the reference of non-ambiguous structures and infer intermediate values.

In the same section, some limitations of the technique affecting pure-amplitude objects were also disclosed. In fact, when an interpolation is applied to sparse data points, a comparative analysis of the stereo views and the depth map retrieved must be performed *a priori*. Areas of depth discontinuities in the 3D cloud arising from the disparity maps can reveal superposition of different elements at various depths. If sample elements are hidden in occluded areas of the stereo views, i.e. in the areas where there is no light transmission, one can not trace their 3D profile and, therefore, surface orientation and borders are under-determined. This lack of information leads to an incomplete representation of the sample and can lead to artefact-connections in the 3D rendering.

Occluding contour artefacts are a standard problem in vision science. In a transmission geometry, it gets specifically critical for pure-amplitude binary samples. This problem can be solved, though, by capturing additional 2D views as constraint to surface orientation determination. Multi-view stereo imaging is able to reconstruct detailed 3D information of a scene and is fully exploited in reflective stereo photometry [327]. However, in the context of X-ray vision, and due to optical indexes in this spectral domain, the reflectivity of a scene can be quite poor.

Simulations with a phase sample show that occlusion ambiguities can be, as well, reduced by using the information on the phase of the object. Indeed, if superimposed structures can be "seen" and if their borders have contrast in transmission, one can still trace their 3D profile under other sample structures.

Ideally, amplitude and phase images are exploited together for stereo purposes. With two input images in each view, additional stereo references can be extracted and further disparity information collected (see, for reference, images of Fig. 5.35, which show different sample components, in phase and amplitude). Furthermore, amplitude and phase views, from the same sample, generate redundant information that can be exploited cooperatively to satisfy the stereo algorithm constraints. A remarkable particularity of coherent lensless imaging techniques is that one can retrieve, simultaneously, information on both, from a single diffraction pattern.

In a second part of our study, described in section 5.4, the implementation of single-acquisition stereo lensless imaging was discussed. An XUV optical setup was mounted, based on the separation

of a high-order harmonics (HH) beam into two coherent sub-beams. Those sub-beams were focused on the sample with a controllable angle, allowing for the capture of a stereo-pair of diffraction patterns, in single acquisition. The setup employed enabled a fine tuning of the time delay, with sub-femtosecond jitter between the two pulses. This makes it, alternatively, suited to perform femtosecond time-resolved X-ray-pump/probe experiments.

Quantitative 3D structural information was, then, achieved from two observation angles, in a setup compatible with single femtosecond acquisition. This temporal resolution was not accomplished, though, due to the low photon flux of the harmonics beam, which conducted us into the use of longer accumulation times in the acquisition of the diffraction patterns. Still, we were able to retrieve depth insights of a pure amplitude sample in a proof-of-principle of computed CDI-stereo imaging. The system employed is perfectly suited to be implemented at XFELs and make use of the high brilliance of these sources [58, 59]. Note that the realisation of synchronized hard X-ray stereo beams is proposed at the European XFEL [68] and a similar beamline is under design at SACLA XFEL, Japan [67]. With more photon flux, computed stereo lensless X-ray imaging allows imaging dynamical processes in 3D with sub-100-nm-spatial voxel and femtosecond-temporal resolution.

To further develop the technique, section 5.5 explored the application of computed X-ray stereo vision to biological samples with predominantly-curved topography. This demonstration exploited two projections from tomographic data of an unstained human chromosome, made available by Nishino *et al.* [244]. The depth map achieved was, however, far from the expected in terms of shape. Indeed, this study highlighted a serious limitation of the technique. In transmission geometry, similar pixel magnitude variations stem from refractive-index changes within the sample (e.g. crossing different materials/densities), or same-refractive-index structures with different thicknesses along the imaging axis. Hence, for samples with curved topographies and smooth composition gradients, a stereo-matching approach applied to two input views does not translate the difference in relative positions of the same feature from two well known viewpoints. Instead, it provides a correspondence between the sample's thickness *versus* constitution/density, which is meaningless as it varies with the imaging axis of the view. This way, the stereo foundations fail, and no depth information can be extracted.

From the results of section 5.5 we conclude, therefore, that in stereo-ambiguous samples, the pre-processing of the input views gains a special role to remove ambiguous content from the scene before the disparity calculations. Indeed, computed stereo X-ray imaging in transmission can only provide reliable depth estimations over particular features. These features constitute the ones from which relative positions in both stereo views can be effectively traced.

With the aim of overcoming the stereo ambiguity in curved topographies and smooth composition gradients, we propose two solutions. One is to include depth information from free-space propagation functions (e.g. using in-line holographic techniques instead of CDI to reconstruct the input stereo views), where out-of-focus features in the in-line 3D stacking could restrict ambiguities. Second is to use contrast surface labels. While we keep the first proposal for a future work, the last one is exploited in section 5.6.

In the study of section 5.6, we tested the idea of using nanoparticles as stereo labels, extending the

Computer Stereo Vision concept to harder X-rays and more complex samples. We exploited two views from a test sample composed by an arrangement of 50-nm-diameter gold spheres spread on a pyramid-shaped indentation. Contrarily to the previous study (section 5.5), the stereo reconstruction achieved in this part was seen to reproduce successfully the pyramidal distribution of nanoparticles and, as well, the object dimensions. The 3D reconstruction was obtained without any *a priori* knowledge, employing just simple background removal. With this demonstration we proved that metallic nanoparticles (or clusters of them), offering high contrast to X-rays, can be used as surface labels to trace the 3D profile of objects. Here, the uniqueness constraint of the computed stereo technique is enforced by the nanoparticles spatial localization, overcoming some ambiguity errors in the implementation of the stereo-matching algorithm. This is particularly impactful for curved surfaces or smooth composition gradients, allowing to overcome the limitations of the technique for these topographies.

Concluding, in this chapter we showed that Computer Stereo Vision concepts can be transposed to XUV and X-rays. Computed lensless X-ray stereo imaging allows obtaining nanometre-scale-spatial resolution of 3D thick objects, in an aberration-free system, only diffraction and dose-limited. Combining these spatial features [2, 10, 12, 13, 242] with the temporal resolution of ultrashort XUV and X-ray pulses [8], this technique opens the way to multidisciplinary studies of 3D ultrafast dynamics at nanometre scales. Stereoscopic coherent imaging systems, combining multiple deflecting optics, will enable researchers to create unprecedented 3D movies of the nano-scale world, with a huge impact in 3D structural imaging of single macromolecules. By using hard-X-ray CDI to recover the stereo views with atomic resolution, specific atoms can, inclusively, be used as local 3D "labels" to fully satisfy the stereo algorithm requirements. For all these reasons, we can, thus, foresee outstanding applications of X-ray machine vision in biology, materials science, medicine and even industry.

Chapter 6

Conclusions

Ultrafast 3D structural imaging of single, non-periodic nanospecimens has become an increasingly important topic of research, allowing to reach the structure and dynamics of large proteins, macromolecular complexes and virus particles. This has motivated the development of coherent lensless imaging techniques, where one can reconstruct a complex-valued image of an object from its diffraction pattern, bypassing the limitations of the conventional lens systems. In this thesis, we performed several studies employing different coherent lensless techniques, proposing and testing improvements to make them more suited to the highly-demanding future of single-shot 3D imaging.

A first part of this work, described in Chapter 3, was dedicated to experimental studies employing 20-femtoseconds-pulse duration coherent XUV radiation from the HHG beamline of LUCA, CEA Saclay. These studies finally aimed at a computational correction of spatial coherence in Fourier transform holography, compatible with single-shot regime. For the purpose, some samples were successfully patterned, employing the technique of FIB. We reported the first experimental demonstration in single shot of a new technique for characterisation of the spatial coherence of a source, with application on Gaussian-Schell beams [178]. The measurement revealed an extremely good magnitude of spatial coherence of LUCA's H25, with a radius $w_c = 3.85 \mu\text{m}$, fit with a root-mean-square error of 2.5% (larger than the radius of the focal spot). The simplicity and versatility of the method used became evident, revealing an enormous potential for single-shot spatial coherence characterisation of the most varied sources, ranging from ultrafast laser-based sources to XFELs and synchrotrons. Indeed, the method is based on the interferometry through a 2D non-redundant array (NRA) of apertures, with different separation distances and orientations, allowing for spatial characterisation of the entire light field in a single shot. Besides, the NRA design is strategically assembled to disentangle the degree of spatial coherence from the intensity distributions of a beam. This feature not only makes it independent of the intensity profile of the beam, but also compatible with beam-pointing instabilities, two critical parameters for conventional coherence measurement techniques in the XUV/X-ray ranges. In this part of the thesis we also presented the formalisms of partial-spatial coherence in Fourier transform holography, showing that any modulation in the object reconstruction induced by a shift-variant phase of the spatial

coherence is avoided by using FTH with punctual references. An extension of the study to holography with extended references would be interesting as future prospect since, as we have seen, shift-variant phases of the spatial coherence may generate superpositions out of phase in the object reconstruction, contributing to its degradation. Changing then for measurements in H33 of LUCA's beamline, we retrieved the magnitude of spatial coherence of the beam under similar experimental conditions to a FTH experiment, inputting this information in the reconstructions. A radius of the coherence function of $w_c = 3.7 \mu\text{m}$ was obtained, with 4% root-mean-square error. We verified that a compensation of this profile in our experimental FTH data offered, however, no substantial improvement to the reconstructions, inclusively inducing additional gradients. Indeed, a profile affected by partial coherence should accuse a radial intensity gradient. This was, however, not visible in any of the reconstructions achieved. We concluded, then, that the intensity distribution of the beam under accumulation regime was the prominent cause, making the accumulated influence of the partial coherence negligible. The expected radial intensity gradient was, however, found in the data from Schlotter *et al.* [200]. As Schlotter demonstrated, a spatially multiplexed Fourier transform hologram in the configuration of Fig. 3.24 entails a significant SNR enhancement in the reconstruction, when all the subimage reconstructions are averaged. We demonstrated that this SNR improvement is, in fact, attributed to the compensation of the effects of spatial coherence. We further expanded this idea and suggested some approaches to be followed in the study of ways to use such samples for spatial-coherence measurements. With a well-characterised simple shape as an object, and the full sample covering the biggest area possible of the beam at the focus, single-shot full-2D characterisation of the complex spatial coherence function could be potentially reached. Moreover, one could have access to the phase of the degree of spatial coherence, in addition to the magnitude obtained with the NRA technique. We provided one example of approximation which could be applied to disentangle the spatial-coherence values from an FTH sample in the configuration described. This approximation was based on the results published by Schlotter for an easier context. We saw, nonetheless, that several others can be applied based, for instance, on symmetry assumptions. Indeed, further efforts are required to develop the technique and, as well, be able to identify the assumption which offers less error. Future work on this topic is, thus, proposed.

The main focus of Chapter 4 was given to the technique of in-line holography, due to the interest it brings to the study of the impact of aberrations in the reconstruction. Indeed, the small reference of FTH works as a spatial filter to the incoming beam, cleaning the aberrations of the reference wave. In in-line holography, in turn, the object is directly illuminated by the incoming beam, and the reference wave constitutes the light that is not scattered by the object. Consequently, all the process is more vulnerable to the imperfections of the illumination, and the reconstruction can lead to distorted reproductions of the original object. This is particularly critical in the XUV and X-ray ranges, where the aberrations actively limit the access to high resolutions [38]. Therefore, in Chapter 4, we proposed and demonstrated a new approach, compatible with single-shot imaging, to correct in-line reconstructions from the aberrations of the illuminating beam. We started the chapter by developing the formalism of in-line holography with waves with aberrations. Here, an approach was proposed, which separated the measured phase map

from the defocus term, allowing for in-line reconstructions with magnification. This approach was explored with simulations using the phase map measured from an XUV beam, focused by two fused-silica spherical mirrors in a KB configuration. We saw that the wavefront aberrations induced by that focusing system were enough to strongly compromise the quality of in-line reconstructions. When accounting with the beam wavefront, we managed to overcome the effects of aberrations, reaching accurate object reconstructions, only affected by smooth modulations arising from the twin image. With the purpose of cleaning the reconstructions from the twin-image effects, we proposed a new algorithmic approach, which allowed a simultaneous correction of in-line holograms from optical aberrations and twin image. We validated the twin-image correction without the aberrated phase-map using experimental data from a biological phase sample. By reconstructing different planes of the sample, with different focused details, we saw that the routine presented good compatibility with 3D imaging. Finally, we were able to validate experimentally the twin image and aberrations correction algorithm, employing a HeNe laser with an astigmatic wavefront. The setup was assembled with a wavefront sensor, which allowed the caption of the phase map and respective Zernike coefficients in the conditions whereby the hologram was recorded. By employing this technique we achieved diffraction-limited reconstructions, without the need of a high-quality beam and, therefore, allowing the imaging of processes using all the photons available. Despite this setup, the technique presented is single-shot compatible and setup-versatile. An implementation using XUV harmonics was also tried, however, due to a set of technical problems, added to a limited beamtime, was not accomplished. It constitutes, thus, a proposal for a future work, accounting as well with in-line samples already fabricated during this thesis, whose production is described in appendix.

The last content Chapter of this manuscript, Chapter 5 was dedicated to the application of concepts from Computer Stereo vision to lensless X-ray imaging. In this context, we developed a local algorithm for stereo matching, with a 3D rendering applied to a lensless X-ray transmission scheme. Through simulations we showed that non-ambiguous 3D features such as edges, in samples, allow overcoming the problems inherent to the transmission geometry in X-ray stereo imaging. Even without conclusive disparity information along all the object area, we saw that we can follow the reference of non-ambiguous structures and infer intermediate values. This simulation also disclosed some limitations, particularly for pure-amplitude objects. Indeed, when an interpolation is applied to sparse data points, a critic analysis of the depth map retrieved must be performed, comparing it with the stereo views. Areas of depth discontinuities in the 3D cloud arising from the disparity maps can reveal superposition of several elements at different depths. Moreover, if sample elements are hidden in occluded areas of the stereo views, i.e. in the areas where there is no light transmission, one can not trace their 3D profile. In these cases, surface orientation and borders can be under-determined. This lack of information leads to an incomplete representation of the sample and can originate artefact-connections in the 3D rendering. On the other hand, we saw with simulations with a phase sample that occlusion ambiguities can be reduced by using the information on the phase of the object. Indeed, if superimposed structures can be "seen" and if their borders (or other features) have contrast in transmission, one can still trace their 3D profile under other

sample structures. Ideally, amplitude and phase views, from the same sample, can be explored together to reduce ambiguity as they generate redundant information that can be exploited cooperatively. A remarkable particularity of coherent lensless imaging techniques is that one can retrieve, simultaneously, information on both, from a single diffraction pattern. In a second part of our study, we discussed the implementation of single-acquisition stereo lensless imaging in an XUV HHG-based setup. We presented a setup based on the separation of a high-order harmonics (HH) beam into two coherent sub-beams, which are later focused on the sample with a controllable angle. Under this scheme a stereo-pair of diffraction patterns can be captured in a single-femtosecond acquisition. Moreover, this system is perfectly suited to be implemented at XFELs and make use of the high brilliance of these sources [58, 59]. Implementing this setup in LUCA's harmonics beamline we were able to retrieve depth insights of a pure amplitude sample in a proof-of-principle of computed CDI-stereo imaging. Even though the setup is compatible with a single femtosecond acquisition, this temporal resolution was not accomplished due to the low photon flux of the harmonics beam, which required longer accumulation times in the acquisition of the diffraction patterns. Hence, with more photon flux, computed stereo lensless X-ray imaging allows imaging dynamical processes in 3D with sub-100-nm-spatial voxel and femtosecond-temporal resolution. To further develop the technique, we applied computed X-ray stereo vision to biological samples with predominantly-curved topography, mainly to explore the limitations of the technique. The results highlighted that, for samples with curved topographies and smooth composition gradients, a stereo-matching approach applied to two input views does not translate the difference in relative positions of the same feature from two well known viewpoints. Instead, it provides a correspondence between the sample's thickness *versus* constitution/density, which is meaningless as it varies with the imaging axis of the view. This way, the stereo foundations fail, and no depth information can be extracted. This allowed to conclude that computed stereo X-ray imaging in transmission can only provide reliable depth estimations over particular features. These features constitute the ones from which relative positions in both stereo views can be effectively traced. With the aim of overcoming the stereo ambiguity in curved topographies and smooth composition gradients, we proposed to use contrast surface labels. We exploited the idea using two views from a test sample composed by an arrangement of 50-nm-diameter gold spheres spread on a pyramid-shaped indentation. We were able to successfully reproduce the pyramidal distribution of nanoparticles and, as well, the object dimensions. The 3D reconstruction was obtained without any *a priori* knowledge, employing just simple background removal. With this demonstration we proved that metallic nanoparticles (or clusters of them), offering high contrast to X-rays, can be used as surface labels to trace the 3D profile of objects. This is particularly impactful for curved surfaces or smooth composition gradients, allowing to overcome the limitations of the technique for these topographies.

Concluding, in this thesis we have further pushed the potential of coherent lensless imaging using the beam properties (coherence, wavefront...) or image vision algorithms for 3D perception. We proved that single-shot coherence measurements are at reach of the new XUV and X-ray sources, with impact for different applications. Moreover, due to this work, X-ray in-line imaging can now reach higher resolutions

by having access to information of the phase of the illuminating beam. This phase correction allows the use of stronger focusing optics, inductive of significant aberrations, and allowing this technique to reach, in a future, competing resolutions with the actual on-demand X-ray imaging techniques. For instance, implementing computed stereo imaging with in-line holographic reconstructions could be a promising achievement in the future. The 3D structural information arising from the reconstruction in several planes of propagation could create an interesting symbiosis with the stereo approach, reducing stereo matching ambiguity and, at the same time, the ambiguity of the out-of-focus features in the 3-dimensional back-propagated in-line image. New algorithms may certainly benefit from such amount of 3D data from only two views to create a fully coherent stereo vision. Others could use this as input to extend their applicability and performance. One could think of plenoptic X-ray imaging for example. We have shown routes towards nanometre-scale-spatial resolution of 3D thick objects, in an aberration-free system, only diffraction and dose-limited. Combining these spatial features [2, 10, 12, 13, 242] with the temporal resolution of ultrashort XUV and X-ray pulses [8], this technique opens the way to studies of 3D ultrafast dynamics at nanometre scales. By using hard-X-ray CDI to recover the stereo views with atomic resolution, specific atoms can, inclusively, be used as local 3D "labels" to fully satisfy the stereo algorithm requirements. For all these reasons, and further more which we are sure to come, we can, thus, foresee an outstanding future for 3D X-ray machine vision, with applications in the most varied fields.

6.1 Future Prospects: XUV SLM

A Spatial Light Modulator (SLM) is a device which allows spatial beam shaping by modifying the original-beam parameters, such as amplitude, phase and state of polarization. It generally consists of a crystalline structure, the orientation of which is electronically controlled [328, 329]. Even though being an extremely versatile device in the visible and infrared ranges, its implementation in the XUV and X-rays is not yet achieved, mainly due to incompatibilities with the technologies used. Moreover, the requirements of high-precision extremely-small features to create a controllable beam shaping; the strong photon absorption of materials in these ranges and, as well, vacuum requirements, make the realisation of short-wavelength radiation SLMs a challenging task. This requires, thus, disruptive approaches.

6.1.1 Setup 1: Pump beam modulated with an SLM

In this test, we exploited the possibility to regulate the phase of a pump beam with an IR/visible SLM, to make it generate a transient intensity mask on a surface, which could induce custom modulations on a XUV beam reflected by it. Fig. 6.1 illustrates the principle.

In this scheme, an IR beam (or a 2ω beam created by directing the IR beam through a BBO) is used as pump beam. The SLM is mounted in reflection geometry, at room environment, and used to modulate the phase of the pump-beam, which is later directed to the interaction vacuum chamber and focused in the "XUV-SLM medium". The medium proposed here is a vanadium dioxide (VO_2) film. VO_2

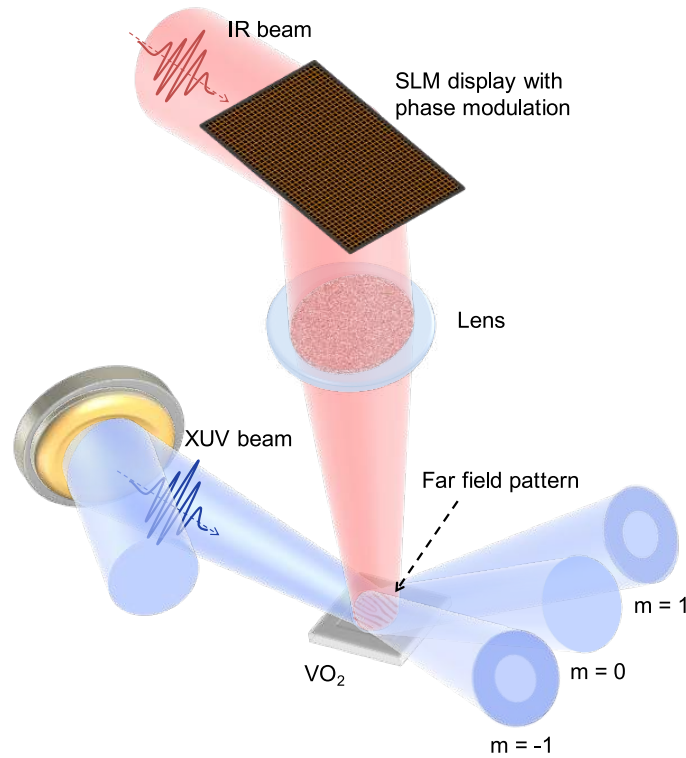


Figure 6.1: **Setup for an XUV SLM, where the phase of a pump beam is modulated with a conventional SLM, generating a transient intensity map at the far field, which will imprint custom modulations on a grazing-incident XUV beam.** In this scheme, an orbital angular momentum (OAM) is imprinted to the XUV beam, by means of a transient fork-grating mask, imprinted by an IR beam in a vanadium dioxide (VO₂) film. Light beams carrying OAM are characterised by having a helical wavefront accompanied by a phase singularity in their centre [330]. They show an azimuthal phase dependence in the form $\exp(-im\varphi)$, where m is the *topological charge* and φ is the azimuthal coordinate in the plane perpendicular to the propagation of the beam. Such beams carry an OAM of mh^- per photon [331]. The most common light beams carrying OAM display Laguerre-Gaussian modes characterised by a donut-shaped intensity profile. Currently, interaction between matter and photons carrying OAM is an intensively studied topic, with a large variety of applications [332]. For this reason, there is a large theoretical and experimental effort towards the generation of vortex beams with new coherent light sources [333–338].

is a strongly-correlated material of particular interest because of a near-room-temperature thermally activated insulator-to-metal transition (IMT) [339–342]. This IMT was already exploited to perform transient grating spectroscopy with an XUV probe, reached at an average fluency of 15 mJ/cm^2 of the pump laser [343]. Thus, the focused intensity pattern of the pump-beam excites the VO₂, generating a metal-opaque diffraction mask, which modulates the XUV-probe beam reflected in this surface, in grazing incidence.

With the purpose of testing the operation of an SLM for implementation in this scheme, we used a Liquid Crystal on Silicon (LCoS) reflective Spatial Light Modulator (SLM) from Meadowlark Optics, operating at the wavelengths 400 - 1650 nm [328]. This SLM contains a crystal layer which is nematic and can rotate under the effect of a voltage, causing local phase shifts on the incident beam. The matrix consists of 512×512 crystals, with a pixel pitch of $15 \mu\text{m}$, corresponding to a total array size of $7.68 \times 7.68 \text{ mm}$. These crystals can be considered numerically as pixels. The phase mask, coded in gray

level as an image, is sent to the SLM via connection to a computer. In Fig. 6.2 (c) one can observe an example of phase map used in experimental tests with the SLM. It was obtained by employing the iterative Gerchberg-Saxton algorithm described in Section 2.3.1.2, assuming a uniform/neural amplitude in the SLM given by Fig. 6.2 (a) and the desired amplitude at the VO₂ position, given by Fig. 6.2 (b). This fork-grating mask, as illustrated in Fig. 6.1, is responsible for imprinting an orbital angular momentum (OAM) in the XUV beam.

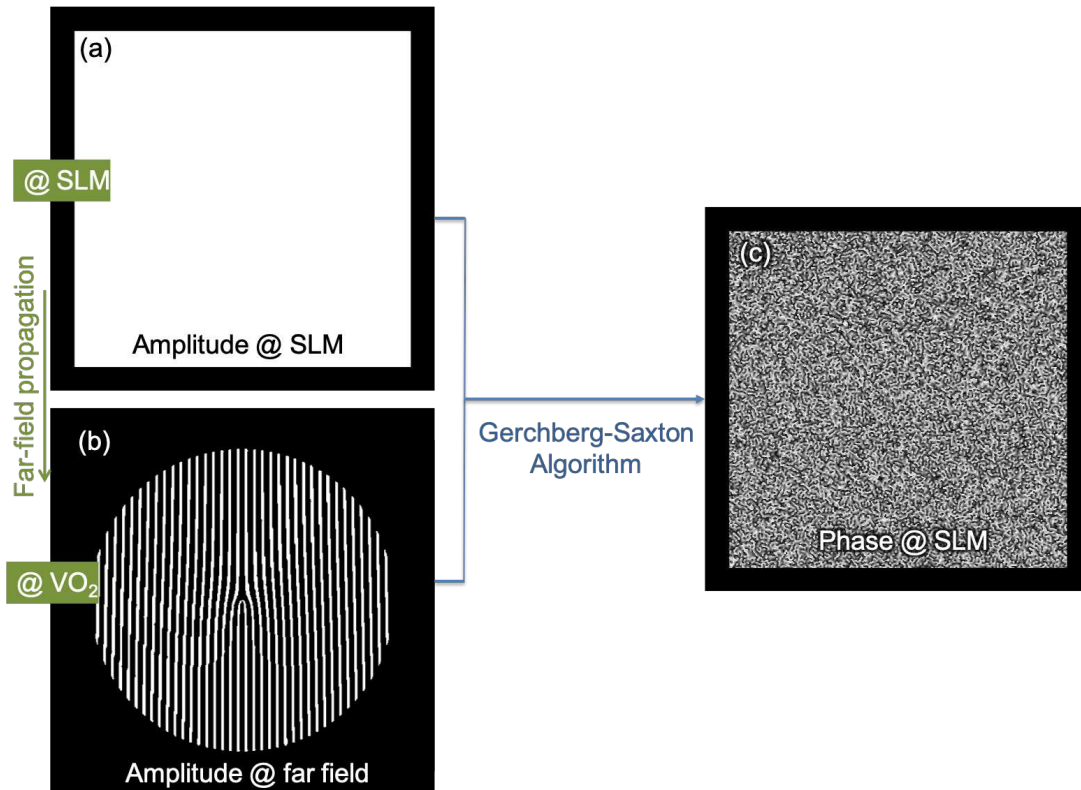


Figure 6.2: **Schematic of the input and output images, used in the implementation of the Gerchberg-Saxton algorithm, to extract the phase map at the SLM.** (a) Input image depicting a neutral amplitude at the SLM (note that the white square is defined with the dimensions of the SLM). (b) Input image of the GS algorithm defining the amplitude of the beam, reflected by the SLM, after propagation until the far field (i.e., at the VO₂ film). (c) Output phase map, defining the phase modulation at the SLM, which will affect the incident beam, in order to create the amplitude pattern of (b) at the VO₂ position.

Inputting a phase modulation with the form of Fig. 6.2 (c) in the SLM, the far field image, created upon interaction with an expanded HeNe beam was observed. The image, captured with a visible-range CCD can be found in Fig 6.3. Observing the image, one can identify a fork-shaped structure, as expected. The resulting image, though, presented an intense speckle content, preventing the creation of an effective grating.

In order to evaluate the origin of the speckles, other phase maps were tested. Fig. 6.4 (b) shows an example, corresponding to a rectangular profile in the far field (Fig. 6.4 (a), as inputted in the GS algorithm). The respective reconstruction employing the same expanded HeNe laser can be observed in Fig. 6.4 (c), showing as well a strong speckle content. The same measurement, this time performed with

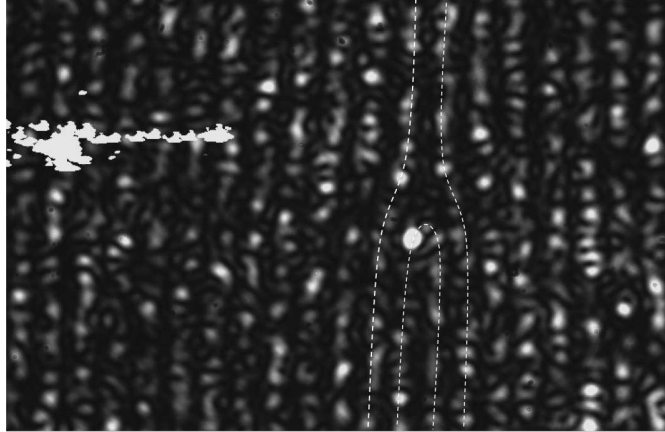


Figure 6.3: **Experimental measurement of a fork-grating intensity map at the far field of the SLM.** The image was obtained employing a HeNe laser ($\lambda = 635$ nm), corresponding to the wavelength of the available calibration file. The region of the fork is highlighted with white dashed lines, for better understanding. The image is affected by a strong speckle content.

the LUCA's IR beam can be found partially in Fig. 6.4 (d). Besides the considerably lower distribution of photons, when compared to 6.4 (c), the image presents the same speckle content, discarding the possibility of it being caused by properties of the laser. The lower distribution of photons arises from the poor definition of the phase steps, which is responsible, as well, for the strong zero-order beam found at the bottom of Fig. 6.4 (d). This poor definition is caused by the lack of calibration to the IR wavelength. Indeed, the nonlinear optical response of the liquid crystal (LC) to voltage needs to be calibrated to allow a custom definition of the phase output of the beam. In our case, we were only in possession of the calibration file for the 635-nm laser at the time of these tests. Nevertheless, the study revealed the severity of the speckles, affecting the quality of the produced pattern and precluding the advance of the experiment in this format.

After some bibliography consulting, we found that the speckles are inherent to LC-SLMs and no technique succeeded so far to correct their presence [344]. As explained in [344, 345], these speckles have two causes:

1. the pixelated (digital) character of the SLM display, that introduces phase discontinuities to the computer-generated hologram (CGH);
2. the mutual interference between the neighbouring beams in the reconstructed image plane of a CGH when they are very close to each other.

6.1.2 Setup 2 : Interference of two pump beams

Here we propose a second setup, where the hologram imprinted in the VO_2 is generated not by one modulated beam, but by the interference of two. Fig. 6.5 (a) illustrates the principle, also aiming at an XUV beam with induced orbital angular momentum. The setup described was optimised for LUCA's harmonics beamline, accounting with its optics and distance limitations. We opted for the creation of a

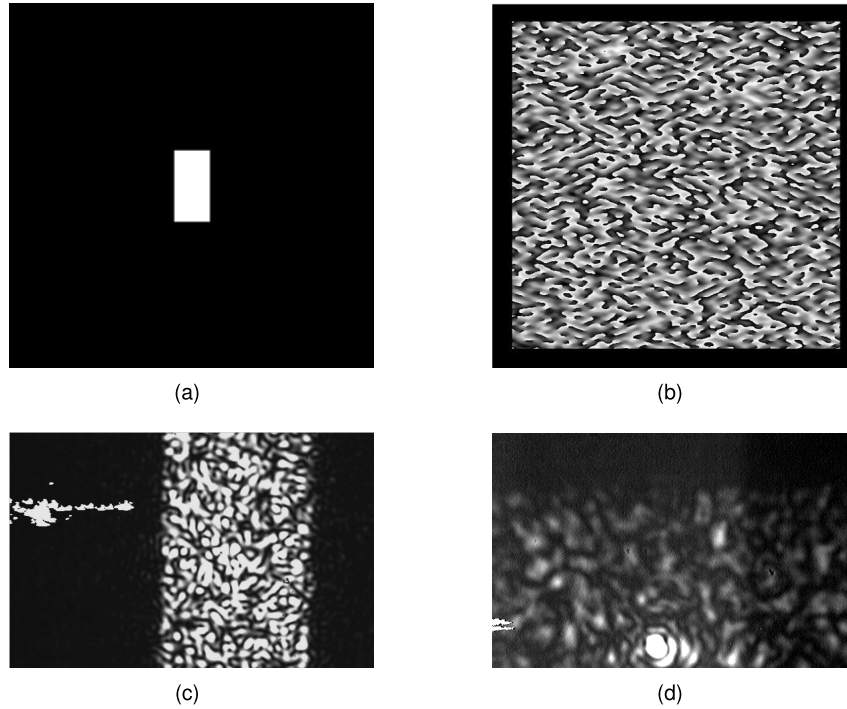


Figure 6.4: **Example of a generated phase map introduced at the SLM and respective far-field measurements employing two different sources.** (a) Input image of the GS algorithm (along with Fig. 6.4 (a)), defining the amplitude of the beam at the VO₂ film position. (b) Output phase map defining the phase map to modulate in the SLM in order to create the amplitude pattern of (a) at the VO₂. (c) Experimental measurement of a rectangular intensity map at the far field of the SLM, employing a HeNe laser. (d) The same as (c) but employing an IR beam from LUCA.

diffractive transient mask (hologram) at the VO₂ film, which simultaneously focuses the harmonics and imprints OAM. As advantages, we discard the need of focusing optics or spectrometers, since the whole job is performed by a proper definition of the hologram. Additionally, in this configuration, we are not limited by the pixelization of the SLM in the pump beam, allowing for smaller structures at the VO₂.

In order to generate a fork grating with focusing properties (Fig. 6.5 (b)) we make a focused IR Gaussian beam interfere with a collimated IR beam with OAM, in the interaction region of the VO₂. For the convergence of the first pump beam, we should consider that the focal length of the hologram to the harmonic with order H, F_H , will be H times greater than that of the pump beam, R, i.e. $F_H = H \times R$ (see Fig. 6.5 (a) for F_H and R). In Fig. 6.5 (b)-(d) one can see some simulation results. These results were achieved for: 2-mm hologram size on the VO₂ (diameter); radius of curvature, R, of 2 cm (i.e. distance VO₂ - focal spot of the converging pump beam); 15° angle between the two pump beams; distance VO₂-CCD of 54 cm, calculated for the focal spot of H27 (H = 27).

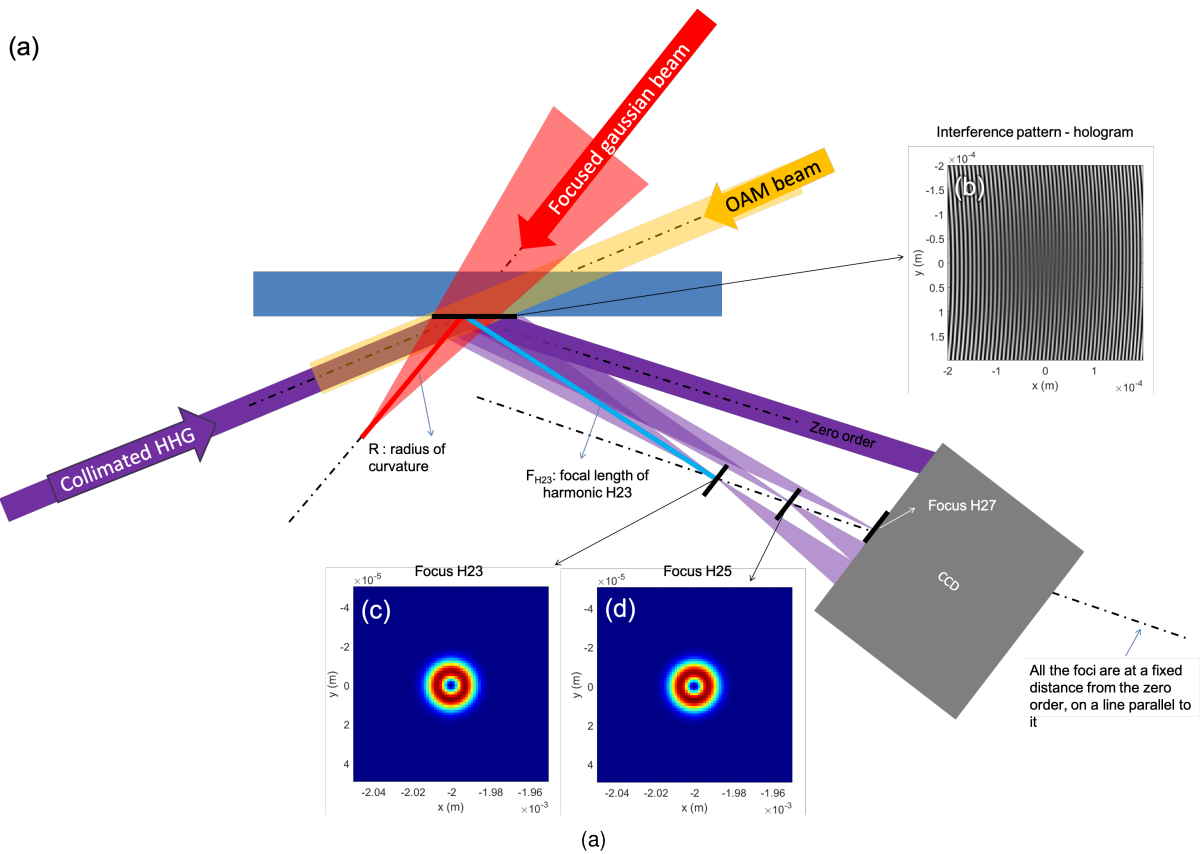


Figure 6.5: **Setup for generation of a hologram at the VO_2 film, which works as a transient diffraction optics to the harmonics beam, separating, focusing and imprinting OAM in each harmonic.** (a) Setup, optimized for LUCA's harmonics beamline. (b) Zoom at the center of the hologram (simulation results). (c) Donut-shaped intensity profile of the H23 at its focus, after reflection in the hologram from (b). Note that this shape corresponds to a Laguerre-Gaussian mode and is characteristic of beams carrying OAM. (d) Respective image of H25 with induced OAM.

Bibliography

- [1] H. N. Chapman, P. Fromme, A. Barty, T. A. White, R. A. Kirian, A. Aquila, M. S. Hunter, J. Schulz, D. P. DePonte, U. Weierstall, et al. Femtosecond X-ray protein nanocrystallography. *Nature*, 470(7332):73–77, 2011.
- [2] M. M. Seibert et al. Single mimivirus particles intercepted and imaged with an X-ray laser. *Nature*, 470(7332):78–81, 2011.
- [3] T. Ekeberg, M. Svenda, C. Abergel, F. R. Maia, V. Seltzer, J.-M. Claverie, M. Hantke, O. Jönsson, C. Nettelblad, G. Van Der Schot, et al. Three-dimensional reconstruction of the giant mimivirus particle with an X-ray free-electron laser. *Physical review letters*, 114(9):098102, 2015.
- [4] E. Nango, A. Royant, M. Kubo, T. Nakane, C. Wickstrand, T. Kimura, T. Tanaka, K. Tono, C. Song, R. Tanaka, et al. A three-dimensional movie of structural changes in bacteriorhodopsin. *Science*, 354(6319):1552–1557, 2016.
- [5] M. Minitti, J. Budarz, A. Kirrander, J. Robinson, D. Ratner, T. Lane, D. Zhu, J. Glowonia, M. Kozina, H. Lemke, et al. Imaging molecular motion: Femtosecond x-ray scattering of an electrocyclic chemical reaction. *Physical review letters*, 114(25):255501, 2015.
- [6] H. N. Chapman, S. P. Hau-Riege, M. J. Bogan, S. Bajt, A. Barty, S. Boutet, S. Marchesini, M. Frank, B. W. Woods, W. H. Benner, et al. Femtosecond time-delay X-ray holography. *Nature*, 448(7154):676–679, 2007.
- [7] C. Günther, B. Pfau, R. Mitzner, B. Siemer, S. Roling, H. Zacharias, O. Kutz, I. Rudolph, D. Schöndelmaier, R. Treusch, et al. Sequential femtosecond X-ray imaging. *Nature Photon.*, 5(2):99–102, 2011.
- [8] B. Vodungbo, J. Gautier, G. Lambert, A. B. Sardinha, M. Lozano, S. Sebban, M. Ducouso, W. Boutu, K. Li, B. Tudu, et al. Laser-induced ultrafast demagnetization in the presence of a nanoscale magnetic domain network. *Nature communications*, 3:999, 2012.
- [9] T. Gorkhover, S. Schorb, R. Coffee, M. Adolph, L. Foucar, D. Rupp, A. Aquila, J. D. Bozek, S. W. Epp, B. Erk, et al. Femtosecond and nanometre visualization of structural dynamics in superheated nanoparticles. *Nature photonics*, 10(2):93, 2016.

- [10] A. Barty, S. Boutet, M. J. Bogan, S. Hau-Riege, S. Marchesini, K. Sokolowski-Tinten, N. Stojanovic, H. Ehrke, A. Cavalleri, S. Düsterer, et al. Ultrafast single-shot diffraction imaging of nanoscale dynamics. *Nature photonics*, 2(7):415, 2008.
- [11] T. Gorkhover, A. Ulmer, K. Ferguson, M. Bucher, F. R. Maia, J. Bielecki, T. Ekeberg, M. F. Hantke, B. J. Daurer, C. Nettelblad, et al. Femtosecond X-ray Fourier holography imaging of free-flying nanoparticles. *Nature Photonics*, 12(3):150, 2018.
- [12] D. Gauthier, M. Guizar-Sicairos, X. Ge, W. Boutu, B. Carré, J. Fienup, and H. Merdji. Single-shot femtosecond X-ray holography using extended references. *Physical review letters*, 105(9):093901, 2010.
- [13] A. Ravasio, D. Gauthier, F. Maia, M. Billon, J. Caumes, D. Garzella, M. Géléoc, O. Gobert, J.-F. Hergott, A. Pena, et al. Single-shot diffractive imaging with a table-top femtosecond soft X-ray laser-harmonics source. *Physical review letters*, 103(2):028104, 2009.
- [14] M. Murnane, R. Bartels, A. Paul, S. Backus, H. Kapteyn, I. Christov, Y. Liu, D. Attwood, and C. Jacobson. Fully spatially coherent EUV light generated using a small-scale laser. page WB1, 2002.
- [15] X. Ge, W. Boutu, D. Gauthier, F. Wang, A. Borta, B. Barbrel, M. Ducouso, A. I. Gonzalez, B. Carré, D. Guillaumet, et al. Impact of wave front and coherence optimization in coherent diffractive imaging. *Opt. Express*, 21(9):11441–11447, 2013.
- [16] T. Remetter, P. Johnsson, J. Mauritsson, K. Varjú, Y. Ni, F. Lépine, E. Gustafsson, M. Kling, J. Khan, R. Lopez-Martens, et al. Attosecond electron wave packet interferometry. *Nat. Phys.*, 2(5):323–326, 2006.
- [17] T. Gaumnitz, A. Jain, Y. Pertot, M. Huppert, I. Jordan, F. Ardana-Lamas, and H. J. Wörner. Streaking of 43-attosecond soft-X-ray pulses generated by a passively CEP-stable mid-infrared driver. *Optics express*, 25(22):27506–27518, 2017.
- [18] J. Huijts. *Broadband coherent X-ray diffractive imaging and developments towards a high repetition rate mid-IR driven keV high harmonic source*. PhD thesis, Université Paris Sud, 2019.
- [19] G. O. Williams, A. Gonzalez, S. Künzel, L. Li, M. Lozano, E. Oliva, B. Iwan, S. Daboussi, W. Boutu, H. Merdji, et al. Fourier transform holography with high harmonic spectra for attosecond imaging applications. *Opt. Lett.*, 40(13):3205–3208, 2015.
- [20] T. Popmintchev, M. Chen, P. Arpin, M. M. Murnane, and H. C. Kapteyn. The attosecond nonlinear optics of bright coherent X-ray generation. *Nature Photon.*, 4(12):822–832, 2010.
- [21] J.-F. Hergott, M. Kovacev, H. Merdji, C. Hubert, Y. Mairesse, E. Jean, P. Breger, P. Agostini, B. Carré, and P. Salières. Extreme-ultraviolet high-order harmonic pulses in the microjoule range. *Physical Review A*, 66(2):021801, 2002.

- [22] A. L'Huillier, T. Auguste, P. Balcou, B. Carre, P. Monot, P. Salieres, C. Altucci, M. Gaarde, J. Larson, E. Mevel, et al. High-order harmonics: A coherent source in the XUV Range. *J. Nonlinear Optic. Phys. Mat.*, 4(03):647–665, 1995.
- [23] T. Popmintchev, M.-C. Chen, D. Popmintchev, P. Arpin, S. Brown, S. Ališauskas, G. Andriukaitis, T. Balčiunas, O. D. Mücke, A. Pugzlys, et al. Bright Coherent Ultrahigh Harmonics in the KeV X-ray Regime from Mid-Infrared Femtosecond Lasers. *Science*, 336(6086):1287–1291, 2012.
- [24] R. A. Ganeev, M. Suzuki, M. Baba, H. Kuroda, and T. Ozaki. Strong resonance enhancement of a single harmonic generated in the extreme ultraviolet range. *Opt. Lett.*, 31(11):1699–1701, 2006.
- [25] H. Kim, I. Kim, V. Tosa, Y. Lee, and C. Nam. High brightness harmonic generation at 13 nm using self-guided and chirped femtosecond laser pulses. *Appl. Phys. B*, 78(7-8):863–867, 2004.
- [26] L. Le Déroff, P. Salières, B. Carré, D. Joyeux, and D. Phalippou. Measurement of the degree of spatial coherence of high-order harmonics using a Fresnel-mirror interferometer. *Phys. Rev. A*, 61:043802, 2000.
- [27] R. Sandberg, D. Raymondson, C. La-O-Vorakiat, A. Paul, K. Raines, J. Miao, M. Murnane, H. Kapteyn, W. Schlotter, et al. Tabletop soft-X-ray Fourier transform holography with 50 nm resolution. *Opt. Lett.*, 34(11):1618–1620, 2009.
- [28] D. T. Attwood. Soft X-rays and Extreme Ultraviolet Radiation: principles and applications. *Cambridge University Press*, 1999.
- [29] M. Guizar Sicaireos. *Methods for coherent lensless imaging and X-ray wavefront measurements*. 2010.
- [30] J. Miao, P. Charalambous, J. Kirz, and D. Sayre. Extending the methodology of X-ray crystallography to allow imaging of micrometre-sized non-crystalline specimens. *Nature*, 400(6742):342, 1999.
- [31] G. Van Der Schot, M. Svenda, F. R. Maia, M. Hantke, D. P. DePonte, M. M. Seibert, A. Aquila, J. Schulz, R. Kirian, M. Liang, et al. Imaging single cells in a beam of live cyanobacteria with an X-ray laser. *Nature communications*, 6:5704, 2015.
- [32] *Hawk website*, <http://xray.bmc.uu.se/hawk/>.
- [33] H. N. Capman and K. A. Nugent. Coherent lensless X-ray imaging. *Nature Photon.*, 4(12):833–839, 2010.
- [34] S. Marchesini, A. Schirotzek, C. Yang, H.-t. Wu, and F. Maia. Augmented projections for ptychographic imaging. *Inverse Problems*, 29(11):115009, 2013.
- [35] J. R. Fienup. Reconstruction of an object from the modulus of its Fourier transform. *Optics letters*, 3(1):27–29, 1978.

- [36] V. Elser. Phase retrieval by iterated projections. *JOSA A*, 20(1):40–55, 2003.
- [37] G. Tadesse, W. Eschen, R. Klas, V. Hilbert, D. Schelle, A. Nathanael, M. Zilk, M. Steinert, F. Schrempel, T. Pertsch, et al. High resolution XUV Fourier transform holography on a table top. *Scientific reports*, 8(1):8677, 2018.
- [38] A.-S. Morlens, J. Gautier, G. Rey, P. Zeitoun, J.-P. Caumes, M. Kos-Rosset, H. Merdji, S. Kazamias, K. Cassou, and M. Fajardo. Submicrometer digital in-line holographic microscopy at 32 nm with high-order harmonics. *Optics letters*, 31(21):3095–3097, 2006.
- [39] T. Latychevskaia and H.-W. Fink. Practical algorithms for simulation and reconstruction of digital in-line holograms. *Appl. Opt.*, 54(9):2424–2434, 2015.
- [40] R. Coisson. Spatial coherence of synchrotron radiation. *Applied optics*, 34(5):904–908, 1995.
- [41] I. a. Vartanyants, A. Singer, a. P. Mancuso, O. M. Yefanov, A. Sakdinawat, Y. Liu, E. Bang, G. J. Williams, G. Cadenazzi, B. Abbey, H. Sinn, D. Attwood, K. a. Nugent, E. Weckert, T. Wang, D. Zhu, B. Wu, C. Graves, A. Scherz, J. J. Turner, W. F. Schlotter, M. Messerschmidt, J. Lüning, Y. Acremann, P. Heimann, D. C. Mancini, V. Joshi, J. Krzywinski, R. Soufli, M. Fernandez-Perea, S. Hau-Riege, a. G. Peele, Y. Feng, O. Krupin, S. Moeller, and W. Wurth. Coherence properties of individual femtosecond pulses of an X-Ray free-electron laser. *Physical Review Letters*, 107(14):144801, 2011.
- [42] P. Thibault and A. Menzel. Reconstructing state mixtures from diffraction measurements. *Nature*, 494(7435):68, 2013.
- [43] L. Whitehead, G. Williams, H. Quiney, D. Vine, R. Dilanian, S. Flewett, K. Nugent, A. G. Peele, E. Balaur, and I. McNulty. Diffractive imaging using partially coherent X rays. *Physical review letters*, 103(24):243902, 2009.
- [44] S. Mallick and M. L. Roblin. Fourier-transform holography in partially coherent light. *Nouvelle Revue d'Optique Appliquée*, 1(2):5–6, mar 1970. doi: 10.1088/0029-4780/1/2/410. URL <https://doi.org/10.1088/0029-4780/1/2/410>.
- [45] K. Murata, T. Asakura, and H. Fujiwara. Effects of spatial coherence on holography. *Opt. Acta*, 17:5, 1970.
- [46] G. J. Williams, H. M. Quiney, A. G. Peele, and K. A. Nugent. Coherent diffractive imaging and partial coherence. *Physical Review B*, 75(10):104102, 2007.
- [47] J. Gautier, P. Zeitoun, C. Hauri, A. S. Morlens, G. Rey, C. Valentin, E. Papalarazou, J. P. Goddet, S. Sebban, F. Burgy, et al. Optimization of the wave front of high order harmonics. *Eur. Phys. J. D*, 48(3):459–463, 2008.

- [48] N. D. Loh, D. Starodub, L. Lomb, C. Y. Hampton, A. V. Martin, R. G. Sierra, A. Barty, A. Aquila, J. Schulz, J. Steinbrener, et al. Sensing the wavefront of x-ray free-electron lasers using aerosol spheres. *Opt. Express*, 21(10):12385–12394, 2013.
- [49] R. Neutze, R. Wouts, D. van der Spoel, E. Weckert, and J. Hajdu. Potential for biomolecular imaging with femtosecond X-ray pulses. *Nature*, 406(6797):752–757, 2000.
- [50] H. N. Chapman, A. Barty, M. J. Bogan, S. Boutet, M. Frank, S. P. Hau-Riege, S. Marchesini, B. W. Woods, S. Bajt, W. H. Benner, et al. Femtosecond diffractive imaging with a soft-X-ray free-electron laser. *Nature Physics*, 2(12):839, 2006.
- [51] H. Wei. Fundamental limits of ankylography due to dimensional deficiency. *Nature*, 480(7375):E1, 2011.
- [52] G. Wang, H. Yu, W. Cong, and A. Katsevich. Non-uniqueness and instability of ankylography. *Nature*, 480(7375):E2, 2011.
- [53] P. Thibault. Feasibility of 3D reconstructions from a single 2D diffraction measurement. *arXiv preprint arXiv:0909.1643*, 2009.
- [54] C.-C. Chen, H. Jiang, L. Rong, S. Salha, R. Xu, T. G. Mason, and J. Miao. Three-dimensional imaging of a phase object from a single sample orientation using an optical laser. *Physical Review B*, 84(22):224104, 2011.
- [55] R. Xu, H. Jiang, C. Song, J. A. Rodriguez, Z. Huang, C.-C. Chen, D. Nam, J. Park, M. Gallagher-Jones, S. Kim, et al. Single-shot three-dimensional structure determination of nanocrystals with femtosecond X-ray free-electron laser pulses. *Nature communications*, 5:4061, 2014.
- [56] M. Yabashi and H. Tanaka. The next ten years of X-ray science. *Nature Photonics*, 11(1):12, 2017.
- [57] J. Duarte, R. Cassin, J. Huijts, B. Iwan, F. Fortuna, L. Delbecq, H. Chapman, M. Fajardo, M. Kovacev, W. Boutu, et al. Computed stereo lensless X-ray imaging. *Nature Photonics*, 13(7):449–453, 2019.
- [58] *European XFEL facts and figures*, <https://www.xfel.eu/facility/overview>.
- [59] *LCLS parameters – update December 2017*. Linac Coherent Light Source, 2017.
- [60] *SwissFEL website*, <https://www.psi.ch/en/swissfel>.
- [61] L. S. S. Adrian Mancuso. *Overview of the European XFEL and the SPB/SFX instrument: Opportunities for microfluidic sample delivery (and more)*, 2017.
- [62] P. Emma, R. Akre, J. Arthur, R. Bionta, C. Bostedt, J. Bozek, A. Brachmann, P. Bucksbaum, R. Coffee, F.-J. Decker, et al. First lasing and operation of an ångstrom-wavelength free-electron laser. *nature photonics*, 4(9):641, 2010.

- [63] J. Kern, R. Alonso-Mori, J. Hellmich, R. Tran, J. Hattne, H. Laksmono, C. Glöckner, N. Echols, R. G. Sierra, J. Sellberg, et al. Room temperature femtosecond X-ray diffraction of photosystem II microcrystals. *Proc. Natl. Acad. Sci.*, 109(25):9721–9726, 2012.
- [64] T. Ishikawa, H. Aoyagi, T. Asaka, Y. Asano, N. Azumi, T. Bizen, H. Ego, K. Fukami, T. Fukui, Y. Furukawa, et al. A compact X-ray free-electron laser emitting in the sub-ångström region. *nature photonics*, 6(8):540, 2012.
- [65] H. Yoneda, Y. Inubushi, M. Yabashi, T. Katayama, T. Ishikawa, H. Ohashi, H. Yumoto, K. Yamauchi, H. Mimura, and H. Kitamura. Saturable absorption of intense hard X-rays in iron. *Nature communications*, 5:5080, 2014.
- [66] A. Doerr. The new XFELs. *Nature Methods*, 15(1):33, 2018.
- [67] T. Osaka, T. Hirano, Y. Sano, Y. Inubushi, S. Matsuyama, K. Tono, T. Ishikawa, K. Yamauchi, and M. Yabashi. Wavelength-tunable split-and-delay optical system for hard X-ray free-electron lasers. *Optics express*, 24(9):9187–9201, 2016.
- [68] W. Lu, B. Friedrich, T. Noll, K. Zhou, J. Hallmann, G. Ansaldo, T. Roth, S. Serkez, G. Geloni, A. Madsen, et al. Development of a hard X-ray split-and-delay line and performance simulations for two-color pump-probe experiments at the European XFEL. *Review of Scientific Instruments*, 89(6):063121, 2018.
- [69] J. L. Thomaston, R. A. Woldeyes, T. Nakane, A. Yamashita, T. Tanaka, K. Koiwai, A. S. Brewster, B. A. Barad, Y. Chen, T. Lemmin, et al. XFEL structures of the influenza M2 proton channel: Room temperature water networks and insights into proton conduction. *Proceedings of the National Academy of Sciences*, 114(51):13357–13362, 2017.
- [70] S. Horrell, S. V. Antonyuk, R. R. Eady, S. S. Hasnain, M. A. Hough, and R. W. Strange. Serial crystallography captures enzyme catalysis in copper nitrite reductase at atomic resolution from one crystal. *IUCrJ*, 3(4):271–281, 2016.
- [71] M. Schmidt. Mix and inject: Reaction initiation by diffusion for time-resolved macromolecular crystallography. *Advances in Condensed Matter Physics*, 2013, 2013.
- [72] D. Wang, U. Weierstall, L. Pollack, and J. Spence. Double-focusing mixing jet for XFEL study of chemical kinetics. *Journal of synchrotron radiation*, 21(6):1364–1366, 2014.
- [73] J. J. Turner, X. Huang, O. Krupin, K. A. Seu, D. Parks, S. Kevan, E. Lima, K. Kisslinger, I. McNulty, R. Gambino, et al. X-ray diffraction microscopy of magnetic structures. *Physical review letters*, 107(3):033904, 2011.
- [74] M. Sacchi, H. Popescu, N. Jaouen, M. Tortarolo, F. Fortuna, R. Delaunay, and C. Spezzani. Magnetic imaging by Fourier transform holography using linearly polarized X-rays. *Optics express*, 20(9):9769–9776, 2012.

- [75] C. Stamm, T. Kachel, N. Pontius, R. Mitzner, T. Quast, K. Holldack, S. Khan, C. Lupulescu, E. Aziz, M. Wietstruk, et al. Femtosecond modification of electron localization and transfer of angular momentum in nickel. *Nature materials*, 6(10):740, 2007.
- [76] J. N. Eckstein, A. I. Ferguson, and T. W. Hänsch. High-resolution two-photon spectroscopy with picosecond light pulses. *Phys. Rev. Lett.*, 40:847–850, 1978.
- [77] D. Strickland and G. Mourou. Compression of amplified chirped optical pulses. *Opt. Commun.*, 55(6):447–449, 1985.
- [78] A. McPherson, G. Gibson, H. Jara, U. Johann, T. S. Luk, I. McIntyre, K. Boyer, and C. K. Rhodes. Studies of multiphoton production of vacuum-ultraviolet radiation in the rare gases. *JOSA B*, 4(4): 595–601, 1987.
- [79] M. Ferray, A. L’Huillier, X. Li, L. Lompre, G. Mainfray, and C. Manus. Multiple-harmonic conversion of 1064 nm radiation in rare gases. *Journal of Physics B: Atomic, Molecular and Optical Physics*, 21(3):L31, 1988.
- [80] P. B. Corkum. Plasma perspective on strong field multiphoton ionization. *Phys. Rev. Lett.*, 71: 1994–1997, 1993.
- [81] M. Lewenstein, P. Balcou, M. Y. Ivanov, A. L’Huillier, and P. B. Corkum. Theory of high-harmonic generation by low-frequency laser fields. *Phys. Rev. A*, 49(3):2117–2132, 1994.
- [82] J. Duarte, R. Cassin, A. I. González, M. Fajardo, W. Boutu, and H. Merdji. Single-shot spatial coherence characterization of X-ray sources. *To be submitted to Optics Letters*, page 1, 2019.
- [83] E. L. Falcão-Filho, V. Gkortsas, A. Gordon, and F. X. Kärtner. Analytic scaling analysis of high harmonic generation conversion efficiency. *Opt. Express*, 17(13):11217–11229, 2009.
- [84] S. Hadrich, J. Rothhardt, A. Klenke, M. Krebs, A. Hoffmann, O. Pronin, V. Pervak, J. Limpert, and A. Tunnermann. High harmonic generation of fiber laser systems with more than 100 μ W average power per harmonic. In *Lasers and Electro-Optics (CLEO), 2014 Conference on*, pages 1–2. IEEE, 2014.
- [85] P. Zeitoun, G. Faivre, S. Sebban, T. Mocek, A. Hallou, M. Fajardo, D. Aubert, P. Balcou, F. Burgy, D. Douillet, et al. A high-intensity highly coherent soft X-ray femtosecond laser seeded by a high harmonic beam. *Nature*, 431(7007):426–429, 2004.
- [86] G. Lambert, T. Hara, D. Garzella, T. Tanikawa, M. Labat, B. Carre, H. Kitamura, T. Shintake, M. Bougeard, S. Inoue, et al. Injection of harmonics generated in gas in a free-electron laser providing intense and coherent extreme-ultraviolet light. *Nat. Phys.*, 4(4):296–300, 2008.
- [87] F. Brizuela, C. Heyl, P. Rudawski, D. Kroon, L. Rading, J. M. Dahlström, J. Mauritsson, P. Johnsson, C. Arnold, and A. L’Huillier. Efficient high-order harmonic generation boosted by below-threshold harmonics. *Scientific reports*, 3:1410, 2013.

- [88] D. Rupp, N. Monserud, B. Langbehn, M. Sauppe, J. Zimmermann, Y. Ovcharenko, T. Möller, F. Frassetto, L. Poletto, A. Trabattoni, et al. Coherent diffractive imaging of single helium nanodroplets with a high harmonic generation source. *Nature communications*, 8(1):493, 2017.
- [89] S. Dobosz, G. Doumy, H. Stabile, P. D'oliveira, P. Monot, F. Réau, S. Hüller, and P. Martin. Probing hot and dense laser-induced plasmas with ultrafast XUV pulses. *Physical review letters*, 95(2):025001, 2005.
- [90] J.-F. Hergott, P. Salières, H. Merdji, L. Le Deroff, B. Carré, T. Auguste, P. Monot, P. D'OLIVEIRA, D. Descamps, J. Norin, et al. XUV interferometry using high-order harmonics: Application to plasma diagnostics. *Laser and Particle Beams*, 19(1):35–40, 2001.
- [91] A. Schiffrin, T. Paasch-Colberg, N. Karpowicz, V. Apalkov, D. Gerster, S. Mühlbrandt, M. Korbman, J. Reichert, M. Schultze, S. Holzner, et al. Optical-field-induced current in dielectrics. *Nature*, 493(7430):70, 2013.
- [92] P. Antoine, A. L'Huillier, and M. Lewenstein. Attosecond pulse trains using high-order harmonics. *Phys. Rev. Lett.*, 77:1234–1237, 1996.
- [93] A. Baltuška, T. Udem, M. Uiberacker, M. Hentschel, E. Goulielmakis, C. Gohle, R. Holzwarth, V. Yakovlev, A. Scrinzi, T. W. Hänsch, et al. Attosecond control of electronic processes by intense light fields. *Nature*, 421(6923):611–615, 2003.
- [94] R. Lopez-Martens, K. Varjú, P. Johnsson, J. Mauritsson, Y. Mairesse, P. Salieres, M. B. Gaarde, K. J. Schafer, A. Persson, S. Svanberg, et al. Amplitude and phase control of attosecond light pulses. *Phys. Rev. Lett.*, 94:033001, 2005.
- [95] M. Drescher, M. Hentschel, R. Kienberger, G. Tempea, C. Spielmann, G. A. Reider, P. B. Corkum, and F. Krausz. X-ray pulses approaching the attosecond frontier. *Science*, 291(5510):1923–1927, 2001.
- [96] M. Drescher, M. Hentschel, R. Kienberger, M. Uiberacker, V. Yakovlev, A. Scrinzi, T. Westerwalbesloh, U. Kleineberg, U. Heinzmann, and F. Krausz. Time-resolved atomic inner-shell spectroscopy. *Nature*, 419(6909):803, 2002.
- [97] R. Kienberger, E. Goulielmakis, M. Uiberacker, A. Baltuska, V. Yakovlev, F. Bammer, A. Scrinzi, T. Westerwalbesloh, U. Kleineberg, U. Heinzmann, et al. Atomic transient recorder. *Nature*, 427(6977):817, 2004.
- [98] H. Niikura, F. Légaré, R. Hasbani, M. Y. Ivanov, D. Villeneuve, and P. Corkum. Probing molecular dynamics with attosecond resolution using correlated wave packet pairs. *Nature*, 421(6925):826, 2003.
- [99] D. Sayre. Imaging processes and coherence in physics. *Springer Lecture Notes in Physics*, 112:229–235, 1980.

- [100] S. Marchesini, H. He, H. N. Chapman, S. P. Hau-Riege, A. Noy, M. R. Howells, U. Weierstall, and J. C. Spence. X-ray image reconstruction from a diffraction pattern alone. *Physical Review B*, 68(14):140101, 2003.
- [101] N. Loh, C. Y. Hampton, A. V. Martin, D. Starodub, R. G. Sierra, A. Barty, A. Aquila, J. Schulz, L. Lomb, J. Steinbrener, et al. Fractal morphology, imaging and mass spectrometry of single aerosol particles in flight. *Nature*, 486(7404):513, 2012.
- [102] C. Bostedt, E. Eremina, D. Rupp, M. Adolph, H. Thomas, M. Hoener, A. De Castro, J. Tiggesbäumker, K.-H. Meiwes-Broer, T. Laarmann, et al. Ultrafast X-ray scattering of xenon nanoparticles: imaging transient states of matter. *Physical review letters*, 108(9):093401, 2012.
- [103] D. Gabor. A new microscopic principle. *Nature*, 161(4098):777–778, 1948.
- [104] U. Schnars and W. Jueptner. *Digital holography*. Springer, 2005.
- [105] S. Aoki and S. Kikuta. X-ray holographic microscopy. *Japanese Journal of Applied Physics*, 13(9):1385, 1974.
- [106] Y. Suzuki and A. Takeuchi. Gabor holography with speckle-free spherical wave in hard X-ray region. *Japanese Journal of Applied Physics*, 51(8R):086701, 2012.
- [107] N. Watanabe and S. Aoki. Three-dimensional tomography using a soft X-ray holographic microscope and CCD camera. *Journal of synchrotron radiation*, 5(3):1088–1089, 1998.
- [108] S. P. Krüger, K. Giewekemeyer, S. Kalbfleisch, M. Bartels, H. Neubauer, and T. Salditt. Sub-15 nm beam confinement by two crossed x-ray waveguides. *Optics Express*, 18(13):13492–13501, 2010.
- [109] J. C. Aguilar, M. Misawa, K. Matsuda, S. Rehman, M. Yasumoto, Y. Suzuki, A. Takeuchi, and L. Berriel-Valdos. Starlet transform applied to digital Gabor holographic microscopy. *Applied optics*, 55(24):6617–6624, 2016.
- [110] A. Rosenhahn, F. Staier, T. Nisius, D. Schäfer, R. Barth, C. Christophis, L.-M. Stadler, S. Streit-Nierobisch, C. Gutt, A. Mancuso, et al. Digital in-line holography with femtosecond VUV radiation provided by the free-electron laser FLASH. *Optics express*, 17(10):8220–8228, 2009.
- [111] I. T. Ra’anan, M. E. Siemens, O. Cohen, M. M. Murnane, H. C. Kapteyn, and K. A. Nelson. Ultrafast extreme ultraviolet holography: dynamic monitoring of surface deformation. *Optics letters*, 32(3):286–288, 2007.
- [112] J. Lim, H. J. Shin, and C. K. Hong. High-resolution soft X-ray digital in-line holographic microscopy. *Japanese Journal of Applied Physics*, 50(7R):072504, 2011.
- [113] G. W. Stroke. Lensless Fourier-transform method for optical holography. *Appl. Phys. Lett.*, 6(10):201–203, 1965.

- [114] S. Aoki, Y. Ichihara, and S. Kikuta. X-ray hologram obtained by using synchrotron radiation. *Jpn. J. Appl. Phys.*, 11(12):1857, 1972.
- [115] S. Eisebitt, J. Lüning, W. Schlotter, M. Lörger, O. Hellwig, W. Eberhardt, and J. Stöhr. Lensless imaging of magnetic nanostructures by X-ray spectro-holography. *Nature*, 432(7019):885, 2004.
- [116] S. Marchesini, S. Boutet, A. E. Sakdinawat, M. J. Bogan, S. Bajt, A. Barty, H. N. Chapman, M. Frank, S. P. Hau-Riege, A. Szöke, et al. Massively parallel X-ray holography. *Nature photonics*, 2(9):560, 2008.
- [117] A. V. Martin, A. J. D’Alfonso, F. Wang, R. Bean, F. Capotondi, R. A. Kirian, E. Pedersoli, L. Raimondi, F. Stellato, C. H. Yoon, et al. X-ray holography with a customizable reference. *Nature communications*, 5:4661, 2014.
- [118] D. Stickler, R. Frömter, H. Stillrich, C. Menk, C. Tieg, S. Streit-Nierobisch, M. Sprung, C. Gutt, L.-M. Stadler, O. Leupold, et al. Soft X-ray holographic microscopy. *Applied Physics Letters*, 96(4):042501, 2010.
- [119] S. Roy, D. Parks, K. Seu, R. Su, J. Turner, W. Chao, E. Anderson, S. Cabrini, and S. Kevan. Lensless X-ray imaging in reflection geometry. *Nature Photonics*, 5(4):243, 2011.
- [120] M. Guizar-Sicairos and J. R. Fienup. Direct image reconstruction from a Fourier intensity pattern using HERALDO. *Optics letters*, 33(22):2668–2670, 2008.
- [121] D. Gauthier. *Imagerie nanométrique ultra-rapide par diffraction cohérente de rayonnement extrême-UV produit par génération d’harmoniques d’ordre élevé*. PhD thesis, Université Paris Sud-Paris XI, 2012.
- [122] H. N. Chapman, A. Barty, S. Marchesini, A. Noy, S. P. Hau-Riege, C. Cui, M. R. Howells, R. Rosen, H. He, J. C. Spence, et al. High-resolution ab initio three-dimensional X-ray diffraction microscopy. *JOSA A*, 23(5):1179–1200, 2006.
- [123] D. A. Shapiro, Y.-S. Yu, T. Tyliczszak, J. Cabana, R. Celestre, W. Chao, K. Kaznatcheev, A. D. Kilcoyne, F. Maia, S. Marchesini, et al. Chemical composition mapping with nanometre resolution by soft X-ray microscopy. *Nature Photonics*, 8(10):765, 2014.
- [124] B. Kaulich, P. Thibault, A. Gianoncelli, and M. Kiskinova. Transmission and emission x-ray microscopy: operation modes, contrast mechanisms and applications. *Journal of Physics: Condensed Matter*, 23(8):083002, 2011.
- [125] M. R. Howells, T. Beetz, H. N. Chapman, C. Cui, J. Holton, C. Jacobsen, J. Kirz, E. Lima, S. Marchesini, H. Miao, et al. An assessment of the resolution limitation due to radiation-damage in X-ray diffraction microscopy. *Journal of electron spectroscopy and related phenomena*, 170(1-3):4–12, 2009.

- [126] Q. Shen, I. Bazarov, and P. Thibault. Diffractive imaging of nonperiodic materials with future coherent X-ray sources. *Journal of synchrotron radiation*, 11(5):432–438, 2004.
- [127] X. Ge. *Imagerie ultrarapide à l'échelle nanométrique par diffraction XUV cohérente*. PhD thesis, Paris 11, 2012.
- [128] J. R. Fienup. Reconstruction of a complex-valued object from the modulus of its Fourier transform using a support constraint. *JOSA A*, 4(1):118–123, 1987.
- [129] W. Xu, M. Jericho, I. Meinertzhagen, and H. Kreuzer. Digital in-line holography for biological applications. *Proceedings of the National Academy of Sciences*, 98(20):11301–11305, 2001.
- [130] "Lens diffraction: what it is, and how to avoid it", <https://static.bhphotovideo.com/explora/sites/default/files/styles/top>
- [131] J. W. Goodman. Introduction to Fourier optics. *Roberts & Company Publishers*, 1996.
- [132] J. Jackson. *Classical Electrodynamics*. Wiley, 3rd edition, 1999.
- [133] E. Wolf and E. Marchand. Comparison of the Kirchhoff and the Rayleigh–Sommerfeld theories of diffraction at an aperture. *JOSA*, 54(5):587–594, 1964.
- [134] D. Paganin. *Coherent X-ray optics*. Number 6. Oxford University Press on Demand, 2006.
- [135] K. Morgan, K. K. Siu, and D. Paganin. The projection approximation and edge contrast for x-ray propagation-based phase contrast imaging of a cylindrical edge. *Optics express*, 18(10):9865–9878, 2010.
- [136] E. H. Tsai, I. Usov, A. Diaz, A. Menzel, and M. Guizar-Sicairos. X-ray ptychography with extended depth of field. *Optics express*, 24(25):29089–29108, 2016.
- [137] P. Thibault, M. Dierolf, A. Menzel, O. Bunk, C. David, and F. Pfeiffer. High-resolution scanning X-ray diffraction microscopy. *Science*, 321(5887):379–382, 2008.
- [138] M. Dierolf, A. Menzel, P. Thibault, P. Schneider, C. M. Kewish, R. Wepf, O. Bunk, and F. Pfeiffer. Ptychographic X-ray computed tomography at the nanoscale. *Nature*, 467(7314):436, 2010.
- [139] M. Guizar-Sicairos, A. Diaz, M. Holler, M. S. Lucas, A. Menzel, R. A. Wepf, and O. Bunk. Phase tomography from X-ray coherent diffractive imaging projections. *Optics express*, 19(22):21345–21357, 2011.
- [140] J. Samaan. *Étude et applications de l'imagerie sans lentille par diffraction cohérente*. PhD thesis, Paris Saclay, 2016.
- [141] J. Kirz, C. Jacobsen, and M. Howells. Soft X-ray microscopes and their biological applications. *Quarterly reviews of biophysics*, 28(1):33–130, 1995.
- [142] W. F. Schlotter. *Lensless Fourier transform holography with soft X-rays*. PhD thesis, Stanford University, 2007.

- [143] J. R. Fienup. Phase retrieval algorithms: a comparison. *Applied optics*, 21(15):2758–2769, 1982.
- [144] K. Nugent, A. Peele, H. Quiney, and H. Chapman. Diffraction with wavefront curvature: a path to unique phase recovery. *Acta Crystallographica Section A: Foundations of Crystallography*, 61(3):373–381, 2005.
- [145] T. A. Pitts and J. F. Greenleaf. Fresnel transform phase retrieval from magnitude. *IEEE transactions on ultrasonics, ferroelectrics, and frequency control*, 50(8):1035–1045, 2003.
- [146] Y. M. Bruck and L. Sodin. On the ambiguity of the image reconstruction problem. *Optics communications*, 30(3):304–308, 1979.
- [147] R. Bates. Fourier phase problems are uniquely solvable in more than one dimension. I: Underlying theory. *Optik (Stuttgart)*, 61:247–262, 1982.
- [148] R. W. Gerchberg. A practical algorithm for the determination of phase from image and diffraction plane pictures. *Optik*, 35:237–246, 1972.
- [149] S. Marchesini. Invited article: A unified evaluation of iterative projection algorithms for phase retrieval. *Review of scientific instruments*, 78(1):011301, 2007.
- [150] P. Thibault. *Algorithmic methods in diffraction microscopy*. Cornell University Ithaca, 2007.
- [151] R. Könnecke. *Multiple and extended references in Fourier transform holography*. PhD thesis, Technischen Universität Berlin, 2010.
- [152] H. Nyquist. Certain topics in telegraph transmission theory. *Transactions of the American Institute of Electrical Engineers*, 47(2):617–644, 1928.
- [153] C. E. Shannon. Communication in the presence of noise. *Proceedings of the IEEE*, 86(2):447–457, 1998.
- [154] D. Sayre. Some implications of a theorem due to Shannon. *Acta Crystallographica*, 5(6):843–843, 1952.
- [155] J. Miao and D. Sayre. On possible extensions of X-ray crystallography through diffraction-pattern oversampling. *Acta Crystallographica Section A: Foundations of Crystallography*, 56(6):596–605, 2000.
- [156] S. Jericho, J. Garcia-Sucerquia, W. Xu, M. Jericho, and H. Kreuzer. Submersible digital in-line holographic microscope. *Rev. Sci. Instrum.*, 77(4):043706, 2006.
- [157] T. Latychevskaia, J.-N. Longchamp, and H.-W. Fink. When holography meets coherent diffraction imaging. *Opt. Express*, 20(27):28871–28892, 2012.
- [158] A. Pogany, D. Gao, and S. Wilkins. Contrast and resolution in imaging with a microfocus X-ray source. *Review of Scientific Instruments*, 68(7):2774–2782, 1997.

- [159] M. Wilson. Microscope resolution: concepts, factors and calculation. *Leica Microsystems Science Lab*, 2016.
- [160] E. Abbe. VII.—On the estimation of aperture in the microscope. *Journal of the Royal Microscopical Society*, 1(3):388–423, 1881.
- [161] X. Ge, M. Ducouso, W. Boutu, B. Tudu, B. Barbrel, D. Gauthier, A. Borta, A.-I. Gonzalez, F. Wang, B. Iwan, et al. Sub-100 nanometer lensless probing of Co/Pd magnetic nanodomains using a table-top femtosecond soft X-ray harmonic source. *Journal of Modern Optics*, 60(17):1475–1483, 2013.
- [162] R. Cassin. *Imagerie nanométrique ultra-rapide par diffraction cohérente de rayonnement XUV produit par génération d'harmoniques d'ordre élevés*. PhD thesis, Université paris sud 11, LRI; Paris Saclay, 2017.
- [163] M. Guizar-Sicairos, S. T. Thurman, and J. R. Fienup. Efficient subpixel image registration algorithms. *Optics letters*, 33(2):156–158, 2008.
- [164] L. Le Déroff, P. Salières, B. Carré, D. Joyeux, and D. Phalippou. Measurement of the degree of spatial coherence of high-order harmonics using a Fresnel-mirror interferometer. *Physical Review A*, 61(4):043802, 2000.
- [165] A. Singer, F. Sorgenfrei, A. P. Mancuso, N. Gerasimova, O. Yefanov, J. Gulden, T. Gorniak, T. Senkbeil, A. Sakdinawat, Y. Liu, et al. Spatial and temporal coherence properties of single free-electron laser pulses. *Optics express*, 20(16):17480–17495, 2012.
- [166] C. Iaconis and I. A. Walmsley. Direct measurement of the two-point field correlation function. *Optics letters*, 21(21):1783–1785, 1996.
- [167] C.-C. Cheng, M. Raymer, and H. Heier. A variable lateral-shearing Sagnac interferometer with high numerical aperture for measuring the complex spatial coherence function of light. *Journal of Modern Optics*, 47(7):1237–1246, 2000.
- [168] M. Santarsiero and R. Borghi. Measuring spatial coherence by using a reversed-wavefront Young interferometer. *Optics letters*, 31(7):861–863, 2006.
- [169] L. Le Déroff, P. Salières, B. Carré, D. Joyeux, D. Phalippou, P. Monot, P. D'OLIVEIRA, T. Auguste, H. Merdji, and J.-F. Hergott. Temporal and spatial coherence of high order harmonics. *Laser physics*, 10(1):294–302, 2000.
- [170] Y. Mejía and A. I. González. Measuring spatial coherence by using a mask with multiple apertures. *Optics Communications*, 273(2):428–434, 2007.
- [171] A. I. González and Y. Mejía. Nonredundant array of apertures to measure the spatial coherence in two dimensions with only one interferogram. *JOSA A*, 28(6):1107–1113, 2011.

- [172] B. Thompson and E. Wolf. Two-beam interference with partially coherent light. *JOSA*, 47(10): 895–902, 1957.
- [173] S. Cho, M. A. Alonso, and T. G. Brown. Measurement of spatial coherence through diffraction from a transparent mask with a phase discontinuity. *Optics letters*, 37(13):2724–2726, 2012.
- [174] K. A. Sharma, T. G. Brown, and M. A. Alonso. Phase-space approach to lensless measurements of optical field correlations. *Optics express*, 24(14):16099–16110, 2016.
- [175] F. Kashani, M. R. H. Rad, and B. Ghafary. Real time measurement of the spatial coherence using non-redundant two-dimensional aperture array. *Optik*, 123(15):1317–1321, 2012.
- [176] Y. Jiang, T. Pfeifer, A. Rudenko, O. Herrwerth, L. Foucar, M. Kurka, K. Kühnel, M. Lezius, M. F. Kling, X. Liu, et al. Temporal coherence effects in multiple ionization of N₂ via XUV pump-probe autocorrelation. *Physical Review A*, 82(4):041403, 2010.
- [177] J. Clark, X. Huang, R. Harder, and I. Robinson. High-resolution three-dimensional partially coherent diffraction imaging. *Nature communications*, 3:993, 2012.
- [178] A. I. Gonzalez. *Single shot lensless imaging with coherence and wavefront characterization of harmonic and FEL sources*. PhD thesis, Université Paris Sud-Paris XI, 2015.
- [179] W. Boutu. *Dynamique de la generation d'harmoniques dans les atomes et les molecules*. PhD thesis, Université Paris Sud-Paris XI, 2007.
- [180] R. W. Boyd. *Nonlinear optics*. Elsevier, 2003.
- [181] E. Constant, D. Garzella, P. Breger, E. Mével, C. Dorrer, C. Le Blanc, F. Salin, and P. Agostini. Optimizing high harmonic generation in absorbing gases: Model and experiment. *Physical Review Letters*, 82(8):1668, 1999.
- [182] A. L. Lytle. *Phase matching and coherence of high-order harmonic generation in hollow waveguides*. PhD thesis, Citeseer, 2008.
- [183] E. Georgiadou. Study of harmonic generation with a two-color field. Technical report, Lund university, LRAP-375, 2007.
- [184] J. L. Krause, K. J. Schafer, and K. C. Kulander. High-order harmonic generation from atoms and ions in the high intensity regime. *Phys. Rev. Lett.*, 68(24):3535–3538, 1992.
- [185] E. Takahashi, N. Nabekawa, and K. Midorikawa. Generation of 10- μ J coherent extreme-ultraviolet light by use of high-order harmonics. *Opt. Lett.*, 27(21):1920–1922, 2002.
- [186] P. M. Paul, E. Toma, P. Breger, G. Mullot, F. Augé, P. Balcou, H. Muller, and P. Agostini. Observation of a train of attosecond pulses from high harmonic generation. *Science*, 292(5522): 1689–1692, 2001.

- [187] R. A. Ganeev, M. Baba, M. Suzuki, and H. Kuroda. Optimization of harmonic generation from boron plasma. *J. Appl. Phys.*, 99(10):103303, 2006.
- [188] *Center for X-ray optics*, <http://www.cxro.lbl.gov/>.
- [189] T. Young. I. The Bakerian lecture. Experiments and calculations relative to physical optics. *Philosophical transactions of the Royal Society of London*, (94):1–16, 1804.
- [190] F. Zernike. The concept of degree of coherence and its application to optical problems. *Physica*, 5(8):785–795, 1938.
- [191] S. Divitt, Z. J. Lapin, and L. Novotny. Measuring coherence functions using non-parallel double slits. *Optics express*, 22(7):8277–8290, 2014.
- [192] S. Divitt and L. Novotny. Spatial coherence of sunlight and its implications for light management in photovoltaics. *Optica*, 2(2):95–103, 2015.
- [193] B. Stoklasa, L. Motka, J. Rehacek, Z. Hradil, and L. Sánchez-Soto. Wavefront sensing reveals optical coherence. *Nature communications*, 5:3275, 2014.
- [194] H. Westfahl Jr, S. A. Lordano Luiz, B. C. Meyer, and F. Meneau. The coherent radiation fraction of low-emittance synchrotrons. *Journal of synchrotron radiation*, 24(3):566–575, 2017.
- [195] *RP Photonics website*, <https://www.rp-photonics.com/coherence.html>.
- [196] L. Mandel and E. Wolf. *Optical coherence and quantum optics*. Cambridge university press, 1995.
- [197] J. W. Goodman. *Statistical optics*. John Wiley & Sons, 2015.
- [198] F. Dubois, M.-L. N. Requena, C. Minetti, O. Monnom, and E. Istasse. Partial spatial coherence effects in digital holographic microscopy with a laser source. *Applied optics*, 43(5):1131–1139, 2004.
- [199] U. Gopinathan, G. Pedrini, and W. Osten. Coherence effects in digital in-line holographic microscopy. *JOSA A*, 25(10):2459–2466, 2008.
- [200] W. Schlotter, R. Rick, K. Chen, A. Scherz, J. Stöhr, J. Lüning, S. Eisebitt, C. Günther, W. Eberhardt, O. Hellwig, et al. Multiple reference Fourier transform holography with soft x rays. *Applied Physics Letters*, 89(16):163112, 2006.
- [201] B. Moths and A. Ourmazd. Bayesian algorithms for recovering structure from single-particle diffraction snapshots of unknown orientation: a comparison. *Foundations of Crystallography*, 67(5):481–486, 2011.
- [202] S.-K. Son, L. Young, R. Santra, et al. Impact of hollow-atom formation on coherent x-ray scattering at high intensity. *Physical Review A*, 83(3):033402, 2011.

- [203] H. N. Chapman. X-ray free-electron lasers for the structure and dynamics of macromolecules. *Annual review of biochemistry*, 2019.
- [204] S. Witte, V. T. Tenner, D. W. Noom, and K. S. Eikema. Lensless diffractive imaging with ultra-broadband table-top sources: from infrared to extreme-ultraviolet wavelengths. *Light: Science & Applications*, 3(3):e163, 2014.
- [205] L. Poletto, F. Frassetto, F. Calegari, S. Anumula, A. Trabattoni, and M. Nisoli. Micro-focusing of attosecond pulses by grazing-incidence toroidal mirrors. *Optics express*, 21(11):13040–13051, 2013.
- [206] P. Ferraro, S. De Nicola, A. Finizio, G. Coppola, S. Grilli, C. Magro, and G. Pierattini. Compensation of the inherent wave front curvature in digital holographic coherent microscopy for quantitative phase-contrast imaging. *Appl. Opt.*, 42(11):1938–1946, 2003.
- [207] L. Miccio, D. Alfieri, S. Grilli, P. Ferraro, A. Finizio, L. De Petrocellis, and S. Nicola. Direct full compensation of the aberrations in quantitative phase microscopy of thin objects by a single digital hologram. *Appl. Phys. Lett.*, 90(4):041104, 2007.
- [208] C. Roddier and F. Roddier. Diffraction-limited imaging of unknown objects through fixed unknown aberrations using interferometry. *JOSA A*, 7(10):1824–1833, 1990.
- [209] A. Stadelmaier and J. H. Massig. Compensation of lens aberrations in digital holography. *Opt. Letters*, 25(22):1630–1632, 2000.
- [210] M. Bayraktar, A. Chopra, G. Rijnders, K. Boller, and F. Bijkerk. Wavefront correction in the extreme ultraviolet wavelength range using piezoelectric thin films. *Opt. Express*, 22(25):30623–30632, 2014.
- [211] C. Zuo, Q. Chen, W. Qu, and A. Asundi. Phase aberration compensation in digital holographic microscopy based on principal component analysis. *Opt. Lett.*, 38(10):1724–1726, 2013.
- [212] E. Cuhe, P. Marquet, and C. Depeursinge. Simultaneous amplitude-contrast and quantitative phase-contrast microscopy by numerical reconstruction of Fresnel off-axis holograms. *Appl. Opt.*, 38(34):6994–7001, 1999.
- [213] E. Hecht, R. Dal Col, R. W. Talavera, and J. M. G. Pérez. *Óptica*. Addison Wesley, 2000.
- [214] G. Yoon. *Presentation "Aberrations theory"*, http://cfao.ucolick.org/pubs/presentations/eyedesign/05_aberrations_GY.pdf.
- [215] *"Astronomical optics part 4: optical aberrations"*, <http://www.handprint.com/ASTRO/ae4.html>.
- [216] J. C. Wyant and K. Creath. Basic wavefront aberration theory for optical metrology. *Appl. Opt. and Opt. Eng.*, 11(s 29):2, 1992.

- [217] J. Hartmann. *Bemerkungen über den Bau und die Justirung von Spektrographen*. Springer, 1900.
- [218] P. Mercère, P. Zeitoun, M. Idir, S. Le Pape, D. Douillet, X. Levecq, G. Dovillaire, S. Bucourt, K. A. Goldberg, P. P. Naulleau, et al. Hartmann wave-front measurement at 13.4 nm with λ EUV/120 accuracy. *Opt. Lett.*, 28(17):1534–1536, 2003.
- [219] F. Sanson, A. Pandey, F. Harms, G. Dovillaire, E. Baynard, J. Demailly, O. Guilbaud, B. Lucas, O. Neveu, M. Pittman, et al. Hartmann wavefront sensor characterization of a high charge vortex beam in the extreme ultraviolet spectral range. *Optics letters*, 43(12):2780–2783, 2018.
- [220] J. Koliyadu. *Spatio-temporal characterization of high harmonic generation for plasma diagnostics*. PhD thesis, Instituto Superior Técnico, 2018.
- [221] *Phasics website*, <http://www.phasics.com/technology/lateral-shearing-interferometry.html>.
- [222] J.-C. Chanteloup. Multiple-wave lateral shearing interferometry for wave-front sensing. *Appl. Opt.*, 44(9):1559–1571, 2005.
- [223] J. Duarte. *Coherent XUV imaging*. PhD thesis, Instituto Superior Técnico, 2015.
- [224] T. Latychevskaia and H.-W. Fink. Solution to the twin image problem in holography. *Phys. Rev. Lett.*, 98(23):233901, 2007.
- [225] M. Tegze and G. Faigel. X-ray holography with atomic resolution. *Nature*, 380(6569):49, 1996.
- [226] W. Bragg and G. L. Rogers. Elimination of the unwanted image in diffraction microscopy. *Nature*, 167(4240):190, 1951.
- [227] E. N. Leith and J. Upatnieks. Wavefront reconstruction with diffused illumination and three-dimensional objects. *Josa*, 54(11):1295–1301, 1964.
- [228] O. Bryngdahl and A. Lohmann. Single-sideband holography. *JOSA*, 58(5):620–624, 1968.
- [229] S. Tong, H. Li, and H. Huang. Energy extension in three-dimensional atomic imaging by electron emission holography. *Physical review letters*, 67(22):3102, 1991.
- [230] J. Barton. Removing multiple scattering and twin images from holographic images. *Physical review letters*, 67(22):3106, 1991.
- [231] K. Nugent. Twin-image elimination in Gabor holography. *Optics communications*, 78(3-4):293–299, 1990.
- [232] X. H. Huang, J.-M. Zuo, and J. C. Spence. Wavefront reconstruction for in-line holograms formed by pure amplitude objects. *Applied surface science*, 148(3-4):229–234, 1999.
- [233] J. F. Arocena, T. A. Rothwell, and M. R. Shegelski. Iterative reconstruction of in-line electron holograms. *Micron*, 36(1):23–30, 2005.

- [234] C. Cho, B. Choi, H. Kang, and S. Lee. Numerical twin image suppression by nonlinear segmentation mask in digital holography. *Optics express*, 20(20):22454–22464, 2012.
- [235] L. Rong, Y. Li, S. Liu, W. Xiao, F. Pan, and D. Wang. Iterative solution to twin image problem in in-line digital holography. *Optics and Lasers in Engineering*, 51(5):553–559, 2013.
- [236] W. Zhang, L. Cao, D. J. Brady, H. Zhang, J. Cang, H. Zhang, and G. Jin. Twin-image-free holography: a compressive sensing approach. *Physical review letters*, 121(9):093902, 2018.
- [237] R. Corman, W. Boutu, A. Campalans, P. Radicella, J. Duarte, L. Bally-Cuif, N. Dray, F. Harms, G. Dovillaire, S. Bucourt, and H. Merdji. Lensless microscopy platform for single cell and tissue visualization. *Biomedical Optics Express*, page 1, 2020.
- [238] P. Homer, B. Rus, J. Hrebicek, and J. Nejd. Wavefront sensing in XUV: HHG beam profile measurement. In *Adaptive optics: Methods, analysis and applications*, page APDP5. Optical Society of America, 2011.
- [239] Y. Liu, M. Seaberg, D. Zhu, J. Krzywinski, F. Seiboth, C. Hardin, D. Cocco, A. Aquila, B. Nagler, H. J. Lee, et al. High-accuracy wavefront sensing for x-ray free electron lasers. *Optica*, 5(8):967–975, 2018.
- [240] M. Seaberg, R. Cojocar, S. Berujon, E. Ziegler, A. Jaggi, J. Krempasky, F. Seiboth, A. Aquila, Y. Liu, A. Sakdinawat, et al. Wavefront sensing at X-ray free-electron lasers. *Journal of Synchrotron Radiation*, 26(4), 2019.
- [241] *Imagine Optics*. <https://www.imagine-optic.com/>.
- [242] L. Redecke, K. Nass, D. P. DePonte, T. A. White, D. Rehders, A. Barty, F. Stellato, M. Liang, T. R. Barends, S. Boutet, et al. Natively inhibited Trypanosoma brucei cathepsin B structure determined by using an X-ray laser. *Science*, 339(6116):227–230, 2013.
- [243] J. Miao, T. Ishikawa, I. K. Robinson, and M. M. Murnane. Beyond crystallography: diffractive imaging using coherent X-ray light sources. *Science*, 348(6234):530–535, 2015.
- [244] Y. Nishino, Y. Takahashi, N. Imamoto, T. Ishikawa, and K. Maeshima. Three-dimensional visualization of a human chromosome using coherent X-ray diffraction. *Physical review letters*, 102(1):018101, 2009.
- [245] Y. Takahashi, N. Zettsu, Y. Nishino, R. Tsutsumi, E. Matsubara, T. Ishikawa, and K. Yamauchi. Three-dimensional electron density mapping of shape-controlled nanoparticle by focused hard X-ray diffraction microscopy. *Nano letters*, 10(5):1922–1926, 2010.
- [246] M. Holler, J. Raabe, A. Diaz, M. Guizar-Sicairos, C. Quitmann, A. Menzel, and O. Bunk. An instrument for 3D x-ray nano-imaging. *Review of Scientific Instruments*, 83(7):073703, 2012.
- [247] E. Thomson. *Stereoscopic roentgen pictures*. 1896.

- [248] H. Andruleit, M. Geisen, and S. Stäger. Stereo-microscopy of coccolithophores-modern applications for imaging and morphological analysis. *Journal of nanoplankton research*, 28(1):1–16, 2006.
- [249] M. Hoshino, K. Uesugi, J. Pearson, T. Sonobe, M. Shirai, and N. Yagi. Development of an X-ray real-time stereo imaging technique using synchrotron radiation. *Journal of synchrotron radiation*, 18(4):569–574, 2011.
- [250] S.-C. GLEBER, J. Thieme, W. Chao, and P. Fischer. Stereo soft X-ray microscopy and elemental mapping of haematite and clay suspensions. *Journal of microscopy*, 235(2):199–208, 2009.
- [251] J. Miao, T. Ishikawa, B. Johnson, E. H. Anderson, B. Lai, and K. O. Hodgson. High resolution 3D X-ray diffraction microscopy. *Physical review letters*, 89(8):088303, 2002.
- [252] K. Schmidt, J. Spence, U. Weierstall, R. Kirian, X. Wang, D. Starodub, H. Chapman, M. Howells, and R. Doak. Tomographic femtosecond X-ray diffractive imaging. *Physical review letters*, 101(11):115507, 2008.
- [253] M. Gallagher-Jones, Y. Bessho, S. Kim, J. Park, S. Kim, D. Nam, C. Kim, Y. Kim, O. Miyashita, F. Tama, et al. Macromolecular structures probed by combining single-shot free-electron laser diffraction with synchrotron coherent X-ray imaging. *Nature communications*, 5:3798, 2014.
- [254] S. P. Parker. *Encyclopedia of science and technology*, volume 21. McGraw-Hill, 1997.
- [255] H. Kim and K. Sohn. 3D reconstruction from stereo images for interactions between real and virtual objects. *Signal Processing: Image Communication*, 20(1):61–75, 2005.
- [256] C. E. Lyman, D. E. Newbury, J. Goldstein, D. B. Williams, A. D. Romig Jr, J. Armstrong, P. Echlin, C. Fiori, D. C. Joy, E. Lifshin, et al. *Scanning electron microscopy, X-ray microanalysis, and analytical electron microscopy: a laboratory workbook*. Springer Science & Business Media, 2012.
- [257] O. Faugeras. *Three-dimensional computer vision: a geometric viewpoint*. MIT press, 1993.
- [258] D. V. Papadimitriou and T. J. Dennis. Epipolar line estimation and rectification for stereo image pairs. *IEEE transactions on image processing*, 5(4):672–676, 1996.
- [259] E. Rosten and T. Drummond. Machine learning for high-speed corner detection. In *European conference on computer vision*, pages 430–443. Springer, 2006.
- [260] C. Harris and M. Stephens. A combined corner and edge detector. In *Alvey vision conference*, volume 15, page 50. Citeseer, 1988.
- [261] J. Shi and C. Tomasi. Good features to track. In *Computer Vision and Pattern Recognition, 1994. Proceedings CVPR'94., 1994 IEEE Computer Society Conference on*, pages 593–600. IEEE, 1994.

- [262] S. Leutenegger, M. Chli, and R. Y. Siegwart. BRISK: Binary robust invariant scalable keypoints. In *2011 International conference on computer vision*, pages 2548–2555. IEEE, 2011.
- [263] H. Bay, T. Tuytelaars, and L. Van Gool. Surf: Speeded up robust features. In *European conference on computer vision*, pages 404–417. Springer, 2006.
- [264] M. Muja and D. G. Lowe. Fast matching of binary features. In *Computer and Robot Vision (CRV), 2012 Ninth Conference on*, pages 404–410. IEEE, 2012.
- [265] M. Muja and D. G. Lowe. Fast approximate nearest neighbors with automatic algorithm configuration. *VISAPP (1)*, 2(331-340):2, 2009.
- [266] D. G. Lowe. Distinctive image features from scale-invariant keypoints. *International journal of computer vision*, 60(2):91–110, 2004.
- [267] R. I. Hartley. In defense of the eight-point algorithm. *IEEE Transactions on pattern analysis and machine intelligence*, 19(6):580–593, 1997.
- [268] R. Hartley and A. Zisserman. *Multiple view geometry in computer vision*. Cambridge university press, 2003.
- [269] M. A. Fischler and R. C. Bolles. Random sample consensus: a paradigm for model fitting with applications to image analysis and automated cartography. *Communications of the ACM*, 24(6):381–395, 1981.
- [270] M. Kanbara, T. Okuma, H. Takemura, and N. Yokoya. A stereoscopic video see-through augmented reality system based on real-time vision-based registration. In *Virtual Reality, 2000. Proceedings. IEEE*, pages 255–262. IEEE, 2000.
- [271] M. Humenberger, C. Zinner, M. Weber, W. Kubinger, and M. Vincze. A fast stereo matching algorithm suitable for embedded real-time systems. *Computer Vision and Image Understanding*, 114(11):1180–1202, 2010.
- [272] G. Egnal and R. P. Wildes. Detecting binocular half-occlusions: empirical comparisons of five approaches. *IEEE Transactions on pattern analysis and machine intelligence*, 24(8):1127–1133, 2002.
- [273] Y. S. Heo, K. M. Lee, and S. U. Lee. Robust stereo matching using adaptive normalized cross-correlation. *IEEE Transactions on Pattern Analysis and Machine Intelligence*, 33(4):807–822, 2011.
- [274] J. Kim et al. Visual correspondence using energy minimization and mutual information. In *Computer Vision, 2003. Proceedings. Ninth IEEE International Conference on*, pages 1033–1040. IEEE, 2003.

- [275] W. E. L. Grimson. A computer implementation of a theory of human stereo vision. *Phil. Trans. R. Soc. Lond. B*, 292(1058):217–253, 1981.
- [276] D. Marr and T. Poggio. A computational theory of human stereo vision. *Proc. R. Soc. Lond. B*, 204(1156):301–328, 1979.
- [277] H. H. Baker. Depth from edge and intensity based stereo. Technical report, STANFORD UNIV CA DEPT OF COMPUTER SCIENCE, 1982.
- [278] J. E. Banks, M. Bennamoun, K. Kubik, and P. Corke. *A taxonomy of image matching techniques for stereo vision*. Queensland University of Technology, 1997.
- [279] S. T. Barnard and W. B. Thompson. Disparity analysis of images. *IEEE Transactions on Pattern Analysis and Machine Intelligence*, (4):333–340, 1980.
- [280] N. Ayache and B. Faverjon. Efficient registration of stereo images by matching graph descriptions of edge segments. *International Journal of Computer Vision*, 1(2):107–131, 1987.
- [281] D. Scharstein and R. Szeliski. A taxonomy and evaluation of dense two-frame stereo correspondence algorithms. *International journal of computer vision*, 47(1-3):7–42, 2002.
- [282] M. Gong, R. Yang, L. Wang, and M. Gong. A performance study on different cost aggregation approaches used in real-time stereo matching. *International Journal of Computer Vision*, 75(2):283–296, 2007.
- [283] F. Tombari, S. Mattoccia, L. Di Stefano, and E. Addimanda. Classification and evaluation of cost aggregation methods for stereo correspondence. In *Computer Vision and Pattern Recognition, 2008. CVPR 2008. IEEE Conference on*, pages 1–8. IEEE, 2008.
- [284] P. Yao, H. Zhang, Y. Xue, and S. Chen. As-global-as-possible stereo matching with adaptive smoothness prior. *IET Image Processing*, 13(1):98–107, 2018.
- [285] T. Kanade, H. Kano, S. Kimura, A. Yoshida, and K. Oda. Development of a video-rate stereo machine. In *Proceedings 1995 IEEE/RSJ International Conference on Intelligent Robots and Systems. Human Robot Interaction and Cooperative Robots*, volume 3, pages 95–100. IEEE, 1995.
- [286] A. Hosni, C. Rhemann, M. Bleyer, C. Rother, and M. Gelautz. Fast cost-volume filtering for visual correspondence and beyond. *IEEE Transactions on Pattern Analysis and Machine Intelligence*, 35(2):504–511, 2013.
- [287] K.-J. Yoon and I. S. Kweon. Adaptive support-weight approach for correspondence search. *IEEE Transactions on Pattern Analysis and Machine Intelligence*, 28(4):650–656, 2006.
- [288] D. Min, J. Lu, and M. N. Do. Joint histogram-based cost aggregation for stereo matching. *IEEE transactions on pattern analysis and machine intelligence*, 35(10):2539–2545, 2013.

- [289] A. Hosni, M. Bleyer, M. Gelautz, and C. Rhemann. Local stereo matching using geodesic support weights. In *ICIP*, volume 9, pages 2093–2096. Citeseer, 2009.
- [290] M. A. Helala and F. Z. Qureshi. Accelerating cost volume filtering using salient subvolumes and robust occlusion handling. In *Asian Conference on Computer Vision*, pages 316–331. Springer, 2014.
- [291] M. Bleyer and C. Breiteneder. Stereo matching—state-of-the-art and research challenges. In *Advanced topics in computer vision*, pages 143–179. Springer, 2013.
- [292] Q. Yang. Stereo matching using tree filtering. *IEEE Transactions on Pattern Analysis and Machine Intelligence*, 37(4):834–846, 2015.
- [293] X. Mei, X. Sun, W. Dong, H. Wang, and X. Zhang. Segment-tree based cost aggregation for stereo matching. In *Proceedings of the IEEE Conference on Computer Vision and Pattern Recognition*, pages 313–320, 2013.
- [294] Q. Yang. Local smoothness enforced cost volume regularization for fast stereo correspondence. *IEEE Signal Processing Letters*, 22(9):1429–1433, 2015.
- [295] K. Zhang, Y. Fang, D. Min, L. Sun, S. Yang, S. Yan, and Q. Tian. Cross-scale cost aggregation for stereo matching. In *Proceedings of the IEEE Conference on Computer Vision and Pattern Recognition*, pages 1590–1597, 2014.
- [296] Q. Yang, L. Wang, R. Yang, S. Wang, M. Liao, and D. Nister. Real-time global stereo matching using hierarchical belief propagation. In *BMVC*, volume 6, pages 989–998, 2006.
- [297] V. Kolmogorov and R. Zabih. Computing visual correspondence with occlusions using graph cuts. In *Computer Vision, 2001. ICCV 2001. Proceedings. Eighth IEEE International Conference on*, volume 2, pages 508–515. IEEE, 2001.
- [298] Q. Yang, L. Wang, R. Yang, H. Stewénus, and D. Nistér. Stereo matching with color-weighted correlation, hierarchical belief propagation, and occlusion handling. *IEEE Transactions on Pattern Analysis and Machine Intelligence*, 31(3):492–504, 2009.
- [299] Q. Yang, L. Wang, and N. Ahuja. A constant-space belief propagation algorithm for stereo matching. In *Computer vision and pattern recognition (CVPR), 2010 IEEE Conference on*, pages 1458–1465. IEEE, 2010.
- [300] T. Taniai, Y. Matsushita, and T. Naemura. Graph cut based continuous stereo matching using locally shared labels. In *Proceedings of the IEEE Conference on Computer Vision and Pattern Recognition*, pages 1613–1620, 2014.
- [301] M. G. Mozerov and J. van de Weijer. Accurate stereo matching by two-step energy minimization. *IEEE Transactions on Image Processing*, 24(3):1153–1163, 2015.

- [302] C. Zhang, Z. Li, Y. Cheng, R. Cai, H. Chao, and Y. Rui. Meshstereo: A global stereo model with mesh alignment regularization for view interpolation. In *Proceedings of the IEEE International Conference on Computer Vision*, pages 2057–2065, 2015.
- [303] G. Facciolo, C. De Franchis, and E. Meinhardt. MGM: A significantly more global matching for stereovision. In *BMVC 2015*, 2015.
- [304] H. Hirschmuller. Stereo processing by semiglobal matching and mutual information. *IEEE Transactions on pattern analysis and machine intelligence*, 30(2):328–341, 2008.
- [305] Q. Tian and M. N. Huhns. Algorithms for subpixel registration. *Computer Vision, Graphics, and Image Processing*, 35(2):220–233, 1986.
- [306] A. Fusiello, V. Roberto, and E. Trucco. Efficient stereo with multiple windowing. In *Computer Vision and Pattern Recognition, 1997. Proceedings., 1997 IEEE Computer Society Conference on*, pages 858–863. IEEE, 1997.
- [307] X. Hu and P. Mordohai. Evaluation of stereo confidence indoors and outdoors. In *Computer Vision and Pattern Recognition (CVPR), 2010 IEEE Conference on*, pages 1466–1473. IEEE, 2010.
- [308] X. Ye, Y. Gu, L. Chen, J. Li, H. Wang, and X. Zhang. Order-based disparity refinement including occlusion handling for stereo matching. *IEEE Signal Processing Letters*, 24(10):1483–1487, 2017.
- [309] A. Spyropoulos, N. Komodakis, and P. Mordohai. Learning to detect ground control points for improving the accuracy of stereo matching. In *Proceedings of the IEEE Conference on Computer Vision and Pattern Recognition*, pages 1621–1628, 2014.
- [310] M.-G. Park and K.-J. Yoon. Leveraging stereo matching with learning-based confidence measures. In *Proceedings of the IEEE Conference on Computer Vision and Pattern Recognition*, pages 101–109, 2015.
- [311] M. Poggi and S. Mattoccia. Learning a general-purpose confidence measure based on o (1) features and a smarter aggregation strategy for semi global matching. In *3D Vision (3DV), 2016 Fourth International Conference on*, pages 509–518. IEEE, 2016.
- [312] A. Seki and M. Pollefeys. Patch based confidence prediction for dense disparity map. In *BMVC*, volume 2, page 4, 2016.
- [313] M. Poggi, F. Tosi, and S. Mattoccia. Quantitative evaluation of confidence measures in a machine learning world. In *International Conference on Computer Vision (ICCV 2017); IEEE: New York, NY, USA*, 2017.
- [314] S. Kim, D. Min, S. Kim, and K. Sohn. Unified confidence estimation networks for robust stereo matching. *IEEE Transactions on Image Processing*, 28(3):1299–1313, 2019.

- [315] H. Hirschmüller, P. R. Innocent, and J. Garibaldi. Real-time correlation-based stereo vision with reduced border errors. *International Journal of Computer Vision*, 47(1-3):229–246, 2002.
- [316] O. Veksler. Stereo correspondence with compact windows via minimum ratio cycle. *IEEE Transactions on Pattern Analysis & Machine Intelligence*, (12):1654–1660, 2002.
- [317] M. Frucci and G. S. di Baja. From segmentation to binarization of gray-level images. *Journal of Pattern Recognition Research*, 1:1–13, 2008.
- [318] D. L. Pham, C. Xu, and J. L. Prince. Current methods in medical image segmentation. *Annual review of biomedical engineering*, 2(1):315–337, 2000.
- [319] I. Sobel. An isotropic 3×3 image gradient operator. *Machine vision for three-dimensional scenes*, pages 376–379, 1990.
- [320] J. M. Prewitt. Object enhancement and extraction. *Picture processing and Psychopictorics*, 10(1):15–19, 1970.
- [321] R. B. Rusu, Z. C. Marton, N. Blodow, M. Dolha, and M. Beetz. Towards 3D point cloud based object maps for household environments. *Robotics and Autonomous Systems*, 56(11):927–941, 2008.
- [322] I. Amidror. Scattered data interpolation methods for electronic imaging systems: a survey. *Journal of electronic imaging*, 11(2):157–177, 2002.
- [323] R. Sibson et al. A brief description of natural neighbour interpolation. *Interpreting multivariate data*, 21:21–36, 1981.
- [324] P. H. Torr and A. Zisserman. MLESAC: A new robust estimator with application to estimating image geometry. *Computer Vision and Image Understanding*, 78(1):138–156, 2000.
- [325] B. Chen, R. A. Dilanian, S. Teichmann, B. Abbey, A. G. Peele, G. J. Williams, P. Hannaford, L. Van Dao, H. M. Quiney, and K. A. Nugent. Multiple wavelength diffractive imaging. *Physical Review A*, 79(2):023809, 2009.
- [326] M. R. Howells, P. S. Charalambous, H. He, S. Marcesini, and J. C. Spence. Off-axis zone plate monochromator for high-power undulator radiation. In *Design and Microfabrication of Novel X-Ray Optics*, volume 4783, pages 65–74. International Society for Optics and Photonics, 2002.
- [327] Y. Furukawa, C. Hernández, et al. Multi-view stereo: a tutorial. *Foundations and Trends® in Computer Graphics and Vision*, 9(1-2):1–148, 2015.
- [328] Meadowlark LCoS-SLM website, <https://www.meadowlark.com/small-512-512-spatial-light-modulator-p-139?mid=18>.

- [329] L. J. Hornbeck. Digital light processing for high-brightness high-resolution applications. In *Projection Displays III*, volume 3013, pages 27–40. International Society for Optics and Photonics, 1997.
- [330] M. Padgett, J. Courtial, and L. Allen. Light's orbital angular momentum. *Physics Today*, 57(5): 35–40, 2004.
- [331] L. Allen, M. W. Beijersbergen, R. Spreeuw, and J. Woerdman. Orbital angular momentum of light and the transformation of Laguerre-Gaussian laser modes. *Physical Review A*, 45(11):8185, 1992.
- [332] J. P. Torres and L. Torner. *Twisted photons: applications of light with orbital angular momentum*. John Wiley & Sons, 2011.
- [333] C. Hernandez-Garcia, J. Vieira, J. Mendonça, L. Rego, J. San Roman, L. Plaja, P. Ribic, D. Gauthier, and A. Picon. Generation and applications of extreme-ultraviolet vortices. In *Photonics*, volume 4, page 28. Multidisciplinary Digital Publishing Institute, 2017.
- [334] D. Gauthier, P. R. Ribič, G. Adhikary, A. Camper, C. Chappuis, R. Cucini, L. DiMauro, G. Dovillaire, F. Frassetto, R. Généaux, et al. Tunable orbital angular momentum in high-harmonic generation. *Nature communications*, 8:14971, 2017.
- [335] P. R. Ribič, B. Rösner, D. Gauthier, E. Allaria, F. Döring, L. Foglia, L. Giannessi, N. Mahne, M. Manfreda, C. Masciovecchio, et al. Extreme-ultraviolet vortices from a free-electron laser. *Physical Review X*, 7(3):031036, 2017.
- [336] J. Vieira, R. Trines, E. Alves, R. Fonseca, J. Mendonça, R. Bingham, P. Norreys, and L. Silva. High orbital angular momentum harmonic generation. *Physical review letters*, 117(26):265001, 2016.
- [337] V. Petrillo, G. Dattoli, I. Drebot, and F. Nguyen. Compton scattered X-gamma rays with orbital momentum. *Physical review letters*, 117(12):123903, 2016.
- [338] D. Gauthier, S. Kaassamani, D. Franz, R. Nicolas, J.-T. Gomes, L. Lavoute, D. Gaponov, S. Février, G. Jargot, M. Hanna, et al. Orbital angular momentum from semiconductor high-order harmonics. *Optics letters*, 44(3):546–549, 2019.
- [339] S. Wall, S. Yang, L. Vidas, M. Chollet, J. M. Glowina, M. Kozina, T. Katayama, T. Henighan, M. Jiang, T. A. Miller, et al. Ultrafast disordering of vanadium dimers in photoexcited VO₂. *Science*, 362(6414):572–576, 2018.
- [340] L. Vidas, C. M. Günther, T. A. Miller, B. Pfau, M. Schneider, E. Guehrs, R. E. Marvel, K. A. Hallman, R. F. Haglund Jr, S. Eisebitt, et al. Nanoscale spectroscopic imaging of phase separation in a correlated material by resonant X-ray holography. *arXiv preprint arXiv:1612.07998*, 2016.
- [341] A. Cavalleri. Disorder at the border. *Science*, 362(6414):525–526, 2018.

- [342] M. F. Jager, C. Ott, P. M. Kraus, C. J. Kaplan, W. Pouse, R. E. Marvel, R. F. Haglund, D. M. Neumark, and S. R. Leone. Tracking the insulator-to-metal phase transition in VO₂ with few-femtosecond extreme UV transient absorption spectroscopy. *Proceedings of the National Academy of Sciences*, 114(36):9558–9563, 2017.
- [343] E. Sistrunk, J. Grilj, J. Jeong, M. G. Samant, A. X. Gray, H. A. Dürr, S. S. Parkin, and M. Gühr. Broadband extreme ultraviolet probing of transient gratings in vanadium dioxide. *Optics express*, 23(4):4340–4347, 2015.
- [344] K. L. Włodarczyk, J. J. Kaakkunen, P. Vahimaa, and D. P. Hand. Efficient speckle-free laser marking using a spatial light modulator. *Applied Physics A*, 116(1):111–118, 2014.
- [345] Y. Hayasaki, M. Nishitani, H. Takahashi, H. Yamamoto, A. Takita, D. Suzuki, and S. Hasegawa. Experimental investigation of the closest parallel pulses in holographic femtosecond laser processing. *Applied Physics A*, 107(2):357–362, 2012.

Nomenclature

β	Imaginary part of the refractive index of a material.
∇^2	Laplace operator.
Δ_r	Pixel size of the reciprocal space of the plane of the detector, measured in $[m^{-1}]$.
δ	Dirac delta function.
δ_{lat}	Achievable lateral resolution.
Δ_{obj}	Pixel size in the object and reconstruction (real space) planes.
Δ_p	Hologram pixel size.
λ	Laser beam wavelength.
\mathcal{F}	Fourier Transformation.
\mathcal{R}	Resolution.
μ	Magnetic permeability of the medium.
ν_{cutoff}	Cutoff frequency.
ω	Radiation's angular frequency.
ω_o	Fundamental laser frequency.
ψ	Scalar wave function.
ρ, θ	Polar coordinates.
σ_{max}	Nyquist frequency: maximum frequency, which can be reconstructed.
\arg	Argument of a complex number/function.
θ_i	Grazing incidence angle.
θ_{max}	Maximum diffraction angle.
$\tilde{\psi}$	Fourier transform of the scalar wave function ψ .

\tilde{I}	Fourier transform of the far-field intensity pattern at the detector. Autocorrelation of the object/sample.
\tilde{n}	Complex refractive index of a material.
ε	Electric permittivity of the medium.
φ	Phase of a wave.
\vec{r}	Vector of position.
a	Characteristic dimension of the (diffracting) object.
c	Speed of light.
D	Beam diameter at the plane of detection.
DOF	Depth of field.
e	Thickness of the object.
F	Fresnel Number
f_1, f_2	Lenses' focal lengths.
$F_{scaling}$	Scaling factor, which transforms the space of spatial frequencies (measured in $[m^{-1}]$) into the real space coordinates (measured in $[m]$) in a Fraunhofer diffraction pattern.
f_X, f_Y	Spatial frequency coordinates in the plane of the hologram/detector.
FOV	Field of view of the reconstruction, given in real (object) space dimensions.
h	Planck's constant.
$H(X, Y)$	Hologram.
I	Intensity distribution.
i	Unit imaginary number.
I_p	Ionization potential.
j	Summation index.
k	Wave vector.
k_{\perp}	Spatial frequency of the angular spectrum transverse to the direction of propagation.
L	General source-detector distance.
L_1, L_2	Lineouts of the reconstruction image.

m, n Generalised indexes.

N Number of pixels that translates the extent of a discretized plane (it can refer to both directions, vertical or horizontal, if both have the same number of pixels).

n Real part of the refractive index of a material.

N_o Number of pixels in the detector matrix corresponding to the size of the object.

N_{signal} Number of pixels at the detector, which samples the diameter of the diffraction pattern/hologram.

O Oversampling ratio.

$O(X, Y)$ Object contribution to the complex field at the hologram plane.

$o(x, y)$ Object contribution to the spatially transmitted field at the sample.

$R(X, Y)$ Reference contribution to the complex field at the hologram plane.

$r(x, y)$ Reference contribution to the spatially transmitted field at the sample.

$r(x, y, z)$ Modulus of vector of position - distance.

r_{\perp} Cartesian coordinates transverse to the direction of propagation (x, y) .

$t(x, y)$ Transmittance function at the sample/object plane.

$t_o(x, y)$ Object contribution to the transmittance function at the plane of the sample.

$t_r(x, y)$ Reference contribution to the transmittance function at the plane of the sample.

u, v Frequency coordinates in the Fourier domain plane of the detector.

$U_h(X, Y)$ Complex field at the hologram plane.

U_p Ponderomotive energy.

$U_0(x, y)$ Amplitude of the incident field on the object/sample.

$U_{diff}(X, Y)$ Complex diffracted field.

$U_{inc}(x, y)$ Incident field on the object/sample.

$U_o(x, y)$ Spatially transmitted field at the plane of the object/sample.

X, Y Coordinates in the plane of the hologram/detector.

x, y Coordinates in the plane of the object.

Z Distance between object and detector.

z Optical axis.

Fourier Transform Holography and Spatial Coherence

$\Gamma(\vec{r}_n, \vec{r}_m; t_n, t_m)$ Mutual coherence function.

$\Lambda(\vec{r})$ Autocorrelation of the function that describes the geometry of each NRA aperture.

μ_{nm} Complex degree of spatial coherence measured at the points n and m .

τ Temporal delay.

$\vec{\rho}$ Position of a point in the plane of detection.

$\vec{d}_{nm} = \vec{r}_n - \vec{r}_m$ Spatial distance between two points generalised by the indexes n and m . This separation is measured in the same plane, perpendicular to the optical axis.

$\vec{d}_r = (\vec{r} - \vec{r}_r)$ Distances between the object and a punctual reference.

\vec{r}_r Position of the reference aperture.

$h(\vec{r})$ Geometry of each NRA aperture.

$I_{norm}(\vec{r})$ Normalised intensity profile of the beam illuminating the sample.

$J(\vec{r}_n, \vec{r}_m)$ Mutual intensity between the field oscillations measured at the positions \vec{r}_n and \vec{r}_m .

$J'_0(\vec{r}_n, \vec{r}_m)$ Mutual intensity of the exit pupil at the plane of the object/NRA.

N Number of apertures of the NRA or number of the subimage reconstructions in FTH with multiple references.

O_n Reconstructed subimage achieved for each the reference n in FTH with multiple references.

$O_R(\vec{r}_r, \vec{r})$ Object reconstruction.

$O_{norm_n}(\vec{r}_n, \vec{r})$ Normalised reconstruction of the subimage n in FTH with multiple references.

$O_{norm}(\vec{r})$ Composed reconstruction achieved from the average of the normalised $O_{norm_n}(\vec{r}_n, \vec{r})$.

S_0 Total intensity of the field through the NRA.

$V(\vec{r}, t)$ Field oscillation at a specific position and time.

w_c Radius (FWHM) of a Gaussian distribution of the magnitude of the complex degree of spatial coherence.

w_I Radius (FWHM) of a Gaussian distribution of intensity.

$J_0(\vec{r}_n, \vec{r}_m)$ Mutual intensity of the field at the sample position ($z = 0$).

In-Line Holography and Waves with Aberrations

$\Delta_{\mathcal{F}}$ Pixel size in the intermediate Fourier plane.

$\mathcal{P}(x, y)$ Generalised pupil function.

$\varphi_{obj}(x, y)$ Phase shift induced by the object to the incident wave.

ξ, η Coordinates in the plane of the wavefront sensor.

$a'(x, y)$ Updated value of $a(x, y)$ after each iteration of the algorithm.

$a(x, y)$ Absorption of the object.

$B(X, Y)$ Background image at the detector.

C_n^m Zernike coefficient of indexes m and n .

$H_0(X, Y)$ Normalised hologram.

M Magnification factor.

r_1 Distance between the object and the source of spherical waves.

r_2 Distance between the detector and the source of spherical waves.

$R_n^m(\rho)$ Radial component of the Zernike polynomial with indexes m and n .

$S(u, v)$ Fourier transform of the Fresnel function.

$s(x, y)$ Fresnel function.

$t'_o(x, y)$ Updated value of $t_o(x, y)$ after each iteration of the algorithm.

$U_{wfs}(\xi, \eta)$ Spatially transmitted field at the plane of the wavefront sensor.

$U_r(x, y)$ Reconstructed field in the object's plane.

$W(\rho, \theta)$ Effective path-length error that modulates the aberrated phase of a plane.

$W_p(X, Y)$ Effective path-length error that modulates the aberrated phase of the known reference wave at the detector, $R(X, Y)$.

$W_{obj}(x, y)$ Effective path-length error that modulates the aberrated phase of the reference wave at the plane of the object.

x_0 Source/pinhole position in x .

y_0 Source/pinhole position in y .

z_0 Source/pinhole position in the optical axis.

$Z_n^m(\rho, \theta)$ Zernike polynomial of indexes m and n .

z_{wfs} Wavefront sensor position in z .

XUV Spatial Light Modulator

- φ Azimuthal coordinate in the plane perpendicular to the propagation of the beam, which contributes to the azimuthal phase dependence of light beams carrying OAM.
- F_H Focal length of the hologram to the harmonic with order H.
- m Topological charge.
- H Harmonic order.
- R Distance VO_2 - focal spot of the converging pump beam.

Computed Stereo Imaging

- $(x_1 - x_2)$ Disparity value of the left view picture with respect to the right view.
- $(x_2 - x_1)$ Disparity value of the right view picture with respect to the left view.
- α Weighting factor of the cost function for disparity calculations.
- Δ_z z -axis component of the 3D voxel of the stereo reconstruction.
- κ, ζ Parameters of the algorithm for outliers removal.
- σ Standard deviation.
- θ_1, θ_2 Stereo angles defined by the angles of the two incident beams on the sample.
- $C(x_o, y_o, d)$ Cost function to be minimised in order to reach the best match for the disparity estimations.
- $C_p(x_o, y_o, d_p)$ Cost function value of the best pixel match.
- D Estimator applied to each disparity value arising from the sorting process for second-order sub-pixel interpolation.
- d Distance between the scanned pixel and the one under evaluation in the routine for disparity estimation.
- d_p Disparity value of p .
- e, e' Conjugate epipoles.
- I_1, I_2 Intensity values of object points measured in stereo planes 1 and 2, respectively.
- l, l' Conjugate epipolar lines.
- N Disparity range.
- p Best pixel match arising from the sorting process.

x_1, x_2 Coordinates measured at each stereo plane 1 and 2, respectively, corresponding to projections in these planes of the object coordinate x_o .

x_o Object point measured in the x -axis.

z_o Depth of a point in real space.

F Fundamental matrix.

$\mathbf{m}_1, \mathbf{m}_2, \mathbf{n}_1, \mathbf{n}_2$ Point projections from object points m and n in stereo planes 1 and 2, respectively.

M Synthetic camera matrix.

S Skew-symmetric matrix.

\mathbf{x}, \mathbf{x}' Image coordinates of matching points in a stereo pair.

Glossary

(X)FEL	(X-ray) Free-Electron Laser
2D	Two-Dimensional
3D	Three-Dimensional
AFM	Atomic Force Microscope
ALS	Advanced Light Source
ATTO	Groupe ATTOphysique, LIDYL, CEA
BBO	Beta-Barium Borate crystal
BL29XUL	Hard X-ray undulator beamline at SPring-8
CCD	Charge-coupled device
CDI	Coherent Diffraction Imaging or Coherent Diffractive Imaging
CEA	Commissariat à l'Énergie Atomique et aux Énergies Alternatives
CEP	Carrier Envelope Phase
CGH	Computer-Generated Hologram
CMOS	Complementary Metal-Oxide-Semiconductor
CPA	Chirped-Pulse Amplification
CSNSM	Center for Nuclear Science and Material Sci- ences
DFTH	Digital Fourier Transform Holography
DFT	Discrete Fourier Transform
DIHM	Digital In-Line Holographic Microscopy
DL	Diffraction-limited
DOF	Depth Of Focus
FFT	Fast Fourier Transform
FIB	Focused Ion Beam
FOV	Field of View
FTH	Fourier Transform Holography
FT	Fourier Transformation

FWHM	Full Width at Half Maximum
FZP	Fresnel Zone Plate
GS	Gerchberg-Saxton algorithm
GoLP	Group of Lasers and Plasmas
HDR	High Dynamic Range
HERALDO	Holography with Extended Reference by Auto-correlation Linear Differential Operator
HHG	High-order Harmonics Generation or High Harmonic Generation
HH	High-order Harmonics
IMT	Insulator-to-Metal Transition
INESC-MN	Instituto de Engenharia de Sistemas e Computadores - Microsistemas e Nanotecnologias
IPFN	Instituto de Plasmas e Fusão Nuclear
IR	Infrared
IST	Instituto Superior Técnico
KB	Kirkpatrick-Baez
LCLS	Linac Coherent Light Source
LC	Liquid Crystal
LIDYL	Laboratoire Interactions, DYnamiques et Lasers
LOA	Laboratoire d'Optique Appliquée
LUCA	Laser Ultra Court Accordable
MSAC	M-estimator SAmple Consensus
MSER	Maximally Stable Extremal Regions
NA	Numerical aperture
NRA	Non-Redundant Array
OAM	Orbital Angular Momentum
OAP	Off-Axis Parabola
PMMA	PMMA Poly(Methyl Methacrylate)
PtV	Peak-to-Valey
RMS	Root Mean Square
RMS	Root mean square
SACLA	SPring-8 Angstrom Compact free electron LAser
SEM	Scanning Electron Microscope/Microscopy
SLAC	Stanford Linear Accelerator Center

SLIC	Saclay Laser-matter Interaction Center
SLM	Spatial Light Modulator
SNR	Signal-to-Noise Ratio
SVD	Singular-Value Decomposition
URA	Uniformly Redundant Array
UV-X	UltraViolet-to-X-ray spectral range
UV	Ultraviolet
XUV	Extreme Ultraviolet

Author Contributions

Scientific projects typically require a large degree of collaboration, and this PhD project was no exception. This section specifies the work performed by the author.

Chapter 3

I designed the samples and participated in their fabrication with W. Boutu. I designed the experiments and built the setup together with R. Cassin (apart from the source). In the single-shot characterisation of the spatial coherence of H25, I collected the data together with R. Cassin. I collected and analysed the data of Fourier transform holography and NRA measurements for the part of the case study (helpful discussions with H. Merdji, W. Boutu, D. Gauthier are acknowledged). I came up with the idea of using particular configurations of FTH sample to compensate for the effects of spatial coherence (helpful work of A. Gonzalez is acknowledged) and, as well, to perform measurements of the spatial coherence of a source. Further efforts are required for both ideas.

Chapter 4

I developed the reasoning and built the algorithm of in-line holography with waves with aberrations for simulations and reconstructions (fruitful discussions with Marta Fajardo and Gareth Williams are acknowledged). I also performed the simulations. I developed the new algorithm, first implementing the twin-image correction code from Tatiana Latychevskaia and after further extending it to include the wavefront correction. For the test with experimental data from a biological sample, I performed the reconstructions and provided the code for further data analyses of the system (the experimental data provided by R. Corman for this thesis is acknowledged). For the experimental validation using a HeNe laser, I built the setup and performed the experiment and data analysis (fruitful discussions with Marta Fajardo are acknowledged; also the help from Jayanath koliyadu and availability of all the X-GoIP team with the material in earlier trials of the experiment are acknowledged). I also participated in the experimental attempt in the XUVs performed at *Laboratoire d'Optique Appliquée* (LOA), together with Jayanath Koliyadu (help and fruitful discussions with Philippe Zeitoun are acknowledged). I participated in the fabrication of in-line test samples fabricated at INESC–MN with the help of Diana Leitão (helpful discussions and availability of Prof. Susana Freitas are acknowledged).

Chapter 5

I developed the algorithms for departing from two CDI stereo views to a 3D reconstruction, employing Computer Stereo Vision methods: from the pre-processing and disparity computations to the 3D rendering. I performed the simulations and the data analysis for all the experimental samples presented in this manuscript (helpful discussions with H. Merdji are acknowledged). I helped to acquire some experimental data at LUCA's HHG beamline (single dual-diffraction pattern acquisition), even though I did not mount the setup nor was responsible for the experiment. I came up with the idea of using contrast labels to improve the performance of the algorithm to stereo-ambiguous samples.

Future Prospects

I designed the experiment for the first setup presented in the "Future Prospects" section. I used the GS algorithm to generate the input images for the visible SLM and performed the test experiments, with HeNe and IR beams, calibrating issues such as the image gray-scale and state of polarization vs phase imprint (help from D. Gauthier is acknowledged). I designed together with D. Gauthier, W. Boutu and H. Merdji the second experiment. Me and D. Gauthier performed the simulations.

Appendix A

Coordinate Systems

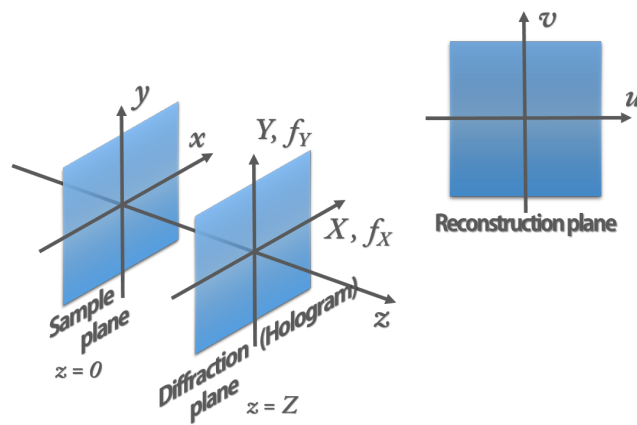


Figure A.1: Coordinate system adopted for Fourier transform holography.

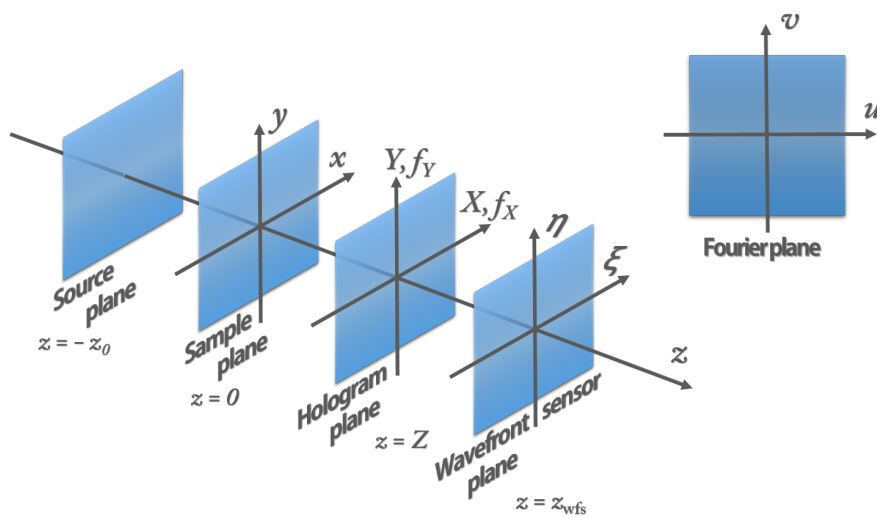


Figure A.2: Coordinate system adopted for In-line holography.

Appendix B

Convolution and Correlation Notation

Assuming the following relations denote Fourier transformation:

$$\mathcal{F}\{g(x)\}(X) = G(X) \quad (\text{B.1})$$

$$\mathcal{F}\{h(x)\}(X) = H(X). \quad (\text{B.2})$$

Convolution Notation

$$g \otimes h = \int_{-\infty}^{\infty} g(x)h(x' - x)dx \quad (\text{B.3})$$

$$\mathcal{F}\{g \otimes h\}(X) = G(X)H(X) \quad (\text{B.4})$$

Autocorrelation Notation

$$g \star g = \int_{-\infty}^{\infty} g(x)g^*(x - x')dx \quad (\text{B.5})$$

$$g \star g = \int_{-\infty}^{\infty} g^*(x)g(x + x')dx \quad (\text{B.6})$$

Cross-correlation Notation

$$g \star h = \int_{-\infty}^{\infty} g(x - x')h(x)dx \quad (\text{B.7})$$

$$g \star h = \int_{-\infty}^{\infty} g(x)h(x + x')dx \quad (\text{B.8})$$

Appendix C

FT Theorems

1 Linearity:

$$\mathcal{F}\{\alpha g + \beta h\} = \alpha \mathcal{F}\{g\} + \beta \mathcal{F}\{h\} \quad (\text{C.1})$$

2 Similarity:

$$\mathcal{F}\{g(x, y)\} = G(f_x, f_y) \Rightarrow \mathcal{F}\{g(ax, by)\} = \frac{1}{|ab|} G\left(\frac{f_x}{a}, \frac{f_y}{b}\right) \quad (\text{C.2})$$

3 Shift:

$$\mathcal{F}\{g(x - a, y - b)\} = G(f_x, f_y) e^{-j2\pi(f_x a + f_y b)} \quad (\text{C.3})$$

4 Rayleigh's:

$$\iint_{-\infty}^{\infty} |g(x, y)|^2 dx dy = \iint_{-\infty}^{\infty} |G(f_x, f_y)|^2 df_x df_y \quad (\text{C.4})$$

5 Convolution:

$$\mathcal{F}\left\{\iint_{-\infty}^{\infty} g(\xi, \eta) h(x - \xi, y - \eta) d\xi d\eta\right\} = G(f_x, f_y) H(f_x, f_y) \quad (\text{C.5})$$

6 Autocorrelation:

$$\mathcal{F} \left\{ \iint_{-\infty}^{\infty} g(\xi, \eta) g^*(x - \xi, y - \eta) d\xi d\eta \right\} = |G(f_x, f_y)|^2 \quad (\text{C.6})$$

$$\mathcal{F} \left\{ |g(x, y)|^2 \right\} = \iint_{-\infty}^{\infty} G(\xi, \eta) G^*(\xi - f_x, \eta - f_y) d\xi d\eta \quad (\text{C.7})$$

Appendix D

Batch file of the fabrication of in-line test samples

This appendix includes the batch file of the fabrication process used for the fabrication of in-line test samples at INESC-MN.

Batch #2 - Summary

1. Samples

Small (7mm) Si bare substrates with 500umx500um SiN membrane

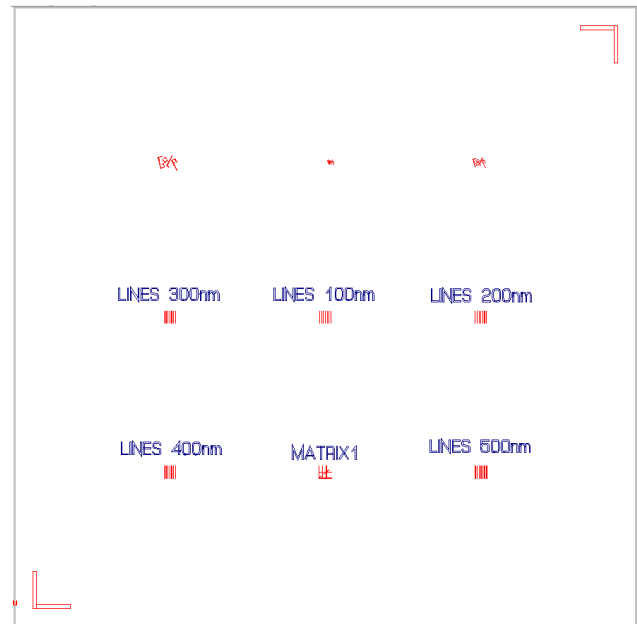
2. Coating:

Layer#1 PMMA 950k 30sec@3krpm – bake 4min@160sec

Layer#2 PMMA 950k 30sec@3krpm – bake 4min@160sec

3. Ebeam Exposure

3.1. Mask Layout : area 500um x500um

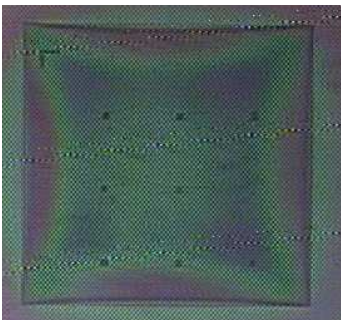


3.2. Samples

A&B : 10kV, 10um, Dose=100uC/cm²

C&D : 10kV, 10um, Dose=80uC/cm²

Optical microscope images



Sample D: Exposure had to be repeated

4. Au deposition

Cr 50A/Au500A deposition in Alcatel (sputtering system)

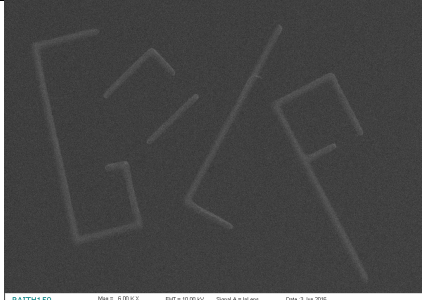
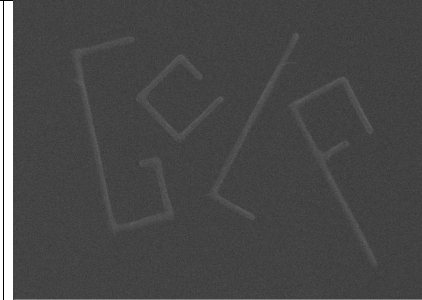
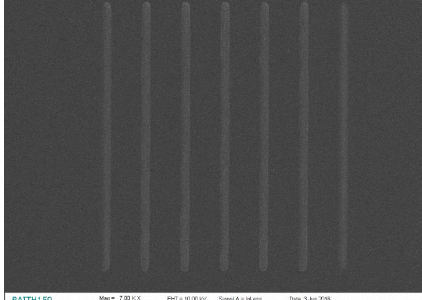
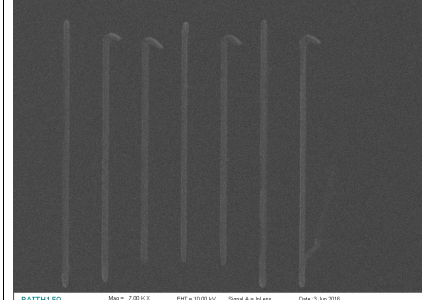
5. Liftoff

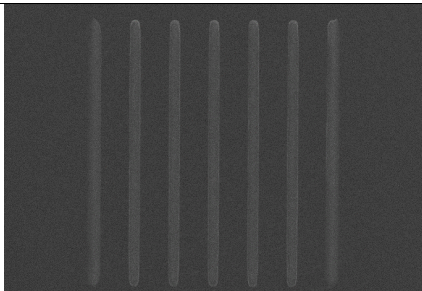
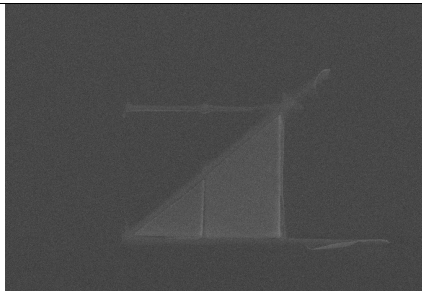
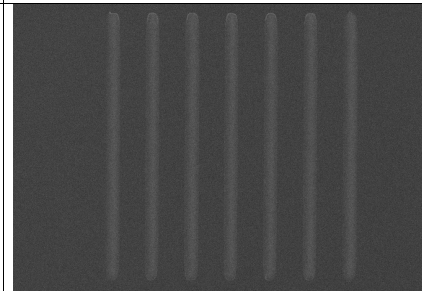
Wetbench: PMMA Remover@60°C, no ultrasounds

Membrane of Sample B was damaged during this process.

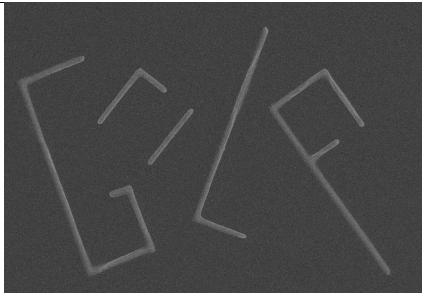
6. SEM Inspection vs Mask Design

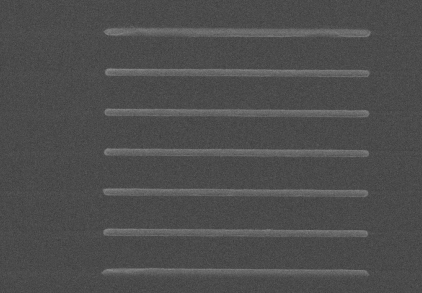
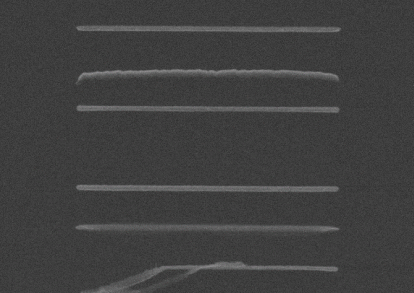
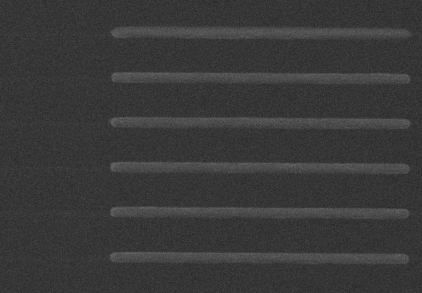
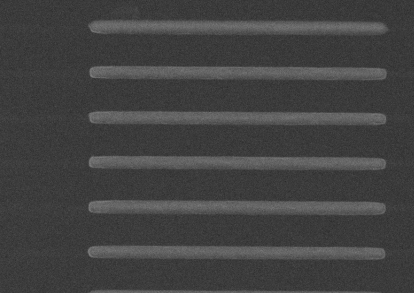
Sample A: 100uC/cm2. Expected: better pattern definition, but larger feature sizes

<p>Golp 3x amplification</p>  <p>RAITH150 Mag = 6.50K X EHT = 10.00 kV WD = 13 mm Signal A = H-Lens Aperture Size = 7.000 µm Date: 3 Jun 2016 Time: 16:22:31</p>	<p>Golp 1x amplification</p>  <p>RAITH150 Mag = 11.31K X EHT = 10.00 kV WD = 13 mm Signal A = H-Lens Aperture Size = 7.000 µm Date: 3 Jun 2016 Time: 16:20:26</p>	<p>Golp 2x amplification</p>  <p>RAITH150 Mag = 0.50 K X EHT = 10.00 kV WD = 13 mm Signal A = H-Lens Aperture Size = 7.000 µm Date: 3 Jun 2016 Time: 16:19:25</p>
<p>Lines Nominal size 300 nm</p>  <p>RAITH150 Mag = 7.00 K X EHT = 10.00 kV WD = 13 mm Signal A = H-Lens Aperture Size = 7.000 µm Date: 3 Jun 2016 Time: 16:24:34</p>	<p>Lines Nominal size 100 nm</p>  <p>RAITH150 Mag = 7.00 K X EHT = 10.00 kV WD = 13 mm Signal A = H-Lens Aperture Size = 7.000 µm Date: 3 Jun 2016 Time: 16:26:57</p>	<p>Lines Nominal size 200 nm</p>  <p>RAITH150 Mag = 7.00 K X EHT = 10.00 kV WD = 13 mm Signal A = H-Lens Aperture Size = 7.000 µm Date: 3 Jun 2016 Time: 16:25:21</p>

<p>Lines Nominal size 400 nm</p>  <p>RAITH150 Mag = 7.00 K X EHT = 10.00 kV WD = 13 mm Signal A = H-Lens Aperture Size = 7.000 µm Date: 3 Jun 2016 Time: 16:21:35</p>	<p>Matrix</p>  <p>RAITH150 Mag = 7.00 K X EHT = 10.00 kV WD = 13 mm Signal A = H-Lens Aperture Size = 7.000 µm Date: 3 Jun 2016 Time: 16:20:10</p>	<p>Lines Nominal size 500 nm</p>  <p>RAITH150 Mag = 7.00 K X EHT = 10.00 kV WD = 13 mm Signal A = H-Lens Aperture Size = 7.000 µm Date: 3 Jun 2016 Time: 16:20:05</p>
--	---	--

Sample C: 80uC/cm2. Expected: pattern definition quality can be affected slightly, but smaller feature sizes

<p>Golp 3x amplification</p>  <p>RAITH150 Mag = 6.20 K X EHT = 10.00 kV WD = 13 mm Signal A = H-Lens Aperture Size = 7.000 µm Date: 3 Jun 2016 Time: 16:40:06</p>	<p>Golp 1x amplification</p> <p>PATTERNED NOT DEFINED!</p>	<p>Golp 2x amplification</p>  <p>RAITH150 Mag = 0.70 K X EHT = 10.00 kV WD = 13 mm Signal A = H-Lens Aperture Size = 7.000 µm Date: 3 Jun 2016 Time: 16:50:15</p>
--	--	--

<p>Lines Nominal size 300 nm (scan rotated 90°)</p>  <p>RAITH150 Mag = 7.00 K X EHT = 10.00 kV Signal A = HiLens Date = 3 Jun 2016 WD = 13 mm Aperture Size = 7.500 µm Time = 16:40:25</p>	<p>Lines Nominal size 100 nm</p> <p>PATTERNED NOT DEFINED!</p>	<p>Lines Nominal size 200 nm (scan rotated 90°)</p>  <p>RAITH150 Mag = 7.00 K X EHT = 10.00 kV Signal A = HiLens Date = 3 Jun 2016 WD = 13 mm Aperture Size = 7.500 µm Time = 16:41:02</p>
<p>Lines Nominal size 400 nm (scan rotated 90°)</p>  <p>RAITH150 Mag = 7.00 K X EHT = 10.00 kV Signal A = HiLens Date = 3 Jun 2016 WD = 13 mm Aperture Size = 7.500 µm Time = 16:37:28</p>	<p>Matrix (scan rotated 90°)</p>  <p>RAITH150 Mag = 7.00 K X EHT = 10.00 kV Signal A = HiLens Date = 3 Jun 2016 WD = 13 mm Aperture Size = 7.500 µm Time = 16:39:45</p>	<p>Lines Nominal size 500 nm (scan rotated 90°)</p>  <p>RAITH150 Mag = 7.00 K X EHT = 10.00 kV Signal A = HiLens Date = 3 Jun 2016 WD = 13 mm Aperture Size = 7.500 µm Time = 16:42:05</p>

Appendix E

Publications

The publication of the work produced in this thesis will be done through three main articles.

- A first article, published in *Nature Photonics*, describes the application of computed X-ray stereo lensless imaging, following the work presented in Chapter 5. The full article can be found in the link: <https://www.nature.com/articles/s41566-019-0419-1>.

- A second paper describes the technique for single-shot spatial coherence characterization of X-ray sources and its validation through simulation and experiment, following part of the work from Chapter 3. This article will be soon submitted for publication, following here the last version at the moment of the writing of this manuscript.

- A third paper will present the results on digital in-line holography corrected from aberrations by resorting to wavefront sensor measurements, as reported in Chapter 4. This article is in preparation, being in a too early version to be included here.

Single-shot spatial coherence characterization of ultrafast X-ray sources

JOANA DUARTE,¹ AURA INÉS GONZÁLEZ,^{1,2} RÉMY CASSIN,¹ RANA NICOLAS,¹ WILLEM BOUTU,¹ MARTA FAJARDO,³ AND HAMED MERDJI^{1,*}

¹LIDYL, CEA, CNRS and Université Paris-Saclay, CEA Saclay 91191 Gif-sur-Yvette, France

²Amplitude Technologies, 2 rue du Bois Chaland, 91090 Lisses, France

³Instituto de Plasmas e Fusão Nuclear, IST Lisboa, Portugal

*Corresponding author: hamed.merdji@cea.fr

Spatial coherence is a crucial source parameter in many applications ranging from atomic and molecular physics to metrology or imaging. In lensless imaging, for example, it can strongly impact the image formation, which is even more stringent when the source exhibits shot-to-shot variations of the spatial coherence. Single-shot characterization of the degree of spatial coherence of a source is thus crucial. However, current techniques either require parallel intensity measurements or the use of several masks, being incompatible with a single-shot analysis. Here, we present a new method which allows for a single-shot characterization of the spatial coherence, while being compatible with beam-pointing instabilities. The method is based on the far field interference produced by a 2D non-redundant array (NRA) of apertures, designed in a strategic configuration to disentangle, simultaneously, the degree of spatial coherence and the intensity distributions of a beam. We report a demonstration in single shot using an intense femtosecond HHG source. A statistical study of the spatial coherence fluctuations in different regimes shows the robustness of the method. This technique will find scientific applications at several ultrafast laser-based sources as well as X-ray free electron lasers and synchrotrons.

1. INTRODUCTION

Ultrafast soft and hard X-ray sources, whether high-harmonic generation (HHG) beamlines or X-ray free electron lasers (XFELs), present partial spatial coherence [1-3]. Moreover, these sources exhibit shot-to-shot variations of this parameter along with other spatial properties, including beam-pointing. The ultrashort pulse duration of such sources requires unambiguous single-shot characterization methods to address these phenomena. Current methods to characterize the spatial coherence of an X-ray beam either require parallel intensity

measurements [4-6], or the use of sequential measurements [1, 7-11], which are incompatible with a single-pulse characterization. Beam-pointing instabilities, which strongly affect HHG and XFEL sources, have been reported to be critical in coherence studies based on sequential single-shot measurements [1]. Besides the challenge of measuring this parameter with temporal resolution, the use of characterized X-ray sources had been seen to improve the quality of the results in multiple applications [12-18]. For example, knowing the coherence of a source helps to understand the physics behind the generation process [1, 4], opening the way to X-ray beam shaping. Furthermore, diffraction is based on the spatial coherence [19], making the knowledge of this parameter important for applications based on interferometric techniques. This is the case for example of lensless imaging, where the information on the partial coherence of the source can be used as input in phase-retrieval algorithms, to improve the image quality of 2D or even 3D reconstructions [13-16]. In this letter we propose and demonstrate a new method to measure the magnitude of the degree of spatial coherence of a source. The proposed technique is based on the interferometry through a 2D non-redundant array (NRA) of apertures, with different separation distances and orientations, allowing for spatial characterisation of the entire light field in a single shot. Moreover, the NRA design is strategically assembled to disentangle a shift-invariant degree of spatial coherence from the intensity distribution of a beam. This feature not only makes it independent of the intensity profile of the beam, but also compatible with beam-pointing instabilities, two critical parameters for conventional coherence measurement techniques in the soft and hard X-ray ranges [1].

2. METHODS

We propose to use an NRA to measure the spatial coherence of X-ray sources. The principle is based on the correlation between pairs of apertures $\{i, j\}$ ($i, j = 1, 2, \dots, N$) and can be understood as an extension of the Young double-aperture interferometer [5, 6, 11]. Here, series of double-pinhole interferograms, corresponding to different separation distances and orientations, are acquired simultaneously. The degree of spatial coherence is, then, retrieved from the Fourier transform (FT) of

the diffraction pattern of the field through the NRA. This Fourier spectrum has the form:

$$\tilde{I}(\vec{r}, z) = \Lambda(\vec{r}) \otimes \left[\sum_{i=1}^N I_i \delta(\vec{r}) + \sum_{i=j+1}^N \sum_{j=1}^{N-1} \sqrt{I_i I_j} \times \left\{ \mu_{ij} \delta(\vec{r} - \vec{d}_{ij}) + \mu_{ij}^* \delta(\vec{r} + \vec{d}_{ij}) \right\} \right], \quad (1)$$

where $\Lambda(\vec{r})$ is the autocorrelation of the function that describes the geometry of the apertures, (I_i, I_j) are the individual beam intensities at the correspondent apertures $\{i, j\}$ and μ_{ij} is the complex degree of spatial coherence. For an NRA, this consists of a distribution of peaks centered at the different separation vectors, $\vec{d}_{ij} = \vec{r}_i - \vec{r}_j$, between the apertures of the array. The magnitude of the spatial coherence for each pair of apertures $\{i, j\}$ is, then, estimated from:

$$|\mu_{ij}| = \frac{|C_{ij}| S_0}{\sqrt{I_i I_j} |C_0|}, \quad (2)$$

where $S_0 = \sum I_i$ is the total intensity of the field through the NRA and $|C_0|$ and $|C_{ij}|$ are, respectively, the magnitudes of the central peak of the Fourier spectrum and the peak centered at \vec{d}_{ij} [6].

With this basis, one can now generate an NRA of $N = 3$ apertures in a configuration where $|\vec{d}_{ij}|$ is constant for all the aperture-pairs $\{i, j\}$, Fig. 1(a). The autocorrelation of such array comprises six peaks located at each separation vector \vec{d}_{ij} , Fig. 1(b). From Eq. (2) we have a set of 3 equations. For a shift-invariant magnitude of coherence ($|\vec{d}_{12}| = |\vec{d}_{23}| \Rightarrow |\mu_{12}| = |\mu_{23}|$), which is true for all Gaussian-Schell beams [6,7,10,14], the solution for this set can be found in terms of the intensity of only one of the apertures. Considering this reference aperture I_1 , we obtain:

$$|\mu_{ij}| I_1 = \frac{c_{12} c_{13} S_0}{c_{23} |C_0|} \quad (3)$$

$$I_2 = I_1 \left(\frac{c_{23}}{c_{13}} \right)^2 \quad (4)$$

$$I_3 = I_1 \left(\frac{c_{23}}{c_{12}} \right)^2. \quad (5)$$

The multiplicative factors I_1 and $S_0/|C_0|$, from Eq. (3), can be normalized, after interpolation of the value of spatial coherence to $d_{ij} = 0$, where the condition $\mu_{ii} = 1$ holds. This allows a simultaneous disentanglement of both coherence and intensity contributions in the 3 apertures of the NRA. Using this configuration as basis, one can build NRAs with $N > 3$ apertures, generated by different elementary blocks with the spatial arrangement depicted in Fig. 1(a). With such scheme, the degree of coherence is found directly for a set of $N(N - 1)/2$ pairs of apertures, from one single interferogram and without intensity measurements. An example of NRA with 7 apertures alongside with its respective autocorrelation are presented in Fig. 1(c) and Fig. 1(d), respectively.

3. SINGLE SHOT DEMONSTRATION

A 5-aperture NRA was used to characterize the spatial coherence, in single shot of an argon-generated HHG source developed at CEA Saclay. This beamline, dedicated to single shot coherent diffractive imaging [12, 17, 20], is equipped with a

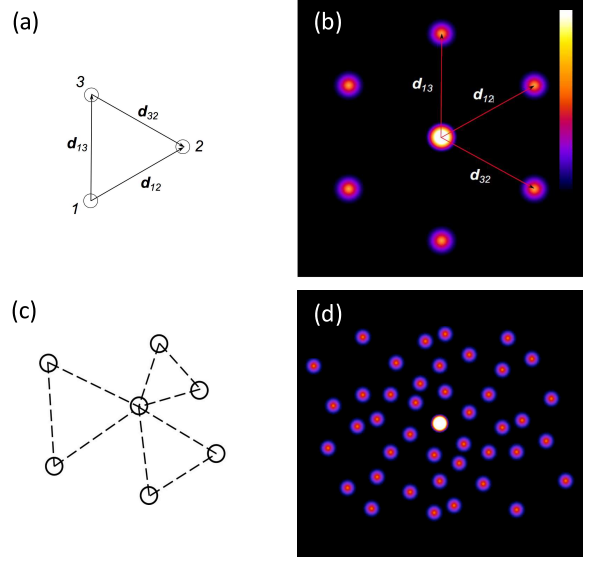


Fig. 1. (a) Array composed by 3 pinholes, with equal separation distances $|\vec{d}_{ij}|$. This NRA-set constitutes the elementary block for NRA's construction, in order to achieve intensity-independent measurements. (b) Autocorrelation of the NRA of (a), featuring the different separation vectors $|\vec{d}_{ij}|$ of the pairs of apertures that constitute the array. (c) Example of a more complex NRA, composed by three sets of elementary blocks from (a), highlighted with dotted lines. (d) Autocorrelation of the NRA from (c).

22.5° off-axis parabola that selects and focuses the 25th harmonic onto the NRA within a 4.5 μm focal spot (see Fig. 2(a)). The latter was designed to explore the degree of coherence over all the spatial extent of the beam (Fig. 2(b)). The far-field diffraction pattern was recorded with an XUV CCD camera, positioned 52-mm away from the sample. The camera sensor has 2048 \times 2048 pixels with 13.5 μm -pixels size. Fig. 2(c) shows an experimental diffraction pattern of the NRA acquired in a 20-fs duration shot. Fig. 2(d) presents the Fourier transform of the diffraction pattern of Fig. 2(c), i.e. the experimental autocorrelation of the NRA. We can find in Fig. 2(f), for comparison purposes, the corresponding simulation, acquired for a beam with a uniform intensity profile and full coherence. For both cases, one can observe the 10 peaks with respective conjugates, for the corresponding 10 pairs of holes. Based on the assumption that the coherence is shift invariant, then all the peaks associated with pairs of holes having the same $|\vec{d}_{ij}|$ have the same spatial degree of coherence. The amplitude variations amongst these peaks in Fig. 2(d) originate mostly from the non-uniform intensity profile at the NRA. The NRA autocorrelation of Fig. 2(d) provides two systems of equations, as Eqs. (3)-(5), given by the two sets of tri-equidistant circular references ($i, j = \{1, 2, 3\}$; $i, j = \{1, 4, 5\}$). From those, $|\mu_{ij}|$ was calculated for the respective $|\vec{d}_{ij}|$ values, with the intensity through the aperture 1 (see Fig. 2(b)) used as a common reference. The degree of spatial coherence of the remaining 4 aperture-pairs was obtained from Eq. (2), using the intensity calculated from Eqs. (4)-(5). The retrieved values are plotted as blue points in the graph of Fig. 2(e), where the red curve represents the respective Gaussian fit. The radius of the retrieved spatial coherence is 3.85 μm .

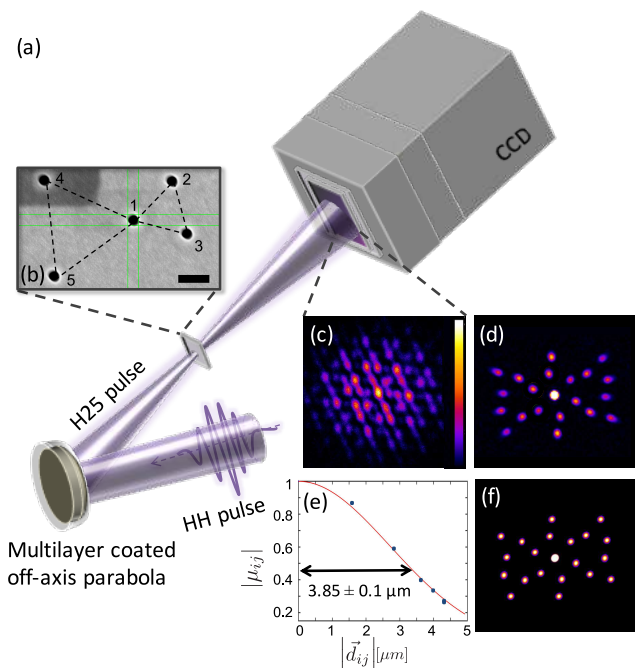


Fig. 2. (a) Single-shot setup used for the measurement of the degree of spatial coherence of the 25th harmonic. (b) SEM image of the NRA sample, consisting of a 75 nm-thick Si₃Ni₄ membrane with a 150 nm gold layer. The NRA has an overall size of 4.5 x 3.2 μm² with circular apertures of 310 nm. The two elementary blocks are connected with dotted lines, for better visualization. The scale-bar corresponds to 1 μm. (c) Measured single-shot diffraction pattern of H25 through the NRA shown in (b). (d) Fourier transform of the diffraction pattern shown in (c), which corresponds to the autocorrelation of the sample in (b). (e) Curve of the degree of spatial coherence, $|\mu_{ij}|$, retrieved from a Gaussian fit of the experimental values obtained for the different separation distances $|\vec{d}_{ij}|$. (f) Simulation of the autocorrelation of an array with the structure of (b), assuming uniform intensity and spatial coherence. Note that all peak values of this autocorrelation image are equal. The color scale of (c) denotes arbitrary units and is common for (c), (d) and (f).

4. ROBUSTNESS OF THE METHOD

A statistical study was performed over 100 single shot diffraction patterns. The HHG parameters were set to reach the highest HH power at the expense of shot-to-shot stability. In Fig. 3 the points in red correspond to the average of the coherence values $|\mu_{ij}|$ retrieved from the Fourier transform of the 21 successful diffraction patterns, over the whole data set. They correspond to the average of the coherence values achieved for the single-shot cases which allowed reconstructing all the peaks of NRA autocorrelation. The radius of the degree of spatial coherence was estimated to 4.1 μm. The $|\mu_{ij}|$ points in green were computed from the Fourier transform of the numerical accumulation of these 21 “best” diffraction patterns. The spatial coherence magnitude curve in green corresponds to a fit over these points, illustrating a case of an “ideal”-stable beam pointing. A radius of coherence of 3.6 μm was obtained. Finally, the coherence curve from the sum of the 100 diffraction patterns, corresponding to a real accumulation, is shown in purple. Note that the 79 “unsuccessful” patterns show missing peaks in the reconstruction of the NRA autocorrelation due to the high beam-pointing deviations, since the diameter of the beam

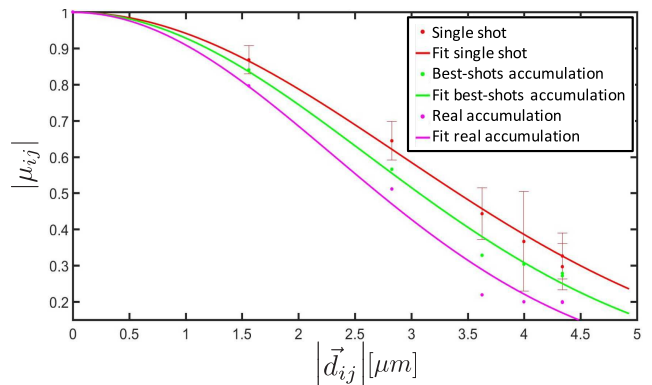


Fig. 3. Curves of the measured degree of spatial coherence, $|\mu_{ij}|$, obtained from the fitting of Gaussian functions to the experimental values, obtained for the different separation distances $|\vec{d}_{ij}|$. In red: degree of spatial coherence fitted from the $|\mu_{ij}|$ average values (red dots) obtained from single-shot diffraction patterns. The data were retrieved only from the 21 best diffraction patterns, which allowed reconstructing all the peaks of the NRA autocorrelation spectrum. The error bars correspond to the standard deviations of the $|\mu_{ij}|$ values. In green: coherence curve fitted from the $|\mu_{ij}|$ values (green dots) computed from the Fourier transform of the incoherent superposition of the same 21 diffraction patterns. In purple: spatial coherence function fitted from the $|\mu_{ij}|$ values (purple dots) computed from the Fourier transform of the incoherent superposition of all the 100 experimental diffraction patterns.

approaches the NRA size. The Gaussian fit points out a degraded degree of coherence with 3.3 μm radius. From the 100 patterns, the average standard deviation obtained for the 6-measured values of $|\mu_{ij}|$ was $\sigma_{\mu_{mean}} = 18\%$, while the maximum standard deviation reached $\sigma_{\mu_{max}} = 37\%$. From the experimental autocorrelations we estimated shot-to-shot intensity fluctuations in the order of $\sigma_I = 42\%$, a value retrieved from the standard deviations of the central-peak amplitudes.

The analysis pointed out a decrease of the experimental radius of the degree of spatial coherence in the accumulation of several shots during the acquisition, compared to the single-shot measurement. This can be explained by the difference between the analytical expression for the spatial coherence, Eq. (2), when considering the accumulation of “M” pulses, which is given by

$$|\mu_{ij}| = \frac{|C_{ij}|}{\sum_{k=1}^M \sqrt{I_i^k I_j^k}} \frac{S_0}{|C_0|}. \quad (6)$$

Indeed, using the accumulation of multiple pulses without individual intensity measurements supposes a unique intensity value for each aperture, which yields $I_N = \sum_{k=1}^M I_n^k$. This assumption induces a reduction of the calculated degree of spatial coherence, in which the error becomes stronger with the increase of the intensity variations from shot to shot. This can be understood from Eqs. (2) and (6) and as has been verified experimentally during an extensive study carried out for different generation parameters of the HH source. In the results presented in Fig. (3), the discrepancy between the average values of spatial coherence measured in the single shot case (red line) and cases of accumulation, was reduced from 20% when using all the 100 shots, down to 12% for the “ideal”-stable beam pointing accumulation. Nevertheless, for all the cases, the diameter of the degree of spatial

coherence of the beam was found to be larger than the focal-spot size, revealing a highly coherent source. The results are in agreement with previous results in coherent diffractive imaging experiments [12, 17, 20].

This further illustrates the effect of the beam-pointing, partial coherence and intensity fluctuations of the beam on the effective spatial coherence measurements through different techniques, under accumulation regimes. In the case of the Young double pinhole interferometer, to this beam-pointing instability error is added the error arising from the difference of the intensity between the two apertures, whose impact is even more critical [1].

To further test the accuracy of the method, the effect of beam-pointing fluctuations was simulated. With this purpose, the NRA of Fig. 1(c) was associated to a Gaussian distribution of intensity ($\sigma_I = 5.2 \mu\text{m}$) and a Gaussian degree of coherence ($\sigma_\mu = 4 \mu\text{m}$). The Fourier transform of the respective interferogram was simulated from Eq. (1). Two different beam-pointing cases are displayed in Figs. 4(a) and 4(c). Using the simulated values of C_0 and C_{ij} , and applying Eqs. (3)-(5), the degree of spatial coherence was retrieved assuming unknown intensity values for the two beam positions. The results are shown in Fig. 4(b) and 4(d). Despite the position-shift of the intensity profile with respect to the NRA, we see that the retrieved degrees of spatial coherence, for the two cases, show a good agreement.

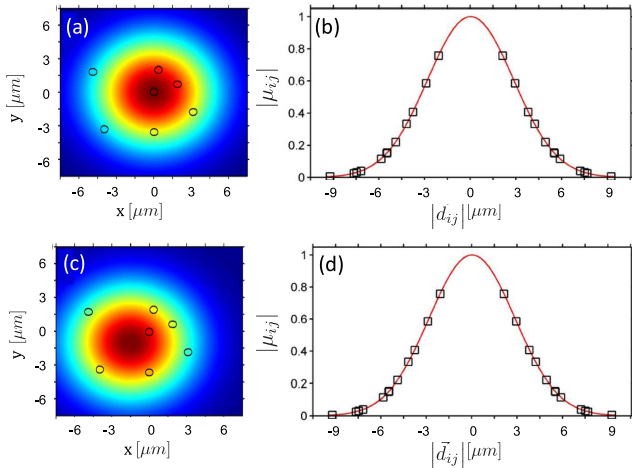


Fig. 4. Gaussian intensity profile (a) centered at the NRA reference aperture and (c) displaced $(-1.6; -1.1) \mu\text{m}$ from it. The aperture positions are denoted with black circles. (b), (d) Simulation of $|\mu_{ij}|$ as a function of the separation distance (red bold line) and retrieved values of the degree of spatial coherence (black squares) for the beam pointing cases (a) and (c), respectively. The calculation of the degree of spatial coherence was achieved after normalization of the intensity, without any assumption with respect to its profile.

5. CONCLUSIONS

In conclusion, we have demonstrated single shot characterization of the magnitude of the complex degree of spatial coherence of Gaussian-Schell beams. The method is based on the interferometry through an NRA, with different separation distances and orientations, allowing for a spatial characterization of the entire light field in a single acquisition. The method is robust with respect to beam-intensity and -pointing fluctuations, which are often critical for soft and hard X-ray sources, also affecting conventional coherence measurements. In the Young double-pinhole interferometer, for instance, there is interference of only one pair of apertures per shot and this pair should be symmetrically

centered in the beam, assuming equal intensity in both apertures. This, however, cannot be ensured when the beam pointing fluctuates [1].

The statistical analysis performed with the proposed technique pointed out a decrease of the degree of spatial coherence in the accumulation mode, when compared to single shot. The radius of the spatial coherence curve was observed to decrease from $4.1 \mu\text{m}$ to $3.6 \mu\text{m}$, in average, for the case of a perfectly stable beam pointing; and down to $3.3 \mu\text{m}$ for a "real", non-selective, accumulation. This can be explained by the effect of the accumulation from the analytical equations for the interference. Our HHG case of study shows that the source parameters and stability can be extremely critical. This applies also to FELs that exhibit high shot-to-shot beam properties fluctuations [1, 3]. These findings can have a direct impact in coherent imaging applications, such as CDI or holography, and can be exploited to correct for the partial coherence of the source. Overall, the simplicity and versatility of the method make it an important tool for single-shot spatial coherence characterization of the most varied sources, ranging from ultrafast laser-based sources to X-ray free electron lasers, X-ray plasma-based lasers and synchrotrons.

Funding. We acknowledge financial support from the European Union through the Future and Emerging Technologies (FET) Open H2020: VOXEL (grant 665207) and PETACom (grant 829153) and the integrated initiative of European laser research infrastructure (LASERLAB-EUROPE) (grant agreement no. 54148). Support from the French ministry of research through the 2013 Agence Nationale de Recherche (ANR) grants "NanoImagine", 2014 "ultrafast lensless Imaging with Plasmonic Enhanced XUV generation (IPEX)", 2016 High repetition rate Laser for Lensless Imaging in the XUV (HELLIX); from the DGA RAPID grant "SWIM", from the Centre National de Compétences en Nanosciences (C'NANO) research program through the NanosciX grant; the LABORatoire d'EXcelence Physique Atoms Lumière Matière LABEX PALM (ANR-10-LABX-0039-PALM), through the grants "Plasmon-X" and "High repetition rate Laser hArmonics in Crystals (HILAC)" and, finally, the Action de Soutien à la Technologie et à la Recherche en Essonne (ASTRE) program through the "NanoLight" grant are also acknowledged. We finally acknowledge financial support from Fundação para a Ciência e a Tecnologia (FCT) through X-ELS (PTDC/FIS-PLA/31868/2017).

Acknowledgment. The authors would like to acknowledge the support of Franck Fortuna and Laurent Delbecq from CSNSM, IN2P3, Orsay, for sample fabrication.

Disclosures. The authors declare no conflicts of interest.

REFERENCES

1. I. A. Vartanyants, A. Singer, A. P. Mancuso, O. M. Yefanov, A. Sakdinawat, Y. Liu, E. Bang, G. J. Williams, G. Cadenazzi, B. Abbey, H. Sinn, D. Attwood, K. a. Nugent, E. Weckert, T. Wang, D. Zhu, B. Wu, C. Graves, A. Scherz, J. J. Turner, W. F. Schlotter, M. Messerschmidt, J. Lüning, Y. Acremann, P. Heimann, D. C. Mancini, V. Joshi, J. Krzywinski, R. Soufli, M. Fernandez-Perea, S. Hau-Riege, A. G. Peele, Y. Feng, O. Krupin, S. Moeller, and W. Wurth, *Phys. Rev. Lett.* **107**, 144801 (2011).
2. L. Le Déroff, P. Salières, B. Carré, D. Joyeux, and D. Phalippou, *Phys. Rev. A* **61**, 043802 (2000).
3. A. Singer, F. Sorgenfrei, A. P. Mancuso, N. Gerasimova, O. M. Yefanov, J. Gulden, T. Gorniak, T. Senkbeil, A. Sakdinawat, Y. Liu, D. Attwood, S. Dziarzhytski, D. D. Mai, R. Treusch, E. Weckert, T. Salditt, A. Rosenhahn, W. Wurth, and I. A. Vartanyants, *Opt. Express*, **20**, 17480, (2012).
4. L. Le Déroff, P. Salières, B. Carré, D. Joyeux, D. Phalippou, P. Monot, P. D'Oliveira, T. Auguste, H. Merdji, and J.-F. Hergott, *Laser Phys.* **10**, 294 (2000).

5. Y. Mejía and A. I. González, *Opt. Commun.* **273**, 428 (2007).
6. A. I. González and Y. Mejía, *JOSA A* **28**, 1107 (2011).
7. M. Santarsiero and R. Borghi, *Opt. Lett.* **31**, 861 (2006).
8. B. Thompson and E. Wolf, *JOSA* **47**, 895 (1957).
9. S. Cho, M. A. Alonso, and T. G. Brown, *Opt. Lett.* **37**, 2724 (2012).
10. K. A. Sharma, T. G. Brown, and M. A. Alonso, *Opt. Express* **24**, 16099 (2016).
11. F. Kashani, M. R. H. Rad, and B. Ghafary, *Optik* **123**, 1317 (2012).
12. X. Ge, W. Boutu, D. Gauthier, F. Wang, A. Borta, B. Barbreil, M. Ducouso, A. I. Gonzalez, B. Carré, D. Guillaumet, M. Perdrix, O. Gobert, J. Gautier, G. Lambert, F. R. N. C. Maia, J. Hajdu, P. Zeitoun, and H. Merdji, *Opt. Express* **21**, 11441 (2013).
13. L. Whitehead, G. Williams, H. Quiney, D. Vine, R. Dilanian, S. Flewett, K. Nugent, A. G. Peele, E. Balaur, and I. McNulty, *Phys. Rev. Lett.* **103**, 243902 (2009).
14. G. J. Williams, H. M. Quiney, A. G. Peele, and K. A. Nugent, *Phys. Rev. B* **75**, 104102 (2007).
15. P. Thibault and A. Menzel, *Nature* **494**, 68 (2013).
16. J. Clark, X. Huang, R. Harder, and I. Robinson, *Nat. Commun.* **3**, 993 (2012).
17. D. Gauthier, M. Guizar-Sicairos, X. Ge, W. Boutu, B. Carré, J. R. Fienup, and H. Merdji, *Phys. Rev. Lett.* **105**, 093901 (2010).
18. U. Gopinathan, G. Pedrini, and W. Osten, *JOSA A* **25**, 2459 (2008).
19. J. W. Goodman, *Introduction to Fourier Optics*, 3rd ed. (Roberts and Company, 2005), p. 63.
20. J. Duarte, R. Cassin, J. Huijts, B. Iwan, F. Fortuna, L. Delbecq, H. Chapman, M. Fajardo, M. Kovacev, W. Boutu, and H. Merdji, *Nat. Photonics* **13**, 449 (2019).

Titre : Imagerie Nanométrique 3D Ultrarapide par Rayons X Cohérents

Mots clés : Imagerie 3D, rayons X cohérents, Lasers, Femtoseconde

Résumé : Les techniques d'imagerie sans lentille permettent d'aller au-delà des limites inhérentes à la microscopie classique (à l'aide de lentille par exemple). La configuration d'imagerie par diffraction cohérente permet d'imager des objets non-cristallins à des résolutions limitées en principe à la longueur d'onde (soit quelques dizaines de nanomètres à quelques angströms dans le domaine XUV à X, respectivement). Le travail de cette thèse a consisté à développer et améliorer, expérimentalement et numériquement, des nouvelles techniques d'imagerie 2D et 3D, de résolution nanométrique et en simple tir femtoseconde. Nous constatons cependant que les techniques d'imagerie sans lentille peuvent être limitée par les aberrations et

la cohérence partielle. Des améliorations des techniques d'holographie par correction de front d'onde et de la cohérence sont proposées. In fine, l'exploitation des propriétés de la source permet l'optimisation de la lecture des figures de diffraction ou des hologrammes afin d'obtenir une image la plus fidèle possible en un flash femtoseconde unique. En exploitant des concepts de vision machine, cette thèse a ensuite montré la possibilité d'accéder à la 3D en simple tir à partir de deux figures de diffraction X cohérente prise simultanément sur deux angles stéréo. Ceci ouvre la voie à l'exploration de la matière sur des volumes nanométriques (voxels) résolus à la femtoseconde.

Title : Ultrafast Nanoscale 3D Coherent X-ray Imaging

Keywords : 3D Imaging, Coherent X-rays, Lasers, Femtosecond

Abstract : Coherent lensless imaging techniques can break the limitations associated with conventional microscopy techniques. The configuration of coherent diffraction imaging makes it possible to image isolated non-crystalline objects with spatial resolutions limited, in principle, only by the illuminated wavelength (i.e. a few tens of nanometres to a few angstroms in the XUV and X domains, respectively).

In this thesis, we develop and improve, experimentally and numerically, 2D and 3D lensless imaging techniques, for nanometric resolutions in a femtosecond single shot. Responding to the limitations of these techniques to aberrations and partial coherence,

here, improvements of wavefront and spatial-coherence correction in holographic techniques are proposed. Indeed, the exploitation of the source properties makes possible to optimise the reconstruction from diffraction patterns or holograms in order to obtain the most faithful image possible in a single femtosecond flash. By exploiting machine vision concepts, this thesis also shows the possibility of accessing 3D information in single shots, extracted from two coherent X-ray diffraction patterns, taken simultaneously from two stereo angles. This opens the way towards the exploration of matter on nanometric volumes (voxels) solved at unmatched temporal resolutions.

